Lignin based materials for energy storage applications

A dissertation presented by

Nagore Izaguirre Arostegui

In Fulfilment of the Requirements for the Degree Doctor of Philosophy in Renewable Materials Engineering by the University of the Basque Country UPV/EHU

Under the supervision of

Dr. Rodrigo Llano-Ponte & Dr. Xabier Erdocia

Chemical and Environmental Engineering Department

Faculty of Engineering of Gipuzkoa

Donostia-San Sebastian

2024

Universidad del País Vasco Euskal Herriko Unibertsitatea

“Every accomplishment starts with the decision to try.”

- *Anon*

Agradecimientos

Echo la vista atrás a mis comienzos en esta aventura, y me es inevitable pensar en cuánto he cambiado y evolucionado estos últimos años. Ha supuesto una etapa esencial en mi desarrollo profesional, pero sobre todo personal. He descubierto una profesión que me apasiona, la cual me ha enseñado que con esfuerzo y trabajo duro las recompensas saben mejor, y me he llevado lecciones de vida que sin duda me acompañarán siempre.

En primer lugar quisiera agradecer a mi tutor el Dr. Jalel Labidi y a mis directores de tesis el Dr. Rodrigo Llano-Ponte y el Dr. Xabier Erdocia por depositar su confianza en mí y darme la oportunidad de realizar la tesis bajo su supervisión. Gracias por confiar en mí y darme la libertad de realizar el trabajo. Quisiera agradecer también al Gobierno Vasco por concederme la ayuda de la Formación de Personal Investigador y a la Universidad del País Vasco UPV/EHU, en especial al departamento de Ingeniería Química y Medio Ambiente por acogerme estos años.

Gracias también al Dr. Claudio Gerbaldi y a su grupo GAME Lab, por acogerme y enseñarme durante mi estancia en el Politecnico di Torino, no solo sus conocimientos en electroquímica, también su calidad humana. Gracias también a Polymat, en especial a David Mecerreyes y su grupo, por darme opción a continuar trabajando y aprendiendo del tema en sus instalaciones.

Gracias a mis compañeros del grupo BioRP por la ayuda brindada. Gracias, en especial, a los que habéis hecho del laboratorio mi segundo hogar. Por hacer más amenas esas jornadas interminables y aconsejarme y ayudarme cuando lo he necesitado. Gracias por la cálida acogida a los que estuvisteis en los comienzos, por animarme a empezar y darme la seguridad que necesitaba para creer en mí. A los que estuvisteis durante y seguís estando

ahora, por hacer de mis logros los vuestros y acompañarme cuando más sola y perdida me sentía. Gracias por ser y estar, antes durante y espero que después. Por entendernos entre nosotros e impulsarnos a ser mejores. Gracias a las personas que vinieron de estancia también, por traer un soplo de aire fresco. Cómo no a 'los de arriba', por los *coffee-breaks*, *lunch-breaks* y múltiples otros *breaks* que nos han servido como aliento en nuestra rutina. Han sido fuente de innumerables anécdotas que recordaremos con una sonrisa.

Gracias a mis amigas, las que me traen de vuelta a la realidad, las que me hacen desconectar y ver el mundo desde otra perspectiva. Las que me empujan a luchar y a sacar las garras. Sois incondicionales y os quiero infinito.

Gracias por último a mi familia, mi pilar. Gracias a vosotros soy quien soy. A mi padre por inculcarme valores como el trabajo duro y la perseverancia. A mi madre por siempre estar ahí, por sufrir y celebrar cada momento como si fuera suyo. A mi hermana, por ser mi mayor ejemplo. Por haberme abierto camino y enseñado que lo difícil suele merecer la pena.

Gracias a todas y cada una de las personas que me han acompañado y han dado sentido a los momentos vividos, los altos y los bajos, los llantos y las alegrías, porque lo que hace que un momento sea memorable son las personas con la que los compartes.

Eskerrik asko bihotzez,

Summary

The current energy scarcity requires not only more sustainable practices but also the exploration of unlimited energy sources. To consider energy as sustainable, three factors should be considered: the renewability of the energy source, the adequacy of the storage methods, and the sustainability of energy transport. Essential components for the fulfillment of these requirements are energy storage devices.

Alongside the transition to sustainable energy generation and consumption, there is a growing demand for increased capacity and durability, as well as simpler commodity products being extensively employed as various gadgets. This trend has created a higher demand for materials used in energy storage devices.

However, the materials currently in use are often scarce, and require specific production and utilization processes, resulting in a higher embodied energy in their constituents compared to what they will consume. Therefore, it is essential to develop low-cost, simple-to-process, and environmentally friendly innovative materials. Significant efforts have been made to substitute commonly used inorganic materials with organic alternatives. Recently, even more ambitious plans have emerged to implement "green" materials and technologies.

One such material that aligns perfectly with the requests for green processes and materials is lignocellulosic biomass. It is highly abundant, and a low-cost organic precursor. Moreover, it offers economically feasible and low-cost processing methods. While it has been extensively studied for energy conversion to obtain biofuels, a more recent approach involves utilizing this lignocellulosic biomass as energy storage material, thereby presenting a sustainable alternative to the currently used materials.

A constituent of the lignocellulosic material, until now mostly considered as waste, albeit its versatility, is lignin. It is the most abundant aromatic biopolymer found on earth, with a very complex structure and high heterogeneity. Despite these complexities, lignin is versatile, with plausible applications where it can be incorporated to obtain high-value-added products.

Current research efforts are focusing on incorporating lignin as an energy storage material. The most explored path involves its conversion into carbon. However, this process remains energy-intensive, and alternative methods such as chemical modifications or composite materials have been studied.

This work focuses on the integration of lignin into energy storage materials. For that, various lignin treatments were designed. Lignin was sequentially dissolved to obtain fractions of different molecular weight, resulting in lignins with distinct chemical structures and properties. Moreover, lignin was subjected to numerous modifications to change its functionality and to obtain the one with optimum performance for the selected application.

Finally, composite materials composed of active components and lignin were developed and characterized electrochemically. Alternatively, the modified lignins were employed in the formulation of electrode materials, and half-cell batteries were assembled and tested to evaluate their performance.

Nomenclature

^{13}C NMR	Carbon-13 Nuclear Magnetic Resonance
^{31}P NMR	Phosphorus-31 Nuclear Magnetic Resonance
AC	Activated carbon
AC-KL	Activated carbon-Kraft lignin composites
AC-OL	Activated carbon-organosolv lignin composites
AFM	Atomic Force Microscopy
AIL	Acid Insoluble Lignin
AL	Alkaline Lignin
ASL	Acid Soluble Lignin
BET	Brunauer–Emmett–Teller (BET) method
BKL	Big Kraft lignin
BOL	Big organosolv lignin
C1	Capacitive value of the very low frequency range of the ECM
C2	Capacitive value of the very high frequency range of the ECM
C3	Capacitive value of the high frequency range of the ECM
C4	Capacitive value of the intermediate frequency range of the ECM
C45	Super C45 Carbon Black
CA	Carbohydrates
CAH	Concentrated Acid Hydrolysis
CE	Counter Electrode
CM	Carboxymethylation
CMC	Carboxymethyl cellulose
CMCS	Carboxymethyl chitosan
CMKL	Carboxymethyl Kraft lignin
CML	Carboxymethyl lignin
CMOL	Carboxymethyl organosolv lignin
C_p(CV)	Capacitance calculated from Cyclic Voltammetry
C_p(EIS)	Capacitance calculated from Electrochemical Impedance Spectroscopy
C_p(GCD)	Capacitance calculated from Galvanostatic Charge Discharge
CPE	Constant Phase Element

CV	Cyclic Voltammetry
CVD	Chemical vapor deposition
DAH	Dilute acid hydrolysis
DAP	Dilute acid pretreatment
DCA	Dicarboxylic acid
DE	Delignified eucalyptus
DES	Deep Eutectic Solvents
DLS	Dynamic Light Scattering
DMC	Dimethyl carbonate
DMK	Dimethyl Ketone or Propan-2-one
DMSO	Dimethyl sulfoxide
DOE	Design of Experiments
DRT	Distribution of relaxation time
DSC	Differential Scanning Calorimetry
DTGA	Derivative of the Thermogravimetric analysis
E	Eucalyptus
EA	Elemental Analysis
EC	Ethylene carbonate
ECM	Equivalent Circuit Models
EDLC	Electric double-layer capacitors
EHL	Enzymatically hydrolyzed lignin
EIS	Electrochemical Impedance Spectroscopy
E_S	Energy density
ES	Energy storage
EtOAc	Ethyl acetate
EtOH	Ethanol
F1	Fraction soluble in iPrOH
F2	Fraction soluble in EtOAc
F3	Fraction soluble in EtOH
F4	Fraction soluble in DMK

FI	Fraction Insoluble
FTIR	Fourier Transformed Infrared
G	Graphite
G units	Guaiacyl units
GCD	Galvanostatic Charge Discharge
G-KL	Graphite-Kraft lignin composite
GO	Graphite oxide
GO-KL	Graphite oxide-Kraft lignin composite
G-OL	Graphite-organosolv lignin composite
GO-OL	Graphite oxide-organosolv lignin composite
GPC	Gel Permeation Chromatography
GPE	Gel Polymer Electrolyte
H units	p-Hydroxyphenyl units
HC	Biohard carbon
HPMC	Hydroxy propyl methyl cellulose
I_d	Specific current
IL	Ionic Liquid
i-PrOH	Propan-2-ol
KL	Kraft lignin
L1	External elements of the ECM
L-AC	Lignin-Active carbon composites
LCP	Poly(N-vinyl imidazole)-co-poly(poly(ethylene glycol) methyl ether methacrylate)
LDAM	Low density aromatic monomers
L-G	Lignin-Graphite composites
LIB	Lithium-ion battery
LiFSI	Lithium bis(fluorosulfonyl)imide
LiTFSI	Lithium bis(trifluoromethanesulfonyl)imide
LMWPC	Low molecular weight phenolic compounds
LPE	Liquid-phase exfoliation

LS	Lignosulfonates
MBKL	Methylated big Kraft Lignin
MEK	Methyl Ethyl Ketone or Butan-2-one
MeOH	Methanol
MKL	Methylated Kraft Lignin
ML	Methylated Lignin
M_n	Average molecular number
MOL	Methylated organosolv lignin
MSKL	Methylated small Kraft lignin
MSOL	Methylated small organosolv lignin
M_w	Average molecular weight
NIB	Na-ion batteries
NMC	$LiNi_xMnyCo_zO_2$
NMP	N-methyl-2-pyrrolidone
n-PrOH	*n*-Propanol or Propan-1-ol
NREL	National Renewable Energy Laboratory
OL	Organosolv lignin
OxL	Oxidized lignin
OxKL	Oxidized Kraft lignin
OxOL	Oxidized organosolv lignin
PAN	Polyacrylonitrile
PC	Pseudocapacitor
PE	Polyethylene
PEDOT	Poly(3,4-ethylene dioxythiophene)
PEG	Polyethylene glycol
PEO	Polyethylene oxide
PI	Polydispersity index
post-GCD	Post-Galvanostatic Charge Discharge
PP	Polypropylene
PPy	Polypyrrole

pre-GCD	Pre-Galvanostatic Charge Discharge
PSD	Pore size distribution
PVA	Poly(vinyl alcohol)
PVDF	Poly(vinylidene difluoride)
PVDF-HFP	Poly(vinylidene difluoride-co-hexafluoropropylene) copolymer
PVP	Polyvinylpyrrolidone
Py-GC/MS	Pyrolysis-gas chromatography-mass spectrometry
$Q(I_d)$	Specific capacity
QAH	Quantitative Acid Hydrolysis
R1	Resistance value of the very low frequency range of the ECM
R2	Resistance value of the very high frequency range of the ECM
R3	Resistance value of the high frequency range of the ECM
R4	Resistance value of the intermediate range of the ECM
R_∞	Electrolyte resistance
R_{ct}	Charge transfer resistance
R_{d1}	Diffusion resistance
RE	Reference electrode
RT	Room Temperature
R_{mt}	Mass transfer resistance
R_p	Electrode resistance
S units	Syringyl units
S/G	Syringyl/Guaiacyl units ratio
SC	Supercapacitor
SCA	Sodium chloroacetate
SCE	Saturated calomel electrode
SEI	Solid electrolyte interphase
SEM	Scanning Electron Microscopy
SKL	Small Kraft lignin
SM	Sulfomethylation
SMKL	Sulfomethylated Kraft lignin

SML	Sulfomethylated lignin
SMOL	Sulfomethylated organosolv lignin
SOL	Small organosolv lignin
SOSE	Sequential Organic Solvent Extraction
SPE	Solid Polymer Electrolyte
SSA	Specific surface area
T	Temperature
t	time
$T_{5\%}$	Temperature at which 5% of the mass degraded
$T_{50\%}$	Temperature at which 50% of the mass degraded
TAC	Treated activated carbon
TAC-KL	Treated activated carbon-Kraft lignin composite
TAC-OL	Treated activated carbon-organosolv lignin composite
TAPPI	Technical Association of the Pulp & Paper Industry
TBAP	Tetrabutylammonium perchlorate
t-BuOH	*tert*-Butanol or 2-Methylpropan-2-ol
t_{d1}	Diffusion time
TEM	Transmission Electron Microscopy
TGA	Thermogravimetric analysis
TPC	Total phenolic content
UALPE	Ultrasonic-assisted liquid phase exfoliation
US	Ultrasound
UV	Ultraviolet
V_d	Specific voltage
W_{d3}	Warburg element
WE	Working Electrode
X1	Temperature variable in DOE
X2	Time variable in DOE
X3	Hydrogen peroxide variable in DOE
XPS	X Ray Photoelectron Spectroscopy
Y_{ZP}	Dependent variable in DOE

Z_{imag}	Z imaginary
ZP	Z Potential
Z_{real}	Z real

Table of Contents

4. LIGNIN FRACTIONATION

ANNEX I

1. Introduction

1.1. Current Status and Sustainable Energy

The current environmental issues we are nowadays facing are widely known for some time now. Our present habits of overconsumption and wastefulness are no longer sustainable from the environmental or the energetic aspect. The greenhouse gas emissions are having devastating effects on nature, and the fulfillment of the high energy demands by the utilization of fossil fuels not only aggravates this situation but also creates a need for an alternative since the rhythm at which these fossil fuels are utilized is higher than the one at which they are produced. All this generates an energetic scarcity that should be overcome by other more sustainable and unlimited alternatives [1].

Sustainable energy is defined as "meeting the needs of the present without compromising the ability of future generations to meet their own needs" [2]. This issue must be addressed from 3 different perspectives. On one side, energy needs to come from renewable sources like wind, solar, and water. Besides, the energy generated needs to be stored properly and used effectively. Lastly, ways of transportation need to be sustainable, with effective and efficient means without having an impact on the environment [3].

Transport systems are key to providing citizens with social and economic connections. However, very few households can maintain this carbon-neutral system, and 95% of the fuel used for this purpose comes from fossil sources, being the main contributor of greenhouse gas emissions and consuming 20-25% of the worldwide energy. Some greener alternative vehicles are becoming more common on the market as substitutes for gasoline and diesel cars, with different technologies implementing a more sustainable practice. Some of the most common are hybrid electric, battery electric, fuel-cell, and hydrogen vehicles, which drastically decrease the

impact of greenhouse emissions, some even reaching net-zero emission values when the electricity is sourced from renewable alternatives [4].

Apart from that, the conservation of energy is an important factor to consider. This way, fewer energy sources will be needed and wasteful consumption will be avoided. It is an essential factor when designing and building constructions, even comprising everyday consumer products and commodities, such as energy-efficient semiconductor lamps and occupancy sensors [5].

Finally, renewable energy sources, which are naturally replenished on a human timescale, like wind, sunlight, water movements, and geothermic heat, are essential for the sustainability. Unfortunately, these types of energy productions vary depending on the climate and geographical points, needing more efficient energy storage to optimize the reservoir and avoid the loss of the energy produced when climatic conditions are prolific. Therefore, efficient storage devices are key for the extensive usage and applicability of renewable energy and sustainable transportation [6].

Besides the obvious environmental benefits, the advantages obtained from sustainability are also related to health and social equality. Diseases like coronary heart disease, strokes, obstructive lung disease and cancer, and lower respiratory tract infections are some of the most common associated with environmental pollution [7]. Also, social and economic aspects affect the disadvantaged social groups the most, suffering among other things from energy poverty, and becoming especially vulnerable when fossil fuel prices increase drastically and unexpectedly [8].

Current efforts on transforming our carbon-emissions-intensive environment into carbon-emission-free are essential, and with that comes the need for energy storage devices with increased capacity and durability.

In conjunction with that, new commodity products present in our everyday life, which are more and more specific due to the new needs conceived and technological advances, create a need for more versatile and specific manufacturing processes, where materials with nanoscale-functionalities are produced. Due to the distinct production and utilization of already scarce materials, modern electronics have more embodied energy in their inner constituents than what they will consume [9,10].

Consequently, the need to develop low-cost and environmentally friendly innovative materials is vital. Big efforts have been made to substitute the commonly used inorganic materials for organic ones, but recently, even more ambitious plans to implement "green" materials and "green" technologies have emerged. The aim is to utilize highly abundant and low-cost organic precursors, with economically-feasible and low-cost processing able to biodegrade when electronic materials reach the end of their life cycle [10].

A type of material that perfectly matches the requests for green processes and materials is lignocellulosic biomass. It has been widely studied as a power generator, where thermochemical and biological conversions of lignocellulose have been carried out to obtain biofuels. However, a more recent approach is to use this lignocellulosic biomass as energy storage material, where various attempts to substitute currently used materials have been made, both utilizing the whole lignocellulose and its isolated components, mainly cellulose and lignin [11].

A graphical description of the subject is visible in Figure 1.1.

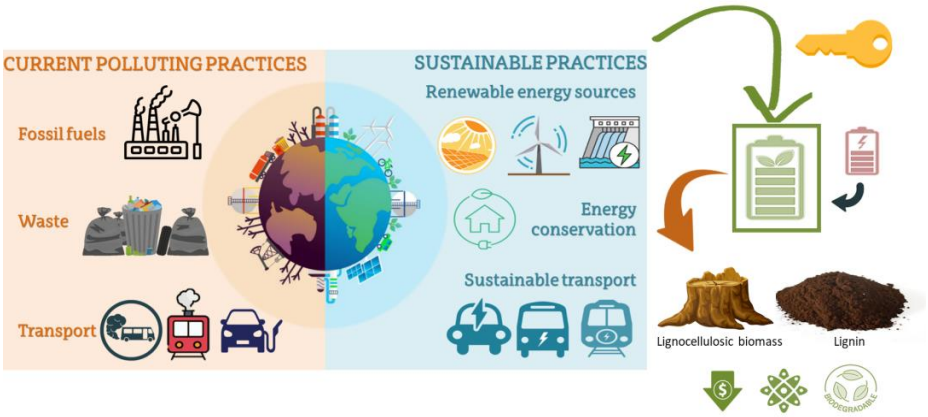

Figure 1.1. The graphical description of current vs. sustainable practices and the key to the development of sustainable energy storage devices.

1.2. LIGNOCELLULOSIC BIOMASS

Lignocellulosic biomass is the most abundant raw material found in nature. It comprises two carbohydrate polymers (cellulose and hemicellulose) and lignin, a heterogeneous aromatic polymer, linked with each other in three-dimensional structures and non-uniform ways [12]. Cellulose is the main component, composing the lignocellulose cell wall, and forming long and oriented microfibrils, which then form longer fibrils [13]. Hemicelluloses are branched, single-chained, and amorphous polymers, forming non-covalent cross-links with cellulose fibrils [14].

Adversely, lignin fills the free spaces between cellulose and hemicellulose in the plant cell wall, holding together the lignocellulose matrix. It provides rigidity and strength to plant tissues, controls the fluid flow, and protects the plant from biochemical stresses [15]. Biomass composition can depend on various factors like source or environmental factors, but generally, 40-60% of the total dry matter of biomass is composed of cellulose, followed by 10-40% of hemicellulose, and 7-35% of lignin [16].

Cellulose is a linear polymer consisting of the dimer D-anhydroglucose units covalently linked by β-1,4-glycosidic bonds, consisting of 500-1400 units, with varying polymerization degrees depending on the source. Hemicelluloses are composed of different saccharides (pentoses, hexoses, uronic acid groups, and acetyl groups) in different proportions, depending on the source. Finally, lignin is a three-dimensional polymer composed of three different units, p-hydroxyphenyl (H), syringyl (S), and guaiacyl (G), which are formed by the so-called monolignols p-coumaryl alcohol, coniferyl alcohol, and sinapyl alcohol respectively (shown in Figure 1.2).

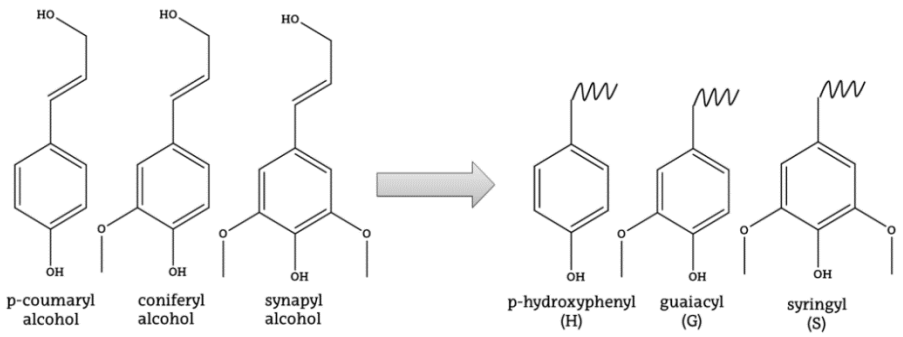

Figure 1.2. Lignin alcohols and monolignols.

These units are interconnected by different bonds, some condensed (β-O-4, α-O-4, and β-β), and some others uncondensed (β-5, β-1, and 5-5). Similarly to hemicellulose, the exact composition varies depending on the source. In general, softwood lignin is only composed of G units, while hardwood lignin contains both S and G units, and herbaceous biomass lignin has all three of the units, although H units are usually below 5%. Otherwise, softwoods are known to have the highest amount of lignin (21-29 wt%), followed by hardwoods (18-25 wt%) and herbaceous biomass (15-24 wt%) [17].

Lignin is randomly polymerized by radical reactions without any specific order and always depends on the monolignols present in the biomass. Adding the fact that unmodified lignin cannot be extracted from nature, it is not possible to determine the species composition and structure of this complex biopolymer.

It is essential to break the lignin-carbohydrate complexes to obtain lignin. However, during the process other linkages present in the lignin macromolecule also break, causing its depolymerization to some extent. The most commonly broken linkage is β-*O*-4, so hardwoods tend to degrade more than softwoods during the process due to the higher content of this linkage. The average percentage values of monolignol units and linkages for each lignocellulosic biomass type are listed in Table 1.1 and illustrated in Figure 1.3.

Table 1.1. Lignin composition and most common linkages depending on the source [18].

	Softwoods	***Hardwoods***	***Herbaceous***
Monolignol units	mainly G	G and S	G, S, and H
S	95-100%	≈50%	20-54%
G	0-5%	≈50%	33-88%
H	-	-	5-33%
		Linkages	
β-O-4	45-60%	60-62%	74-84%
β-5 and 5-O-4	9–12%	3–11%	5–11%
β-β and γ-O-α	2–6%	3-12%	1–7%
(5-5), (α-O-4), and (β-O-5)	5-7%	<1%	-
(4-O-5)	1-9%	1-7%	-
(β-1) and (α-O-α)	2%	2%	-

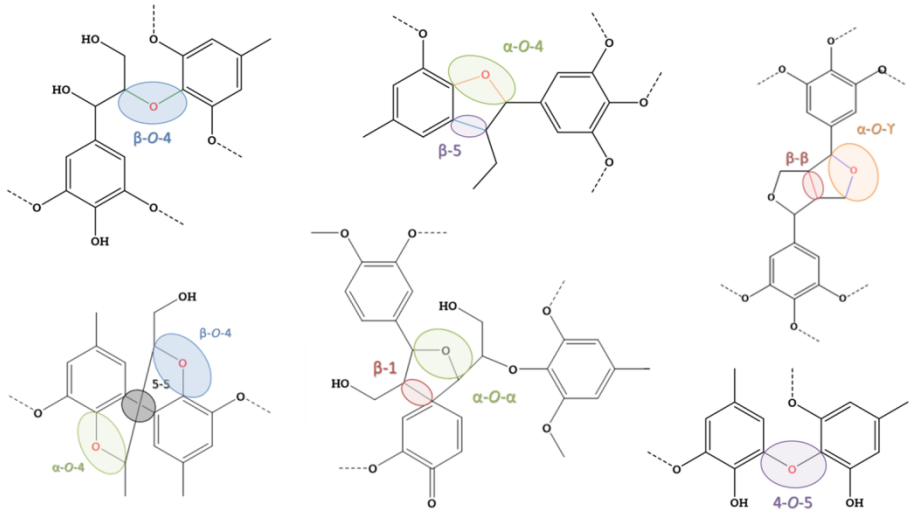

Figure 1.3. The most common linkages in lignin macromolecules.

There are some applications in which lignocellulose is utilized as received, others where a pretreatment needs to be carried out, and some others in which lignocellulosic components have to be separated. This last procedure is especially interesting for obtaining optimum applicabilities for each compound, since they have quite different structures and compositions, and can suit different purposes. Cellulose isolation has been extensively carried out for centuries, making paper one of the most used products in everyday life, composed entirely of cellulose. Adversely, lignin has been considered a waste from the paper industry for decades, ignoring its great potential for a wide variety of applications due to its complex structure and high aromaticity, unique quality for biomaterials.

Within the complex aromatic structure of lignin, some functional groups are interesting to further valorize lignin for more specific high-value applications. The aliphatic and phenolic hydroxyl groups are the most reactive functional groups, but methoxy groups can also be found extensively. Not having enough complexity by itself, isolation or lignocellulosic fractionation processes greatly influence the characteristics

of the lignin obtained, as the process can alter the structure of functional groups of the molecules [19].

1.3. LIGNIN ISOLATION

The treatment carried out on the biomass also affects the lignin obtained, each treatment having its own specific modified lignins. C-C bond cleavage, condensation degree, molecular weight, and variations in the number of functional groups are important differences affecting the applications to which they can be targeted [18].

The lignin isolation methods can be divided into two types. The first one, referred to as the delignification process, encompasses ways in which lignin has been separated from the other components by its solubilization. The other, liberates lignin from its matrix, by the conversion of cellulose and hemicellulose into carbohydrates.

1.3.1. DELIGNIFICATION PROCESSES

There are various delignification methods, based on different alterations of lignin for its solubilization. The most common and widely spread method at the industrial scale is alkaline delignification. Different processes can be found depending on the reactants and conditions used, but they are all based on solubilizing lignin and obtaining delignified biomass. Alkaline media enables the deprotonation of phenolic hydroxyl groups, promoting its solubilization, as well as its separation from the hemicellulose by the cleavage of lignin-carbohydrate bonds, and its fragmentation by the breakage of the β-*O*-4 bond. Over 90% of all the chemical pulp produced comes from the Kraft pulping process [17]. It is carried out in a NaOH and Na_2S aqueous solution, where HS^- ions present in the medium enhance the delignification process, obtaining high-quality pulp. However, the harsh

conditions of the process induce degradation and repolymerization of lignin, obtaining highly condensed molecules, with few β-*O*-4 bonds, and thiol groups in the form of a solution referred to as black liquor. The lignin dissolved can be separated and recovered by acid precipitation, but it is mainly incinerated to obtain energy that fulfills the requirements of the pulping process. In addition, the chemicals employed are recovered. Thus, this process is the most widespread [20].

Kraft lignin (KL) is considered a high molecular weight lignin type, due to the condensation reactions that happen during the Kraft-pulping process. It is precipitated by the addition of acid: phenolic compounds in lignin get protonated, their hydrophilicity reduces, and eventually, it precipitates. The same mechanism is applied in the LignoBoost technology, designed in 2002 to maximize lignin yields and eliminate salt impurities [21]. Another approach was developed to eliminate the sulfite compounds created during the pulping process, called LignoForce [22]. This method is based on the oxidation of lignin to remove sulfide compounds that highly limit its applicability.

The sulfite process is the second most important pulping process, also based on alkaline delignification. In this case, sulfite (SO_3^{2-}) or bisulfite (HSO_3^-) salts are used to react and sulfonate the active sites of lignin (α-positions of the aromatic rings) creating benzyl sulfonate groups, highly soluble in water, even in acidic media. This property makes lignosulfonates (LS) interesting for further applications [23]. However, the high degradation rate and high sulfur content of the lignin, as well as the drastic decrease in the market share, make it an uncertain prospect to use as feedstock [24].

Soda pulping is the third traditional pulping process, usually used for the pulping of non-woody biomass. It is a similar process to the Kraft but without the addition of Na_2S, which reduces depolymerization reactions,

yielding alkali-stable enol ether motifs. Another soda pulping process applied to herbaceous biomass is the aqueous alkali pretreatment, a treatment also using NaOH but applying milder conditions and obtaining liquors rich in monomeric phenols, lignin oligomers, and hydroxyl acid derived from carbohydrates. Some other alkaline methods rely on liquid or anhydrous ammonia instead of NaOH, which is easily recovered [25].

Acidic media can also promote biomass fractionation, in this case, promoting the hydrolysis of the carbohydrate polymers (hemicellulose and cellulose). Acidic media also affects lignin, causing the cleavage of the β-*O*-4 bond and the removal of the hydroxyl in the α-position, forming the intermediate benzylic carbenium ions, which can repolymerize or further react with the proton to enol ethers. Dilute acid pretreatment (DAP) fragments lignin and partially solubilizes it along with the hemicellulose. When it is carried out in batch mode, lignin condenses and redeposits on the unsolubilized biomass. A flow-through mode can be applied to avoid this and delignify lignin more efficiently, removing the solubilized lignin fractions from the heating zone, avoiding redeposition, yielding hemicellulose carbohydrates, and lignin oligomers and monomers. However, the complete isolation of lignin from the liquor remains a challenge. An alternative method is steam explosion pretreatment, which consists of creating pressure with steam/water followed by a sudden pressure release that opens the matrix of the lignocellulosic biomass disrupting the fibers and easing the lignin extraction [26].

Switching aqueous solvents for organic can considerably increase the delignification efficiency of the process and subsequently separate it from the solubilized hemicellulose oligomers by acid precipitation. This process is called organosolv pulping and it has great potential as a biorefinery process due to its ability to isolate the three main lignocellulosic components. Lignin and hemicellulose dissolve in the pulping process,

obtaining a solid cellulosic pulp as a solid product. To obtain lignin, it can easily get precipitated from the liquor and separated by filtration, remaining the hemicellulose dissolved [27]. Moreover, the process is highly tunable, being able to use a variety of organic solvents (methanol, ethanol, butanol, tetrahydrofuran or dioxane) and acids as catalysts. The lignin obtained is relatively pure, so there is no need to remove undesired compounds as in the case of Kraft. However, due to its tunability, many efforts are still made to optimize the process by altering conditions of severity and considering the addition of different catalysts [18].

Solvolytic extraction can be combined with heterogeneous redox catalysts in reductive catalytic fractionation methods to simultaneously dissolve and depolymerize lignin, producing lignin oil. Ionic liquids (ILs) can also be used to dissolve the lignocellulosic components. IL dissolutions dissolve all three components, while ionosolv pulping dissolves both hemicelluloses and lignin. In the IL dissolution method, cellulose can be precipitated by using an anti-solvent before the lignin precipitation, and cellulose with low crystallinity can be obtained, beneficial for downstream conversions. Ionosolv pulping is highly similar to organosolv pulping, but with the advantage that lower temperatures can be applied in the process. Nevertheless, ILs are usually costly and difficult to recover [28].

The last delignification process is the oxidative one, similar to pulp bleaching. Hydrogen peroxide or oxygen is used to transform lignin into low-molecular-weight products like phenolic compounds, quinones, and aliphatic and carboxylic acid structures [29].

1.3.2. CARBOHYDRATE CONVERSION

In these methods, the carbohydrate polymers (cellulose and hemicellulose) are converted and solubilized in the media, obtaining lignin as an insoluble residue or as a precipitate. The most common method is the acid-catalyzed carbohydrate conversion, where monosaccharides are obtained through concentrated acid hydrolysis (CAH). The conversion can also be performed in lower acid concentrations, counteracted by higher temperatures, called dilute acid hydrolysis (DAH). Acidified ILs can also be used, enhancing hydrolysis by making glycosidic bonds more accessible. Alternatively, mechanocatalytic depolymerization has also been applied, by milling the biomass previously impregnated in acid and dissolving it completely. A post-hydrolysis step needs to be carried out to obtain the lignin precipitate, either monophasic or biphasic, the latter one being useful for the obtaining of lower molecular weight lignin.

Similar to acid-treated, enzymatic hydrolysis is also a common practice, usually applied after pretreatment to decrease the recalcitrance of the biomass. Lignin is obtained as solid residue along with some other residual carbohydrates, yielding low-purity lignin but with the potential to be further valorized. Biomass can also be thermally treated, obtaining gaseous products and char. Char is composed mainly of lignin-derived compounds, while gaseous products are condensed into an oil composed of carbohydrate products and lignin monomers and oligomers [30].

1.4. CONVENTIONAL APPLICATIONS FOR LIGNIN

Lignin has been widely produced as a side product or waste in industrial pulp and biofuel processes. Due to the high worldwide production of lignosulfonates liquor and their advantage of being water soluble compared to their analog technical lignins, LS have been widely employed in a variety

of markets as commodity products, meaning that they have been incorporated into the processes without any prior modification or purification. They are non-toxic and properties like purity or sulfonation degree can be easily established. Nevertheless, the determination of their exact physicochemical properties is quite complex, so the characterization of LS has stayed semiquantitative, and they have been applied as bulk, low-value, commodity products like concrete and clay additives and pellet binders for animal feed [31].

There are, however, specialty products derived from lignin, which require processes of different complexities depending on the product and characterizations needed. This enables obtaining more specific molecular structures and properties, specially designed with an application in mind. The more specific the molecule obtained, with unique properties, the higher its value in the market. Therefore, it is key to design processes to obtain advanced molecules derived from lignin for its incorporation as a high-value-added product and increase the profitability of sustainable productions like biorefineries and raw materials like lignocellulosic biomass. Many researchers have recently focused on the incorporation of lignin in a wide variety of advanced materials, obtaining nanomaterials or highly functionalized lignins to use in biomedical, energy storage, or other materials synthesis [32].

Some still quite simple procedures are, for instance, carbonization to obtain lignin-derived carbon black to use as conductive coatings, water-based inks, or textile inks [33]. Lignin can also be modified and depolymerized to use as phenolic resins to work as extenders, cutting agents, or co-reactants during resin synthesis [34]. These depolymerization reactions are widely applied and have a large research interest, due to the high potential of lignin to be the source of many chemicals, and more specifically, phenolic compounds. Some approaches can be used to obtain products that allow their use

without adding any further steps. For example, lignin-derived vanillin has been incorporated and used as a vanilla fragrance in cosmetics and flavoring in the food industry [17]. Nevertheless, it is more common with polymerization reactions to obtain a highly heterogeneous product, with up to 30 different lignin-derived aromatic compounds unable to separate from each other, and therefore no specific application to be incorporated in. A recent approach to overcome this issue is funneling, which aims to design processes where only a small amount of intermediate products will be obtained, and the transformation towards the targeted products will be fulfilled [35].

Another approach is to narrow down the heterogeneity of lignin by solvent extraction methods. Depending on the objective, different methods have been designed, some of the most common being the acid precipitation, solvent fractionation and membrane filtration [36]. Especially the solvent extraction method is highly customizable, since solvents of different properties can be chosen in order to obtain lignin fractions of certain characteristics, and therefore, properties [37].

Extensive research has also been done on incorporating lignin into advanced composite materials. A wide variety of materials formulations can be found in literature, with studies observing the lignin structure and properties, and how this affects other materials, enabling and giving knowledge in further incorporation of lignin in higher value applications [38]. Lignin is considered a good matrix for thermoplastic biocomposites, creating good bonding with natural fibers [39]. Lignin's original function is being the glue of other lignocellulosic components (cellulose and hemicellulose) and providing integrity and mechanical strength to wood and other lignocellulosic materials. Lignin can be incorporated in composite matrices up to 40 wt%, increasing the crystallinity degree and crystallization rate, and improving thermal and mechanical properties. It can also be used for thermosetting

formulations, either as resin (as the monomer containing the hydroxyl group) or as the composite due to the highly branched, functionalized, and with free positions for substitution reactions [40].

To valorize lignin even further, lignin-derived nanoparticles, nanocapsules, nanofibers, nanotubes, and other nanostructures have been synthesized and applied for different applications, one of the main ones being the biomedical sector [38]. Lignin has many qualities like antimicrobial, antioxidant, and UV-absorbing properties that are interesting to be applied in biomedical applications like drug or gene delivery and tissue engineering [41]. Besides, nanolignins have a higher surface area, enhancing their properties as blends, as well as other inherent properties like antioxidant capacity [38]. Nevertheless, until lignin proves to be cytocompatible and cytotoxic, the biomedical application seems to not be realistic [18].

Another current hot topic is the application of materials for energy storage applications. Batteries and supercapacitors are considered crucial for the transition into renewable energies and the use of electric vehicles. However, these devices are composed of scarce and expensive components that make this current alternative unviable. Therefore, implementing lignocellulosic components, derived from lignocellulose, can fix this problem [10,11,42].

1.5. ENERGY STORAGE (ES)

Advances in technology, initiatives for carbon-neutral emissions, and the prosperity of renewable energy sources present a challenge to the current energy storage systems [43]. With estimations that world energy demand will triple by the end of the century, new energy networks are needed to fulfill future energy demands sustainably [44]. Electricity is consumed right when it is generated, but locations where electricity is generated and consumed usually differ, needing storage systems as a solution. There are

different energy storage systems depending on how energy is transformed for its storage and its subsequent utilization since electricity can hardly be stored as it is.

Different energy storage systems are classified and explained in Figure 1.4. Chemical energy is the main energy storage system currently used for transport and electricity generation. This type of storage system stores energy in the chemical bonds of the atoms and molecules, and when these react and the bonds get broken, the energy is released and converted to thermal and mechanical energy. This energy then gets transformed into electric energy by heat engines. Some of the most common chemical fuels are coal, gasoline, diesel, and liquefied petroleum gas. However, this system can also house renewable fuels like hydrogen, synthetic natural gas, biofuels, and thermo-chemical energy.

Hydrogen is a clean, highly abundant, and non-toxic fuel, produced from any primary source and releases water vapor as an emission. Synthetic natural gas is produced from organic matter degradation, mainly as CH_4 and CO_2. Biofuels can substitute the current hydrocarbon fuels by transforming biomass into liquid or gas from short hydrocarbons. The main thermo-chemical energy storage system is based on ammonia dissociation into H_2 and N_2. It is an endothermic reaction, so it happens when the chemical reactor where it is stored absorbs enough solar thermal energy. When the reverse reaction happens, the resynthesis of ammonia, energy is released due to the exothermic reaction, and the solar energy stored is recovered.

Electrochemical energy is created from the electron movements of the chemical reactions, creating electric energy with a specific current depending on the voltage and time. There are two main types of storage: electrochemical batteries and electrochemical capacitors. While the first

type is considered electrochemical, the second is classified as electrical storage.

Wind and solar energy storage are the most important application used in electrochemical storage devices. Different cells or batteries can be classified according to their ability to recharge. Primary cells or batteries are not rechargeable. Secondary batteries, on the other hand, are recharged by passing through a current to provoke the reverse reaction to the one happening when used. While primary batteries are mainly aqueous, secondary batteries can be both aqueous and non-aqueous. Another kind of primary battery is the reserve cells, used for long storage. They are assembled without the addition of electrolytes and can be stored in adverse conditions. Finally, fuel cells are mainly fueled by hydrogen, and can produce electricity as long as there is fuel.

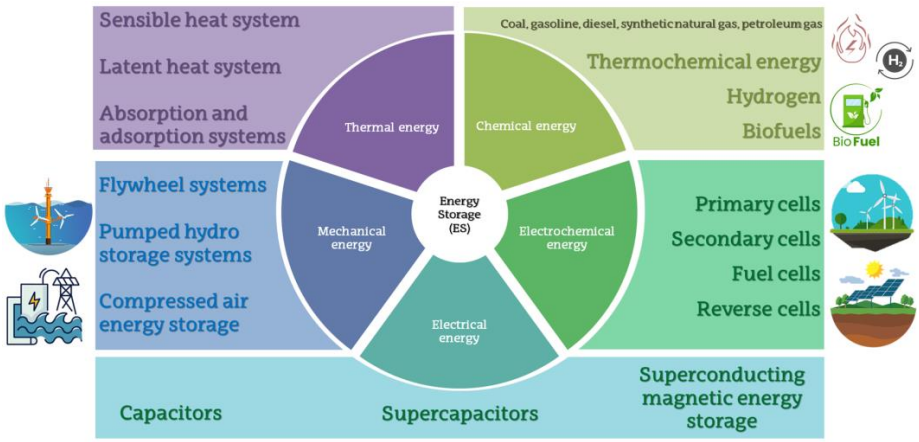

Figure 1.4. ES system classification.

The main systems categorized as electrical energy storage devices are capacitors. They are usually used in cases where high currents are needed, but they have low capacitance, and therefore, can only be used for short periods. Supercapacitors have a greater capacity and can be recharged without damage, filling the gap between capacitors and conventional

batteries. Superconducting magnetic energy storage devices store the magnetic energy produced in a superconducting coil and store it under cryogenic temperatures.

Another storage system is mechanical energy. These systems are useful to convert and store energy from water, wave, and tidal winds. The most used one is the flywheel system, which has a big rotating cylinder that when spinning, creates kinetic energy that gets mechanically stored. This system is interesting for electric locomotives, where these flywheel systems are located by the rail side and used as static batteries. Pumped hydro storage is used in different-level reservoirs, where energy is created when water is moved from the top level to the bottom. Finally, compressed air energy is created when air is pressurized by a compressor and stored underground.

The final energy storage system is thermal energy, which is a system that stores heat or cold and releases it when necessary. It is interesting as energy conservation in industrial and residential buildings, and water heating or electricity generation [44].

1.6. Electrochemical Energy Storage (EES) devices

Batteries are highly potential energy storage systems with quick response, reliability, and low self-discharge rate. While each storage type has its advantages, reason why different systems should be developed for different purposes, electrochemical energy storage systems are considered key for the energy transition into carbon neutrality [45].

A traditional battery is composed of one or various electrochemical cells. If the cells are connected in series, the battery will be designed to provide a

specific voltage (V_d), while if they are connected in parallel, they will provide a specific current (I_d).

The energy density of a cell will be dependent on the total charge transferred (per weight or volume) for a full discharge in a period and a specific and constant current. This is called specific capacity ($Q(I_d)$) and it is an important factor to consider when designing a battery. It is desirable to design batteries with the least amount of cells, as they imply more simple management and less cost. Therefore, cells with high energy density are of great interest.

Cells usually have three components: two electrodes and an electrolyte. One electrode is called the anode while the other is the cathode. Chemical reactions inside the cell that enable electrochemical storage and electrical energy generation happen there.

The anode is the reductant, while the cathode is the oxidant. Therefore, an oxidation reaction happens in the anode, releasing an electrode that travels to the cathode, where it is used for a reduction reaction. Electron transfer is enabled by the electrolyte present in the cell. However, there is an electronic component in the process, where ions are formed in the reaction, also needing to transfer through the system, but from an external circuit. A separation between the electrodes is needed for these two processes to happen. A way to merge the ionic conductivity while forcing the ions to transfer to an external circuit is by implementing solid electrolytes or insulating separators impregnated with a liquid electrolyte. If the chemical reaction is reversible, the battery can be rechargeable. For that, current must be applied to the battery to reach the initial state [46].

The oldest rechargeable batteries are lead-acid, while the most common nowadays are the lithium-ion batteries (LIBs). There are different types

depending on the metal used: lithium cobalt oxide ($LiCoO_2$), lithium iron phosphate ($LiFePO_4$), lithium-ion manganese oxide batteries (Li_2MnO_4, Li_2MnO_3, LMO), and lithium nickel manganese cobalt oxide ($LiNiMnCoO_2$). They are generally attractive due to their portability, high energy density, and fast response time. Some are used for portable devices like mobile phones, laptops, and cameras ($LiMnO_2$) while others are used in medical instruments ($LiNiMnCoO_2$ and Li_2MnO_4). However, they are expensive and have limited capacity [43].

1.6.1. LIBs

Lithium-ion batteries are considered as the most capable energy storage system for the fulfillment of a more environmentally sustainable lifestyle.

However, LIB devices need to become smaller, lighter, safer, and cheaper to become extensively employed and reach the current market demands. Therefore, the use of more sustainable materials is crucial. New battery systems are being studied, where polyvalent cations are used as cathode materials, such as the bivalent Mg^{2+} and Zn^{2+} and the trivalent Al^{3+}. Other more available metals like Na, Zn, K, Mg, and Al are also being studied as cheaper alternatives, placing special emphasis on Na ion batteries (NIBs), due to their similarity in technology and chemistry needed for Li-ion batteries, facilitating the transition [45]. Nevertheless, technology is not optimized for NIBs as it is for LIBs, and lithium remains the metal of choice for most consumer products.

Rechargeable LIB is composed of four components: an anode, a cathode, an organic liquid electrolyte, and a separator.

The most extended anode materials are carbon-based, composed by graphite or graphene. Binary anodes can also be used, preparing a mixture of carbon materials with metal oxides like $Li_4Ti_5O_{12}$, TiO_2, and Fe_2O_3.

Cathode materials are composed of multimetal oxide materials. Metals like cobalt, nickel, and manganese in their crystal structure with added lithium-forming compounds like $LiNi_xMnyCo_zO_2$ (NMC), $LiCoO_2$ (LCO), and $LiNi_xCo_yAl_zO_2$ (NCA), metal phosphates ($LiFePO_4$ (LFP) and $LiMnPO_4$), and spinel oxides ($LiMn_2O_4$ (LMO) and $LiMn_xNi_yO_4$ (LNMO)) are used. NMC is predicted to maintain as the dominant cathode material in the future [47].

The liquid electrolytes employed are organic, a rational mixture of dimethyl carbonate (DMC) and ethylene carbonate (EC) with lithium salts added. This salt can be the perchlorate ($LiClO_4$), fluoroborate ($LiBF_4$), fluorophosphate ($LiPF_6$), or sulfonyl imide (LiFSI and LiTFSI), for instance [48].

Separators are also needed to avoid short circuits of the battery, employing thin and porous single or multiplayer polymers like polyethylene (PE), polypropylene (PP), or Celgar (PP/PE), as well as glass-fiber mats, or even cellulose-based compounds, gaining interest lately [49].

Both anode and cathode electrodes have a binder, which helps with the adhesion of the components like active material and conductive additives on the current collectors. The most common binder materials are poly(vinylidene difluoride) (PVDF) and its copolymer poly(vinylidene difluoride-co-hexafluoropropylene) (PVDF-HFP), while carbon black is the most common conductive additive and Cu is the anode current collector and Al the cathode current collector [50].

1.6.2. Novel and sustainable materials for LIBs

The assembly of a battery entails many different components and materials. LIBs are considered the main system to fulfill future requirements. Unfortunately, this can entail a supply risk due to the scarce and expensive raw materials that compose LIBs. Moreover, the production and post-production processes entail environmental risks and hazards.

Organic polymers are considered the main alternative to this issue since they are derived from abundant sources and are highly tunable. They can replace the cathode, the main battery component that entails the highest amount of metallic materials. Polypyrrole (PPy) and poly(3,4-ethylene dioxythiophene) (PEDOT) are the main organic conductive polymers studied as substituents for metallic cathode materials. Nevertheless, biopolymers, already produced naturally, highly accessible, and with low cost are more sustainable alternatives than organic synthetic polymers. These biopolymers would also be degradable and non-toxic, promoting a much greener battery assembly and after-life process. Among these biopolymers, lignin is gaining increasing interest in many applications, such as its incorporation as battery material [51] due to its amphiphilicity, surface activity, and redox reactivity properties.

Anodic electrodes are commonly composed of carbonaceous materials, but mainly come from non-renewable fossil-based sources. Most of the works on lignin incorporation into batteries are based on its conversion into carbon materials and substituting the currently used non-renewable fossil-based carbons. Lignin is a promising candidate for its high carbon content and prominent aromatic structure. Moreover, by modulating its structure, different carbon materials can be obtained and diverse needs for different types of batteries can be fulfilled. Porous carbons derived from lignin have been fabricated as active materials of electrodes. The porosity is a key factor for the battery performance, preferring large pores as they ease the diffusion kinetics and strengthen the conductivity network of the conductive ions. Moreover, lignin has been combined with other polymers like polyacrylonitrile (PAN), poly(vinyl alcohol) (PVA), and polyethylene oxide (PEO) to obtain carbon fibers and used as anodes, also being able to further functionalize with transition metals like Si or Fe [52].

A similar thing happens with the binder, the separator, and electrolyte materials, also indispensable components that jeopardize battery safety and sustainability.

The most commonly used binder is PVDF, which needs N-methyl-2-pyrrolidone (NMP) as the solvent. Although the binder is one of the minor components of a battery, it has an important role in adhering and providing good mechanical properties to the electrode. PVDF is quite expensive and does not provide any additional functionality to the electrode. Moreover, NMP is a highly toxic solvent, whose utilization should be avoided [53]. Recently, the role of lignin as an electrode binder has been studied, which would reduce drastically the cost and toxicity of the process.

LIB electrolytes are mainly liquids, composed of organic solvents (DMC/EC) and lithium salts, that can include some other additional salts. Separators are impregnated by this solvent mixture, which creates a separation between the cathode and anode to avoid short circuits. Biopolymers like cellulose, chitin, lignin, or agarose can also substitute the currently used ceramic, glass microfiber, or polyolefin-based polyethylene (PE) and polypropylene (PP) separators. Lignin was electrospuned with PVA or PAN and highly porous inter-connected structures were obtained. It was also found that lignin accomplished the function of suppressing the Li dendrite formation.

However, liquid rechargeable batteries can entail risks during the charge-discharge processes, as the liquid can leak and create, for instance, a short circuit or explosion of the batteries. Therefore, the implementation of Gel Polymer Electrolytes (GPEs) and Solid Polymer Electrolytes (SPEs) is highly promoted by current research. GPEs are composed of polymers and salts, providing structure and ionic conduction respectively. Utilizing lignin as an additive or being part of the polymeric framework can give added

mechanical strength and safety to the batteries. For example, lignin was internally cross-linked with polyvinylpyrrolidone (PVP) or poly(N-vinyl imidazole)-co-poly(poly(ethylene glycol) methyl ether methacrylate) (LCP) [52].

Therefore, the implementation of biobased products as battery materials is highly encouraged, not only due to their high availability but also for their biodegradability and easier after-life management [54].

1.6.3. SUPERCAPACITORS

Supercapacitors (SCs), along with LIBs, are among the most promising devices for the energy transition. Similar to the batteries, they are composed of two electrodes (anode and cathode), a separator, and an electrolyte. They store and release energy by adsorbing or desorbing the ions at the interface created between the electrode materials and electrolyte. There are two main types of SCs: electrochemical double-layer capacitors (EDLCs) and pseudocapacitors (PCs). When an electrical potential is applied, EDLCs create a double layer of charge when the ions of the electrolyte get separated and adsorbed on the surface of the electrode. When the reverse process happens, the stored energy is released by the charge-separation phenomena.

On the other hand, when a potential is applied to PCs, reversible faradaic redox reactions happen on the electrode material, creating a charge that passes across the double layer, creating a current [55]. SCs electrodes are mainly based on carbonaceous materials that possess high surface area and appropriate pore-size distribution for the necessary capacitance. Due to the estimated high demand, many works are focusing on the development of novel materials with enhanced properties for this application [56].

Similar to the case of batteries, lignocellulosic materials, especially lignin, are making their way to be considered as a feasible alternative. Lignin-derived carbons have been used as active materials for SCs [57], and studies focusing on different activation processes have been carried out, along with carbonization and combinations with polymers like PAN or different metal oxides [58].

1.7. INCORPORATION AND MODIFICATION OF LIGNIN IN EES

As explained in earlier sections, there are different types of lignin with different specific properties. This should be assessed before the selection of the lignin type for its purpose, and further purification, fractionation, or modifications should also be considered.

One of the main modifications of lignin is its conversion into carbon. One of the mildest procedures for that is hydrolyzation. Hydrolyzed lignin has been found to have good capacitance and high stability and is usually obtained between 120-200 °C and 250-300 °C for acid- or based-catalyzed methods respectively [59], compared to the 400-1000 °C needed for the conventional carbonization of lignin. The obtained carbonaceous materials can greatly differ depending on the process conditions and if other doping agents or reagents have been added to obtain specific performance or added functionality [60].

Some other works are based on using synthetic lignins and study their properties according to their structure. Syringol and guaiacol monomers were used for the synthesis of both homopolymers (lignins of polymerized S or G units only) and copolymers (polymer of both S and G units), along with the addition of hydroquinone to study the effect of extended redox moieties

on the hybrid materials. It was observed that the higher amount of redox moieties enhanced the performance of the film [61].

Other works depolymerized lignin into its aromatic monomers (LDAMs) to increase the quinone quantity and use it as a precursor in the synthesis of synthetic polymers [62]. PPy was also synthesized in aqueous LS, combining quinones present in LS and PPy electrochemistry [63,64]. The lignosulfonates process, however, is an outdated pulping method, and efforts to incorporate other lignin types like Kraft have also been made. Alkali lignin (AL)-PPy composites were synthesized similarly [65], along with KL-PPy which were also subsequently carbonized [66]. Similar works have been done with PEDOT, combined with LS [67], KL [68], AL [68], or modified AL by graft sulfonation [69], as well as with polyaniline, in this case mostly with LS lignin [70–72].

Other combinations with polymers and lignin were produced and used as separators. Most studies are based on composite obtaining and its posterior electrospinning process to obtain highly porous and thermally stable separators. Zhao et al. (2015) fabricated Lignin-PAN electrospun separators for LIBs [73]. Similarly, lignin-PVA electrospun fibers were used as LIBs separator [74].

Other research focused on obtaining gel polymer electrolytes, both with lignocellulose matrix or lignin-based matrix. Some works used just lignocellulose as the membrane [75], one of them even adding H_2SO_4 to act as a plasticizer and conducting ion [76], while others added another natural polymer called hydroxy propyl methyl cellulose (HPMC) with enhanced swelling effect [77]. Lignocellulose was also combined with other polymers: added into PAN matrix to promote lithium salt dissociation and enhance conductivity [78], added into PVA matrix to enhance mechanical properties [79], or to polyethylene glycol (PEG) membranes [80]. Composites with

other biopolymers were also carried out, like potato starch, increasing the liquid electrolyte uptake and enhancing the ionic conductivity [81] or chitosan [82]. Alternatively, isolated lignin was also added to the same matrixes mentioned: PVA [83], PVP [84], PEG [85], or even chitosan [86]. Moreover, modifications of lignin like allylation [87] and fractionation of lignin for the obtaining of low molecular weight particles [88] were studied.

Another common alternative for incorporating lignin in LIBs or SCs is the combination of lignin with carbonaceous materials like active carbon or graphite.

Further work was done on different functionalizations and modifications of lignin for its enhanced performance for composite formation with carbonaceous materials. A common modification of lignin is its oxidation. In this sense, an oxidation reaction was carried out for the replacement of the methoxy groups in KL for phenolic hydroxyl groups, increasing the hydroxyquinone groups, considered as the active redox sites in lignin [89]. Additionally, a research study focused on assessing the effect of the sulfonation degree on ionic conductivity and water solubility [90]. In another work, the already prepared lignin-carbon composite was cross-linked for better adhesion and combined faradaic and non-faradaic charge [91].

1.8. REFERENCES

[1] Sharma V, Tsai M-L, Nargotra P, Chen C-W, Sun P-P, Singhania RR, et al. Journey of lignin from a roadblock to bridge for lignocellulose biorefineries: A comprehensive review. Sci Total Environ 2023;861:160560. https://doi.org/10.1016/j.scitotenv.2022.160560.

[2] Prasad S, Sheetal KR, Venkatramanan V, Kumar S, Kannojia S. Sustainable energy: Challenges and perspectives. Sustain. Green Technol. Environ. Manag., Springer Singapore; 2019, p. 175–97. https://doi.org/10.1007/978-981-13-2772-8_9/TABLES/6.

[3] Afgan NH, Al Gobaisi D, Carvalho MG, Cumo M. Sustainable energy development. Renew Sustain Energy Rev 1998;2:235–86. https://doi.org/10.1016/S1364-0321(98)00002-1.

[4] Nieuwenhuijsen MJ. Urban and transport planning pathways to carbon neutral, liveable and healthy cities; A review of the current evidence. Environ Int 2020;140:105661. https://doi.org/10.1016/J.ENVINT.2020.105661.

[5] Too J, Ejohwomu OA, Hui FKP, Duffield C, Bukoye OT, Edwards DJ. Framework for standardising carbon neutrality in building projects. J Clean Prod 2022;373:133858. https://doi.org/10.1016/J.JCLEPRO.2022.133858.

[6] Sayed ET;, Olabi AG;, Alami AH;, Radwan A;, Mdallal A;, Rezk A;, et al. Renewable Energy and Energy Storage Systems. Energies 2023, Vol 16, Page 1415 2023;16:1415. https://doi.org/10.3390/EN16031415.

[7] Chaitanya P, Upadhyay E, Deepak Singh D, Singh V. Nature Environment and Pollution Technology An International Quarterly Scientific Journal Open Access Journal Effective Contribution of Air Pollutants to Physiological and Psychological Human Diseases: A Systematic Review n.d.;21:1943–54. https://doi.org/10.46488/NEPT.2022.v21i04.049.

[8] González-Eguino M. Energy poverty: An overview. Renew Sustain Energy

Rev 2015;47:377–85. https://doi.org/10.1016/J.RSER.2015.03.013.

[9] Perry RH, Green DW, Maloney JO. Thermodynamics: Thermodynamic Analysis Of Processes. Perry's Chem Eng Handb (Ed) Seventh, Int Ed 1997;43:34–6.

[10] Irimia-Vladu M. "Green" electronics: Biodegradable and biocompatible materials and devices for sustainable future. Chem Soc Rev 2014;43:588–610. https://doi.org/10.1039/c3cs60235d.

[11] Wang F, Ouyang D, Zhou Z, Page SJ, Liu D, Zhao X. Lignocellulosic biomass as sustainable feedstock and materials for power generation and energy storage. J Energy Chem 2021;57:247–80. https://doi.org/10.1016/j.jechem.2020.08.060.

[12] Putro JN, Soetaredjo FE, Lin SY, Ju YH, Ismadji S. Pretreatment and conversion of lignocellulose biomass into valuable chemicals. RSC Adv 2016;6:46834–52. https://doi.org/10.1039/C6RA09851G.

[13] Huber GW, Iborra S, Corma A. Synthesis of transportation fuels from biomass: Chemistry, catalysts, and engineering. Chem Rev 2006;106:4044–98. https://doi.org/10.1021/CR068360D/ASSET/IMAGES/MEDIUM/CR068360DF00035.GIF.

[14] Hansen NML, Plackett D. Sustainable films and coatings from hemicelluloses: A review. Biomacromolecules 2008;9:1493–505. https://doi.org/10.1021/BM800053Z/ASSET/IMAGES/LARGE/BM-2008-00053Z_0008.JPEG.

[15] Boerjan W, Ralph J, Baucher M. Lignin Biosynthesis. Annu Rev Plant Biol 2003;54:519–46. https://doi.org/10.1146/annurev.arplant.54.031902.134938.

[16] Figueiredo P, Santos HA. Lignin-based materilas for biomedical applications.

n.d.

[17] Schutyser W, Renders T, Van Den Bosch S, Koelewijn SF, Beckham GT, Sels BF. Chemicals from lignin: An interplay of lignocellulose fractionation, depolymerisation, and upgrading. Chem Soc Rev 2018;47:852–908. https://doi.org/10.1039/c7cs00566k.

[18] Ekielski A, Mishra PK. Lignin for bioeconomy: The present and future role of technical lignin. Int J Mol Sci 2021;22:1–24. https://doi.org/10.3390/ijms22010063.

[19] Yu O, Kim KH. Lignin to materials: A focused review on recent novel lignin applications. Appl Sci 2020;10. https://doi.org/10.3390/app10134626.

[20] Xie ZH, Zhou JH, Li HM, Sun GW. Comparison between green liquor pretreatment-Kraft pulping and conventional Kraft pulping. Adv Mater Res 2013;781–784:2650–3. https://doi.org/10.4028/www.scientific.net/AMR.781-784.2650.

[21] Öhman F, Theliander H, Norgren M, Tomani P, Axegård P. Method for separating lignin from a lignin containing liquid/slurry (Patent application WO2006038863), 2011.

[22] Kouisni L, Holt-Hindle P, Maki K, Paleologou M. The LignoForce System™: A new process for the production of high-quality lignin from black liquor. Pulp Pap Canada 2014;115:18–22.

[23] Li T, Takkellapati S. The current and emerging sources of technical lignins and their applications. Biofuels, Bioprod Biorefining 2018;12:756–87. https://doi.org/10.1002/BBB.1913.

[24] Fatehi P, Ni Y. Integrated forest biorefinery - Sulfite process. ACS Symp Ser 2011;1067:409–41. https://doi.org/10.1021/bk-2011-1067.ch016.

[25] Mousavioun P, Doherty WOS. Chemical and thermal properties of

fractionated bagasse soda lignin. Ind Crops Prod 2010;31:52–8. https://doi.org/10.1016/J.INDCROP.2009.09.001.

[26] Pu Y, Hu F, Huang F, Davison BH, Ragauskas AJ. Assessing the molecular structure basis for biomass recalcitrance during dilute acid and hydrothermal pretreatments. Biotechnol Biofuels 2013;6:1. https://doi.org/10.1186/1754-6834-6-15.

[27] Lindner A, Wegener G. Characterization of Lignins from Organosolv Pulping According to the Organocell Process Part 1. Elemental Analysis, Nonlignin Portions and Functional Groups. Http://DxDoiOrg/101080/02773818808070688 2006;8:323–40. https://doi.org/10.1080/02773818808070688.

[28] Schutyser W, Van Den Bosch S, Renders T, De Boe T, Koelewijn SF, Dewaele A, et al. Influence of bio-based solvents on the catalytic reductive fractionation of birch wood. Green Chem 2015;17:5035–45. https://doi.org/10.1039/c5gc01442e.

[29] Karp EM, Nimlos CT, Deutch S, Salvachúa D, Cywar RM, Beckham GT. Quantification of acidic compounds in complex biomass-derived streams. Green Chem 2016;18:4750–60. https://doi.org/10.1039/c6gc00868b.

[30] Luterbacher JS, Martin Alonso D, Dumesic JA. Targeted chemical upgrading of lignocellulosic biomass to platform molecules. Green Chem 2014;16:4816–38. https://doi.org/10.1039/c4gc01160k.

[31] Gargulak JD, Lebo SE. Commercial use of lignin-based materials. ACS Symp Ser 1999;742:304–20. https://doi.org/10.1021/bk-2000-0742.ch015.

[32] Österberg M, Sipponen MH, Mattos BD, Rojas OJ. Spherical lignin particles: A review on their sustainability and applications. Green Chem 2020;22:2712–33. https://doi.org/10.1039/d0gc00096e.

[33] Snowdon MR, Mohanty AK, Misra M. A study of carbonized lignin as an

alternative to carbon black. ACS Sustain Chem Eng 2014;2:1257–63. https://doi.org/10.1021/SC500086V/ASSET/IMAGES/LARGE/SC-2014-00086V_0006.JPEG.

[34] Gao Z, Lang X, Chen S, Zhao C. Mini-Review on the Synthesis of Lignin-Based Phenolic Resin 2021. https://doi.org/10.1021/acs.energyfuels.1c03177.

[35] Linger JG, Vardon DR, Guarnieri MT, Karp EM, Hunsinger GB, Franden MA, et al. Lignin valorization through integrated biological funneling and chemical catalysis n.d. https://doi.org/10.1073/pnas.1410657111.

[36] Gigli M, Crestini C. Fractionation of industrial lignins: opportunities and challenges. Green Chem 2020;22:4722–46. https://doi.org/10.1039/d0gc01606c.

[37] Domínguez-Robles J, Tamminen T, Liitiä T, Peresin MS, Rodríguez A, Jääskeläinen AS. Aqueous acetone fractionation of kraft, organosolv and soda lignins. Int J Biol Macromol 2018;106:979–87. https://doi.org/10.1016/j.ijbiomac.2017.08.102.

[38] Collins MN, Nechifor M, Tanasă F, Zănoagă M, McLoughlin A, Stróżyk MA, et al. Valorization of lignin in polymer and composite systems for advanced engineering applications – A review. Int J Biol Macromol 2019;131:828–49. https://doi.org/10.1016/J.IJBIOMAC.2019.03.069.

[39] Naegele H, Pfitzer J, Ziegler L, Inone-Kauffmann ER, Eisenreich N. Applications of Lignin Materials and Their Composites (Lignin Applications in Various Industrial Sectors, Future Trends of Lignin and Their Composites). Lignin Polym Compos 2016:233–44. https://doi.org/10.1016/B978-0-323-35565-0.00013-8.

[40] Engelmann G, Ganster J. Lignin Reinforcement in Thermosets Composites. Lignin Polym Compos 2016:119–51. https://doi.org/10.1016/B978-0-323-35565-0.00007-2.

[41] Rangan A, Manjula M V., Satyanarayana KG, Menon R. Lignin/Nanolignin and Their Biodegradable Composites. Biodegrad Green Compos 2016:167–98. https://doi.org/10.1002/9781118911068.CH7.

[42] Klapiszewski Ł, Szalaty TJ, Graś M, Moszyński D, Buchwald T, Lota G, et al. Lignin-based dual component additives as effective electrode material for energy management systems. Int J Biol Macromol 2020;165:268–78. https://doi.org/10.1016/J.IJBIOMAC.2020.09.191.

[43] Hannan MA, Wali SB, Ker PJ, Rahman MSA, Mansor M, Ramachandaramurthy VK, et al. Battery energy-storage system: A review of technologies, optimization objectives, constraints, approaches, and outstanding issues. J Energy Storage 2021;42:103023. https://doi.org/10.1016/J.EST.2021.103023.

[44] Guney MS, Tepe Y. Classification and assessment of energy storage systems. Renew Sustain Energy Rev 2017;75:1187–97. https://doi.org/10.1016/J.RSER.2016.11.102.

[45] Baboo JP, Jakubczyk E, Yatoo MA, Phillips M, Grabe S, Dent M, et al. Investigating battery-supercapacitor material hybrid configurations in energy storage device cycling at 0.1 to 10C rate. J Power Sources 2023;561:232762. https://doi.org/10.1016/j.jpowsour.2023.232762.

[46] Goodenough JB. Electrochemical energy storage in a sustainable modern society. Energy Environ Sci 2013;7:14–8. https://doi.org/10.1039/C3EE42613K.

[47] Kotal M, Jakhar S, Roy S, Sharma HK. Cathode materials for rechargeable lithium batteries: Recent progress and future prospects. J Energy Storage 2022;47. https://doi.org/10.1016/J.EST.2021.103534.

[48] Su X, Xu Y, Wu Y, Li H, Yang J, Liao Y, et al. Liquid electrolytes for low-temperature lithium batteries: main limitations, current advances, and

future perspectives. Energy Storage Mater 2023;56:642–63. https://doi.org/10.1016/J.ENSM.2023.01.044.

[49] Dai X, Zhang X, Wen J, Wang C, Ma X, Yang Y, et al. Research progress on high-temperature resistant polymer separators for lithium-ion batteries. Energy Storage Mater 2022;51:638–59. https://doi.org/10.1016/J.ENSM.2022.07.011.

[50] Das P, Thompson BC. Development of design strategies for conjugated polymer binders in lithium-ion batteries. Polym J 2022:317–41. https://doi.org/10.1038/s41428-022-00708-x.

[51] Budnyak TM, Slabon A, Sipponen MH. Lignin–Inorganic Interfaces: Chemistry and Applications from Adsorbents to Catalysts and Energy Storage Materials. ChemSusChem 2020;13:4344–55. https://doi.org/10.1002/cssc.202000216.

[52] Chen W-J, Zhao C-X, Li B-Q, Yuan T-Q, Zhang Q. Lignin-derived materials and their applications in rechargeable batteries. Green Chem 2022:565–84. https://doi.org/10.1039/d1gc02872c.

[53] Pasquier A Du, Disma F, Bowmer T, Gozdz AS, Amatucci G, Tarascon J -M. Differential Scanning Calorimetry Study of the Reactivity of Carbon Anodes in Plastic Li-Ion Batteries. J Electrochem Soc 1998;145:472–7. https://doi.org/10.1149/1.1838287.

[54] Salado M, Lizundia E, Oyarzabal I, Salazar D. The Role of Critical Raw Materials for Novel Strategies in Sustainable Secondary Batteries 2022. https://doi.org/10.1002/pssa.202100710.

[55] Kaipannan S, Govindarajan K, Sundaramoorthy S, Marappan S. Waste Toner-Derived Carbon/Fe3O4 Nanocomposite for High-Performance Supercapacitor. ACS Omega 2019;4:15798–805. https://doi.org/10.1021/acsomega.9b01337.

[56] Karnan M, Raj AGK, Subramani K, Santhoshkumar S, Sathish M. The fascinating supercapacitive performance of activated carbon electrodes with enhanced energy density in multifarious electrolytes. Sustain Energy Fuels 2020;4:3029–41. https://doi.org/10.1039/c9se01298b.

[57] Zhang K, Liu M, Zhang T, Min X, Wang Z, Chai L, et al. High-performance supercapacitor energy storage using a carbon material derived from lignin by bacterial activation before carbonization. J Mater Chem A 2019;7:26838–48. https://doi.org/10.1039/c9ta04369a.

[58] Tong Y, Yang J, Li J, Cong Z, Wei L, Liu M, et al. Lignin-derived electrode materials for supercapacitor applications: progress and perspectives. J Mater Chem A 2022;11:1061–82. https://doi.org/10.1039/d2ta07203c.

[59] Menezes F, Nascimento V, Gomes G, Strauss M, Junqueira T, Rocha GJM, et al. Depolymerization of enzymatic hydrolysis lignin: review of technologies and opportunities for research. Fuel 2023;342:127796. https://doi.org/10.1016/j.fuel.2023.127796.

[60] Chatterjee S, Saito T. Lignin-Derived Advanced Carbon Materials. ChemSusChem 2015;8:3941–58. https://doi.org/10.1002/cssc.201500692.

[61] Rębiś T, Nilsson TY, Inganäs O. Hybrid materials from organic electronic conductors and synthetic-lignin models for charge storage applications. J Mater Chem A 2016;4:1931–40. https://doi.org/10.1039/C5TA06821E.

[62] Yang W, Wang X, Jiao L, Bian H, Qiao Y, Dai H. Synthetic polymers based on lignin-derived aromatic monomers for high-performance energy-storage materials. J Mater Chem A 2020;8:24065–74. https://doi.org/10.1039/D0TA08635E.

[63] Milczarek G, Inganäs O. Renewable cathode materials from biopolymer/conjugated polymer interpenetrating networks. Science (80-) 2012;335:1468–71. https://doi.org/10.1126/science.1215159.

[64] Ajjan FN, Jafari MJ, Rębiś T, Ederth T, Inganäs O. Spectroelectrochemical investigation of redox states in a polypyrrole/lignin composite electrode material. J Mater Chem A 2015;3:12927–37. https://doi.org/10.1039/c5ta00788g.

[65] Leguizamon S, Díaz-Orellana KP, Velez J, Thies MC, Roberts ME. High charge-capacity polymer electrodes comprising alkali lignin from the Kraft process. J Mater Chem A 2015;3:11330–9. https://doi.org/10.1039/c5ta00481k.

[66] Bober P, Gavrilov N, Kovalcik A, Mičušík M, Unterweger C, Pašti IA, et al. Electrochemical properties of lignin/polypyrrole composites and their carbonized analogues. Mater Chem Phys 2018;213:352–61. https://doi.org/10.1016/J.MATCHEMPHYS.2018.04.043.

[67] Hong N, Qiu X, Deng W, He Z, Li Y. Effect of aggregation behavior and phenolic hydroxyl group content on the performance of lignosulfonate doped PEDOT as a hole extraction layer in polymer solar cells. RSC Adv 2015;5:90913–21. https://doi.org/10.1039/C5RA19676K.

[68] Navarro-Suárez AM, Casado N, Carretero-González J, Mecerreyes D, Rojo T. Full-cell quinone/hydroquinone supercapacitors based on partially reduced graphite oxide and lignin/PEDOT electrodes. J Mater Chem A 2017;5:7137–43. https://doi.org/10.1039/c7ta00527j.

[69] Hong N, Xiao J, Li Y, Li Y, Wu Y, Yu W, et al. Unexpected fluorescent emission of graft sulfonated-acetone–formaldehyde lignin and its application as a dopant of PEDOT for high performance photovoltaic and light-emitting devices. J Mater Chem C 2016;4:5297–306. https://doi.org/10.1039/C6TC01170E.

[70] Roy S, Fortier JM, Nagarajan R, Tripathy S, Kumar J, Samuelson LA, et al. Biomimetic Synthesis of a Water Soluble Conducting Molecular Complex of Polyaniline and Lignosulfonate 2002. https://doi.org/10.1021/bm0255138.

[71] Xu H, Jiang H, Li X, Wang G. Synthesis and electrochemical capacitance performance of polyaniline doped with lignosulfonate. RSC Adv 2015;5:76116–21. https://doi.org/10.1039/C5RA12292A.

[72] Dianat N, Rahmanifar MS, Noori A, El-Kady MF, Chang X, Kaner RB, et al. Polyaniline-Lignin Interpenetrating Network for Supercapacitive Energy Storage. Nano Lett 2021;21:9485–93. https://doi.org/10.1021/ACS.NANOLETT.1C02843/SUPPL_FILE/NL1C02843_SI_001.AVI.

[73] Zhao M, Wang J, Chong C, Yu X, Wang L, Shi Z. An electrospun lignin/polyacrylonitrile nonwoven composite separator with high porosity and thermal stability for lithium-ion batteries 2015. https://doi.org/10.1039/c5ra19371k.

[74] Uddin MJ, Alaboina PK, Zhang L, Cho SJ. A low-cost, environment-friendly lignin-polyvinyl alcohol nanofiber separator using a water-based method for safer and faster lithium-ion batteries. Mater Sci Eng B Solid-State Mater Adv Technol 2017;223:84–90. https://doi.org/10.1016/j.mseb.2017.05.004.

[75] Song A, Huang Y, Zhong X, Cao H, Liu B, Lin Y, et al. Novel lignocellulose based gel polymer electrolyte with higher comprehensive performances for rechargeable lithium–sulfur battery. J Memb Sci 2018;556:203–13. https://doi.org/10.1016/j.memsci.2018.04.003.

[76] Qiu F, Huang Y, Luo C, Li X, Wang M, Cao H. An Acid-Resistant Gel Polymer Electrolyte Based on Lignocellulose of Natural Biomass for Supercapacitors. Energy Technol 2020;8:1–12. https://doi.org/10.1002/ente.202000009.

[77] Luo C, Huang Y, Yin Z, Xu H, Qin X, Li X, et al. A universal natural hydroxy propyl methyl cellulose polymer additive for modifying lignocellulose-based gel polymer electrolytes and stabilizing lithium metal anodes. Mater Chem Phys 2020;250:123174. https://doi.org/10.1016/j.matchemphys.2020.123174.

[78] Ren W, Huang Y, Xu X, Liu B, Li S, Luo C, et al. Gel polymer electrolyte with high performances based on polyacrylonitrile composite natural polymer of lignocellulose in lithium ion battery. J Mater Sci 2020;55:12249–63. https://doi.org/10.1007/s10853-020-04888-w.

[79] Deng X, Huang Y, Song A, Liu B, Yin Z, Wu Y, et al. Gel polymer electrolyte with high performances based on biodegradable polymer polyvinyl alcohol composite lignocellulose. Mater Chem Phys 2019;229:232–41. https://doi.org/10.1016/j.matchemphys.2019.03.014.

[80] Song A, Huang Y, Liu B, Cao H, Zhong X, Lin Y, et al. Gel polymer electrolyte based on polyethylene glycol composite lignocellulose matrix with higher comprehensive performances. Electrochim Acta 2017;247:505–15. https://doi.org/10.1016/j.electacta.2017.07.048.

[81] Song A, Huang Y, Zhong X, Cao H, Liu B, Lin Y, et al. Gel polymer electrolyte with high performances based on pure natural polymer matrix of potato starch composite lignocellulose. Electrochim Acta 2017;245:981–92. https://doi.org/10.1016/j.electacta.2017.05.176.

[82] Han JY, Huang Y, Chen Y, Song AM, Deng XH, Liu B, et al. High-Performance Gel Polymer Electrolyte Based on Chitosan–Lignocellulose for Lithium-Ion Batteries. ChemElectroChem 2020;7:1213–24. https://doi.org/10.1002/celc.202000007.

[83] Shabanov NS, Rabadanov KS, Gafurov MM, Isaev AB, Sobola DS, Suleimanov SI, et al. Lignin-based gel polymer electrolyte for cationic conductivity. Polymers (Basel) 2021;13:1–13. https://doi.org/10.3390/polym13142306.

[84] Liu B, Huang Y, Cao H, Song A, Lin Y, Wang M, et al. A high-performance and environment-friendly gel polymer electrolyte for lithium ion battery based on composited lignin membrane. J Solid State Electrochem 2018;22:807–16. https://doi.org/10.1007/S10008-017-3814-X/FIGURES/8.

[85] Koda K, Taira S, Kubota A, Isozaki T, You X, Uraki Y, et al. Development of Lignin-Based Terpolyester Film and Its Application to Separator Material for Electric Double-Layer Capacitor. J Wood Chem Technol 2019;0:1–161.

[86] Almenara N, Gueret R, Huertas Alonso A, Veettil U, Sipponen M, Lizundia E. Lignin–Chitosan Gel Polymer Electrolytes for Stable Zn Electrodeposition. ACS Sustain Chem Eng 2023;0:null-null. https://doi.org/10.1021/acssuschemeng.2c05835.

[87] Baroncini EA, Stanzione JF. Incorporating allylated lignin-derivatives in thiol-ene gel-polymer electrolytes. Int J Biol Macromol 2018;113:1041–51. https://doi.org/10.1016/J.IJBIOMAC.2018.02.160.

[88] Baroncini EA, Rousseau DM, Strekis CA, Stanzione JF. Viability of Low Molecular Weight Lignin in Developing Thiol-Ene Polymer Electrolytes with Balanced Thermomechanical and Conductive Properties. Macromol Rapid Commun 2021;42:1–9. https://doi.org/10.1002/marc.202000477.

[89] Zhou B, Li J, Liu W, Jiang H, Li S, Tan L, et al. Functional-Group Modification of Kraft Lignin for Enhanced Supercapacitors. ChemSusChem 2020;13:2628–33. https://doi.org/10.1002/cssc.201903435.

[90] Ail U, Phopase J, Nilsson J, Khan ZU, Inganäs O, Berggren M, et al. Effect of Sulfonation Level on Lignin/Carbon Composite Electrodes for Large-Scale Organic Batteries. ACS Sustain Chem Eng 2020;8:17933–44. https://doi.org/10.1021/ACSSUSCHEMENG.0C05397/ASSET/IMAGES/LARGE/SC0C05397_0008.JPEG.

[91] Chaleawlert-umpon S, Liedel C. More sustainable energy storage: Lignin based electrodes with glyoxal crosslinking. J Mater Chem A 2017;5:24344–52. https://doi.org/10.1039/c7ta07686j.

2. OBJECTIVES

The general objective of the thesis was to valorize different types of lignin to use in energy storage devices. For that, different treatments and modification processes were designed and carried out, and the obtained products were characterized accordingly for the subsequent determination of the lignin structure effect and functionality for the chosen application.

This research was separated into different sections, each one focusing on a specific objective:

- Extraction of different types of lignin and their fractionation using the same organic solvent extraction method for obtaining more homogeneous fractions with different physicochemical properties.
- Modification of lignins for their enhanced performance as electrochemical energy storage device materials. On one hand, the design and performance of a novel oxidized lignin nanoparticle production; and on the other, the obtaining and study of different chemically functionalized lignin (carboxymethylated, sulfomethylated and methylated).
- Preparation and characterization of different lignin-carbon composites for enhanced capacitance to use as potential supercapacitor or battery active material.
- Preparation of anodic electrodes with different lignin types, fractions, and modifications as the binder for LIBs

To achieve the mentioned specific objectives, different procedures, and techniques were implemented, selecting the most significant for each work, and explained in different chapters throughout the thesis.

2.1. OUTLINE OF THE THESIS

This thesis is divided into different chapters to achieve the proposed objectives.

In the already shown first chapter, a general introduction and background of the current status have been described. The ongoing environmental issues have been described and energy sustainability has been explained as a plausible alternative. The need to develop low-cost and sustainable materials for energy storage devices has also been addressed as key for the green transition and lignocellulosic materials, more specifically lignin, have been presented as alternative sustainable precursor materials.

Chapter three groups the different methods and techniques followed throughout the thesis. Methods for the characterization of the used raw material, the extracted liquors, and the precipitated lignins are explained. The different chemical, physicochemical, thermochemical, and electrochemical characterization methods are also included. Moreover, the different electrochemical measurement setups used in the thesis were described.

In the fourth chapter, the sequential organic solvent extraction method (SOSE) is designed, and the fractions obtained for both Kraft and organosolv lignins are explained, along with their chemical, physicochemical, and thermochemical properties determination by FTIR, GPC, UV, ^{31}P NMR, Py-GC/MS, TGA, and DSC.

The fifth chapter focuses on the different chemical reactions carried out for the modification of lignin. The chapter is divided into two parts. The first one is focused on the oxidation of lignin. This work was dedicated to enhancing the functionality of lignin while maintaining its integrity and avoiding

degradation and depolymerization reactions. For that, mild oxidizing conditions, with ultrasound irradiation intensification were performed, and the obtained oxidized lignin nanoparticles were characterized by FTIR, GPC, EA, UV, ^{31}P NMR, TGA, DSC, DLS, and TEM. The second part of the chapter is focused on different types of modification, which instead of incrementing the functional groups of lignin (hydroxyl and carboxylic groups), was based on reactions with the existing groups to obtain methylated, carboxymethylated, or sulfomethylated lignin. The modified lignins were characterized by FTIR, GCP, ^{31}P NMR, ^{13}C NMR, DLS, and TGA.

The sixth chapter is targeted at the obtaining of different lignin-carbon composites. For that, two different carbons were chosen (activated carbon and graphite), which were chemically activated, and lignins were deposited on their surface to observe if the addition of lignin enhanced the electrochemical properties. The composites obtained were characterized by FTIR, EA, XPS, BET, DLS, AFM, SEM, CV, EIS, and GCD.

In the seventh chapter, different lignins obtained in the previous chapters were incorporated into the formulation of anodic electrodes for LIBs. The electrochemical performance and battery stability were analyzed by CV, EIS, and GCD measurements.

In the eighth and last chapter, the main conclusions and remarks regarding the current research have been drawn, along with some future perspectives of the work. The scientific production derived from this work has also been included.

3. METHODOLOGY

3.1. RAW MATERIALS

Throughout the thesis two types of lignin were used, Kraft and organosolv. Kraft lignin was obtained by precipitation of the black liquor supplied by a local paper and pulp industry (Papelera Guipuzcoana de Zicuñaga S.A.U., Hernani) derived from *Eucalyptus globulus*. Organosolv lignin was extracted in the lab from *Eucalyptus globulus* chips, also supplied by Papelera Guipuzcoana de Zicuñaga S.A.U.

3.2. CHARACTERIZATION METHODS

3.2.1. CHARACTERIZATION OF RAW MATERIALS

Eucalyptus chips were characterized by the standardized Technical Association of the Pulp & Paper Industry (TAPPI) methods and the National Renewable Energy Laboratory (NREL) protocol.

Moisture, ash, extractive, acid-insoluble lignin (AIL), acid-soluble lignin (ASL), sugar, hemicellulose, and lignin content were determined following the procedures explained in ANNEX I.

3.2.2. CHARACTERIZATION OF LIQUORS

Kraft liquor provided by Papelera Guipuzcoana de Zicuñaga S.A.U. and organosolv liquor were characterized before carrying out the lignin precipitation. pH was determined using a PH BASIC 20 m. Density was determined gravimetrically. Total solid content and inorganic content were determined using TAPPI T650 [1] and TAPPI T211 [2] standards, respectively, while organic content was determined as the difference between the total solid content and inorganic content.

3.2.3. CHARACTERIZATION OF LIGNIN AND LIGNIN COMPOSITES

Lignin samples were characterized with several different techniques. From one side, the chemical composition of the samples was determined by the calculation of purity and quantification of AIL, ASL, char, and ash as well as carrying elemental analysis to determine the percentages of C, N, O, H, and S.

Physicochemical properties were also determined. The main functional groups were identified by Fourier transformed infrared (FTIR) spectroscopy, molecular weight and polydispersity index were measured by gel permeation chromatography (GPC), S/G ratio was obtained by pyrolysis-gas chromatography/mass spectrometry (Py-GC/MS) and hydroxyl content was found out by ultraviolet-visible (UV-vis) spectrophotometric methods and quantitative phosphorus-31 nuclear magnetic resonance (^{31}P NMR) spectroscopy. The chemical structure was also further analyzed by carbon-13 nuclear magnetic resonance (^{13}C NMR), and X-ray photoelectron spectroscopy (XPS) was used for the determination of the chemical composition.

Thermal properties were analyzed by thermogravimetric analysis (TGA) and differential scanning calorimetry (DSC) techniques.

Morphological properties were determined by dynamic light scattering (DLS), atomic force microscopy (AFM), scanning electron microscopy (SEM), and transmission electron microscopy (TEM).

A more in-depth explanation of the equipment and methodologies followed are shown in Annex I.

3.3. ELECTROCHEMICAL CHARACTERIZATION

3.3.1. CHARACTERIZATION OF THE ACTIVE MATERIAL

3.3.1.1. Cyclic Voltammetry (CV)

CV is a powerful electrochemical characterization tool used in different fields like electrochemistry, analytical chemistry, material science, and biochemistry. It is used to characterize redox reactions, determine redox potentials, understand different reaction mechanisms, and study the electrochemical behaviors of different materials. For that, a linear charging potential is applied to the electrode, which sweeps linearly back and forth between the initial and final potential values.

Depending on the electroactive species present, different voltammogram shapes will be obtained, showing the curves of the recorded current-potential values. The shape of the voltammogram can provide information regarding the reactions happening and their reversibility. The anodic peaks correspond to oxidation reactions, while the cathodic peaks correspond to reduction reactions. If these redox reactions are reversible, both peaks will be well defined and show the same peak potential, this being the point at which the peak current occurs. For irreversible reactions, the peak potential will be different and less defined. Moreover, the peak current is related to the standard potential and is proportional to the concentration of the electroactive species. The shape and position of the peaks can provide information about the kinetics and mechanisms of the electrochemical reactions [3].

3.3.1.2. Electrochemical Impedance Spectroscopy (EIS)

EIS is another electrochemical technique used to study the properties as a function of frequency. As opposed to the CV, an alternating current is

applied, and the resulting signaled voltage is recorded. By analyzing the relationship between these two, electrical characteristics like resistance and capacitance can be acquired. The impedance spectrum obtained can give insight into the electrochemical processes happening, such as charge transfer and mass transport.

Impedance is a complex quantity, and it represents the opposition created in the system to the flow of alternating current. It is composed of two elements: the resistance, and the reactance, with the latter being subdivided into capacitance and inductance components. The revelation of these characteristics is interesting to study processes like corrosion, electrochemical reactions, and ion transportation, all of which are valuable in different disciplines, including electrochemistry (fuel cells, batteries, sensors), materials science, and biomedicine.

The two most common ways of representing impedance data are the Nyquist and the Bode diagram, which are related to the circuit and its components. Since the impedance is a complex parameter, the Nyquist plot is represented by the real and imaginary parts of an impedance in a specified frequency range. The real part is plotted on the abscissa, while the imaginary part is represented on the ordinate. At low-frequency ranges, the impedance values of the capacitors are very high, while at high frequencies the impedance value can be considered zero. At medium values, both the real and imaginary parts of the impedance are visible. The Nyquist plots go from high frequencies (left) to low (right) and are helpful to identify the processes happening since different features correspond to different spectral regions. High-frequency regions are usually related to the solution resistance, while low-frequency regions represent electrode kinetics or diffusion processes.

When the frequency information needs to be observed, Bode plots are applied. Bode plots consist of two different graphs: one shows the system's

response in logarithmic magnitude as a function of frequency (known as the magnitude plot), while the other plot shows the phase angle of the response as a function of frequency (the phase plot). The magnitude plot shows the system's gain characteristics throughout different frequencies, while the phase plot provides the time delays between the input and output signals. This form of representing impedance data is useful for the analysis of the stability and phase characteristics of the system.

Another technique used in EIS, particularly for describing the electrical behavior of a complex system, is Equivalent Circuit Modeling (ECM). These models represent the physical and electrochemical characteristics of the system, designed by different electrical components (resistors, capacitors, inductors…) connected in a configuration that reflects the system's characteristics. Each component has associated parameters, and their behavior can be dependent or independent of the frequency. For the determination of these parameters, a fitting process is required, to minimize the differences between the experimental and calculated impedance values. The fitted model can finally be compared to the experimental data extracted from the Nyquist and Bode plots to verify the accuracy of the model [3].

3.3.1.3. Galvanostatic charge/discharge (GCD)

GCD is another electrochemical technique, specially used for the characterization of the energy storage properties (energy storage capacity, efficiency, and behavior) of batteries and supercapacitors. For the measurement, the system (battery or supercapacitor) is connected to a source that provides or absorbs a constant current. When the current is provided to the system, energy is stored. Therefore, the system is charged, whereas when the current is absorbed, energy is released, causing the discharge of the system. During the charging process, the voltage gradually increases until the voltage limit is reached, typically determined depending

on the system measured to avoid overcharging. After the charging, the current is reversed to discharge the device, releasing the energy stored, and making the voltage drop until the specified minimum operating voltage.

The voltage across the charging and discharging is recorded, and by comparing the energy stored with the energy released, the energy efficiency of the device can be determined. As well as the energy loss due to the internal resistance. These GCD experiments can also be carried out at different rates to assess the device's rate capability, and to determine if the device maintains its performance at high-demand conditions (fast rates). Finally, by performing multiple charge-discharge cycles, the life cycle of the device, as well as its potential degradation mechanisms can be determined.

3.3.2. MEASUREMENT SETUP

There are different experimental configurations for the investigation and analysis of the electrochemical processes. Depending on the specific requirements and the electrochemical phenomena wanting to investigate, there are different appropriate setups. In this thesis, two types of setups were used.

3.3.2.1. Three-electrode glass cell

A three-electrode glass cell was used for the electrochemical measurements. The cell consists of two basic electrodes (the working electrode (WE) and the counter electrode (CE)), plus a reference electrode (RE). The three electrodes were immersed in the electrolyte, which provided a path for the flow of the electrons or ions of the system. This flow was created due to the ions and electrodes released because of the chemical reaction happening, which converts the chemical energy into electrical energy.

In the case of three-electrode systems, the voltage is measured between the RE and the WE.

Working electrode

The electrochemical reaction under investigation takes place in the WE. It is used to test a material, an electrode coated with a specific catalyst, or any other surface that wants to be analyzed due to the electrochemical reactions that happen on their surface. Therefore, our synthesized composite materials were used as working electrodes.

Reference electrode

The potential of the WE is measured against the potential of the RE, which is stable and already known. There are different types of RE, depending on the experimental requirements needed and the measurement setup. The RE needs to be compatible with the electrolyte selected, suitable for the potential range needed, stable, and accurate. The most used RE are the saturated calomel electrode (SCE) and the silver/silver chloride electrode (Ag/AgCl).

The chosen RE for our measurements was the Ag/AgCl, and the reaction happening is the one expressed in Equation 3.1:

$$AgCl_{(s)} + e^- \leftrightarrows Ag_{(s)} + Cl^-_{(aq)} \qquad \text{Eq.3.1}$$

Counter electrode

The CE provides a pathway for the current to flow through the circuit, allowing the current to flow between the WE and the RE, balancing the current generated at the WE. It should minimize polarization effects and

provide low resistance. Therefore, it needs to have high electrical conductivity, as well as being chemically inert, and stable. The most used CE are platinum (Pt), graphite, glassy carbon, and gold.

The chosen CE was Pt due to its high conductivity, chemical inertness, and stability.

Electrolyte

There are different types of electrolytes, which should be selected accordingly depending on the experiment. Some common types of electrolytes are aqueous electrolytes like potassium chloride (KCl), sodium sulfate (Na_2SO_4) or dilute acids (H_2SO_4) or bases (NaOH); non-aqueous electrolytes like organic solvents and ionic liquids; or other more specific electrolytes like the ones containing salts like tetrabutylammonium perchlorate (TBAP) or tetraethylammonium tetrafluoroborate ($TEABF_4$), or electrolytes containing supporting ions like lithium ions or chloride ions.

For the three-electrode cell, a 0.1M perchloric acid ($HClO_4$) was used as the electrolyte, due to its wide electrochemical window, good water solubility, and low hygroscopicity. A concentration of 0.1 M was used to suppress the effect of ion migration and provide enough ionic conductivity [4].

3.3.2.2. Two-Electrode Half-Cells

Electrochemical studies of novel materials for Li^+ and Na^+ metal batteries are usually performed in 2-electrode half-cells, due to their easy assembly and sufficient stability. It is used to perform simplified measurements and evaluate the electrochemical behavior of specific electrode materials in terms of electroactivity, stability, and catalytic activity. The type of cells employed in this work were the Swagelok cell and the 2032 coin cells, which are explained in more detailed in Annex I.

Two-electrode half-cells are composed of a working electrode and a counter electrode. The WE is where the chemical reaction takes place, while the CE provides a pathway for the current to flow, completing the circuit and balancing the current generated at the WE.

These types of setups are used for simplified studies to evaluate, for example, different electrode materials. This way, properties like electroactivity, stability, and catalytic activity can be assessed, as well as studies where redox reactions are conducted, or experiments like electrodeposition and electroplating, where metals are deposited onto a substrate.

A commonly used WE in lithium-ion batteries is lithium iron phosphate ($LiFePO_4$). It typically serves as cathode material, and it is widely used due to its stability, safety, and good electrochemical performance. Some materials used as CE in $LiFePO_4$ electrode setups are graphite or other carbonaceous materials, and conductive polymers. The choice of these materials is dependent on the chosen electrolyte, which needs to ensure that no undesired reactions or degradations happen. Moreover, the electrical conductivity needs to be appropriate, providing good electrical conductivity and stability.

The electrolyte is usually a lithium salt dissolved in a solvent. The most common electrolyte used for $LiFePO_4$ is lithium hexafluorophosphate ($LiFP_6$) dissolved in a solvent mixture of ethylene carbonate (EC) and dimethyl carbonate (DMC). Lastly, a separator needs to be placed between the WE and the CE to prevent direct contact and enable the movement of the lithium ions between the electrodes, since during the charge cycle Li^+ ions are extracted from the $LiFePO_4$ and moved to the CE, process that is reversed when the discharge happens [5].

3.4. REFERENCES

[1] T 650 om-15. Solids content of black liquor. Peachtree Corners, GA: 2015.

[2] TAPPI T 211 om-16. Ash in wood, pulp, paper and paperboard: combustion at 525 degrees. Peachtree Corners, GA: 2016.

[3] Napporn TW, Holade Y, Kokoh B, Mitsushima S, Mayer K, Eichberger B, et al. Electrochemical measurement methods and characterization on the cell level. 2018. https://doi.org/10.1016/B978-0-12-811459-9.00009-8.

[4] Arenz M, Markovic NM. Half-Cell Investigations of Cathode Catalysts for PEM Fuel Cells: From Model Systems to High-Surface-Area Catalysts. Fuel Cell Sci Theory, Fundam Biocatal 2010:283–316. https://doi.org/10.1002/9780470630693.ch9.

[5] Heubner C, Maletti S, Lohrberg O, Lein T, Liebmann T, Nickol A, et al. Electrochemical Characterization of Battery Materials in 2-Electrode Half-Cell Configuration: A Balancing Act Between Simplicity and Pitfalls. Batter Supercaps 2021;4:1310–22. https://doi.org/10.1002/batt.202100075.

4. FRACTIONATION OF LIGNIN

4.1. MOTIVATION

The design of novel green methods for lignin extraction has gained a vast interest in recent years in contrast to the traditional delignification process used in the Pulp & Paper industry, such as the Kraft process. In this frame, the organosolv method is the most widely used green method due to its simplicity and solvent recyclability. In addition, the obtained lignin exhibits high phenolic content, good solubility in common organic solvents, and low glass transition temperature. Nevertheless, it is heterogeneous, with a high standard deviation in key parameters such as molecular weight and total phenolic content [1].

The different technical lignins currently found in the market depend on the feedstock and extraction method [2]. In this sense, Kraft lignin (KL) usually presents lower molecular weight than organosolv lignin (OL) and lower than the original lignin found in nature, caused by the high-temperature alkaline conditions employed in the Kraft pulping process [3]. As a result, KL appears with a molecular weight of 200–200000 g/mol, a considerable amount of carbohydrates, and 1–3% sulfur content [4]. Most of the KL produced, around 40–50 million tons per year, is used for energy recovery inside the pulp mill, while an excess remains unused [5]. This remaining lignin can be implemented in a wide range of applications such as dispersants, blends, and composites, as well as aromatic compounds precursor [6], contributing to sustainable practices that their fossil-based analogs hamper.

In the organosolv process, instead of alkaline conditions, organic solvents are used for lignin extraction. The use of organosolv fractionation in modern lignocellulosic biorefineries has been widely studied since it allows operating with green solvents [7]. Moreover, it has the potential to become an optimized process for obtaining high-quality lignin with many attractive

characteristics, such as high purity, due to the lack of sulfur content and low ash content [8].

Different approaches, such as acid precipitation, solvent fractionation, and membrane fractionation processes have been developed to overcome the heterogeneity of lignin, a common drawback in both lignin extraction techniques [9]. Fractionation using organic solvents is an utterly customizable method, where solvents (or solvent mixtures), fractionation step numbers, and used anti-solvents can be adjusted to specific needs or aims [10]. Works, where industrial lignins fractionated in single solvent processes [11], spruce and eucalyptus Kraft lignins fractionated by multiple organic solvents [12], and wheat straw organosolv lignin, wheat straw soda lignin, and softwood Kraft lignin fractionated with different proportions of acetone/water mixtures [13] have been reported, for instance.

The sequential organic solvent extraction (SOSE) method is the most suitable process for obtaining narrower molecular weight fractions [14]. The method designed by Park et al. (2018) used a sequence of different organic solvents with different polarities to separate lignin into different fractions with specific characteristics [14].

The capacity of the organic solvent to solubilize lignin depends on the hydrogen bonding capacity, which increases with short aliphatic hydrocarbon side chains and more hydrogen bond donor sites [3]. Moreover, solvents mixed with water show better solubility than pure solvents, leading to increased hydrogen bonding capacity and facilitating the diffusion of organic solvents into lignin [13]. Nevertheless, the addition of water represents another variable, affecting the properties of the fractions obtained and the unappealing formation of azeotropes, which may also affect the enticement of the process in the economic aspect [15].

4.2. OBJECTIVES

The main objective of the work was to design a SOSE method to fractionate both Kraft and organosolv lignins. The focus was to implement the most sustainable process possible, choose the greenest organic solvents possible, and promote recyclability.

To attain this objective, an initial screening of green organic solvents was performed, and based on the solubility performance, weight average molecular weight (M_w), and polydispersity index (PI) values obtained, the most efficient SOSE method was designed.

The SOSE method performed was designed for obtaining homogeneous Kraft and organosolv lignin fractions, with different molecular weights and chemical structure and functionality, which were subsequently characterized by various physicochemical methods.

4.3. EXPERIMENTAL PROCEDURE

4.3.1. ORGANOSOLV EXTRACTION

Organosolv lignin was extracted from eucalyptus chips using an organosolv method, as described in previous works [16,17]. The optimal reaction conditions were selected as follows: 90 min at 180 ºC, with a solid-to-liquid ratio of 1:7 (w/w), using a mixture of ethanol/H_2O 50/50 (v/v) as solvent and adding 50 mmol/L of oxalic acid as catalyst. Once the reaction was finished, the liquor was separated from the delignified solid by filtration.

Then, this delignified material was washed first with the same ethanol/water mixture employed in the lignin extraction and next with deionized water until neutral pH, and it was further characterized. The

extraction was conducted inside a 1.5 L stainless steel Parr Series 5100 pressure reactor with a temperature control (4836 Controller).

4.3.2. Lignin precipitation

Kraft and organosolv lignins were obtained by reducing the pH of the black liquors. KL was precipitated by adding dropwise concentrated H_2SO_4 (96%) until the pH of the liquor reached a value of 2. OL was obtained by adding twice as much water to the liquor, acidified at pH 2 with H_2SO_4 (96%). Precipitated lignins settled overnight before filtration with a 0.45 μm nylon filter paper and neutralized with water. The filtrated lignins were dried at room temperature.

4.3.3. Selection of the organic solvents and order for the fractionation

Methanol (MeOH), ethanol (EtOH), propan-2-one (DMK), ethyl acetate (EtOAc), propan-1-ol (*n*-PrOH), propan-2-ol (*i*-PrOH), butan-2-one (MEK), and butan-1-ol (*t*-BuOH) were selected as suitable green solvents for the process [15]. These eight solvents were tried separately, and the solubilization yield of lignins and molecular weights of the solubilized lignin fractions were determined. 1 g of lignin was dissolved in 10 mL of solvent and left stirring for 2 h. After that, the mixture was filtered using a nylon filter with a pore size of 0.22 μm. The insoluble fraction was dried at 50 ºC overnight, and the soluble fraction was concentrated with a rotary evaporator below atmospheric pressure and dried in an oven at 50 ºC for two days.

The selection and order of the organic solvents were decided according to the results obtained in this section. The solvents selected provided lignin fractions with different molecular weights and yields. In the case where

various fractions had tangible similarities (similar solubilization yield and molecular weight), the most environmentally friendly solvent was chosen. Therefore, only four solvents were selected. To determine the order, solvents were employed based on their increasing dissolving capacity. Consequently, the solvent with the lowest lignin dissolving capacity was employed first, followed by those with progressively higher capacities, culminating in the use of the solvent with the highest dissolving capacity.

4.3.4. Fractionation of lignins with the sequential extraction

The sequential organic solvent extraction method is described in Figure 4.1.

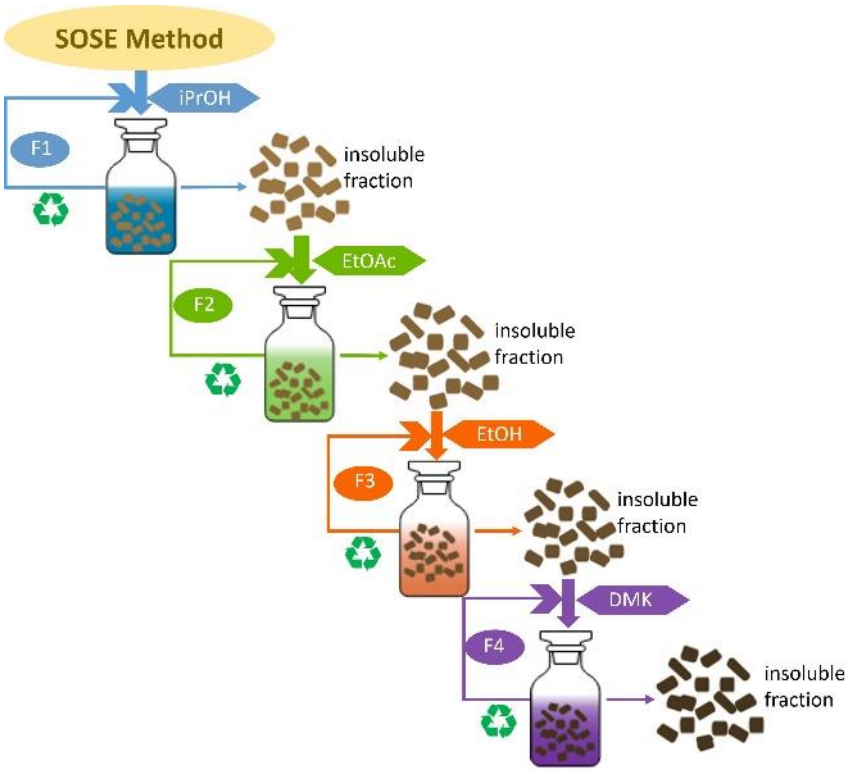

Figure 4.1. SOSE method for both Kraft and organosolv lignins.

As mentioned before, the process started with the solvent possessing the lowest solubility capacity and progressed with increasing solubility capacity. 5 g of lignin were dissolved in 100 mL of solvent and stirred for 2 h. The mixture was then filtered using a 0.22 μm nylon filter. The insoluble fraction was dried overnight in the oven at 50 ºC, while the soluble fraction was rotavaporated to remove the solvent in 75%.

The remaining solution was precipitated using acidified water (H_2SO_4 at pH 2). The precipitated lignin (soluble fraction) was filtered the following day using a 0.22 μm nylon filter membrane, washed with deionized water until a neutral pH, and dried at 30 ºC overnight.

4.3.5. CHARACTERIZATION OF THE LIGNIN FRACTIONS

First, the chemical composition of the lignin fractions was determined. The purity of the fractions obtained was measured by quantitative acid hydrolysis (QAH) [18]. From the hydrolysis performed, AIL or klason lignin was obtained, considered pure lignin, along with ASL and sugar content. Thermogravimetric analyses were also carried out to determine char and ash content. Physicochemical characterization was performed by FTIR, GPC, ^{31}P NMR, UV-vis, and Py-GC/MS. FTIR was used for the identification of the main functional groups, and differences between fractions were observed. GPC was used for the determination of the molecular weights and their polydispersity index.

^{31}P NMR spectroscopy was used for the quantitative analysis of hydroxyl groups (both phenolic and aliphatic) and carboxylic acid OHs. Moreover, the different types of phenolic OH groups and S/G ratios were also determined. UV-vis spectrophotometric methods were used for the determination of conjugated and non-conjugated OH groups. Finally, Py-GC/MS was used for the identification of the lignin derivatives and S/G ratio determination.

Thermal characteristics of lignin and their fraction were analyzed by Thermogravimetric analysis (TGA) and Differential Scanning Calorimetry (DSC).

The procedures followed are explained in Annex I.

4.3.6. Correlation between different properties

The relationship between known interconnected properties of lignin was assessed by the Pearson correlation coefficient between two variables, and linear or asymptotic fits were required by using OriginPro v2020 software.

4.4. Results and Discussion

4.4.1. Characterization of eucalyptus (E) and delignified eucalyptus (DE)

Eucalyptus chips were characterized both before and after the organosolv delignification process.

In the results obtained, a considerable reduction of the lignin content could be observed, this being the objective of the process. The lignin loss resulted in a variation of the content of the remaining compounds, notably the cellulose, which was enriched considerably.

The results are illustrated in Figure 4.2. Percentages of each compound are represented on a dry base (KL and OL moisture contents were 7.72% and 7.45%, respectively) and were comparable to the ones obtained by other authors in similar conditions [19,20].

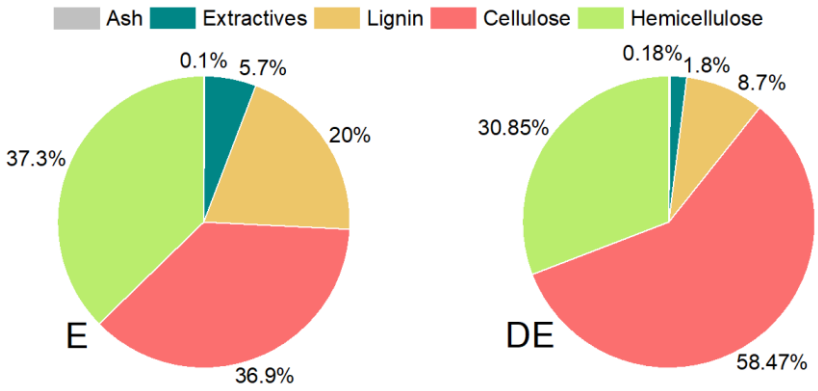

Figure 4.2. Composition of the eucalyptus fibers before and after organosolv treatment.

4.4.2. CHARACTERIZATION OF KRAFT (K) AND ORGANOSOLV (O) LIQUORS

The properties of each liquor are listed in Table 4.1. Significant differences between the two liquors could be observed. Overall, Kraft liquor was richer in solid content, especially inorganic content. This was due to the harsh conditions in which the paper industry extracts lignin, using compounds like NaOH and Na_2S, forming different residual inorganic compounds.

Table 4.1. Properties of Kraft liquor (K) and organosolv liquor (O).

	Density (g/cm³)	**pH**	**Total solid content (%)**	**Organic content (%)**	**Inorganic content (%)**	**Dry lignin content (g/l)**
K	1.09 ± 0.01	13.02 ± 0.03	15.49 ± 2.94	8.55 ± 0.82	8.74 ± 0.00	41.67 ± 5.65
O	0.95 ± 0.01	4.02 ± 0.08	5.57 ± 0.21	5.54 ± 1.17	0.04 ± 0.15	29.11 ± 2.92

The main difference in the delignification processes was the solvent used, consequently varying the pH of the liquors: Kraft liquor had a basic medium, while organosolv lignin had a slightly acidic medium. For this reason, the extracted lignins presented structural and chemical differences.

4.4.3. Yield and molecular weight determination of the initial screening of the solvents for Kraft and organosolv lignin solubilization

Before the SOSE design, different green organic solvents were tested to observe how the molecular structures of these solvents influenced lignin solubilization. For that, eight different solvents were chosen: one ester, two ketones, and five alcohols (three primaries, two secondaries, and one tertiary). The selected solvents, as well as some of their main properties, are shown in Table 4.2.

Table 4.2. Main properties of the selected solvents for the initial screening.

	MeOH	***EtOH***	***DMK***	***EtOAc***	***n-PrOH***	***i-PrOH***	***MEK***	***t-BuOH***
Chemical formula	CH_4O	C_2H_6O	C_3H_6O	$C_4H_8O_2$	C_3H_8O	C_3H_8O	C_4H_8O	C_4H_{10}
Hildebrand	29.7	26.0	19.9	18.2	---	24.4	---	---
Boiling Point (°C)	65.0	78.0	56.0	77.0	97.0	82.6	79.6	82.0
Flammability*	3	3	3	3	3	3	3	3
Health risk*	3	1	1	1	1	1	1	2
Reactivity*	0	0	0	0	0	0	0	0

* NFPA 704: Standard System for the Identification of the Hazards of Materials for Emergency Response

Figure 4.3 and Table 4.3 present the solubilization yield and the molecular weight of the solubilized fraction for all the selected solvents. It can be observed that the solubility yields obtained with KL were higher in all solvents than those for OL. This is probably due to the lower molecular weight of the lignin, which was nearly half as big as the organosolv lignin (3167 and 5800 g/mol). The molecular weights of the solvent fractions maintained a similar tendency, especially in the case of EtOH, EtOAc, *n*-PrOH, *i*-PrOH, MEK, and *t*-BuOH, where M_w values fluctuated identically in KL and OL. The contrary happened with the yields obtained from those solvents.

Table 4.3. Yields, M_w, and PI of each solubilized lignin fraction.

Solvent	***Kraft lignin***			***Organosolv lignin***		
	Yield (%)	**M_w (g/mol)**	**PI**	**Yield (%)**	**M_w (g/mol)**	**PI**
MeOH	89.70	2770	3.8	88.61	5016	3.3
EtOH	79.85	2233	3.3	36.35	2300	3.0
DML	87.97	11985	4.2	87.57	6040	3.7
EtOAc	57.89	1802	2.6	32.90	1931	2.7
n-PrOH	60.62	1507	2.6	24.08	1287	2.7
i-PrOH	33.08	999	2.1	6.46	1014	2.4
MEK	79.43	2275	3.7	38.39	2048	3.1
t-BuOH	61.69	1373	2.5	6.37	1171	2.6

The quantities recovered from KL were significant, while those values diminished drastically for OL fractions. That might be attributed to the PI of the lignins. KL was smaller and more homogeneous than OL (PI of 2.91 and 4.44, respectively), making it more soluble in different solvents. However, OL was larger and more diverse, leading to molecules varying in size and making those bigger molecules more selective to solubilize. That was the reason for obtaining lower yields with OL than with KL for the solvents with lower lignin solubility capacity. MeOH and DMK were the solvents with the highest solubility yields and highest molecular weights in both lignin types.

Even though these two solvents are not constituted by the same functional group (MeOH is a primary alcohol while MEK is a ketone), they are formed by a similar branch, a methyl group. Since it is the smallest alkane branch, the functional groups of the solvents were highly accessible to dissolve small lignin molecules and the bigger ones. EtOH and MEK presented a similar behavior and composition as to MeOH and DMK. EtOH is a primary alcohol and MEK is a ketone, and they are branched with ethyl groups. Since EtOH and MEK have longer branches than MeOH and DMK, it was slightly harder to solubilize the bigger lignin molecules, so the yields and M_w obtained were considerably lower.

The remaining solvents were EtOAc, *n*-PrOH, *i*-PrOH, and *t*-BuOH. These are more impeded than the solvent mentioned before. Apart from being more branched, the functional groups are also different. Even though three of them are alcohols (*n*-PrOH, *i*-PrOH, and *t*-BuOH), they are not the same type of alcohol. *n*-PrOH is primary, *i*-PrOH is secondary, and *t*-BuOH is tertiary. Furthermore, EtOAc is an ester, so the polarities of these four solvents are different, and the order goes *n*-PrOH>*i*-PrOH>*t*-BuOH>EtOAc. However, there was no apparent relation between the polarity of the solvent and the yield or molecular weight of the fraction obtained.

Therefore, it can be concluded that instead of the polarity, the factor affecting the most the lignin solubilization was the molecular size of the solvent, being the most effective the smallest in size, which was more easily accessed to the large macromolecule of lignin. Therefore, the solvents and their order in the sequential fractioning were decided to perform the greenest method possible and to obtain the most different but homogeneous fractions by considering the yields and molecular weights.

Consequently, it was decided that *i*-PrOH, EtOAc, EtOH, and DMK were the most suitable solvents for the process, due to the good yields obtained that

minimized the loss of material in the process, as well as for their different properties, which ensure the obtaining of different lignin fractions.

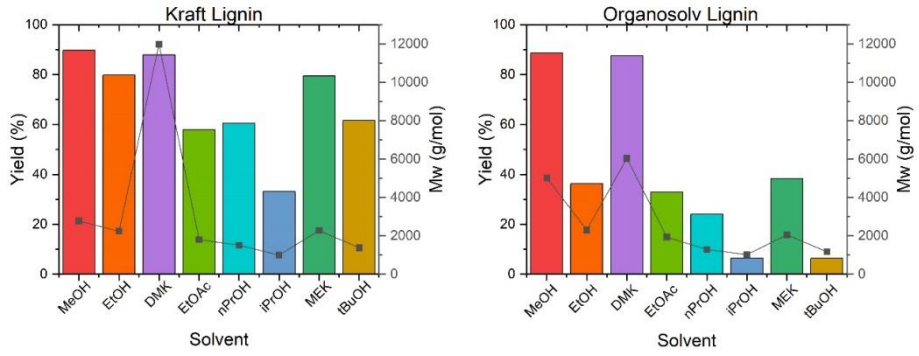

Figure 4.3. Solubilization yields and molecular weight for each lignin type.

4.4.4. YIELDS OF THE SEQUENTIAL ORGANIC SOLVENT EXTRACTION

Figure 4.4 presents the yields of the sequential fractioning. KL was more solubilized than OL, as observed during the solvent screening, probably due to the lower molecular weights. However, the loss during the process was also more significant with KL.

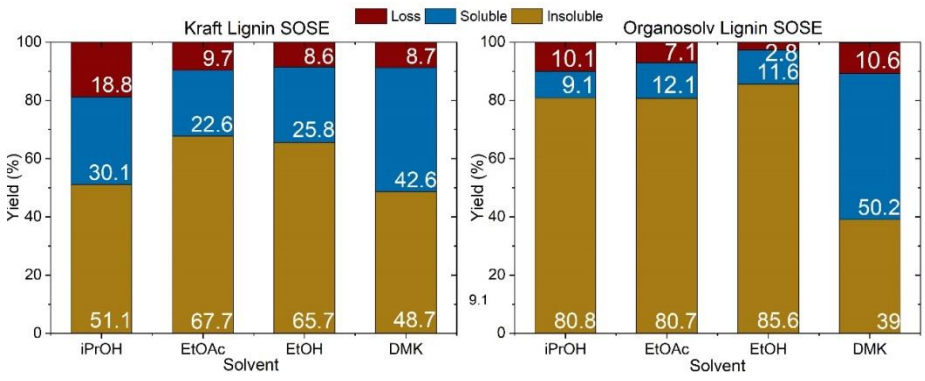

Figure 4.4. Solubilization yields and molecular weight for each lignin type.

Overall, the solubilization percentages remained similar in the first three steps of the sequential extraction. Nevertheless, the solubilized yield considerably increased in the last step, where DMK was used. Similar to the results from the solvent screening, DMK solubilized the most considerable amount of lignin.

4.4.5. Chemical structure

The infrared spectra of Kraft lignin, organosolv lignin, and their fractions are shown in Figure 4.5, reflecting the common and particular structural features and functional groups of the molecules.

The first band observed in the spectra was the broad band at 3400 cm^{-1}, attributed to the O-H stretching of aliphatic hydroxyl groups. It was observed in both lignin types that the sequential fractionation process reduced the amount of this functional group, being nearly inexistent in the insoluble fraction. The band at 2900 cm^{-1} is attributed to the C-H stretching of methoxy, methyl, and methylene groups. In the original Kraft and organosolv lignins, these bands were considerably less intense than in their fractions. In fractioned Kraft lignin, the intensity increased as the fraction number increases, while for fractioned organosolv lignin, this difference, although visible, was not as severe. The intensity of this band increased as the fractionation process advanced, owing to the greater molecular weight of solubilized molecules as a consequence of the prevalence of molecules with side chains containing methyl and methylene groups [21].

This was also visible from the results obtained in Py-GC/MS, where the abundance of pyrolysis-derived products from branched molecules followed the same trend. Bands between 1600 and 1420 cm^{-1} are attributed to the vibration and deformation bands of the C-H groups forming the aromatic rings. Bands at 1325 cm^{-1} correspond to the S ring, while bands at 1260 cm^{-1}

correspond to the G ring. These bands decreased at each step of the cascade fractioning, even though the fluctuation of the S/G ratio was not evident.

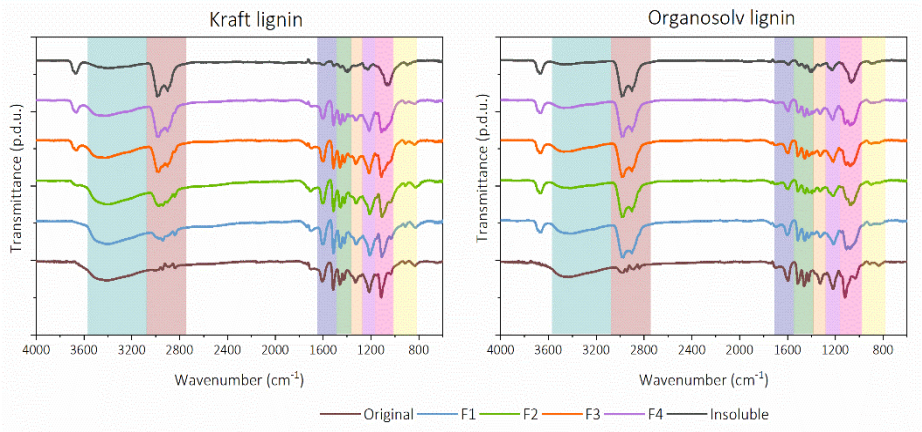

Figure 4.5. FTIR spectra of original and fractionated lignin by the SOSE method.

4.4.6. Molecular weight and lignin purity

M_w and PI were also calculated for the fractions obtained in the SOSE. These values, along with their chemical characterization values, were collected in Table 4.4. Some noticeable differences could be observed from the values in Table 4.3.

For example, the first fraction, soluble in *i*-PrOH, had similar M_w and PI values (Table 4.3). However, from the second step forward, molecular weight values differed due to the removal of the fractions solubilized in the previous steps, which affected the overall values. In this sense, the second fraction (EtOAc) had a decrease of approximately 25% in the M_w for KL F2 and around 30% for OL F2. The third fraction (EtOH) showed a decrease of approximately 9% for KL F3 and about 15% for OL F3, while the fourth fraction (DMK) experienced a decrease around 60% for KL F4 and approximately 24% for OL F4. However, the M_w of insoluble fractions were similar in both lignins (14514 g/mol for KL FI and 14255 g/mol for OL FI).

Table 4.4. M_w, PI, and chemical composition of original and lignin fractions.

	M_w (g/mol)	PI	AIL (%)	ASL (%)	Ash (%)
KL	3167	2.91	73.99 ± 2.24	19.00 ± 0.77	7.01
KL F1	951	1.85	81.64 ± 1.93	14.04 ± 2.95	4.32
KL F2	1310	2.14	75.75 ± 5.95	18.44 ± 2.49	5.81
KL F3	1893	2.39	87.72 ± 0.63	9.14 ± 0.34	3.14
KL F4	4682	3.50	88.68 ± 0.73	8.24 ± 0.25	3.08
KL FI	14514	4.43	83.54 ± 2.59	12.66 ± 0.61	3.80
OL	5800	4.44	90.91 ± 0.82	6.23 ± 0.67	2.86
OL F1	1036	1.61	84.01 ± 2.05	13.79 ± 0.56	2.20
OL F2	1341	1.81	81.42 ± 0.06	17.23 ± 4.01	1.35
OL F3	2096	2.47	85.38 ± 2.00	12.26 ± 0.96	2.36
OL F4	4569	3.08	82.00 ± 2.45	14.71 ± 1.31	3.29
OL FI	14255	3.82	89.02 ± 6.00	7.90 ± 0.54	3.08

Overall, it can be observed that regardless of the origin of the lignins, where KL had a considerably smaller molecular weight than OL (3167 g/mol against 5800 g/mol), the fractions obtained in each fractionation step were very similar. KL F1 and OL F1 fractions obtained from the solubilization of original lignins with *i*-PrOH, the simplest secondary alcohol, were very similar, 951 and 1036 g/mol. The second fractions obtained were solubilized with EtOAc, the ester of ethanol and acetic acid, and had molecular weights between 1310 and 1341 g/mol, respectively. The trend of having similar molecular weights in the same fractions followed throughout the whole process.

The fractions obtained in the third step (EtOH, primary alcohol) showed molecular weights of 1893 and 2096 g/mol, and the fourth step fractions corresponding to DMK had molecular weights of 4682 and 4569 g/mol. Consequently, the SOSE process successfully obtained homogeneous fractions, whether these were from Kraft or organosolv lignin. The PI

increased as the M_w of the fraction raised because the solvent used had higher solubility capacities and, therefore, could solubilize a broader range of molecules. Regarding acid soluble lignin (ASL) and acid insoluble lignin (AIL), OL exhibited a high level of purity (90.91% of AIL, also known as Klason lignin), due to the much milder lignin isolation process compared to the KL (73.99% of AIL).

Additionally, OL had considerably lower ASL content compared to KL due to the purer extraction process from which it was obtained [22]. The higher purity on the initial lignin affected the fractions obtained and their yield. The very high purity of OL prevents its purification and all the obtained OL fractions had similar or lower purity than the initial lignin. However, the SOSE process led to purer fractions of KL, increasing around 10% the purity of most fractions.

Regarding the yields of the fractions recovered, which were depicted in Figure 4.4, it could be observed that they were considerably smaller with OL, especially on the initial fractions, which was related to the higher M_w of this type of lignin. The lignins with high M_w have lower solubility so, at first, OL was less soluble than KL. Nonetheless, the fractionation led to more homogeneous lignin fractions with lower PI, which occurred for both types of lignin confirming that the SOSE process acts equally regardless of the initial lignin nature.

One of the most prominent lignin properties is associated with its hydroxyl content, affecting solubility and reactivity. Consequently, the quantitative determination of the different OH groups present in the molecules is of great importance. To do so, one of the most precise and advanced methods is the quantitative analysis of ^{31}P NMR spectra. Different peaks are associated with different hydroxyl groups, and their integration, compared with the integration of the internal standards, provided their concentrations.

Concentrations of aliphatic OH, C5- substituted OH, guaiacyl OH, p-hydroxyphenyl OH, and carboxylic acid OH groups were obtained in mmol OH/g lignin. Moreover, the S/G ratio was also calculated by dividing C5-substituted OH groups (considered syringyl OH groups due to signal overlap issues) by guaiacyl OH groups. The results are listed in Table 4.5.

Table 4.5. ^{31}P NMR results for KL, OL, and the fractions obtained by the SOSE method.

	OH content (mmol OH/g lignin)					*S/G ratio*
	Al	***S***	***G***	***H***	***CA***	
KL	0.43	1.37	0.25	-	0.21	5.39
KL F1	0.63	3.73	0.82	-	0.55	4.55
KL F2	0.19	1.38	0.40	-	0.19	3.44
KL F3	1.76	3.73	1.28	-	0.34	2.92
KL F4	1.42	2.86	1.24	-	0.31	2.30
KL FI	1.37	0.94	0.43	-	0.10	2.18
OL	1.44	0.98	0.32	-	-	3.08
OL F1	1.41	3.03	1.34	-	0.09	2.27
OL F2	1.52	2.90	0.81	0.05	0.10	3.59
OL F3	1.76	2.69	0.85	-	0.12	3.17
OL F4	2.50	1.89	0.85	-	0.06	2.21
OL FI	3.56	1.11	0.36	-	0.04	1.70

It was confirmed that the lignins came from hardwood due to the lack of p-hydroxyphenyl OH units, only present in softwoods and grasses. S/G ratios obtained were above one, which is also another characteristic of hardwood lignin [23]. Even though the raw material used for both lignin types was the same, there were significant differences in the concentrations of hydroxyl groups. The overall hydroxyl content of OL was more abundant, especially in aliphatic OH groups, three times bigger than in KL. However, the concentration of S OH groups was smaller while maintaining similar G OH

content and not finding any CA hydroxyl groups. Consequently, the S/G ratio was also smaller.

In terms of the influence exerted by the extraction method on the fractions obtained, a different trend was detected for Kraft and organosolv lignin. The first soluble KL fraction (KL F1) had more than twice the hydroxyl groups than the original lignin (KL). However, the most noticeable difference happened with S OH groups, which increased almost three times and reached a high concentration. Nevertheless, the S/G ratio decreased due to the increase of G units. On the contrary, the second fraction obtained (KL F2) had a fewer amount of hydroxyl groups than KL itself. This might be because EtOAC does not have a high solubility capacity, but another reason might be that since being an ester, it does not have free OH groups, and consequently, the fractions solubilized presented fewer OH groups accessible.

The fraction obtained with the third solvent (KL F3) followed a similar trend to the first fraction, where all types of OH increased in their abundance. The most significant rise was with the G OH groups, reaching four times its initial concentration, followed by aliphatic OH groups. S OH groups reached the maximum amount of all the fractions obtained, 3.73 mmol OH/g lignin, yet the S/G ratio decreased since G units increased more than S units in proportion. The last fraction obtained (KL F4) also increased its OH content. Apart from slightly increasing the carboxylic acid content and increasing the aliphatic content, S and G units also increased. G units increased four times their initial content, while S units doubled, so the S/G ratio decreased, obtaining the smallest ratio of all the soluble fractions. In terms of the insoluble fraction remaining after the sequential extraction (KL FI), it was noticeable that it was most abundant in aliphatic hydroxyl content, even though the phenolic hydroxyl content was not that far from that of the initial lignin.

In terms of the OL and its solubilized fractions, it could be seen that overall, the total OH content was higher than in KL. However, the phenolic OH content was similar or even lower than in Kraft lignin, except for the second soluble fractions, since with Kraft lignin, phenolic hydroxyl content was the lowest out of all the Kraft fractions, and with organosolv lignin, the content maintained similarly to its other fractions. The difference in aliphatic OH groups in OL fractions was not significant, except for the last soluble fraction and the insoluble fraction. In terms of the phenolic OH content, soluble fractions more than doubled the amount of those groups compared to the original lignin, the first fraction having the highest concentration of both, the S OH groups and especially the G OH groups.

A UV scan between 400 nm and 260 nm was performed to identify conjugated and non-conjugated OH groups. Phenolic structures can be divided into six structural types, as suggested elsewhere [24]. The unconjugated phenolic structures were estimated using the maxima at 300 and 350–360 nm and conjugated structures were obtained from the maximum at 350–370 nm [24]. Figure 4.6 presents the UV–vis absorption spectra (top) and the derivative absorption spectra (down), used to identify the real position of peaks and resolute the overlapping peaks, as derivative curves are more structured than the original spectra [25].

The numerical absorbance values obtained for both the conjugated and non-conjugated spectral bands are listed in Table 4.6. In this sense, there were no striking differences between the original Kraft and organosolv lignins, with most differences occurring in their fractions.

The identified derivative peaks, which correspond with the main inflections of the spectra, are listed in Tables 4.7 and 4.8. The peaks present in all samples were identified by their λ_{max}, and the main absorption shifts are discussed below.

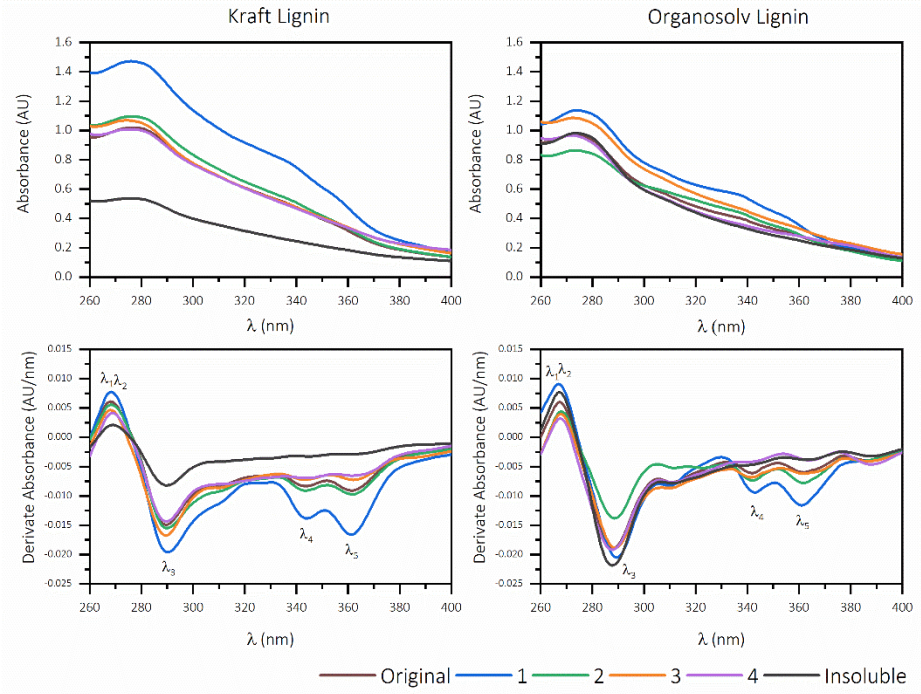

Figure 4.6. UV–vis absorption spectra (top) and the derivative absorption spectra (down) of KL, OL, and the fractions obtained.

Table 4.6. Absorbance values of Kraft and organosolv lignin and their fractions in wavenumbers 280 and 315 nm of the UV-vis range.

	KL	KL F1	KL F2	KL F3	KL F4	KL FI
280 nm	1.01	1.46	1.09	1.05	1.00	0.53
315 nm	0.65	0.96	0.69	0.65	0.64	0.33
	OL	**OL F1**	**OL F2**	**OL F3**	**OL F4**	**OL FI**
280 nm	0.94	1.11	0.84	1.05	0.91	0.95
315 nm	0.52	0.66	0.55	0.61	0.48	0.48

There are two phenomena to take into account. The first is the intensity of the peaks at the regions mentioned above, and the second is the difference in the absorption wavelengths, as absorption at a longer wavelength (bathochromic shift) may be due to the effect of an increased degree of conjugation [26].

In KL, the higher intensities were those of KL F1, both in non-conjugated peaks (λ_1 and λ_2) and in conjugated peak (λ_5). In the conjugated spectrum (350–370 nm), it could be observed that most fractions from Kraft lignins were isochromic, except the KL F3 fraction, which had a bathochromic shift.

Table 4.7. Inflection wavelengths for Kraft lignin and its fractions.

	KL	***KL F1***	***KL F2***	***KL F3***	***KL F4***	***KL FI***
λ1 (nm)	268	268.5	268.5	268	269	269
λ2 (nm)	270.5	271.5	271.5	271	271.5	278.5
λ3 (nm)	289.5	290.5	288.5	289.5	289.5	290
			290			
		300.5	301	300.5	301	300.5
				310		310.5
	314.5		314			
				320.5		
		326.5		325.5		328.5
	340	333.5	335			336.5
λ4 (nm)	343.5	344	343.5	343	344	345.5
						349.5
	355.5	355	356	356	359	
λ5 (nm)	361.5	361.5	361.5	362	361.5	361.5
λ6 (nm)	393.5		398	395.5	397.5	397.5

Nevertheless, there was also a hyperchromic shift observed, with the hyperchromic trend following the pattern KL F1 >KL F2 >KL>KL F3 >KL F4 >KL FI. This indicated that the conjugated absorption was hypochromic for KL F3, KL F4, and KL FI. In the case of OL, the OL F1 fraction exhibited a hypsochromic shift, while the insoluble fraction had a bathochromic shift. The rest of the fractions had an isochromic conjugated spectrum. On the

other hand, the intensity of absorption at the conjugated spectrum followed the trend OL F1 >OL F2 >OL F3 >OL>OL F4 >OL FI.

Table 4.8. Inflection wavelengths of organosolv lignin and its fractions.

	OL	***OL F1***	***OL F2***	***OL F3***	***OL F4***	***OL FI***
λ1 (nm)	267.5	267	268	268	267.5	267
λ2 (nm)	268.5	267.5	269	270	269	268
	276	277.5	275.5	281	282	284
λ3 (nm)	288	289.5	288.5	289	288	288
	297.5	304.5	297.5	297.5	298	
	311	310	312	310	311	311.5
	318.5	315				312
			322.5			
	335	334.5	333.5	335	335	339
λ4 (nm)	342	343	342	341.5	339	347
	351.5	352.5	350.5			
					354	
λ5 (nm)	362	361	362	362		363
	365			365	364	365.5
	375.5		375.5	365.5	375.5	
λ6 (nm)	386.5	388	385	386.5	388	388

The pyrolysis of the samples was performed and the gaseous products were analyzed to quantify the syringyl, guaiacyl, and p-hydroxyphenyl units of lignin and the carbohydrate derivatives of each lignin sample. The percentages of identified lignin, S, G, and H units, and S/G ratios are listed in Table 4.9.

There were some differences between the results obtained by Py-GC/MS and those of ^{31}P NMR. The most noticeable difference was the content of the H groups. From the ^{31}P NMR spectra obtained, only OL F2 contained H units.

Nevertheless, in the results from Py-GC/MS, all the fractions showed some H groups, even though this was the least abundant unit. These differences can be attributed to the nature of the analysis. Since Py-GC/MS is a destructive method, potential confusion in the identification of the pyrolysis products might lead to an increase in H units. In addition, subtle but identifiable differences existed concerning S and G units.

Table 4.9. Percentages of identified lignin, S, G, and H units, and S/G ratio.

	Lignin identified (%)	***S units (%)***	***G units (%)***	***H units (%)***	***S/g ratio***
KL	74.55	51.00	44.90	4.11	1.14
KL F1	92.39	50.89	44.88	4.23	1.13
KLF2	98.25	55.07	42.11	2.82	1.31
KL F3	92.59	53.74	42.31	3.95	1.27
KL F4	92.79	48.15	45.62	6.24	1.06
KL FI	69.09	31.94	43.06	25.00	0.74
OL	91.50	54.88	42.33	2.80	1.30
OL F1	91.97	50.83	44.59	4.58	1.14
OLF2	92.69	48.75	46.39	4.86	1.05
OL F3	87.48	62.94	34.02	3.04	1.85
OL F4	89.35	57.61	39.50	2.88	1.46
OL FI	90.81	47.61	46.17	6.22	1.03

For KL fractions, the content of S units followed the trend KL F2 >KL F3 >KL F1 >KL F4 >KL>KL FI. The G units content followed the trend KL F4 >KL F2 >KL F3 >KL>KL F1 >KL FI. In OL fractions the S units trend was OL>OL F3 >OL F4 >OL F1 >OL F2 >OL FI, while the G units trend was OL F2 >OL FI>OL F1 >OL F4 >OL F3 >OL. S/G ratios also varied, with the following trends: KL F2 >KL F3 > KL>KL F1 >KL F4 >KL FI and OL F2 >OL F3 >OL>OL F1 >OL F4 >OL FI.

The relationship between some interconnected properties of lignin was assessed by the Pearson correlation coefficient. First, the correlation between S/G ratios obtained by Py-GC/MS and ^{31}P NMR are shown in Figure 4.7. The correlation threw a Pearson coefficient of 0.4008 for KL and 0.2649 for OL.

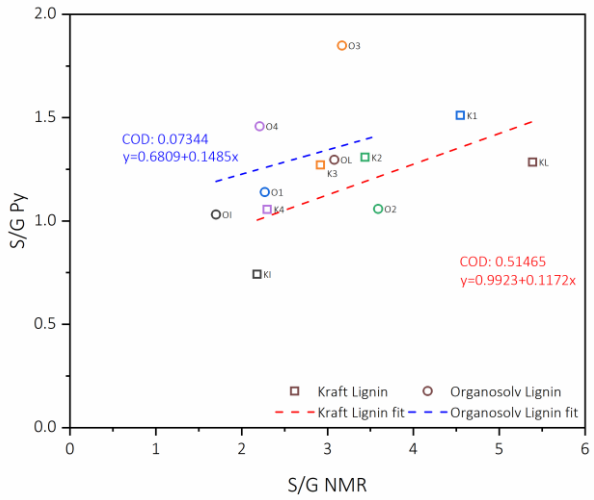

Figure 4.7. Correlation between S/G ratios obtained by Py-GC/MS and ^{31}P NMR.

Moreover, the correlation between S/G ratios obtained by ^{31}P NMR and the M_w is shown in Figure 4.8. On the other hand, Figure 4.9 shows the correlation between the T_g obtained from DSC and the M_w. Finally, Figure 4.10 shows the correlation between T_g (in degrees Kelvin) as obtained from DSC and the M_n according to the Flory–Fox model. The coefficient of determinations shown in Figures 4.7, 4.9 and 4.10 were calculated based on a least squares linear fit. The coefficient of determination calculated in Figure 4.8, alternatively, was calculated based on a least squares exponential asymptotic fit.

It has been previously addressed that fractions with higher molecular weights tend to have less content of S units [27,28]. Consequently, as the fractionation process progressed the S content decreased, leading to a

reduction in the S/G ratio. This trend was visible from the results obtained in the ^{31}P NMR analysis,with trends of KL>KL F1 >KL F2 >KL F3 >KL F4 >KL FI and OL F2 >OL F3 >OL>OL F1 >OL F4 >OL FI.

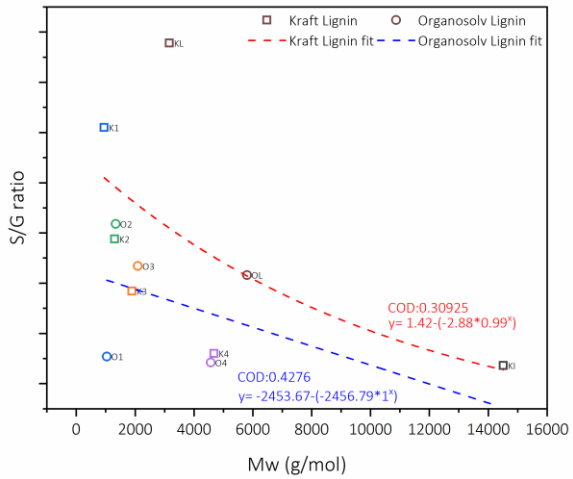

Figure 4.8. Correlation between S/G ratios obtained by ^{31}P NMR and the M_w.

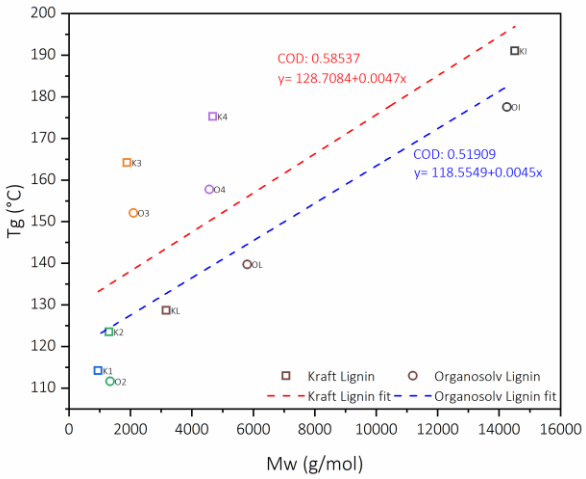

Figure 4.9. Correlation between T_g obtained from DSC and the M_w with a linear fit.

The relationship between the S/G ratio and the M_w can be appreciated in detail in Figure 4.8. It is apparent that, without taking into account the original lignins but their fractions, there was a drastic decrease in the S/G

ratio as the M_w increased. This decrease became more pronounced after approximately 4000 g/mol, as reported by Wang et al. (2018) [29].

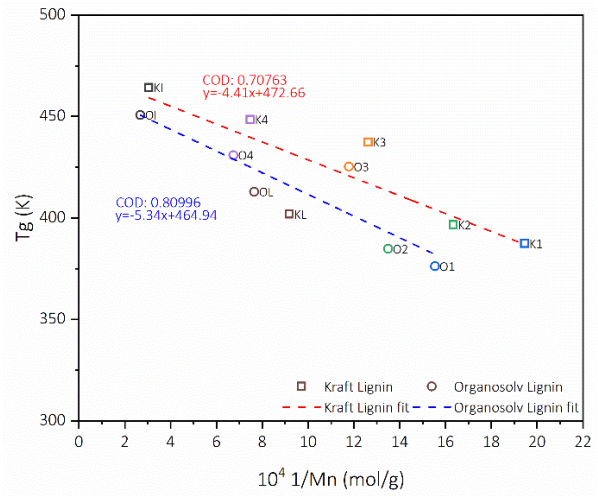

Figure 4.10. Correlation between T_g (in degrees Kelvin) as obtained from DSC and the M_n according to the Flory–Fox model.

The thermogravimetric curves obtained from the samples revealed the thermal stability of the lignins and their fractions. Stability was calculated by the mass loss of the sample at high temperatures. The temperature at which 5% and 50% of the mass degradation occurred was calculated ($T_{5\%}$ and $T_{50\%}$, respectively), as well as the final char residue. Figure 4.11 shows TG and DTG curves of KL (left) and OL (right) and their fractions. Moreover, all the degradation stages and their temperatures are listed in Table 4.10.

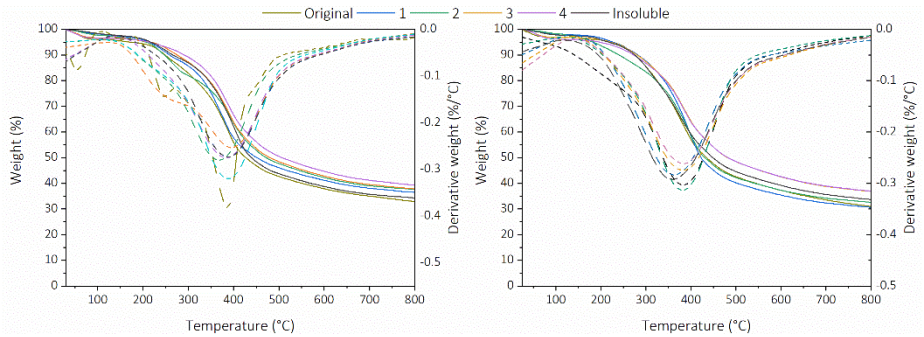

Figure 4.11. TG and DTG curves of Kraft (left) and organosolv (right) lignin and their fractions.

Table 4.10. Temperatures at 5% and 50% mass loss, and char residue at 800 °C for Kraft lignin, organosolv lignin, and their fractions.

	Sample	***KL***	***KL F1***	***KL F2***	***KL F3***	***KL F4***	***KL FI***
TGA	$T_{5\%}$ (°C)	185	205	200	230	210	220
	$T_{50\%}$ (°C)	430	435	470	460	510	440
	Char (%)	42.37	36.61	38.07	37.89	39.84	34.38
DTGA	1st Stage (°C)	60	65	70	55	55	75
	2nd Stage (°C)	150	140	120	180	220	140
	3rd Stage (°C)	240	230	255	240	400	240
	4th Stage (°C)	300	370	430	385		400
	5th Stage (°C)	400					
	Sample	***OL***	***O1***	***O2***	***O3***	***O4***	***OI***
TGA	$T_{5\%}$ (°C)	80	230	185	220	190	220
	$T_{50\%}$ (°C)	370	420	430	480	480	450
	Char (%)	31.85	30.86	32.64	64.59	37.06	33.81
DTGA	1st Stage (°C)	60	60	70	60	60	70
	2nd Stage (°C)	350	385	130	280	260	195
	3rd Stage (°C)			230	385	375	295
	4th Stage (°C)			400	530	520	410

For most samples, the 5% mass degradation occurred in temperatures below or near 100 °C, corresponding to moisture loss. However, the temperature in which 50% of the mass degradation occurred differed. Even though all the $T_{50\%}$ values ranged from 320 to 400 °C, similar trends in the fractions obtained in the fractionation process could be observed. KL F1 and OL F1 fractions had lower $T_{50\%}$, probably because these fractions were the ones with the smallest M_w, and consequently, degraded more easily. However, as the SOSE process continued and the fractions obtained had higher M_w, the $T_{50\%}$ also increased.

The only exception to the rule was for KL F3, where $T_{50\%}$ was lower despite having a higher M_w than KL F2, KL F1, or KL. The reason might be the higher content of aliphatic OH groups in this KL F3 fraction, as they are more degradable than other groups [30]. However, some fractions had a lower $T_{50\%}$ not connected with the easier degradability. The lower amount of char residue means less carbonaceous content, which is not degraded by heating in an inert atmosphere.

As for the DTGA, the different fractions had different numbers of degradation stages and different temperatures. It has been reported that degradation steps between 100 and 150 °C correspond to moisture loss, between 200 and 300 °C is the degradation of polysaccharides and aliphatic alcohols and acids, and at temperatures above 300 °C degrade aromatic rings and S and G compounds into phenols, aldehydes, alcohols, and acids [1].

Figure 4.12 shows the DSC curves of the different lignins and their fractions. The different T_g obtained from the derivative analysis of DSC curves are shown in Table 4.11.

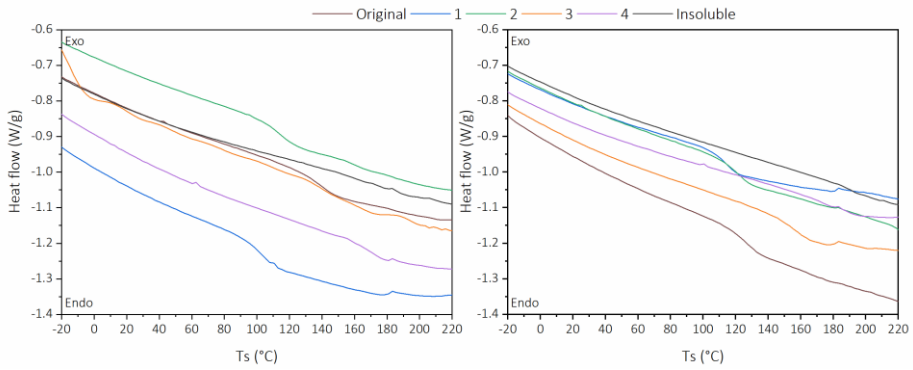

Figure 4.12. DSC curves of Kraft (left), organosolv (right) lignin, and their fractions.

Table 4.11. Glass transition temperatures of Kraft lignin, organosolv lignin, and their fractions.

	KL	***KL F1***	***KL F2***	***KL F3***	***KL F4***	***KL FI***
T_g (°C)	128.67	114.2	123.47	164.18	175.26	191.01
	OL	***OL F1***	***OL F2***	***OL F3***	***OL F4***	***OL FI***
T_g (°C)	139.71	103.01	111.62	152.11	157.75	177.56

The T_g obtained followed the same trend for both KL and OL fractions: KL FI>KL F4 >KL F3 >KL>KL F2 >KL F1, and OL FI>OL F4 >OL F3 >OL>OL F2 >OL F1. It is known that at higher M_w, the T_g presents a directly proportional behavior, which in the case of the obtained lignins presented a significant correlation at the 0.05 level, with a Pearson value of 0.7651 for KL and of 0.7844 for OL (Figure 4.9). The lignins that outlined the linear fit were the fractions extracted with EtOH (KL F3 and OL F3) and DMK (KL F4 and OL F4). These fractions were also the ones showing higher thermal stability in Figure 4.11. The reason for this higher T_g is related to a higher lignin condensation (high M_n), as reported by Allegretti et al. (2018) [31].

Modelling the T_g as a function of the M_n of the different lignin fractions through the Flory-Fox model (shown in Figure 4.10) revealed that the K for Kraft fractions was 3.41, while for organosolv fractions, it was 5.34. $T_{g\infty}$was 472.66 for Kraft fractions and 464.94 for organosolv fractions (Figure 4.8). These values were close to those found by other works for solvolytically fractioned Kraft lignins [14,32].

4.5. CONCLUSIONS

The sequential Organic Solvent Extraction method proved to be efficient for obtaining fractions with homogeneous molecular weights regardless of the extraction method (Kraft or organosolv). The organic solvents were chosen

to ease the separation of different M_w fractions. The selected order provided fractions with ascending M_w.

Furthermore, it was found that these variations in the M_w influenced the structural and thermochemical characteristics of the fractions. Fractions with higher M_w had, lower abundance of S units and OH groups but higher methyl and methoxy groups. Consequently, the S/G ratio also varied, decreasing as the fractionation process advanced. This difference in M_w also influenced the degradation parameters of the fractions, having less degradable lignin molecules with the last fractions obtained in the process.

In conclusion, the different lignin fractions obtained displayed concrete structures and properties, which are presumed to remain consistent even when derived from different lignocellulosic materials. Even though the type of lignin had minor effects on the final characteristics of the fractions, further research is necessary to assess the applicability of the method across a wider range of feedstocks.

The smallest fractions, richer in hydroxyl groups, will be advantageous for processes requiring chemically active lignins. On the other hand, larger lignin fractions are valuable for their incorporation into materials with enhanced thermochemical resistance. These findings highlight the versatility of lignin fractions obtained through this method, catering to diverse industrial applications.

4.6. REFERENCES

[1] Ramakoti B, Dhanagopal H, Deepa K, Rajesh M, Ramaswamy S, Tamilarasan K. Solvent fractionation of organosolv lignin to improve lignin homogeneity: Structural characterization. Bioresour Technol Reports 2019;7. https://doi.org/10.1016/j.biteb.2019.100293.

[2] Matsushita Y. Conversion of technical lignins to functional materials with retained polymeric properties. J Wood Sci 2015;61:230–50. https://doi.org/10.1007/s10086-015-1470-2.

[3] Melro E, Alves L, Antunes FE, Medronho B. A brief overview on lignin dissolution. J Mol Liq 2018;265:578–84. https://doi.org/10.1016/j.molliq.2018.06.021.

[4] Lora JH, Glasser WG. Recent industrial applications of lignin: A sustainable alternative to nonrenewable materials. J Polym Environ 2002;10:39–48. https://doi.org/10.1023/A:1021070006895.

[5] Wenger J, Haas V, Stern T. Why Can We Make Anything from Lignin Except Money? Towards a Broader Economic Perspective in Lignin Research. Curr For Reports 2020;6:294–308. https://doi.org/10.1007/s40725-020-00126-3.

[6] Dessbesell L, Paleologou M, Leitch M, Pulkki R, Xu C (Charles). Global lignin supply overview and kraft lignin potential as an alternative for petroleum-based polymers. Renew Sustain Energy Rev 2020;123:109768. https://doi.org/10.1016/j.rser.2020.109768.

[7] González M, Tejado Á, Peña C, Labidi J. Organosolv pulping process simulations. Ind Eng Chem Res 2008;47:1903–9. https://doi.org/10.1021/ie070432j.

[8] Mesa L, González E, Cara C, González M, Castro E, Mussatto SI. The effect of organosolv pretreatment variables on enzymatic hydrolysis of sugarcane

bagasse. Chem Eng J 2011;168:1157–62. https://doi.org/10.1016/j.cej.2011.02.003.

[9] Gigli M, Crestini C. Fractionation of industrial lignins: opportunities and challenges. Green Chem 2020;22:4722–46. https://doi.org/10.1039/d0gc01606c.

[10] Pang T, Wang G, Sun H, Sui W, Si C. Lignin fractionation: Effective strategy to reduce molecule weight dependent heterogeneity for upgraded lignin valorization. Ind Crops Prod 2021;165:113442. https://doi.org/10.1016/j.indcrop.2021.113442.

[11] Li H, McDonald AG. Fractionation and characterization of industrial lignins. Ind Crops Prod 2014;62:67–76. https://doi.org/10.1016/j.indcrop.2014.08.013.

[12] Tagami A, Gioia C, Lauberts M, Budnyak T, Moriana R, Lindström ME, et al. Solvent fractionation of softwood and hardwood kraft lignins for more efficient uses: Compositional, structural, thermal, antioxidant and adsorption properties. Ind Crops Prod 2019;129:123–34. https://doi.org/10.1016/j.indcrop.2018.11.067.

[13] Domínguez-Robles J, Tamminen T, Liitiä T, Peresin MS, Rodríguez A, Jääskeläinen AS. Aqueous acetone fractionation of kraft, organosolv and soda lignins. Int J Biol Macromol 2018;106:979–87. https://doi.org/10.1016/j.ijbiomac.2017.08.102.

[14] Park SY, Kim JY, Youn HJ, Choi JW. Fractionation of lignin macromolecules by sequential organic solvents systems and their characterization for further valuable applications. Int J Biol Macromol 2018;106:793–802. https://doi.org/10.1016/j.ijbiomac.2017.08.069.

[15] Ajao O, Jeaidi J, Benali M, Abdelaziz OY, Hulteberg CP. Green solvents-based fractionation process for kraft lignin with controlled dispersity and

molecular weight. Bioresour Technol 2019;291:121799. https://doi.org/10.1016/j.biortech.2019.121799.

[16] Alfonsi K, Colberg J, Dunn PJ, Fevig T, Jennings S, Johnson TA, et al. Green chemistry tools to influence a medicinal chemistry and research chemistry based organisation. Green Chem 2008;10:31–6. https://doi.org/10.1039/b711717e.

[17] Gordobil O, Moriana R, Zhang L, Labidi J, Sevastyanova O. Assesment of technical lignins for uses in biofuels and biomaterials : Structure-related properties , proximate analysis and chemical modification. Ind Crop Prod 2016;83:155–65. https://doi.org/10.1016/j.indcrop.2015.12.048.

[18] Sluiter A, Hames B, Ruiz R, Scarlata C, Sluiter J, Templeton D, et al. Determination of structural carbohydrates and lignin in Biomass-Laboratory Analytical Procedure (LAP). 2012. https://doi.org/NREL/TP-510-42618.

[19] Pan X, Arato C, Gilkes N, Gregg D, Mabee W, Pye K, et al. Biorefining of softwoods using ethanol organosolv pulping: Preliminary evaluation of process streams for manufacture of fuel-grade ethanol and co-products. Biotechnol Bioeng 2005;90:473–81. https://doi.org/10.1002/bit.20453.

[20] Dong C, Meng X, Yeung CS, Tse HY, Ragauskas AJ, Leu SY. Diol pretreatment to fractionate a reactive lignin in lignocellulosic biomass biorefineries. Green Chem 2019;21:2788–800. https://doi.org/10.1039/c9gc00596j.

[21] Alekhina M, Ershova O, Ebert A, Heikkinen S, Sixta H. Softwood kraft lignin for value-added applications: Fractionation and structural characterization. Ind Crops Prod 2015;66:220–8. https://doi.org/10.1016/j.indcrop.2014.12.021.

[22] Gordobil O, Egüés I, Labidi J. Modification of Eucalyptus and Spruce organosolv lignins with fatty acids to use as fi ller in PLA 2016;i:45–52.

https://doi.org/10.1016/j.reactfunctpolym.2016.05.002.

[23] Del Río JC, Gutiérrez A, Hernando M, Landín P, Romero J, Martínez ÁT. Determining the influence of eucalypt lignin composition in paper pulp yield using Py-GC/MS. J Anal Appl Pyrolysis 2005;74:110–5. https://doi.org/10.1016/j.jaap.2004.10.010.

[24] Gärtner A, Gellerstedt G, Tamminen T. Determination of phenolic hydroxyl groups in residual lignin using a modified UV-method. Nord Pulp Pap Res J 1999;14:163–70. https://doi.org/10.3183/npprj-1999-14-02-p163-170.

[25] Bosch Ojeda C, Sanchez Rojas F. Recent applications in derivative ultraviolet/visible absorption spectrophotometry: 2009-2011. A review. Microchem J 2013;106:1–16. https://doi.org/10.1016/j.microc.2012.05.012.

[26] Faleva A V., Belesov A V., Kozhevnikov AY, Falev DI, Chukhchin DG, Novozhilov E V. Analysis of the functional group composition of the spruce and birch phloem lignin. Int J Biol Macromol 2021;166:913–22. https://doi.org/10.1016/j.ijbiomac.2020.10.248.

[27] Chen S, Cheng H, Wu S. Pyrolysis characteristics and volatiles formation rule of organic solvent fractionized kraft lignin. Fuel 2020;270:117520. https://doi.org/10.1016/j.fuel.2020.117520.

[28] Tagami A, Gioia C, Lauberts M, Budnyak T, Moriana R, Lindström ME, et al. Solvent fractionation of softwood and hardwood kraft lignins for more efficient uses: Compositional, structural, thermal, antioxidant and adsorption properties. Ind Crops Prod 2019;129:123–34. https://doi.org/10.1016/j.indcrop.2018.11.067.

[29] Wang YY, Li M, Wyman CE, Cai CM, Ragauskas AJ. Fast Fractionation of Technical Lignins by Organic Cosolvents. ACS Sustain Chem Eng 2018;6:6064–72. https://doi.org/10.1021/acssuschemeng.7b04546.

[30] Tejado A, Peña C, Labidi J, Echeverria JM, Mondragon I. Physico-chemical characterization of lignins from different sources for use in phenol-formaldehyde resin synthesis. Bioresour Technol 2007;98:1655–63. https://doi.org/10.1016/j.biortech.2006.05.042.

[31] Allegretti C, Fontanay S, Krauke Y, Luebbert M, Strini A, Troquet J, et al. Fractionation of Soda Pulp Lignin in Aqueous Solvent through Membrane-Assisted Ultrafiltration. ACS Sustain Chem Eng 2018;6:9056–64. https://doi.org/10.1021/acssuschemeng.8b01410.

[32] Passoni V, Scarica C, Levi M, Turri S, Griffini G. Fractionation of Industrial Softwood Kraft Lignin: Solvent Selection as a Tool for Tailored Material Properties. ACS Sustain Chem Eng 2016;4:2232–42. https://doi.org/10.1021/acssuschemeng.5b01722.

5. Lignin Modification

5.1. MOTIVATION

Lignin has been considered as a waste and its implementation as a value-added product for numerous applications has been neglected, despite its interesting chemistry and great potential to substitute the currently used petroleum-based chemicals and materials [1], due to its high heterogeneity and non-organized formation [2]. Recent progress in the development of novel and greener biorefinery processes have been carried out, where not only more sustainable solvents like Ionic Liquids (ILs) and Deep Eutectic Solvents (DES) have been implemented [3], but also lignin transformation and modification processes have been designed for further valorization into high value-added products. Processes like depolymerization, pyrolysis and hydroprocessing have been widely explored, along with ultrafiltration, selective pH precipitation, mechanical membrane filtration, and fractionation utilizing green solvents [4].

One of the most studied strategies for lignin valorization has been its oxidation, a route to obtain smaller molecules, such as aromatic aldehydes (vanillin being industrially manufactured), ketones, and acids [5–7]. By the cleavage of the inter-unit linkages in the lignin molecule, its potential to replace current marketed aromatic compounds from fossil resources has drastically increased. Moreover, the obtaining of these molecules, more homogeneous than their predecessor and highly functionalized due to the increment in reactive functional groups, ease their application as building-block compounds for value-added markets [8], such as adhesives [9], thermosetting polyester coatings [10], nanocarriers for drug delivery [11], antioxidant/antimicrobial agents, light-harvesting complexes, environmental remediation or electrode materials [12].

Numerous selective oxidation reactions have been designed to cleave and functionalize the lignin molecule, emphasizing more sustainable processes like ozonation, catalytic, photocatalytic, US irradiated, and electrochemical oxidation, where more energetically efficient processes are designed [13]. For example, Garedew et al. (2020) reported works where electrocatalytic oxidation processes were carried out at ambient temperature and pressures and different products were obtained by adjusting the potential [14]. Different transition-metal complexes have been used to catalyze the process [15], or alternative solvents like protic ionic liquids [16,17] have been employed. Alternatively, hydrothermal oxidation [18], enzymatic depolymerization [19,20], and functionalization [21,22] procedures have been carried out. The most common products obtained by these processes are the low molecular weight phenolic compounds (LMWPC), such as phenolic aldehydes, ketones, and acids [23].

Conversely, oxidative fractionation of lignin into dicarboxylic acids (DCAs) like muconic, maleic and succinic acids can substitute the currently used [24]. Lastly, the other family of compounds that can be obtained from the oxidation of lignin is the oxidized derivatives of aromatic compounds, also known as quinones. These molecules are interesting since they can act as catalysts in Kraft processes to enhance the performance of the pulping process and as redox-active organic molecules, plausible to replace the redox-active metals presently used in energy storage, leading to the incorporation of a biomass-derived and inexpensive material [25].

An extended amount of work investigating lignin oxidation has based on incorporating and utilizing different chemical catalysts (homogeneous and heterogeneous). A wide variety of compounds have been used as catalyzing agents, starting from the most common

metallic ones, like Cu [26], to TiO_2 doped with bimetals like Cu-Au or Fe-Au [27], as well as KOH [28] or KO^{t}Bu [29]. These catalytic agents have been widely used along with other oxidizing agents like H_2O_2, an extensively used bleaching agent in the paper industry [30]. Hydrogen peroxide is highly susceptible to decomposition reactions, especially when high temperatures and pH are used [30]. It has been reported to be able to react with phenols on lignin, forming phenoxy radicals that later degrade to low molecular weight compounds. Nevertheless, these reactions happen when metals are added or pH is kept at similar values to the pK_a of the peroxide (11.7) [31]. Minor degradation reactions can still happen at milder conditions than explained, with primary reaction products from phenolic structures (primarily quinones) as yields [32].

Lignin can also be valorized by applying US irradiation, which is based on acoustic cavitation. Liquids irradiated in the correct conditions create, expand, and collapse vapor bubbles capable of inducing the formation of radicals by the cavitation effect [33]. This cavitation effect is formed by the implosion of the bubbles, which create localized high pressures and temperatures while the overall liquid maintains a controlled temperature. The US has been mainly used in biorefinery processes to enhance delignification processes, increasing extraction yields and purity. However, more recently, it has been observed that this technology can synthesize lignin nanoparticles, similar to the formation of nanocellulose and nanochitosan entities [34]. When lignin is subjected to ultrasonic forces, the size of the molecule is considerably reduced since the molecular bonds present in the structure are broken down by the energy applied in the form of cavitation effect [35]. Consequently, spherical nanolignins of diameters around 100 nm can be obtained and physically prevented

from re-attaching themselves to avoid their reorganization in bigger molecules [34,36].

Alternatively, another possible choice for lignin valorization is altering its structure by modifying and introducing new functional groups. An interesting approach is the incorporation of hydrophilic functional groups that would ideally help overcome the hurdle processability of Kraft and organosolv lignins [37]. Even though hydrophilic functional groups are present in lignin particles, these are often hindered due to the complex folded structure. Therefore, the introduction of various functional groups into the molecules is an interesting path for its further dissolution in polar solvents like water [38].

Several modifications have been suggested for the synthesis of lignin with tuned properties, for the obtaining of materials with enhanced hydrophilicity, which eases the processability and optimizes the performance of the material for several applications [39–43].

The carboxymethylation reaction is a widely employed modification path to obtain water-soluble particles. It has extensively been used with cellulose, whose high crystallization degree makes its solubilization in water difficult. The obtained carboxymethyl cellulose (CMC) can be applied in industries like food packaging [44], biomedical [45], pharmaceutical [46], and textile [47], along with other products like cleaning supplies and personal care products [46]. Its water solubility and viscosity make it interesting to apply as a thickener, stabilizer, and viscosity modifier of foods and personal care products like toothpaste and lotions, and as a binder in pharmaceutical tablet preparation and in paperboard and boxes for paper and packaging materials [47].

More recently, a similar strategy has been applied to other biomaterials like chitosan, where carboxymethyl chitosan (CMCS) has been considered a promising material in cosmetics [48], drug delivery systems [49], wastewater treatments, food preservation, and membrane technology. Carboxymethylated lignin (CML), on the other hand, is still under research but shows great potential to be applied as a dispersant for clay suspension [50,51], flocculant [52], and afterglow material with excellent phosphorescence [53], a hybrid modifier to improve physical and mechanical properties of fast-growing wood [54], and adsorption agent for heavy metal ions [55].

Another common lignin modification for its further water solubility relies on mimicking the functionalization obtained from the sulfate pulping process of the lignosulfonates into other types of lignin like Kraft and organosolv. Sulfomethylation (SM) reaction is considered a sustainable procedure since no hazardous reactions are needed, and properties like the previously mentioned water solubility, surface activity (enhancing the water dispersibility), ionic properties (being able to ionize in water) and compatibility with polymers are brought to the lignin.

These properties make this modification attractive for applications like dispersants and emulsifiers for several formulations, being the main target in many recently published works. For instance, different molecular weight lignins were studied to find the optimal dispersibility of TiO_2 [56], and different sulfonic group contents were obtained for the study of the formulation for dye dispersion [41]. They have also been applied as dispersants for kaolin [57] and emulsifiers for stabilizing oil-in-water nanoemulsions [43]. Enzymatically hydrolyzed lignin (EHL) [42] has also been employed for these types of emulsions, as for the employment as dispersants for graphite [58]. Lastly, sulfomethylated lignin (SML) has been grafted with other compounds like pyrrolidone or polyacrylic acid as a

dispersant for cobalt blue [59] or as hydrogels in the removal of heavy metal ions in wastewater treatments [60], respectively.

Another modification frequently employed is the alkylation of the lignin hydroxyl groups, in this case, to obtain more stable molecules. The reactivity and functionality can be quite easily modulated by different alkylation reactions, also bringing thermal stability that prevents self-polymerization reactions [61]. It is a way of blocking the hydroxyl groups present in lignin particles, enabling the study of the effect of these OH groups in processes like the formation of lignin nanoparticles, for instance. Blocking these specific functional groups, along with determining the methylation degree, the interaction created between the hydroxyl groups of lignin and the medium can be regulated, consequently controlling the nanoparticle size obtained [62]. This modification, apart from being interesting for the obtaining of nanolignins, the hydrophobic skeleton of methylated lignin (ML) has also been proven as an effective dispersant for carbon nanotubes [63].

5.2. OBJECTIVES

The first part of this chapter aims to produce oxidized lignin nanoparticles, highly functionalized and with great surface area. The designed route to obtain this objective was defined based on the oxidation of Kraft lignin in mild conditions with the combined action of an oxidizing agent (H_2O_2) and ultrasonic cavitation in an innovative integrated mechanism not tested before. This procedure may therefore offer an alternative method for obtaining primary reaction products from the phenolic structures present in lignin, avoiding the more extensively studied pathway to date, which involves low molecular weight redox-active compounds such as quinones. These compounds have been extensively investigated for diverse

applications, from biologic applications due to their immunotoxic, cytotoxic, and carcinogenic properties [64], to electrochemical applications in different types of batteries, including redox-flow batteries [65], zinc-ion batteries [66] or sodium ion batteries [67].

Moreover, obtaining nanosized particles, with an increased ratio of surface to volume are proven to have improved properties, opening new possibilities for the lignin incorporation in a wider range of applications like cosmetics [68], polymer nanocomposites with enhanced mechanical properties, or even energy storage materials [69]. Once the method was validated as appropriate for obtaining oxidized Kraft lignin nanoparticles, the optimal conditions were used to replicate the production of oxidized organosolv lignin nanoparticles.

Conversely, the last part of the chapter is focused on the examination of how diverse lignin modifications influence their inherent properties. While carboxymethylation and sulfomethylation reactions are believed to enhance hydrophilicity to the lignin molecules as a consequence of the increased polarity, the methylation reaction is believed to have the opposite effect, reducing it. This way, although all the modifications have some characteristics in common, such as the generation of more condensed structures and the subsequent enhancement of thermal stability, the divergent chemical nature of the newly incorporated functional groups will bring distinct properties related to processability and aqueous stability. Specifically, carboxymethylation and sulfomethylation reactions incorporate anionic functional groups that facilitate the achievement of good lignin dispersions in water, while methylation reaction promotes the generation of lignin nanoparticles that are also beneficial for lignin stability and enhanced performance.

5.3. EXPERIMENTAL PROCEDURE

5.3.1. SONOCHEMICAL OXIDATION OF LIGNIN

Oxidized lignin nanoparticles were synthesized using different conditions and combined accordingly by an experimental model designed by STRATIGRAPHIC Centurion XV. A Factorial Multilevel design was chosen, with three experimental factors with different levels (3 levels for temperature (T) and time (t) and two levels for [H_2O_2]) and one response variable (Z potential (ZP)). Eighteen different experiments were designed, and the precise conditions for synthesizing each sample are presented in Table 5.1.

Briefly, Kraft lignin (KL) was dissolved in NaOH 4 wt% solution using a solid to liquid ratio of 1:20 (w/v) at room temperature (RT) for 2 h with magnetic stirring (400 rpm). Then, H_2O_2 (50%) was added in a 0.1 equivalent ratio with respect to lignin for selected samples. Afterwards, the temperature was set at 30 °C, 45 °C and 60 °C, and reactions were carried out for 15, 30, and 45 minutes. The selected operation conditions (low temperature and reaction time) with the intensification provided by the sonication allowed for similar results to those reported in the literature [34,70].

The reactions were performed inside a 100 mL jacketed cell using a 20 kHz VCX 750 power supply (Sonics & Materials, USA) equipped with a piezoelectric converter connected to a 13 mm titanium alloy horn (Ti-6Al-4V) with the amplitude set at 57.5 μm. The temperature was kept stable with the help of a high precision thermostat (Huber, Germany) connected to the processing cell. Once the reaction was finished, the product was precipitated using two volumes of 2% (v/v) H_2SO_4 solution. Next, the precipitate was centrifuged and washed three times

with distilled water. Finally, the washed lignins were filtered under pressure with a filter holder (Sartorius, Germany) equipped with a nylon filtering membrane of 0.22 μm pore size and dried at 30 °C. The scheme of the followed procedure is shown in Figure 5.1.

Table 5.1. Reaction conditions for sonochemical oxidation of lignin.

Sample	*T (°C)*	*t (min)*	*[H_2O_2] (eq)*
OxL1	30	15	0
OxL2	30	30	0
OxL3	30	60	0
OxL4	30	15	0.1
OxL5	30	30	0.1
OxL6	30	60	0.1
OxL7	45	15	0
OxL8	45	30	0
OxL9	45	60	0
OxL10	45	15	0.1
OxL11	45	30	0.1
OxL12	45	60	0.1
OxL13	60	15	0
OxL14	60	30	0
OxL15	60	60	0
OxL16	60	15	0.1
OxL17	60	30	0.1
OxL18	60	60	0.1

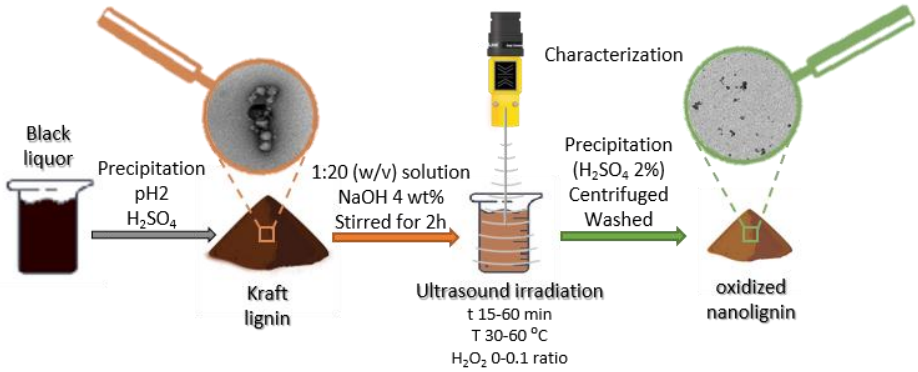

Figure 5.1. Scheme of the sonochemical oxidation reaction methodology.

5.3.2. Characterization of the obtained oxidized lignin nanoparticles

Chemical, physicochemical, and morphological properties of the oxidized samples were obtained by the implementation of different techniques. Quantitative acid hydrolysis (QAH) was performed to determine the purity of the oxidized lignin samples, elemental composition was determined by elemental analysis (EA), using sulfamethazine Leco as calibration. Weight average molecular weight (M_w), number average molecular weight (M_n), and polydispersity index (PI) were determined by GPC.

Chemical properties were observed by FTIR, and UV-vis spectrophotometry was used to determine the total phenolic content (TPC) by the Folin-Ciocalteau method and conjugated and non-conjugated OH groups. ^{31}P NMR was used to quantitatively determine the hydroxyl groups and the S/G ratio, and TGA and DSC were employed for the analysis of thermal properties. Finally, morphological properties were verified by DLS and TEM.

5.3.3. CARBOXYMETHYLATION REACTION

The carboxymethylation reaction conditions followed were the optimum addressed from the work by Konduri et al. (2015) [50], and the reaction mechanism is shown in Figure 5.2.

1 g of KL and OL were dissolved in 60 mL of 0.15 M NaOH. 3 mol of sodium chloroacetate (SCA) for every lignin mol were added in a 100 mL round bottom flask. The reaction was conducted at 150 rpm and 40 °C for 4 hours. After completing the reaction time, the solution was cooled, and the pH was gradually adjusted to 7 by adding 1 M H_2SO_4. The solution was then introduced in a dialysis bag (6-8 kDa pore size) and osmosis was carried out against distilled H_2O for the removal of unreacted reagents. Water was changed every 12h for 2 days, and the solution was dried in an oven at 105 °C.

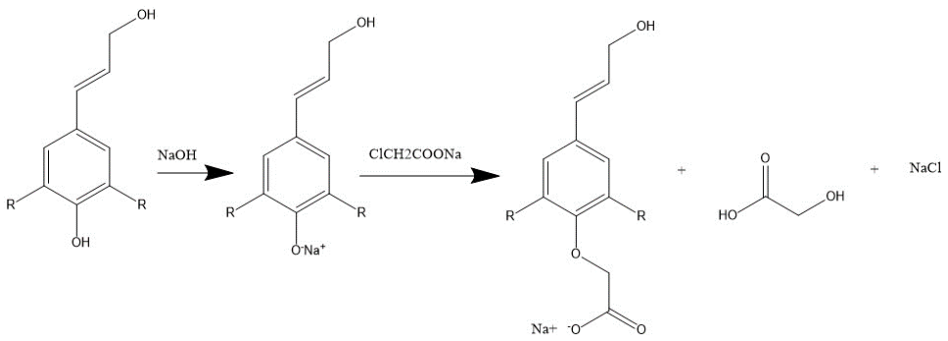

Figure 5.2. Carboxymethylation reaction mechanism of lignin.

5.3.4. SULFOMETHYLATION REACTION

The sulfomethylation reaction conditions followed are the ones addressed by Yang et al. (2014) [71], and the reaction mechanism is shown in Figure 5.3.

1g of lignin was dissolved in 60 mL of 0.15 M NaOH solution. The solution was transferred into a 100 mL round bottom flask and then heated to 70 °C. After that, 0.041 g of 37% formaldehyde was introduced and stirred for 1 h. Subsequently, 0.6 g of Na_2SO_4 was added, and the temperature was raised to 95 °C, maintaining this temperature for 3h. Once the reaction finished, the solution was cooled to room temperature (RT), pH was adjusted to 6, and the solution was dialyzed for several days, changing water every 12h, to remove any unreacted reagents. The modified lignin was dried in an oven at 105 °C.

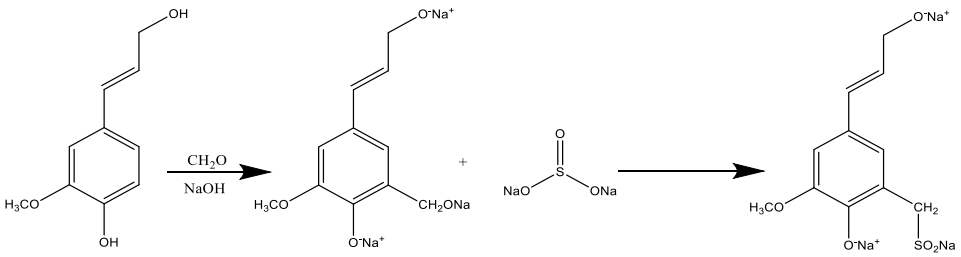

Figure 5.3. Sulfomethylation reaction mechanism of lignin.

5.3.5. METHYLATION REACTION

The methylation reaction followed was described by Sen et al. (2105) [61] and the reaction mechanism is shown in Figure 5.4.

1 g of lignin was dissolved in 15 mL of dimethylsulfoxyde (DMSO). Next, 2 equivalents of NaOH were added to the total phenolic hydroxyl groups of the lignin, along with 10 equivalents of dimethyl carbonate (DMC), the same phenolic OH groups. The solution was then heated to 150 °C and maintained at his temperature for 15 h. Once the reaction finished, it was cooled down to RT and acidified by adding 50 mL of 2 M HCl. The precipitated lignin was filtered using a 0.45 μm pore-sized nylon filter and washed 4 times with 50 mL of deionized water each time. Once the modified lignin was washed, it was dried at 60 °C overnight.

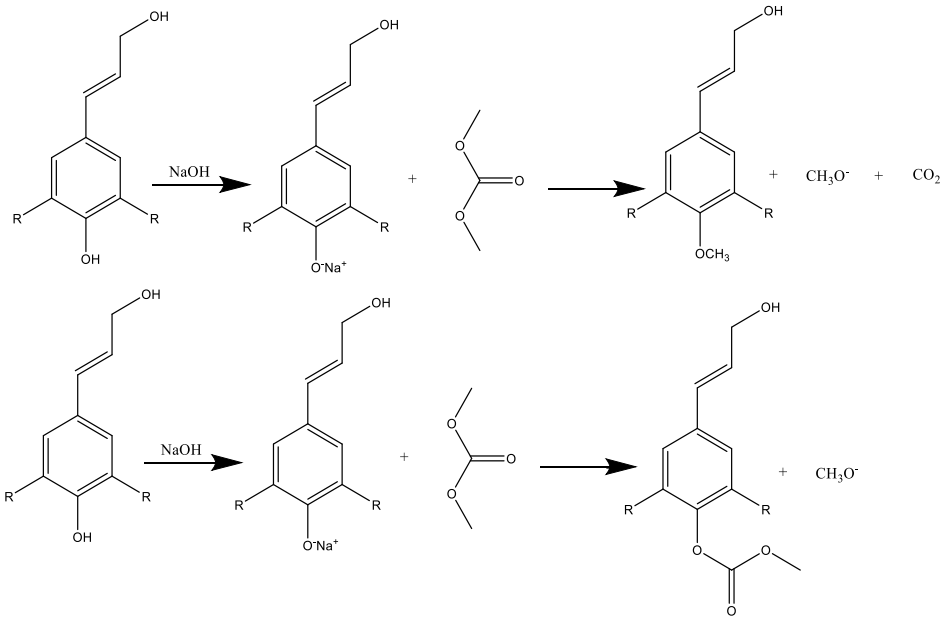

Figure 5.4. Methylation reaction mechanism of lignin.

5.3.6. CHARACTERIZATION OF THE OBTAINED CARBOXYMETHYLATED, SULFOMETHYLATED AND METHYLATED LIGNIN

The samples were analyzed by FTIR, GPC, ^{31}P NMR, ^{13}C NMR, DLS, and TGA and the overall chemical, physicochemical, thermal, and morphological characteristics were determined. Differences in these properties were justified based on the new functional groups introduced to the lignins.

5.4. RESULTS AND DISCUSSION

5.4.1. OXIDIZED LIGNIN NANOPARTICLE PRODUCTION

5.4.1.1. Design of Experiments for sonochemical process

Eighteen experiments were designed using a multilevel factorial method, where T, t, and [H_2O_2] were chosen as experimental factors. T and t were 3

level factors, with 30, 45, and 60 ºC and 15, 30, and 60 min as level values, respectively. On the other hand, [H_2O_2] was a 2-level factor, where 0.0 and 0.1 equivalents of H_2O_2 to lignin were used. The experimental Z potential values for each experiment, measured by Dynamic Light Scattering (DLS) and corresponding to the dependent variable, are summarized in Table 5.2 along with the normalized independent variables.

Table 5.2. Independent normalized variables, temperature (X_1), time (X_2) and [H_2O_2] (X_3), together with the dependent variable values measured (Y_{ZP}).

Sample	X_1	X_2	X_3	Y_{ZP}
OxL1	-1	-1	-1	-42.68
OxL2	-1	0	-1	-43.34
OxL3	-1	1	-1	-45.98
OxL4	-1	-1	1	-33.74
OxL5	-1	0	1	-33.19
OxL6	-1	1	1	-32.68
OxL7	0	-1	-1	-29.91
OxL8	0	0	-1	-32.46
OxL9	0	1	-1	-38.22
OxL10	0	-1	0	-29.91
OxL11	0	0	0	-28.66
OxL12	0	1	0	-32.72
OxL13	1	-1	-1	-33.19
OxL14	1	0	-1	-33.52
OxL15	1	1	-1	-33.91
OxL16	1	-1	1	-29.19
OxL17	1	0	1	-35.39
OxL18	1	1	1	-35.23

Regression coefficients for the full quadratic model of Z potential, their standard deviation and their corresponding statistics value (*t*), according to Student's t-test are listed in Table 5.3. Additionally, the standardized Pareto Diagram for Z Potential is displayed in Figure 5.5.

Table 5.3. Regression coefficients for the full quadratic models of Z Potential.

Coefficients	Y_{ZP}	*Standard deviation*	*t*
b_0	-31.7408[a]	1.16813	-27.1723
b_1	2.5967[a]	0.6398	4.0585
b_2	-1.6771[b]	0.6398	-2.6212
b_3	2.6306[a]	0.5224	4.5186
b_{12}	-0.5650	0.7836	-0.7210
b_{13}	-2.6308[a]	0.6398	-4.1119
b_{23}	0.3788	0.6398	0.5920
b_{11}	-4.0250[a]	1.1082	-3.6321
b_{22}	-0.3538	1.1082	-0.3192

[a]Significant coefficients at the 99% of confidence level.
[b]Significant coefficients at the 95% of confidence level.

As it is shown in Table 5.3, the second order polynomial equation which related ZP dependent variable (Y_{ZP}) with the independent variables, temperature *(X_1),* time *(X_2)* and [H_2O_2] *(X_3)* could be expressed as Equation 5.2:

$$Y_{ZP} = -31.7408 + 2.5967X_1 - 1.6771X_2 + 2.3606X_3 - 0.5650X_1X_2 - 2.6308X_1X_3 + \\ +0.3788X_2X_3 - 4.0250X_1^2 - 0.3538X_2^2 \quad \text{Eq. 5.2}$$

On the other hand, the Pareto diagram verifies that except for the interactions of the variables X_1 X_2, X_2 X_3 and the quadratic effect of the time $\left(X_2^2\right)$the rest of the variables have a significance level higher than 95%. Likewise, it can be observed that temperature and [H_2O_2] negatively affect

the Z potential, while time has a positive influence. Additionally, it can be noticed that [H_2O_2], temperature, and the combination of both ($X_1 X_3$) are the variables with the highest significance.

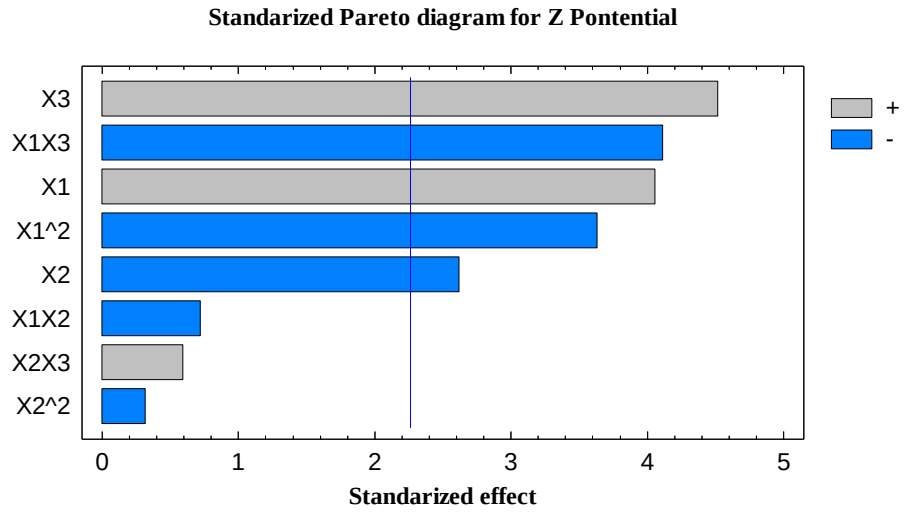

Figure 5.5. Standarized Pareto Diagram for Z Potential.

An ANOVA was conducted to evaluate the validity of the fitted quadratic model for Z potential. Therefore, in Table 5.4 the R^2 coefficient of determination, the adjusted R^2 and the statistical significance of the regression are summarized.

Table 5.4. Analysis of Variance of the full quadratic model for Z potential.

Source	*Sum of squares*	*DF*	*Mean squares*	*F-value*	*P- Value*
Regression	367.5971	8	45.9496	9.3540	0.0015
Error	44.2108	9	4.9123		
Total	411.8079	17	24.2240		
R^2			0.8926		
R^2 (adjusted for df)			0.7972		

According to Table 5.4, the obtained R^2 coefficient of determination was 0.8926. This value indicates that approximately 90% of the total variability in Z Potential could be accounted for by the model. Only a small portion, specifically 10.74% of the total variations, remained unexplained using the selected model. Based on the acquired R^2 determination coefficient, it can be concluded that the model was suitable for describing the interactions between the selected independent variables and the Z potential.

Furthermore, the predictivity of the model, as determined by Fisher's F-test, confirmed its statistical relevance at a confidence level above 95%. This was evident from the F-value for the regression, which yielded a p-value of 0.0015.

As mentioned earlier, with the designed mathematical model, the Z potential of oxidized lignin nanoparticles can be predicted by varying the temperature, time, and [H_2O_2] in the sonochemical process. Using this model, it can be ensured that the minimum Z potential value, indicating greater stability of the oxidized lignin nanoparticles, is achieved under the following conditions: 30 °C, 60 minutes, and without the addition of H_2O_2. These conditions align with Experiment number 3.

Nevertheless, even with knowledge of the optimal point in the sonochemical process, a comprehensive characterization of all the different oxidized lignin nanoparticles obtained in the 18 experiments was conducted in the following sections. This was done to understand how the studied variables influenced all parameters and characteristics of these nanoparticles.

5.4.1.2. Yield, pH change, and total energy delivered to the system.

The total amount of energy delivered to the system was recorded for each sample, which is related to the ultrasonic power and elapsed time by the Equation 5.3:

$$E = P \cdot t \qquad \text{Eq. 5.3}$$

where E is the energy delivered to the system, P is the ultrasonic power, and t is the elapsed time.

The yields of oxidized lignin nanoparticles obtained, listed in Table 5.5, are similar for most of the samples, which means that the product loss is due to the different stages of the process, such as precipitation, centrifugation, and filtration. Even though a considerable amount was lost (around 25%), optimizing the recovery stages could easily reduce this value.

In terms of energy delivered to the system, visible in Figure 5.6, the tendency followed was linear with time. H_2O_2 addition significantly affected the pH variation during the reaction, considerably decreasing the value due to the acidic nature of the compound and its disassociation into HOO^-.

In the experiments where peroxide was not added, the pH remained almost constant; however, its addition decreased the pH values. It is observable that the increase in sonication time favored the dissociation of H_2O_2 especially at medium and high temperatures, since the pH decreased considerably compared to the lower temperatures.

Table 5.5. Yield, total energy delivered to the system, and changes in pH during the reaction for the different oxidative conditions.

Sample	*Yield (%)*	*E (kJ)*	*pH change*
OxL1	76.65	50.54	-0.59
OxL2	74.62	100.00	-0.63
OxL3	75.92	209.45	-0.06
OxL4	72.18	58.40	-0.95
OxL5	72.83	95.70	-1.88
OxL6	74.72	194.00	-1.64
OxL7	74.03	60.39	-0.22
OxL8	76.29	133.61	-0.30
OxL9	68.48	201.60	-0.47
OxL10	76.29	54.83	-1.51
OxL11	74.73	113.20	-2.24
OxL12	74.99	238.12	-2.35
OxL13	71.94	45.95	-0.63
OxL14	73.49	87.09	-0.26
OxL15	71.30	180.56	-0.32
OxL16	66.55	89.28	-3.15
OxL17	69.31	171.1	-2.59
OxL18	73.36	188.84	-2.93

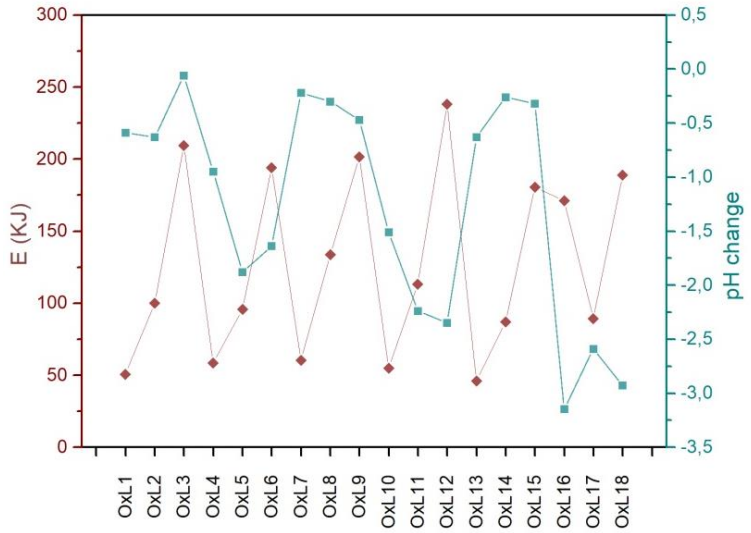

Figure 5.6. Total energy delivered to the system and the change in pH during the reaction for the different oxidative conditions.

5.4.1.3. Chemical composition and elemental analysis of the samples

Oxidized lignin samples were analyzed by QAH, UV-vis spectroscopy, HPLC, and TGA, which enabled the quantification of Acid Insoluble Lignin (AIL), Acid Soluble Lignin (ASL), carbohydrates (CA), and ash content. The mass content of the major components of the samples is listed in Table 5.6. QAH effectively quantifies the purity of the lignin obtained (AIL) to estimate the degree of degradation and quantify the side products (CA, ASL, Ashes…) of each experiment. KL has the least amount of AIL, corresponding to the sample with the highest content of impurities. After oxidation, AIL content increased by at least 15% to almost 20%. ASL content decreases considerably, meaning many of these molecules dissolved during the process. The CA content increased due to the degradation products obtained from the oxidation, the most noticeable rise being in the last three reactions, where the temperature was maximum (60 °C) and hydrogen peroxide was used. The harsher conditions improve the dissociation of lignin into smaller

molecules, such as carboxylic acids or carbohydrates. The ash content, however, decreased with the oxidation reactions. The initial KL presented high inorganic matter, resulting in low purity. Reactions with longer times showed decreased ash content, resulting in a high-purity product.

Table 5.6. Chemical composition of the KL and the oxidized samples.

Sample	*AIL (%)*	*ASL (%)*	*CA (%)*	*Ash (%)*
KL	73.94 ± 0.93	18.99 ± 0.25	1.03 ± 0.21	6.04 ± 1.06
OxL1	87.97 ± 2.67	7.61 ± 1.03	2.89 ± 0.11	1.53 ± 0.97
OxL2	87.78 ± 4.80	6.92 ± 0.04	3.49 ± 0.93	1.81 ± 0.33
OxL3	87.41 ± 1.82	8.00 ± 0.23	3.08 ± 0.16	1.51 ± 0.08
OxL4	86.78 ± 1.32	8.43 ± 1.06	3.09 ± 0.08	1.70 ± 0.68
OxL5	88.92 ± 1.36	6.05 ± 0.25	2.79 ± 0.23	2.24 ± 2.30
OxL6	88.37 ± 3.36	6.91 ± 0.07	3.14 ± 0.02	1.58 ± 0.43
OxL7	89.32 ± 2.53	5.92 ± 0.07	3.65 ± 0.46	1.11 ± 0.09
OxL8	89.75 ± 2.53	5.99 ± 0.22	3.07 ± 0.06	1.19 ± 0.17
OxL9	91.23 ± 0.85	4.29 ± 0.25	3.59 ± 0.48	0.89 ± 0.01
OxL10	89.25 ± 0.67	5.99 ± 0.31	3.88 ± 0.71	0.88 ± 0.20
OxL11	88.20 ± 1.66	6.79 ± 0.43	4.11 ± 0.48	0.90 ± 0.12
OxL12	87.41 ± 0.59	6.42 ± 0.25	4.36 ± 0.46	1.81 ± 0.88
OxL13	92.60 ± 0.32	6.29 ± 0.11	0 ± 0.00	1.11 ± 0.07
OxL14	89.25 ± 1.24	5.40 ± 0.34	3.59 ± 4.88	1.76 ± 0.45
OxL15	85.75 ± 2.05	4.78 ± 0.18	8.48 ± 0.62	0.99 ± 0.79
OxL16	84.02 ± 2.36	5.67 ± 0.30	8.91 ± 0.58	1.40 ± 0.33
OxL17	86.03 ± 0.84	5.50 ± 0.30	7.76 ± 1.18	0.71 ± 0.02
OxL18	85.68 ± 1.00	4.65 ± 0.13	8.70 ± 0.17	0.97 ± 0.10

The results obtained from the Elemental Analysis are listed in Table 5.7. Carbon, hydrogen, nitrogen, oxygen, and sulfur content were determined, useful to deduce how external functional groups to lignin (HOO^- from the peroxide or SO_4^{2-} from the sulfuric acid used for precipitation) adhere to the

samples depending on the reaction conditions. KL is primarily composed of carbon (62.44 ± 0.38%); however, carbon content increased with the sonochemical oxidation, reaching up to 66.41 ± 0.76% in the case of OxL9.

The second most abundant element in lignin biopolymers is oxygen, with values around 25%. KL was the sample with the highest O content, with 26.98 ± 0.54%, while most of the oxidized lignins had around 23-24%, the least being the OxL3 with 23.41 ± 0.28%. However, this does not necessarily mean that KL is the sample with the highest functionality. Lignin macromolecules are formed by crosslinking monolignols through several linkages, ether bonds being the most common. Therefore, the high amount of O can be related to the high amount of ether groups rather than hydroxyl or carbonyl [72]. In terms of hydrogen, it increased with the reaction time, with the set point at 5.20 ± 0.02% and reaching values of 5.69 ± 0.19%; the same trend followed throughout the samples.

Regarding S content, KL contains 5.07 ± 0.16 %, increasing to 6.08 ± 0.05 % in the case of OxL3 and decreasing to 3.93 ± 0.11 % in the case of OxL18. This might be influenced by the temperature in which the reaction occurred, contributing to the pH change. In the case of the lowest temperature conditions (30 °C), the lignins obtained have higher S content and lower O content than the ones compared with the samples obtained at the highest temperature conditions (60 °C). This also concurs with the pH change and, consequently, the dissociation of H_2O_2 to HOO^-. The samples obtained at 30 °C had fewer HOO^- ions to associate with, so when precipitated with H_2SO_4, they had more active sites for the adhesion of S atoms. Conversely, the samples obtained at 60 °C had a higher content of HOO^- ions, promoting their attachment before the precipitation with H_2SO_4. Finally, the N content did not fluctuate in the process, which is insignificant, to the point where it could be considered N-free. This parameter, however, is determined by the nature of the raw material rather than by the process [73].

Table 5.7. Elemental analysis of the KL and the oxidized samples.

	C (%)	*H (%)*	*N (%)*	*S (%)*	*O (%)*
KL	62.44 ± 0.38	5.20 ± 0.02	0.31 ± 0.03	5.07 ± 0.16	26.98 ± 0.54
OxL1	64.97 ± 0.13	5.69 ± 0.19	0.32 ± 0.02	5.43 ± 0.11	23.60 ± 0.40
OxL2	64.87 ± 0.63	5.51 ± 0.16	0.30 ± 0.02	5.47 ± 0.09	23.84 ± 0.85
OxL3	64.71 ± 0.18	5.47 ± 0.03	0.33 ± 0.03	6.08 ± 0.05	23.41 ± 0.28
OxL4	64.59 ± 0.50	5.45 ± 0.03	0.30 ± 0.04	4.91 ± 0.15	24.75 ± 0.66
OxL5	64.49 ± 0.18	5.38 ± 0.06	0.31 ± 0.02	5.04 ± 0.05	24.79 ± 0.26
OxL6	63.53 ± 0.54	5.26 ± 0.08	0.28 ± 0.01	5.14 ± 0.05	25.80 ± 0.66
OxL7	64.48 ± 1.08	5.28 ± 0.08	0.30 ± 0.02	5.19 ± 0.16	24.75 ± 1.32
OxL8	65.25 ± 0.49	5.34 ± 0.05	0.30 ± 0.02	5.46 ± 0.08	23.64 ± 0.63
OxL9	66.41 ± 0.76	5.22 ± 0.09	0.33 ± 0.01	4.39 ± 0.16	23.64 ± 1.00
OxL10	64.00 ± 0.09	5.68 ± 0.05	0.31 ± 0.01	4.63 ± 0.03	25.39 ± 0.16
OxL11	63.53 ± 0.65	5.55 ± 0.04	0.28 ± 0.03	4.88 ± 0.13	25.76 ± 0.84
OxL12	63.45 ± 0.44	5.37 ± 0.12	0.30 ± 0.02	5.03 ± 0.06	25.86 ± 0.54
OxL13	66.03 ± 0.33	5.45 ± 0.04	0.33 ± 0.01	4.51 ± 0.09	23.68 ± 0.47
OxL14	66.00 ± 0.47	5.32 ± 0.05	0.32 ± 0.02	4.34 ± 0.09	24.02 ± 0.58
OxL15	66.37 ± 0.62	5.46 ± 0.01	0.34 ± 0.03	4.32 ± 0.18	23.50 ± 0.83
OxL16	64.79 ± 0.16	5.48 ± 0.02	0.28 ± 0.02	4.99 ± 0.07	24.45 ± 0.16
OxL17	65.83 ± 0.61	5.40 ± 0.03	0.32 ± 0.01	4.07 ± 0.08	24.39 ± 0.67
OxL18	65.78 ± 0.63	5.38 ± 0.01	0.31 ± 0.02	3.93 ± 0.11	24.60 ± 0.77

5.4.1.4. Physicochemical properties of the samples

The M_n, M_w, and PI values for KL and the oxidized samples are listed in Table 5.8, and the chromatogram curves obtained for each sample are shown in Figure 5.7. Overall, M_w increased slightly in the process, validating that mild oxidation conditions are not enough for the degradation and depolymerization of the lignin, maintaining the molecular structure relatively stable.

Table 5.8. Average molecular number (M_n), average molecular weight (M_w), and polydispersity index (PI) of the different lignins.

	M_n (g/mol)	M_w (g/mol)	PI
KL	856	2590	3.0
OxL1	828	2497	3.0
OxL2	852	2532	3.0
OxL3	849	2595	3.1
OxL4	851	2608	3.1
OxL5	871	2690	3.1
OxL6	901	2887	3.2
OxL7	860	2583	3.0
OxL8	876	2678	3.1
OxL9	1029	3580	3.5
OxL10	964	3204	3.3
OxL11	898	2821	3.1
OxL12	930	3002	3.2
OxL13	933	3071	3.3
OxL14	1003	3549	3.5
OxL15	1005	3549	3.5
OxL16	897	2774	3.1
OxL17	933	3168	3.4
OxL18	945	3348	3.5

It can be observed that values stayed similar to the original sample (KL) or increased slightly. The increase in the values could be attributed to condensation reactions happening after the creation of radicals and their following association. Moreover, this condensation phenomenon happened when the reaction conditions were aggravated, especially time and temperature.

When the temperatures used were low (30 °C), time did not affect the M_w (M_w(OxL1) ≈ M_w(OxL2) ≈ M_w(OxL3)). However, when temperature rose to 45 °C, the M_w showed a slight increase which was significant when time was extended to 60 min. (M_w(OxL9)).

Adding H_2O_2 also promoted a slight increment in M_w, although this change was not remarkable. Finally, it was observed that at the highest temperature (60 °C), increasing the time above 30 min did not have any influence, but the addition of H_2O_2 at that longer times reduced the M_w. (M_w(OxL14) ≈ M_w(OxL15)>, M_w(OxL17) ≈ M_w(OxL18)). This phenomenon can be observed from the curves obtained, since samples OxL9, OxL13, OxL14, and OxL15 are the ones from which the most significant changes can be observed, with the highest peak at a retention time of around 21 min, signifying a higher M_w proportion.

In terms of PI, the changes were not substantial. A similar phenomenon attributed to the change in M_w could be applied, where mild conditions in the reaction did not affect the molecular composition. In contrast, the higher conditions created new molecular structures due to bond cleavages and recondensation, increasing the general heterogeneity. Still, the increase in PI can be considered neglectable.

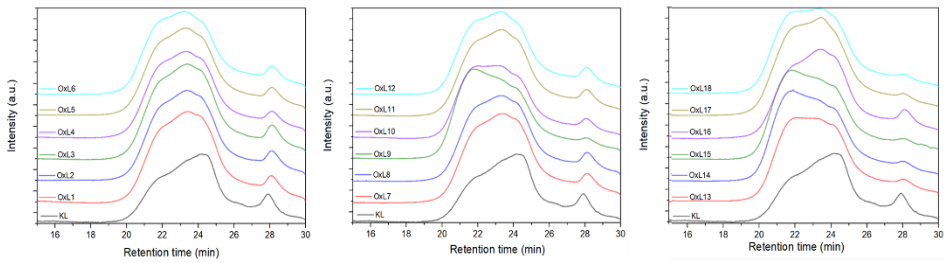

Figure 5.7. The chromatogram curves obtained for KL and its oxidized analogues.

The FTIR spectra are illustrated in Figure 5.8, and the assignments for each frequency range are listed in Annex I, in Table A.1. Structural features and

functional groups of the lignins can be observed. The broad bands obtained at 3400 cm^{-1} are attributed to O-H stretching in aliphatic and phenolic hydroxyl groups. This band intensified in all the oxidized samples, meaning the OH content increased during the process. C=O stretching, attributed to bands at 1708 cm^{-1}, also increased, more clearly seen in a close-up look in Figure 5.9.

On the other hand, aromatic skeletal vibration bands at 1610 cm^{-1} slightly decreased their intensity with the oxidation reactions, along with the bands at 1329 cm^{-1} and 1217 cm^{-1}, attributed to S ring and G ring stretching. This means that a mild decomposition happened in lignin due to aromatic cleavage. Moreover, the decrease in intensity of the bands at 1150 cm^{-1} implies a decrease in aliphatic ether groups.

Consequently, aromatic rings and aliphatic ether bonds cleavage led to an increase in carboxylic and hydroxyl groups, particularly noticeable in samples subjected to prolonged times and low temperatures (30 °C, OxL3) and medium duration reactions at medium temperatures (45 °C, OxL8, and OxL11), with or without the addition of hydrogen peroxide. Notably, at high temperatures (60 °C), the absence of H_2O_2 favored the process, with significant variations observed in reactions of short and extended durations (OxL13 and OxL15) [74].

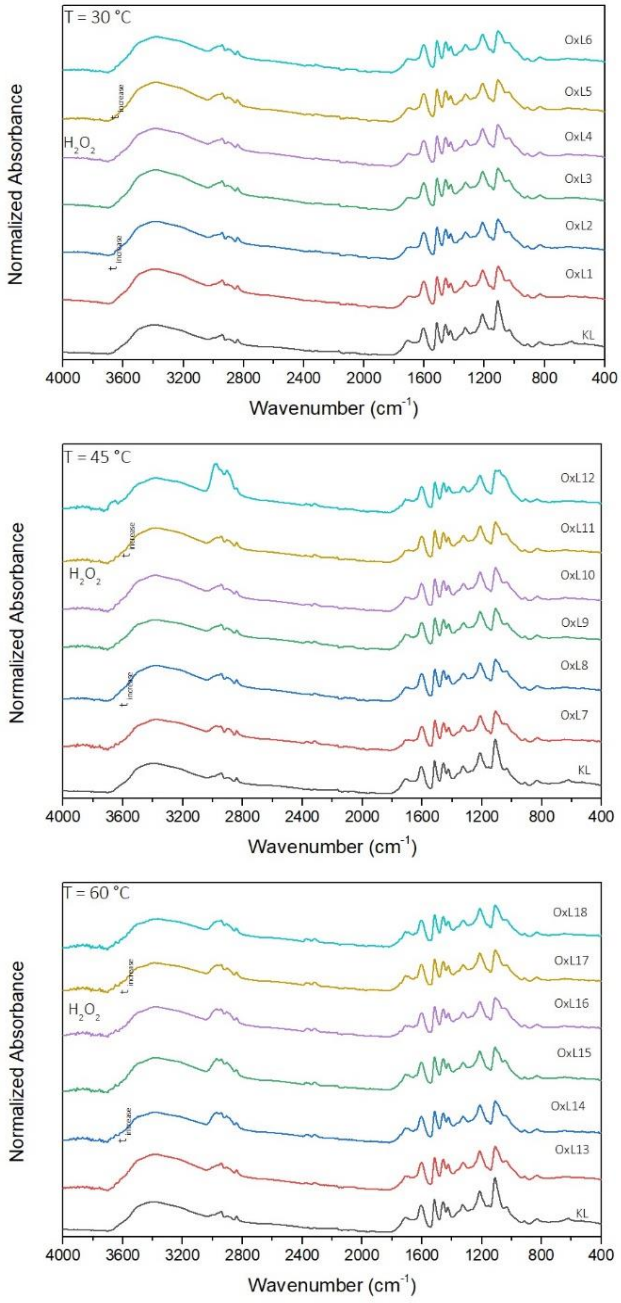

Figure 5.8. FTIR spectra of KL and oxidized lignin samples.

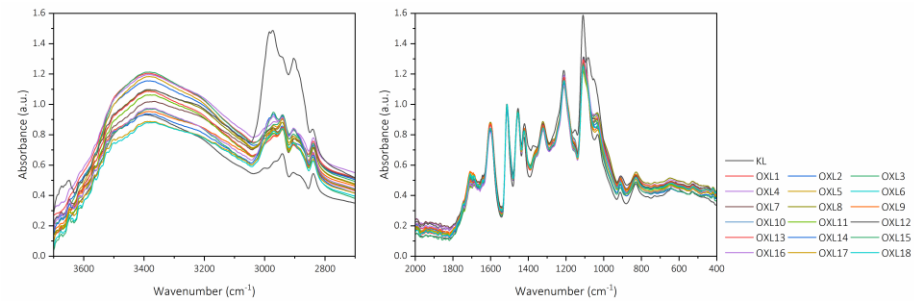

Figure 5.9. A close-up look to the characteristic bands of the oxidized samples.

In some cases, shorter times favored the increment of TPC, while longer times, specifically when temperatures were also higher, led to the formation of molecules with more OH groups. At short times (15 min), the temperature increase aggravated the loss of OH groups, showing a linear trend (a decrease from 0.013 mmol/g at 30 °C, to 0.095 mmol/g at 45 °C, to 0.009 mmol/g at 60 °C). When H_2O_2 was added, a similar trend was observed: the OH concentration decreased inversely proportional to time. Medium times were optimal at medium temperatures, whereas longer times had the best results at high temperatures.

This could be because low temperatures did not allow breaking aromatic rings, and substituting aliphatic and phenolic OH groups did not require extended time. On the other hand, due to the aggravation of reaction conditions caused by the temperature increase, short times were sufficient for partial cleavage of lignin's aromatic ring, leading to the creation of new functional groups, like hydroxyl groups. However, with longer times, there was a tendency for repolymerization, which once again led to a decrease in OH content, as condensation reactions happened within this functional group. UV absorption bands were also recorded from 400 to 260 nm, as illustrated in Figure 5.10. The absorption peaks at 280 nm correspond to non-conjugated OH groups, while values at 315 nm correspond to the conjugated OH groups. Samples obtained at low temperatures followed the

same trend as in TPC, where longer times reduced the OH content the most, both conjugated and non-conjugated. All samples reduced their content in conjugated and non-conjugated OH groups, although this change was irrelevant. Nevertheless, it was at medium temperatures where the reduction of these functional groups was the most pronounced, while high temperatures resulted in the least reduction, with a similar trend, albeit with variations in time and addition of H_2O_2.

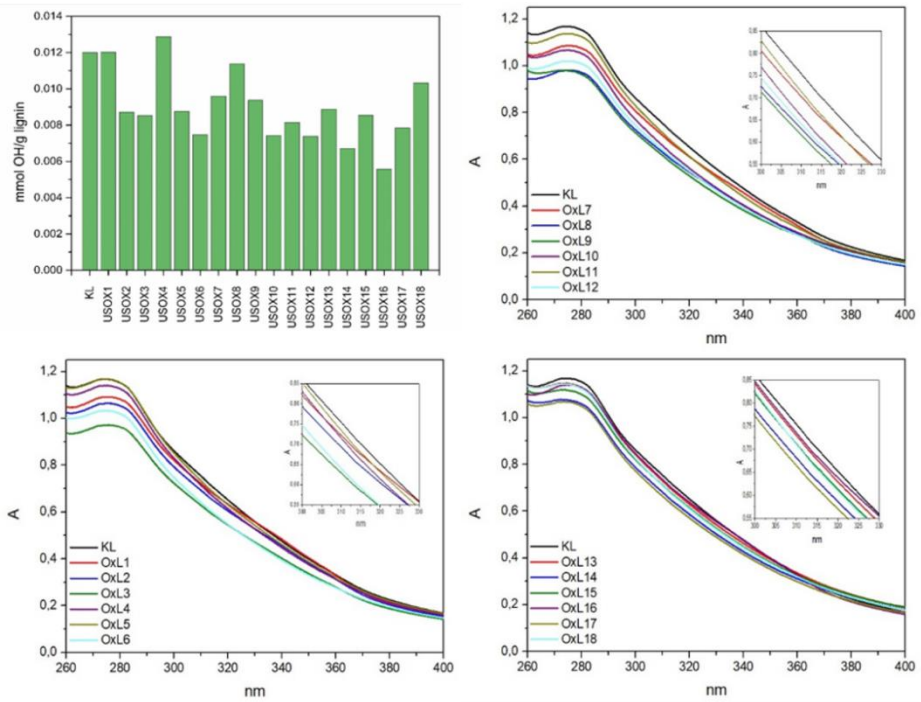

Figure 5.10. Total Phenolic Content (TPC) and conjugated and non-conjugated OH groups.

Different OH groups in lignin were identified and quantitatively determined by ^{31}P NMR spectroscopy. Peaks associated with aliphatic OH, C5-substituted OH, guaiacyl OH, p-hydroxyphenyl OH, and carboxylic acid OH were integrated and compared with the integration value obtained for the internal standard N-Hydroxy-5-norbornene-2,3-dicarboxylic acid imide

(NHND) to get OH mmol/g lignin concentration values. Besides, S/G ratios were also obtained. The results obtained are listed in Table 5.9. All the samples lacked from H unit due to the hardwood origin of the Kraft lignin; overall, an increase in OH content can be observed for all the treated samples. The increase in hydroxyl content indicates that the conditions used were not strong enough for condensation or depolymerization reactions, which validates these conditions as suitable for the oxidation of lignin. Ultrasonic forces fragmented the condensed structures. Therefore, S and G units freed themselves from the macromolecule, regaining the OH group from which condensation occurred. Since the C5 of the aromatic ring is free in G units, their reactivity is higher and easier to condense. Consequently, G units are more abundant in condensed structures, and when fractioned, the released units are also G units [76].

Total phenolic content (TPC) increased in all treated samples. The lowest temperatures, without the addition of hydrogen peroxide, proved to be even more effective in increasing phenolic OH content (OxL1 and OxL2), where the most extended times were the most effective (OxL3). OxL3 achieved the optimal results, with the highest OH content, both aliphatic and phenolic. This differs from the results obtained from the Folin-Ciocalteau method, where longer times led to less TPC at the lowest temperatures.

The efficiency in medium and high temperatures, with the addition of H_2O_2, was not so satisfactory, meaning the harsher conditions did not positively influence the results (OxL9 and OxL18). Nevertheless, in the harshest conditions (OxL16 and OxL17), short and medium times showed better results compared to longer times (OxL18). However, once again, these results were not in concordance with those obtained with the Folin method. In the case of sample OxL9, the TPC measurements showed medium values, but an increase was observed as time increased under the harshest conditions (60 ºC and H_2O_2 addition).

Table 5.9. Quantification of different hydroxyl content (mmol/g lignin) and S/G ratio for selected samples.

	Aliphatic OH	*C5-substituted (S) OH*	*Guaiacyl (G) OH*	*p-Hydroxyphenyl (H) OH*	*Carboxylic acid OH*	*Total phenolic OH*	*S/G ratio*
KL	0.05	0.18	0.06	-	0.04	0.24	3.17
OxL1	0.06	0.21	0.07	-	0.03	0.28	2.86
OxL2	0.06	0.20	0.07	-	0.03	0.27	2.86
OxL3	0.07	0.25	0.09	-	0.03	0.34	2.89
OxL9	0.06	0.20	0.06	-	0.04	0.26	3.08
OxL16	0.06	0.20	0.07	-	0.03	0.27	2.83
OxL17	0.06	0.21	0.07	-	0.04	0.28	2.88
OxL18	0.04	0.20	0.07	-	0,01	0.27	2.67

Aliphatic OH groups also increased in all samples except for OxL18, which decreased due to condensation reactions. Aliphatic hydroxyl groups are more reactive than phenolic hydroxyl groups [76], meaning that these conditions might be where condensation reactions start instead of oxidation. In carboxylic acid OH groups, a clear tendency could not be observed. While moderate conditions, such as low temperature and medium time (OxL2) and high temperature with low time (OxL16) yielded lower COOH content, harsher conditions favored the formation of more of this group. Nevertheless, OxL18 had the considerably lowest COOH content, following the same mechanism that caused the reduction in aliphatic content.

In terms of the S/G ratio, all the treated samples showed a decrease in their S/G ratio, indicating an increase of G units over S units. OxL18 had the smallest ratio, but observing the individual concentrations of G and S OH groups, OxL3 proved to be the most effective in increasing both S and G units.

It notably increased the value of S OH mmol, which is the most challenging compound to react with, while using low temperatures without the addition of an oxidizing agent.

This matches with the results obtained from FTIR spectra, where the intensity of the band at 1150 cm^{-1} decreased, suggesting the cleavage of aliphatic ether bonds and an increase in C=O and OH groups. These changes happened at low temperatures and without the addition of hydrogen peroxide because ultrasound irradiation was efficient at low temperatures, enabling the oxidation of lignin without undesirable phenomena such as agglomeration, depolymerization, and degradation. The quantity of oxidized functional groups increased with the prolongation of the reaction time, whereas the conditions remained too mild for the occurrence of further reactions. When heat and H_2O_2 were supplied, these other reactions started, exceeding the intended oxidation step and resulting in the production of degraded samples.

5.4.1.5. Thermal properties of the samples

Thermogravimetric Analysis was performed for each sample. The obtained TGA and DTGA curves are illustrated in Figure 5.12, and the values of mass loss at 5% and 50% ($T_{5\%}$ and $T_{50\%}$) along the degradation stages are listed in Table 5.10. $T_{5\%}$ corresponds to the temperature at which 5% of the mass degrades. Overall, most samples have a $T_{5\%}$ between 150 and 200 °C. Typically, moisture is evaporated before, meaning its content is lower than 5%, except for OxL5 and OxL6, where their $T_{5\%}$ is at 75 °C. $T_{50\%}$ corresponds to the temperature in which 50% of the mass is lost. Most $T_{50\%}$ values are around 425 and 475 °C, with few exceptions exceeding that (OxL4 with 540 °C and OxL15 with 520 °C).

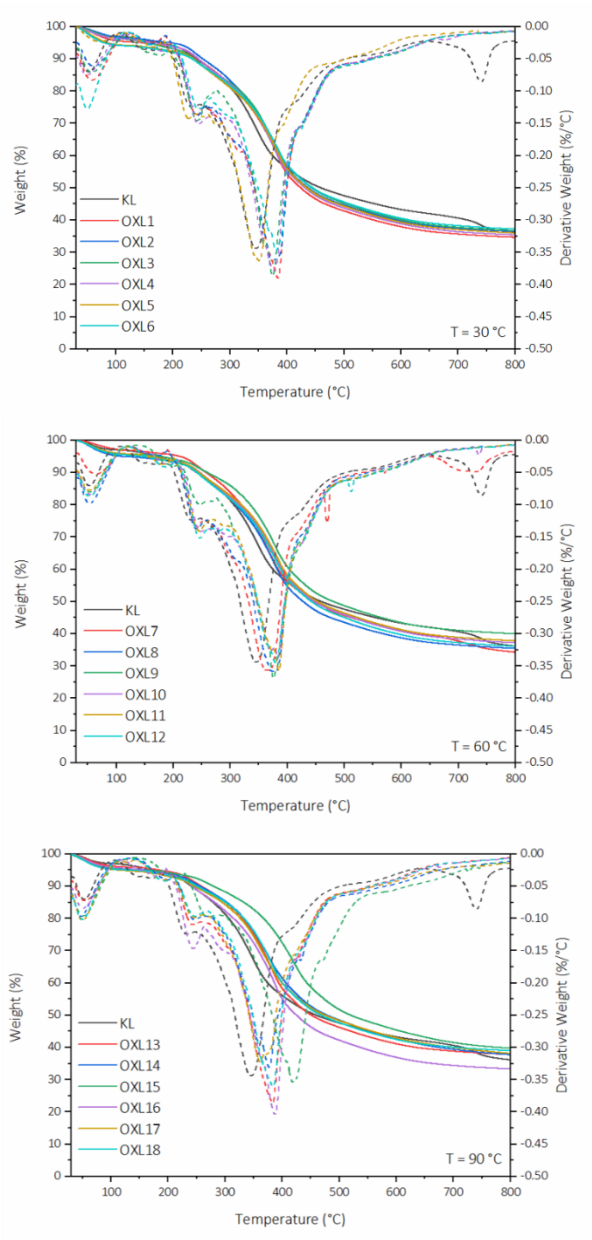

Figure 5.11. TG and DTG curves of KL and its oxidized samples.

DTGA curves depict the different degradation stages happening at different temperatures. The first degradation stages happening below 150 °C are due to moisture loss. The second degradation stage happens between 200 and 300 °C, corresponding to the degradation of polysaccharides and aliphatic

alcohols and acids. Finally, aromatic ring cleavage and degradation of syringyl and guaiacyl units into phenolic compounds happen at temperatures above 300 °C [77,78].

The first degradation step was due to the moisture loss of the sample, happening at 50-60 °C in all cases. The second significant mass loss happened around 200 and 300 °C, with minor degradation. In this step, small molecules were degraded, while the main part of the lignin sample was lost between 350 and 460 °C. Finally, a few samples had residual matter, which degraded at around 700 °C. OxL4 and OxL15 have the highest thermal stability, while OxL1, OxL8, and OxL16 have the lowest. This might be due to the condensed structures being more considerable in the first ones and scarcer in the last ones. The main degradation temperatures were also higher for samples OxL4 and OxL15, while KL and OxL5 had the lowest.

Differential Scanning Calorimetry curves are shown in Figure 5.12, and the T_g-s obtained are listed in Table 5.10. It can be observed that values ranged around 116-118 °C or around 97 °C. This fluctuation of T_g values could be related to the heterogeneous nature of lignin samples since a correlation between T_g and PI was noticed. KL and other oxidized samples maintained a similar polydispersity value, around 3.0-3.3, while samples OxL9, OxL14, OxL15, OxL17, and OxL18 have a PI value of 3.4-3.5. This small increase in PI entailed a reduction in the T_g of nearly 20 °C, which negatively affected to the rigidity when temperatures approach that T_g value.

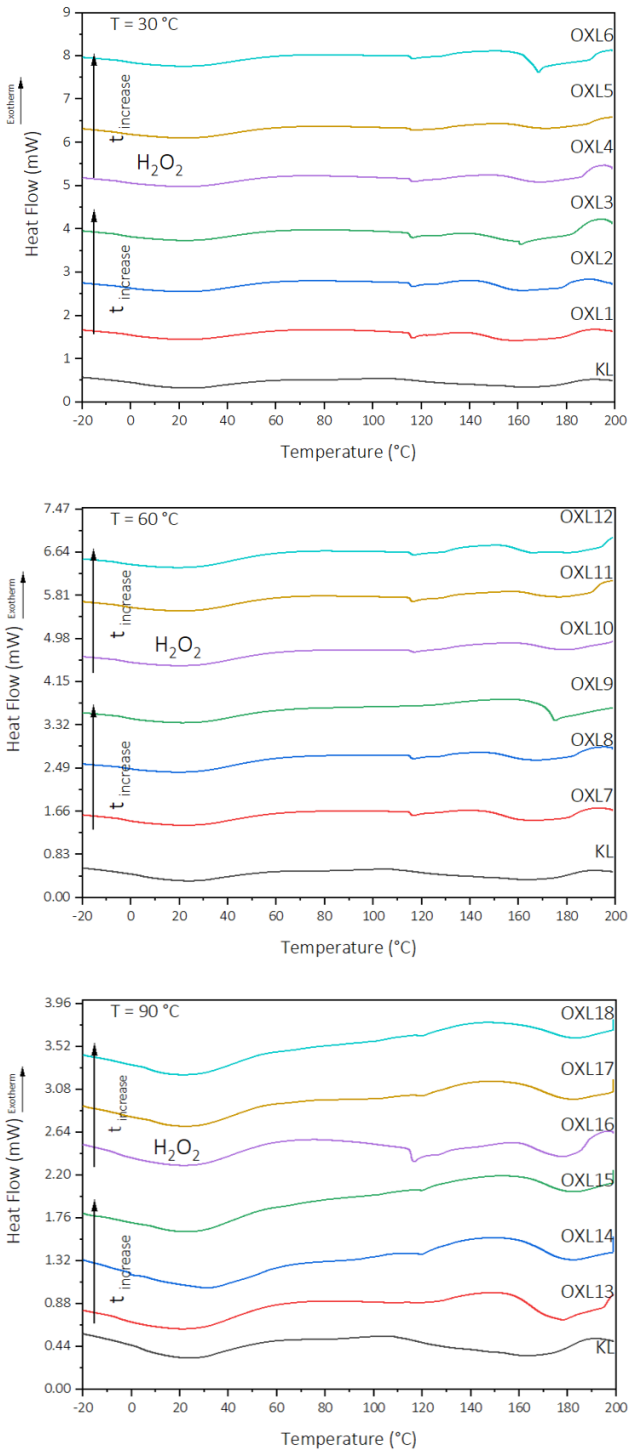

Figure 5.12. DSC curves of KL and its oxidized samples.

Table 5.10. Mass loss at 5% and 50% ($T_{5\%}$ and $T_{50\%}$), degradation stages of KL and oxidized samples, and glass transition temperatures (T_g).

	$T_{5\%}$ (°C)	$T_{50\%}$ (°C)	Degradation stages (°C)	Char (%)	T_g (°C)
KL	175	460	**50**/150/175/**225**/**350**/425/550/**740**	36.05	116.4
OxL1	150	425	**60**/160/**240**/320/**375**/425/525/600	34.59	116.6
OxL2	175	440	**60**/160/**240**/300/**375**/425/525/600	36.40	116.8
OxL3	150	445	**60**/150/175/**240**/**375**/425/525/600	36.67	116.6
OxL4	200	540	**60**/175/225/**300**/360/**460**/525/650	40.31	116.9
OxL5	75	440	**60**/160/**225**/250/275/**350**/375/475/650	35.94	117.3
OxL6	75	445	**50**/150/175/**250**/300/**375**/425/525/600	37.16	116.9
OxL7	200	450	**70**/175/**220**/**375**/425/**475**/575/**725**	34.20	116.8
OxL8	100	425	**50**/190/**220**/290/310/**375**/425/525/700	35.43	116.9
OxL9	175	475	**50**/**200**/**250**/**375**/430/525/600	39.94	100.0
OxL10	150	450	**50**/150/**190**/**250**/300/**375**/425/525/600/730	37.16	117.0
OxL11	150	450	**50**/150/**190**/**250**/280/**390**/425/525/600/700	37.77	116.6
OxL12	150	450	**50**/150/**190**/**250**/275/**390**/425/510/600/700	36.05	117.0
OxL13	180	450	**50**/125/190/**220**/**390**/425/525/600/700	37.76	117.8
OxL14	150	475	**50**/**200**/**220**/**375**/420/525/600	37.69	97.1
OxL15	150	520	**50**/220/**260**/**420**/475/600/725	38.89	97.0
OxL16	150	425	**50**/150/175/250/300/**390**/425/525/675	33.28	116.7
OxL17	100	475	**50**/125/190/**220**/**375**/425/525/600/675	38.05	97.2
OxL18	100	475	**50**/200/**250**/300/**390**/425/525/600/700	38.95	97.2

*In red and bold the temperatures in which the main degradation occurred. In black bold the other significant degradations.

5.4.1.6. Morphological properties of the samples

Z potential (mV), conductivity (mS/cm), size average (nm), and dispersity index were measured for all samples by DLS. The ZP refers to the value of the electric charge of the surface of the particle, which can determine the stability and the tendency of the particles to aggregate themselves. High ZP

values (positive or negative) imply that they have good physical stability due to the electric repulsion and the high charge surface, disabling the aggregation and growth in size. Values between +30 mV and -30 mV indicate instability, with van der Waals forces being able to act upon the particles, creating aggregates. When this value is higher than +30 mV or minor than -30 mV, the particles have sufficient repulsive force to be physically stable in dispersion.

ZP values have already been shown in Table 5.2, listed as dependent variables for the fit of the experimental data for the DOE. Nevertheless, it is also visible in this current section as it is interesting to compare along the other data obtained from DLS. From Figure 5.13, most lignins presented moderate stability, while some presented incipient stability. KL has incipient stability; however, most samples have values from -30 mV to -40 mV. This means that the process was effective in forming more stable particles. Three samples reached really good stability: OxL1, OxL2, and OxL3. These were obtained at the lowest temperature (30 °C), at various times, without adding H_2O_2. It was observed that ZP decreased with sonication time almost linearly, a trend that was similar in samples obtained at 45 °C (OxL7, OxL8, and OxL9), and 60 °C (OxL13, OxL14, and OxL15), without H_2O_2. Nevertheless, these higher temperatures, created more unstable particles. The reason for this phenomenon might be that these stronger conditions promoted the degradation of lignin into smaller particles and induced repolymerization, resulting in less stable particles with a higher dispersity index.

Particle size, conductivity and dispersity index were measured similarly, and values obtained are shown in Figures 5.14, 5.15, and 5.16 respectively. Values were recorded through photon dispersion caused by the particle being dispersed in water. Depending on the particle size and its interaction with the medium, it disperses differently and yields different values. This

method is interesting for providing a quantitative value of the particle size due to the rapid data collection and the easy obtaining of the results. However, the information obtained might differ from other qualitative methods like SEM o TEM since these particles observed are no longer dispersed or dissolved when analyzed.

There was not a visible correlation between ZP and size average. Nevertheless, the smallest particles, OxL3 and OxL18, had the highest conductivity values, almost doubling the values of the other samples. These two samples had the longest reaction times, contributing to higher H content, probably due to the formation of hydroxyl groups that improve stability. Overall, regarding morphological properties, OxL3 was the sample with the best results since it had the highest ZP, highest conductivity, smallest size, and lowest dispersity index.

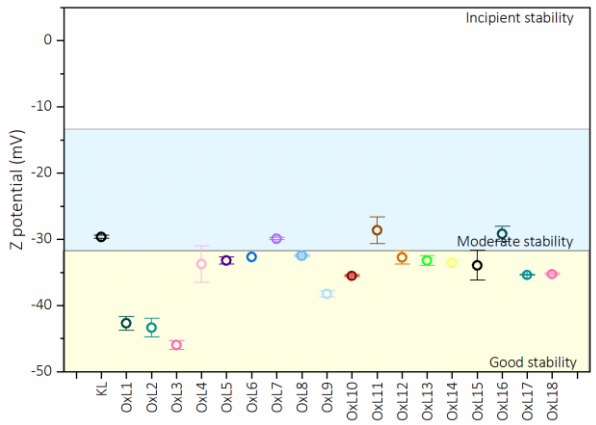

Figure 5.13. Z potential (mV) of KL and the oxidized nanoparticles.

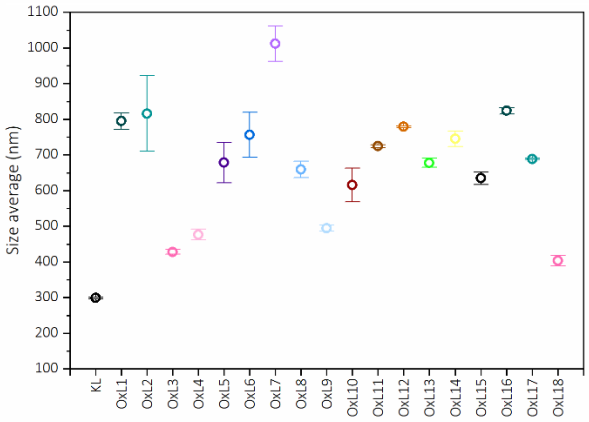

Figure 5.14. Size average (nm) of KL and the oxidized nanoparticles.

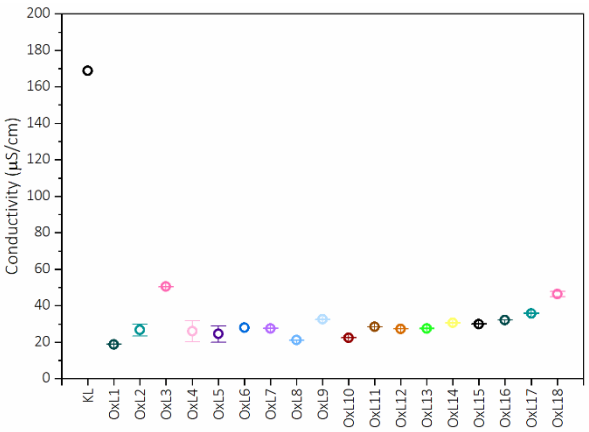

Figure 5.15. Conductivity (mS/cm) of KL and the oxidized nanoparticles.

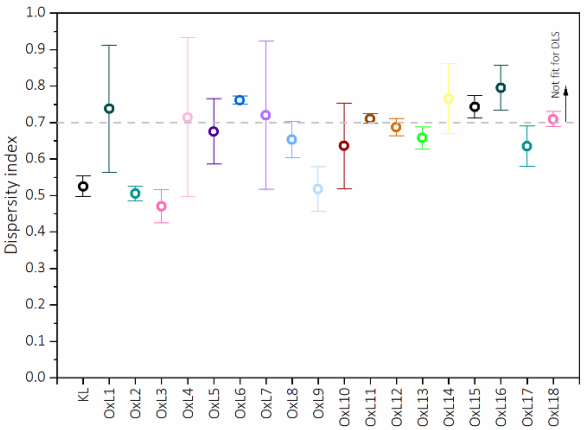

Figure 5.16. Dispersity index of KL and the oxidized nanoparticles.

Selected lignin particles were dispersed in water at a concentration of 0.1 wt% and prepared for TEM analysis. The images obtained at a 500 nm scale and negative contrast are shown in Figure 5.17, and aggregate particle types and average particle size values are listed in Table 5.11. It should be mentioned that the size values obtained from DLS and TEM differ due to the nature of the analyses. The first was measured by dispersing samples in a liquid media and measuring the light scattering of dispersed bodies, while the latter was dried and just particles were imaged. Therefore, size values obtained from DLS were higher, but a similar trend in the values change could be observed from both techniques.

Images obtained by TEM displayed that the reaction reduced the sizes and influenced the dispersion, aggregation, and agglomeration of the lignin particles. KL particles had considerably bigger diameters than the sonochemically oxidized samples, which demonstrated the influence of the process on the final particles when times were medium or high. The average particle size of OxL1 and OxL16 maintained quite similar to the value of KL, obtaining particles with diameters ranging from 125 to 150 nm, regardless the addition of H_2O_2 and the applied temperature. With the increase of time at low temperatures (OxL2 and OxL3), a drastic reduction of size could be observed, where 25 nm sized particles were measured. A decrease was also observed with time in the case of OxL17 and OxL18, but the particles obtained did not reduce so drastically. Medium temperatures and long times were also effective in obtaining nanolignin (OxL9) since the smallest particles quantified by this technique were observed under these conditions.

Another noteworthy parameter that can be assessed using this technique is the tendency to create particle clusters. Initially, KL particles were tightly bound, creating agglomerations. However, even with the mildest reaction conditions (30 °C during 15 min), these clusters significantly reduced, as can be observed in the image of OxL1, where the particle size was much smaller, and the agglomerates were minor.

As the reaction time increased to 30 min (OxL2), particles switched from being tightly bound to slightly bound, forming agglomerations instead of aggregates [79]. This indicated that the interactions with the highest force were broken and replaced by those with lighter force. When the reaction time reached 60 min, particle-particle forces were hardly noticeable, with mostly free particles (OxL3). Agglomerations reoccurred when the temperature raised to 45 °C while maintaining the longest reaction time (OxL9). This phenomenon was significantly amplified when the temperature was further increased to 60 °C while maintaining the one-hour reaction time (OxL18).

For these observations, it can be concluded that the reaction time had a greater influence on the agglomeration formation than the reaction temperature. Samples obtained at 60 °C after 15 and 30 min (OxL16 and OxL17, respectively) consisted of loose molecules with no visible particle-particle interactions. Moreover, the addition of H_2O_2 did not appear to have an apparent effect on agglomeration.

Additionally, it has also been established that the particles with higher molecular weights tend to have smaller particle sizes [80], as they initiate the nucleation during lignin precipitation and exhibit a more hydrophobic nature. The absence of small M_w lignins means that they do not coat the larger molecules, as these are the ones that precipitate subsequently [81].

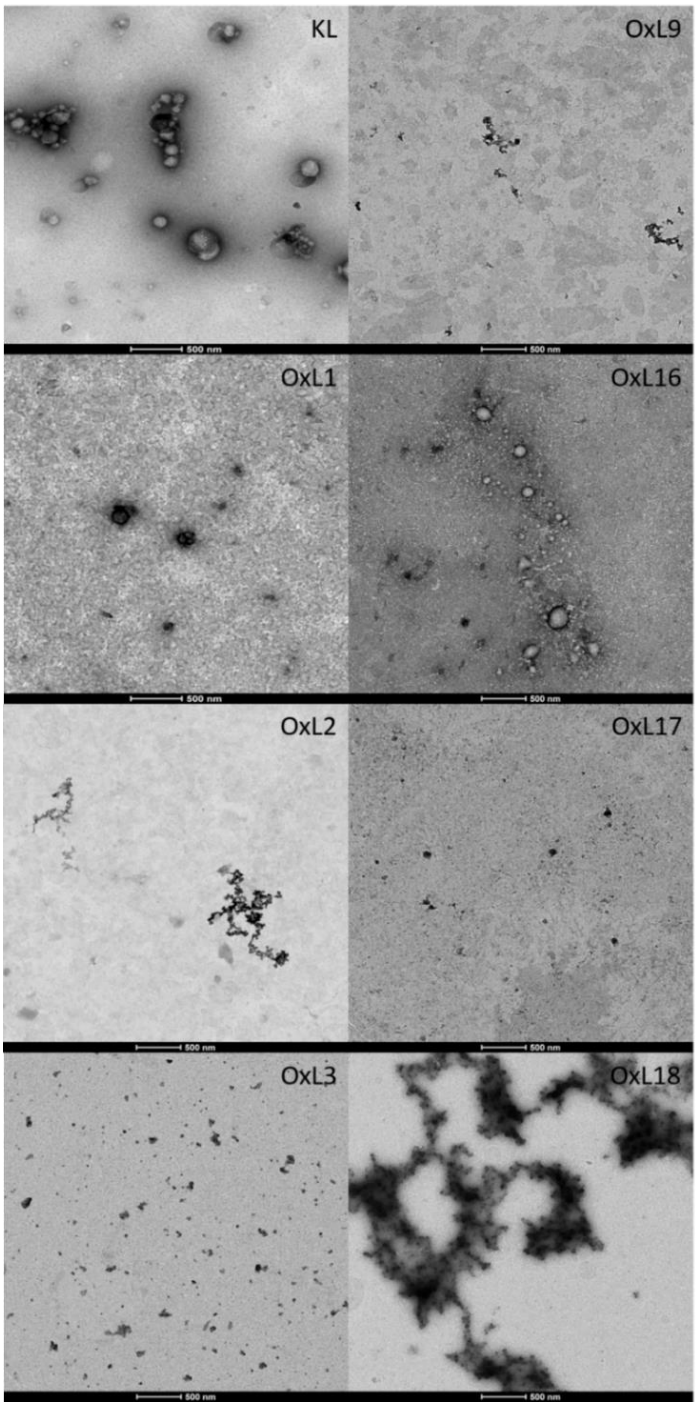

Figure 5.17. TEM images of KL, OxL1, OxL2, OxL3, OxL9, OxL16, OxL17, and OxL18.

Table 5.11. Particle aggregation type and size, and particle size in mm of KL and oxidized samples.

Sample	*Particle aggregation type*	*Average particle size range (nm)*
KL	Big agglomerations	124.1 ± 34.6
OxL1	Small agglomerations	153.0 ± 39.9
OxL2	Medium aggregates	25.9 ± 2.8
OxL3	Free particles	25.8 ± 4.0
OxL9	Small aggregates	17.8 ± 2.7
OxL16	Small agglomerates	144.0 ± 25.5
OxL17	Free particles	123.5 ± 71.0
OxL18	Big aggregates	103.7 ± 67.8

5.4.1.7. Scaling up perspectives

The use of ultrasound irradiation has been widely evaluated for pilot and industrial scales, where both technical and economic feasibilities have been studied. The energy density (E_s) is a key factor for determining this since it takes into account the main parameters of the sonication treatment: power, duration, and volume [82]. However, the processing type should be similar to have a solid scaling. The current work experiments were carried out at three different times (15, 30, and 60 min). Other conditions like temperature and [H_2O_2] did not considerably affect the E_s of each experiment, as seen in Figure 5.6. Experiments with 15 min of duration consumed overall around 50 kJ, while the ones with 30 and 60 min consumed around 75 and 250 kJ, respectively. The volume of the solutions prepared and sonicated was 60 mL for all of them. Therefore, 800, 1250, and 4170 kJ/L were consumed for 15, 30 and 60 min treatments.

In terms of overall sustainability, there have been works where certain metrics have been applied to consider processes as green [4]. Generally speaking, the proposed process complies with this category, due to the

utilization of waste derived from the paper and pulp industry, with no conflicting interests with alimentary products, and with the implementation of ultrasonic cavitation. Moreover, this work has concluded that adding peroxide as an oxidizing agent has detrimental effects, and no other catalyst compounds have been added, easing the posterior processing of the obtained waste or side products of the designed process.

5.4.1.8. Validation of the process for OL

Once different conditions for the obtaining of oxidized KL nanoparticles were considered, it was concluded that the optimal experimental conditions used where the ones applied for sample OxL3. Low temperature (30 °C), no peroxide addition, and long times (1 h) were optimal to simultaneously obtain nanosized and more oxidized lignin, which can further ease its incorporation into numerous applications. Therefore, to validate the process as effective, the OL extracted in Chapter 4 was employed, and the influence of the lignin type in the nanoparticle production was assessed. Similar to the KL, FTIR, GPC, TGA, and DLS techniques were used to observe chemical, physicochemical, thermal and morphological changes.

As stated previously in Chapter 4, the organosolv lignin is considerably bigger and purer than the KL, due to the milder condition in which it is usually extracted. Therefore, differences in the sonochemical reaction designed for the KL oxidation and nanolignin production might happen. The results obtained from the characterization of the OL and the sonochemically oxidized OL (called OxOL) are listed in Table 5.12 and shown in Figure 5.18. It can be observed that the reaction considerably increased the M_w of the oxidized sample, reaching M_w of 10393 g/mol, almost doubling the weight of the original OL. Nevertheless, the PI of OxOL drastically decreased, resulting in highly homogeneous lignin.

Table 5.12. GPC results (M_w, M_n and PI), DLS results (Z potential, conductivity, Z average and PI) and TGA results ($T_{5\%}$, $T_{50\%}$ and different degradation stages observed) for OL and its oxidized sample (OxOL).

	OL	***OxOL***
GPC results		
M_w (g/mol)	5800	10393
M_n (g/mol)	1306	2104
PI	4.44	1.94
DLS results		
Z Potential (mV)	-29.326 ± 2.132	-20.634 ± 0.363
Conductivity	0.012 ± 0.000	0.014 ± 0.001
Z average (nm)	1240 ± 85	591 ± 9
PI	0.494 ± 0.016	0.602 ± 0.119
TGA results		
$T_{5\%}$ (°C)	95.5	194.0
$T_{50\%}$ (°C)	393.2	504.0
Degradation Stages (°C)	48.5/**362**	77/110.5/**377**

*In red and bold the temperatures in which the main degradation occurred.

To further investigate changes in the physicochemical properties, the functional groups were assessed by FTIR, which showed an increase in the band associated with the O-H stretching vibration at 3400 cm^{-1}, while maintaining a similar intensity of the band associated with C=O at 1700 cm^{-1}. An increase in the region of 2400-200 cm^{-1} was also observed, with the increase of the bands attributed to alquine (C≡C) groups at the region 2260-2190 cm^{-1} or cetene groups (C=C=C) at 2150 cm^{-1}. These changes verify the successful oxidation reaction also carried out in organosolv lignins, where a lignin with a richer functionality and reactivity was obtained.

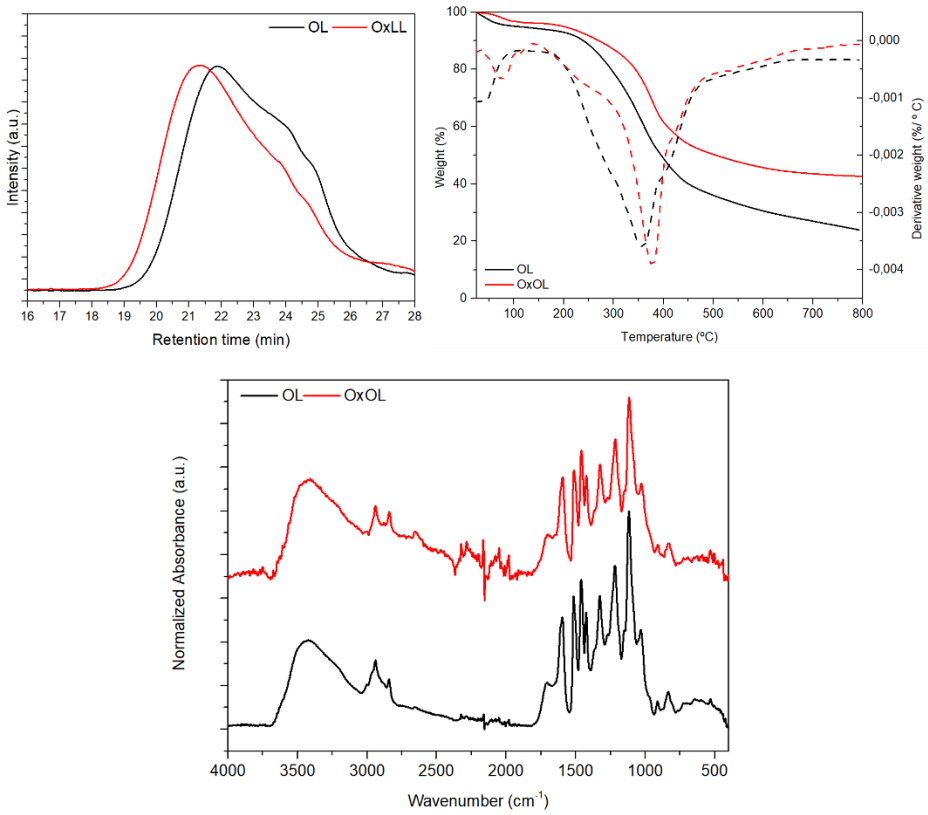

Figure 5.18. On the top left side, the GPC chromatogram obtained for both OL and OxOL samples can be seen, along with the TGA and DTG curves on the top right side, and the FTIR spectra in the bottom.

Morphological properties were observed by DLS, where Z potential, conductivity, Z average and PI values were measured. Although the higher functionality of the OxOL did not result in more water-stable particles, since a slightly lower Z potential was obtained, drastic particle size reduction was obtained, with half the size of Z average values (591 nm for OxOL whereas for OL the value obtained was 1240 nm). This, once again shows that the molecular size of the particle did not affect the particle size. A similar phenomenon was observed with KL, but in that case, the M_w increase was not as considerable, and the particle size changes were observed from the TEM rather than from DLS. In this case, however, DLS was enough to determine the success in obtaining nanoparticles.

Finally, thermal properties were analyzed by TGA. Temperatures rose to 800 °C following the procedure explained in Annex I, and $T_{5\%}$, $T_{50\%}$, and different degradation stages were observed. Since higher M_w lignin was obtained from the process, the thermal behavior of the molecules also improved. $T_{5\%}$ and $T_{50\%}$ values were considerably higher than the ones obtained for the original OL, and the main degradation stage of the oxidized OL was also shown to be higher, concluding a higher thermal stability of the OxOL.

5.4.2. CARBOXYMETHYLATED, SULFOMETHYLATED, AND METHYLATED LIGNIN CHARACTERIZATION

All the FTIR spectra obtained for the lignins employed for the different modification reactions, and their modified analogs are shown in Figure 5.19, and a list of the main functional groups identified, and their band associations can be found in Table A.1 in Annex I.

The broad band at around 3400 cm^{-1} for the O-H stretching vibrations, 2940-2840 cm^{-1} for methyl and methylene C-H stretching, 1708 cm^{-1} for C=O stretching, and other bands around 1610 and 1150 cm^{-1} for different skeletal aromatic vibrations were the main bands found in lignin FTIR spectra. KL showed a considerable intensity on the OH band, more intense compared to OL, albeit being derived from the same raw material (*Eucalyptus globulus*). This was a consequence of the delignification process, since the Kraft process employed harder conditions than organosolv, breaking up more lignin bonds and therefore creating a smaller and more functionalized lignin.

Both KL and OL were fractioned in a previous work [78] by a solvent extraction method, where the biggest and smallest fractions obtained were modified in the current work. SKL had a very high hydroxyl and carbonyl

content compared to the BKL and the initial KL, like the case with OL, where SOL also showed more intense bands at 3400 cm^{-1} and 1708 cm^{-1}.

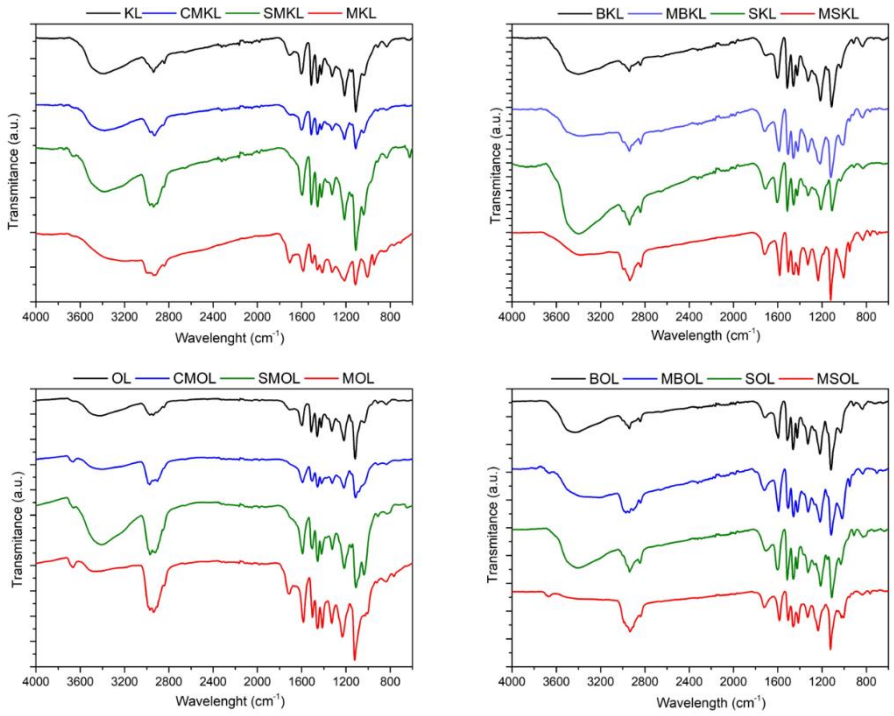

Figure 5.19. FTIR spectra of modified and unmodified lignin samples.

In terms of the effect seen on the carboxymethylation reactions, both CMKL and CMOL showed a significant decrease in the O-H stretching band compared to their KL and OL analogs. Alkaline conditions of the reaction make the aromatic hydroxyl groups strong nucleophiles, reacting with the sodium chloroacetate and yielding carboxymethylated aromatic rings [50]. Therefore, a decrease in the O-H vibration band was observed for all the reactions, and an increase of the methyl and methylene C-H stretching vibrations, due to the new $-CH_2COOH$, $-CH_2SOOH$, $-OCH_3$, and $-COOCH_3$ groups present in the modified lignins.

The rest of the bands associated with the aromatic skeletal vibrations and aliphatic hydroxyl groups did not show major differences after the modification [55,83], as a consequence of the selectivity of the reactions of CM and SM. Only the aromatic OH groups were modified while the aliphatic OH groups remained intact. Therefore, the band at 3400 cm^{-1} for samples CMKL, CMOL, SMKL, and SMOL could be attributed to aliphatic OH and unreacted phenolic OH groups. Contrarily, the methylation reaction did not show the same selectivity, reacting with all types of OH groups, therefore showing a more significant change in the 3400 cm^{-1} band intensity.

The molecular weights and their polydispersity index were calculated by GPC. The values obtained are listed in Table 5.13 and the chromatogram curves obtained for all the samples are shown in Figure 5.20.

Table 5.13. M_w, M_n, and PI values for the original lignins and their modified analogs.

	***M_w* (g/mol)**	***M_n* (g/mol)**	***PI***		***M_w* (g/mol)**	***M_n* (g/mol)**	***PI***
KL	5048	1149	4.39	OL	6374	1537	4.15
SKL	3312	1128	2.94	SOL	1856	953	1.95
BKL	9131	2407	3.79	BOL	8753	2439	3.59
Carboxymethylated							
CMKL	19154	1456	4.54	CMOL	10710	2503	4.28
Sulfomethylated							
SMKL	23234	3124	7.44	SMOL	11618	2554	4.55
Methylated							
MKL	9080	1669	4.39	MOL	14203	2222	6.39
MSKL	6474	1371	4.72	MSOL	6594	1414	4.66
MBKL	15374	3948	3.89	MBOL	19979	4014	4.98

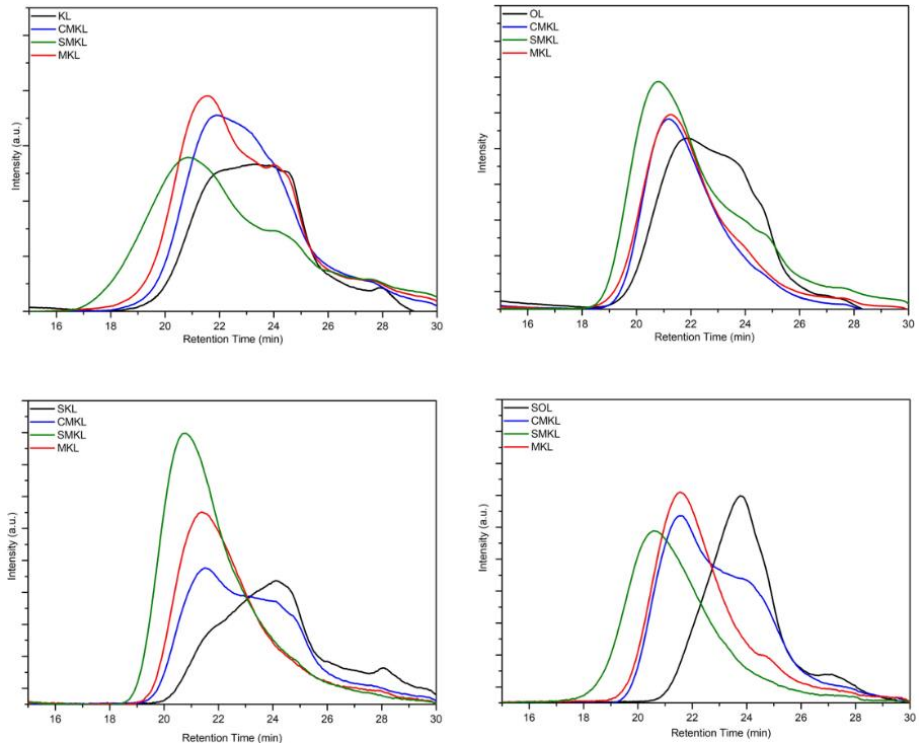

Figure 5.20. Chromatograms obtained from the GPC.

Overall, it could be observed that the chemical reactions increased the M_w of the lignins. In the case of the carboxymethylation reactions, both KL and OL considerably increased their M_w. In the case of KL, the M_w nearly quadrupled in CMKL, whereas for OL, CMOL increased by less than double. This phenomenon might be attributed to the fact that larger lignin molecules tend to have less functionalized groups like OH, and the ones present are more hindered and less reactive, obtaining a lower carboxymethylation degree with larger-sized particles [50]. The carboxymethylation reaction, in general, increases the M_w of the lignin not only due to the replacement of hydroxyl groups with carboxymethyl groups but also due to the condensation reactions happening during the process [52].

An almost identical behavior was observed with the sulfomethylation reactions, where the M_w of both SMKL and SMOL increased in the same

proportions as for CMKL and CMOL [56]. Nevertheless, with the methylation reaction, considerably smaller molecules were obtained, probably due to the formation of more stable lignins, which have been reported to prevent self-polymerization reactions [61].

As these three chemical reactions are based on the generation of alkoxide ions of the lignins, which then act as strong nucleophiles and subsequently react with various reagents to introduce new functionalities, it becomes essential to quantify the OH groups present in both the unmodified and modified lignins to determine the efficacy of the chemical reactions. The most effective method for quantitative analysis is the ^{31}P NMR, where different OH groups are displayed in different regions of the spectra. This allows individual identification, integration, and subsequent quantification of the concentrations of each type of OH group present in the sample. The results obtained are shown in Figure 5.21, values are listed in Table 5.14, and the spectra obtained for each sample are shown in Figures 5.22 and 5.23.

The carboxymethylation reaction has proven effective in substituting phenolic hydroxyl groups in both KL and OL. Approximately 20% of the syringyl OH groups (equivalent to the C5 substituted OH groups) in KL and OL reacted, while 16% and 31% of the guaiacyl OH groups in KL and OL reacted, respectively. In the case of p-hydroxyphenyl OH, nearly 30% of the quantified groups in KL reacted, compared to 17% in OL. Overall, about 20% of the total phenolic hydroxyl content in both KL and OL reacted, with a lower yield in OL, due to the higher molecular weight and consequently, lower reactivity compared to KL. Regarding aliphatic (Al) OH content, no significant changes were observed due to the selectivity of the reaction [50,54]. In the case of the sulfomethylation reaction, while it also showed selectivity in the reactivity of the Al OH groups, there was a reduction of approximately 20%. This reduction is likely due to the condensation and self-polymerization side reactions rather than the actual sulfomethylation

reaction. It was also observed that the aromatic OH group most susceptible to sulfomethylation was the G group, previously reported as the most reactive out of all the three aromatic lignin monomers. However, this trend was not consistently observed with OL, where different values were obtained. Although the CM reaction was similar in both cases, the SM reaction presented differences. This disparity can be attributed, once again, to the difference in M_w, as larger molecules exhibit more sterical hindrance, making it difficult for undesired side reactions like self-polymerization to occur. This results in a smaller reduction in OH content and less condensed modified lignins.

Regarding the methylation reaction, it was found to be the most efficient at reducing all types of OH groups, particularly when lignin molecules are smaller, as the OH groups are more accessible.

The values obtained with ^{13}C NMR after the integration of different spectral regions are listed in Table 5.15. The band attributed to the carbonyl content at 191 ppm showed that the modification reactions affected the presence of the functional group on the sample, disappearing completely the signal in all the modified Kraft samples, and almost completely disappearing the signal for the organosolv modifications. The signal at ~175 ppm, attributed to the -COOH content [55,84], was only visible in the case of CMKL and CMOL, verifying the effectiveness of the carboxymethylation reaction. Another visible change observed from all the reactions (the carboxymethylation, the sulfomethylation, and the methylation) was the significant increase in the signals in the range of 0-50 ppm, confirming the insertion of additional alkyl branches, due to the increase in C-C bond signals.

All the integration values obtained were normalized to obtain 6.12 ppm at the region of the methoxyl content, as suggested in previous works [85,86]. Overall, it can be observed that the modified lignins contained more

condensed structures, as can also be deduced from the M_w values obtained. Moreover, the oxygenated aromatic content and the overall aromaticity of the modified lignin molecules also increased. It can therefore be deduced that these modifications, apart from being appropriate to apply in water-based formulation, can also be interesting due to their aromaticity and electron conjugation, increasing the electron movement along the molecules and enhancing their performance as electroactive material or components.

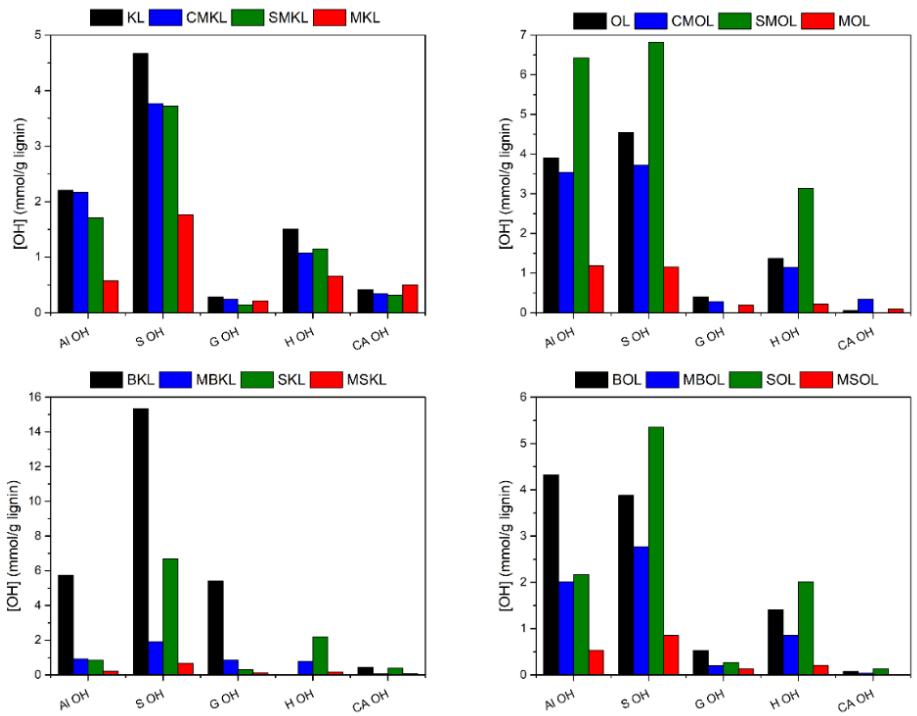

Figure 5.21. ^{31}P NMR results obtained for all the samples.

Table 5.14. Concentrations of the different OH types, quantified by ^{31}P NMR.

	Contents of different hydroxyl groups (mmol/g)					*S/G ratio*	*TOTAL OH*	*TOTAL PhOH*
	Al OH	*S OH*	*G OH*	*H OH*	*CA OH*			
KL	2.20	4.67	0.29	1.51	0.42	16.3	9.08	6.46
CMKL	2.17	3.77	0.24	1.08	0.34	15.7	7.60	5.09
SMKL	1.71	3.72	0.14	1.15	0.32	25.9	7.04	5.01
MKL	0.58	1.77	0.21	0.66	0.50	8.4	3.71	2.63
OL	3.90	4.55	0.40	1.37	0.06	11.3	10.28	6.32
CMOL	3.54	3.72	0.28	1.14	0.34	13.3	9.01	5.14
SMOL	6.42	6.81	0.00	3.13	0.00	6.0	16.37	9.95
MOL	1.19	1.15	0.19	0.21	0.09	2.8	2.84	1.56
BKL	5.75	15.34	5.43	0.00	0.44	2.8	26.96	20.77
MBKL	0.92	1.91	0.86	0.78	0.06	2.2	4.52	3.54
BOL	4.32	3.88	0.53	1.40	0.07	7.3	10.21	5.81
MBOL	2.01	2.77	0.20	0.85	0.04	13.6	5.86	3.82
SKL	0.84	6.69	0.31	2.20	0.38	21.6	10.42	9.21
MSKL	0.23	0.67	0.12	0.17	0.07	5.7	1.25	0.96
SOL	2.16	5.35	0.27	2.01	0.13	20.1	9.93	7.63
MSOL	0.53	0.85	0.13	0.21	0.00	6.3	1.73	1.19

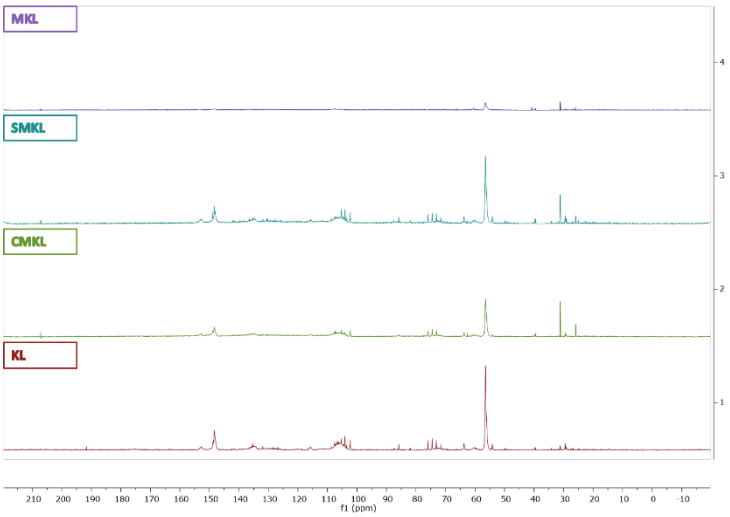

Figure 5.22. ^{13}C NMR spectra of KL and the modified analogs.

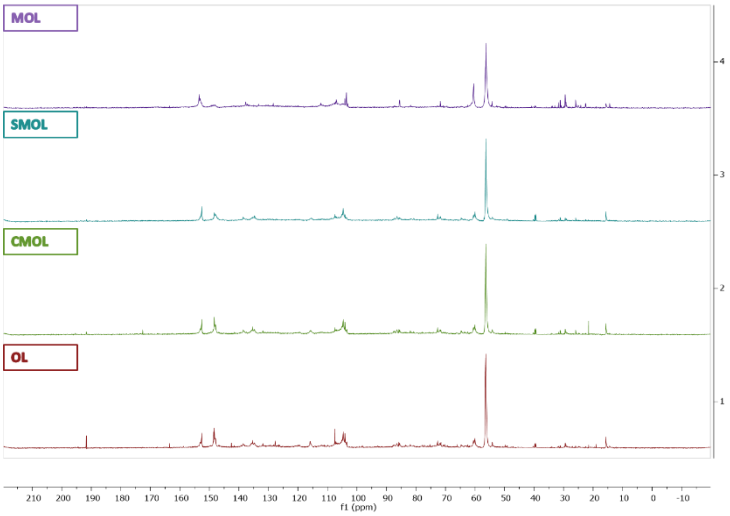

Figure 5.23. ^{13}C NMR spectra of OL and the modified analogs.

Table 5.15. Integration values of the different spectral regions identified in the modified and unmodified KL and OL samples.

Spectral region	*Chemical shift range (ppm)*	*KL*	*CMKL*	*SMKL*	*MKL*	*OL*	*CMOL*	*SMOL*	*MOL*
Methoxyl content	57-54	6.12	6.12	6.12	6.12	6.12	6.12	6.12	6.12
Aromatic methine carbons	125-103	5.28	8.90	9.16	9.75	7.61	7.52	8.16	7.22
Aromatic carbon-carbon structures	141-125	2.78	7.14	6.10	-	4.49	4.67	5.03	6.00
Oxygenated aromatic carbons	160-141	2.87	5.41	4.40	6.94	4.69	4.38	16.54	3.83
Carbon from carbonyl-type structures	195-190	0.09	-	-	-	0.02	0.03	0.05	0.25
Degree of condensation	125-103	5.28	8.90	9.16	9.75	7.61	7.52	8.16	7.22

Figure 5.24 displays the ZP values and conductivity values obtained for the modified and unmodified lignin particles, while Figure 5.25 illustrates the ZP distributions. Unmodified lignins, KL, and OL exhibited ZP values around -30 mV, which is indicative of incipient to good stability.

The carboxymethylation reaction had different effects on the particle stability depending on the lignin type. It resulted in increased ZP values for CMOL but slightly deteriorated ZP values for CMKL. The sulfomethylation reaction maintained a similar ZP value for SMKL with a slight improvement, while considerable changes occurred for SMOL, with a ZP value of nearly -45 mV.

In contrast, methylation reaction did not significantly affect the ZP values of either MKL or MOL, yielding values very similar to the KL and OL. However, when the methylation reaction was carried out with the lignin fractions (SKL, SOL, BKL, and BOL), a different trend could be observed. On one side, the smaller fractions, characterized by lower Mw, displayed lower ZP values, indicating poorer stability, compared to the larger fractions.

This difference was particularly pronounced in the Kraft lignin fractions. Higher ZP values were obtained for MSKL and MSOL compared to the unmodified fractions, resulting in highly stable particles for MSKL. Nevertheless, this trend was not consistent with BKL and BOL, where lower ZP values were obtained after modification.

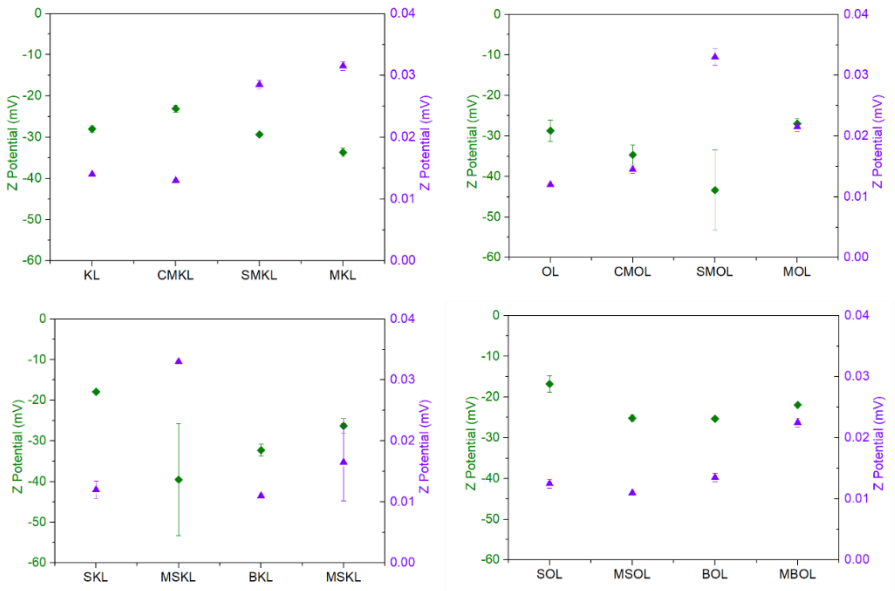

Figure 5.24. Z Potential and conductivity values for the modified and unmodified lignin particles.

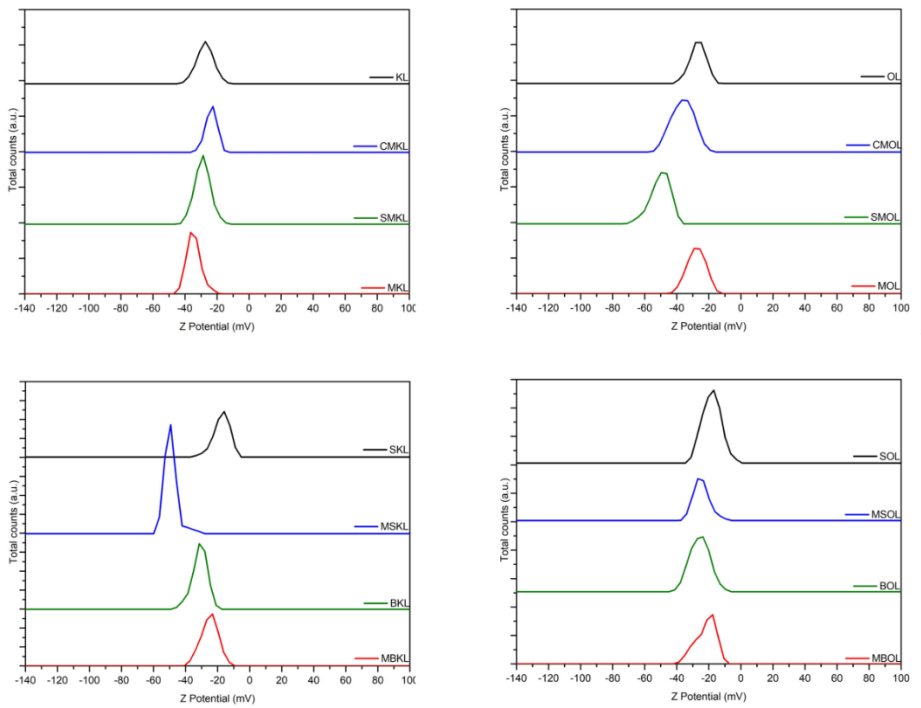

Figure 5.25. Z Potential distribution plots for all the samples.

From these observations, it can be deduced that different lignin types achieved their most stable state through different modifications. For KL, the methylation reaction yielded molecules with the lowest ZP and highest conductivity, with even more significant improvements when the precursor of this modification were small KL molecules. On the other hand, for OL, it was the sulfomethylation reaction the one producing the most stable particles.

In terms of the Z average, different trends were observed depending on the lignin type, as shown in Figure 5.25 and Figure 5.28. CMKL showed the highest particle size among all the samples, with a size of more than tripled compared to the original KL particles. This size slightly decreased for SMKL and showed a minor increase with MKL. When examining the fluctuation of ZP values, an inverse relationship could be observed between ZP and particle size, with larger particles when ZP values were smaller. A small ZP value suggested that the ions presented on the surface were not abundant enough to maintain a stable dispersion in the medium, which promotes particle aggregation.

This phenomenon did not necessarily correlate with the actual M_w values. For example, OL had a M_w of 600 g/mol, whereas CMOL, its carboxymethylated counterpart, had a significantly higher M_w of 10700 g/mol due to the self-polymerization side reactions during the process. Nevertheless, the addition of CM functional groups in CMOL led to a slight increase in the ZP value, which consequently resulted in slightly more stable water dispersions and a reduced tendency to agglomerate. This modification resulted in lignin particles that were four times smaller (1200 nm for OL vs. 300 nm for CMOL). This trend can be extrapolated to other samples, where similar Z average values were obtained for samples with similar ZP values, while larger Z average values were obtained for samples with lower ZP values.

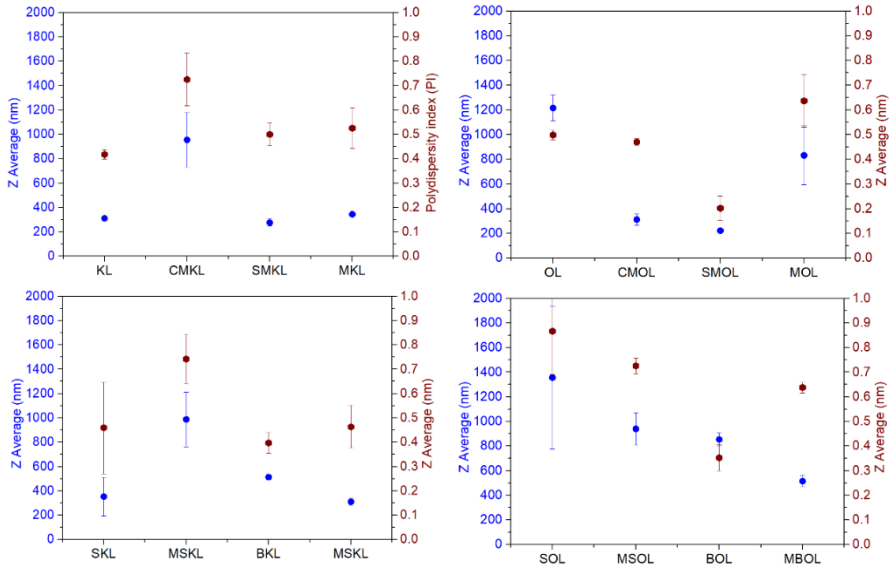

Figure 5.26. Z average and polydispersity (PI) values for the modified and unmodified lignin particles.

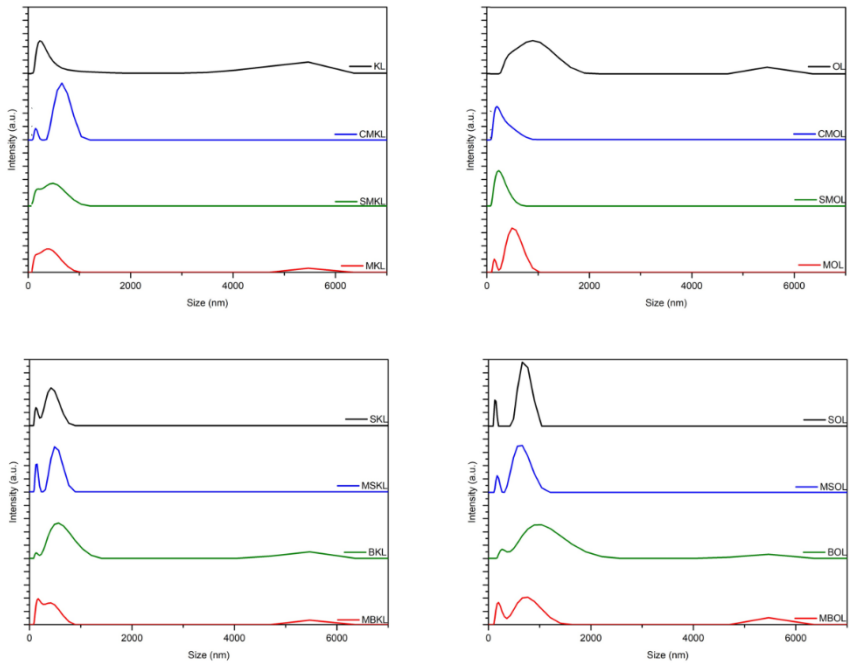

Figure 5.27. Size distribution by intensity for all the samples.

Thermogravimetric analysis of the lignins and their modified analogs was carried out. The $T_{5\%}$, $T_{50\%}$, different degradation stages identified, and the char (%) residue amount values are listed in Table 5.16, and the TGA and DTG curves are depicted in Figures 5.28 and 5.29.

Table 5.16. $T_{5\%}$, $T_{50\%}$, different degradation stages identified, and the char (%) residue of the modified and unmodified lignin samples.

	$T_{5\%}$ (°C)	*$T_{50\%}$ (°C)*	*Degradation stages (°C)*	*Char (%)*
KL	166	424	56/150/252/**385**	33.89
CMKL	113	643	74/109/**307**	47.69
SMKL	116	698	85/108/**307**/380/726	45.32
MKL	120	553	62/**162**/**407**/530	44.32
OL	103	397	**385**	23.92
CMOL	101	629	82/**307**/357/461/530/	47.54
SMOL	96	599	84/**282**/356/530/661	46.01
MOL	215	673	61/189/**380**/**411**/531/580	48.45
SKL	212	448	**370**	36.49
MSKL	141	482	76/153/**390**/536	41.64
SOL	225	420	**362**	30.68
MSOL	199	518	59/187/**385**/535	43.52
BKL	210	502	**384**	39.30
MBKL	169	751	43/169/**373**/**411**/533	49.69
BOL	190	480	**393**	36.96
MBOL	143	470	66/170/**344**/400/533	41.57

*In red and bold the temperatures in which the main degradation occurred.

The modifications were effective in producing more thermally stable molecules, resulting in considerably higher mass content (char residue) when exposed to high temperatures of 800 °C under an inert atmosphere. In the case of CM and SM reactions, the modified lignins showed lower degradation stage temperatures, with the primary one occurring at 307 °C

in both cases, as compared to the 385 °C of KL. Moreover, the $T_{50\%}$ was reached at significantly higher temperatures, increasing it by more than 200 °C.

In the case of the methylation reactions, there was also an improvement in the thermal stability of the lignin, although the difference was not as pronounced, likely due to the formation of smaller M_w particles. An interesting difference from the other modification lies in the degradation stages, where two main degradation stages were observed in the methylated samples. Since the methylation reaction can follow two different pathways, resulting in the production of two different molecules, as shown in Figure 5.4, there are consequently two different temperatures at which modified lignins undergo degradation

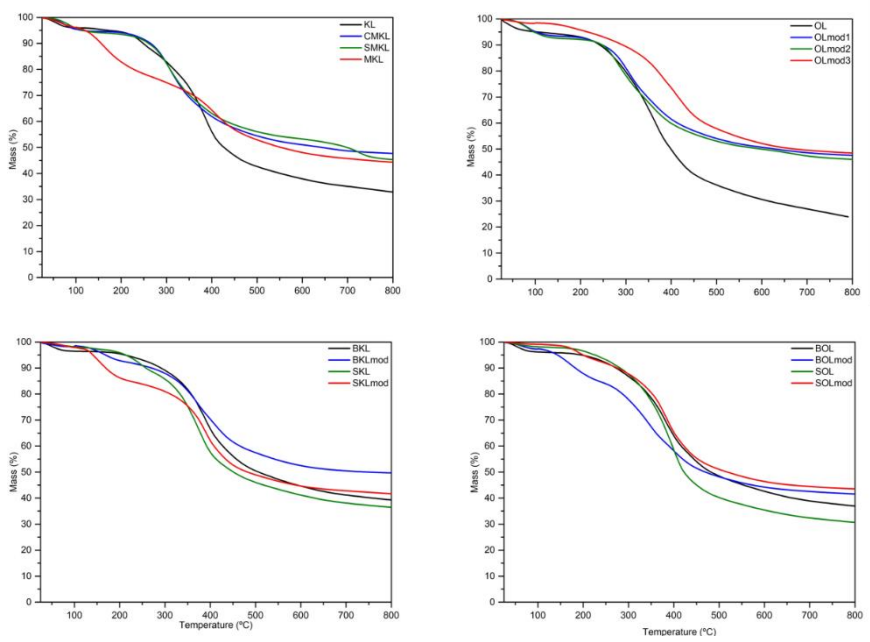

Figure 5.28. TGA curves of the unmodified and modified lignin samples.

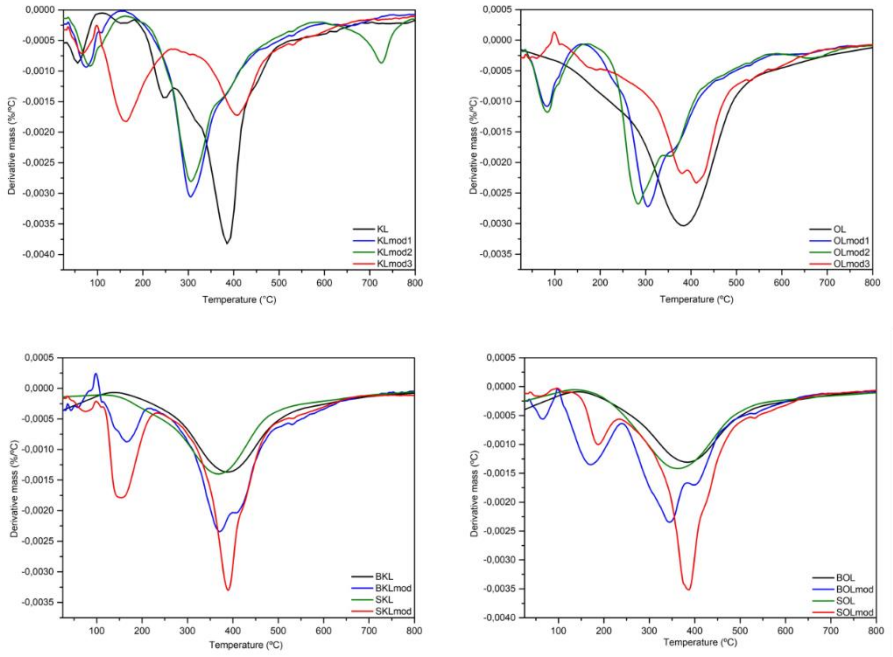

Figure 5.29. DTG curves of the unmodified and modified lignin samples.

5.5. CONCLUSIONS

The sonochemically assisted oxidation reactions of lignin were investigated under mild conditions, where temperature and time were increased, and H_2O_2 was added as a catalyst to produce more functionalized lignin particles, enabling the downstream valorization processes. All the obtained samples were physicochemically modified. Ultrasound irradiation proved to be effective in generating lignin nanoparticles even under mild conditions, enhancing the impact of the reaction conditions.

It was observed through ^{31}P NMR technique that phenolic hydroxyl groups increased the most at low temperatures (30 °C), with no oxidizing agent and long reaction times (60 min), corresponding to the OxL3 sample. FTIR spectra confirmed the increase in carboxylic

groups, proving the oxidation reactions with this novel approach. Long reaction times favored oxidation reactions at low temperatures, while medium temperatures yielded better results with medium reaction times, rather than extremes within the selected range. On the other hand, high temperatures resulted in higher degrees of oxidation regardless of reaction time. Concerning morphology, OxL3 also exhibited the highest Z potential, conductivity, and smallest size and dispersity.

It can be established that, despite the limited increase in the concentration of the oxidized functional groups, there was an increment of phenolic hydroxyl and carboxylic groups, validating the oxidation reactions. Beyond these chemical transformations, significant changes in morphology were observed, suggesting that sonication enabled their transformation for added-value applications. This makes it a successful and sustainable alternative to the currently used thermochemical processes.

The implementation of the optimal conditions obtained from the study with KL into OL was carried out to observe the versatility of the method. Therefore, OL particles were sonochemically oxidized as the OxL3 sample, at low temperatures and long times. The oxidized OL obtained also showed increased functionality and thermal stability, with much higher M_w values and lower particle sizes, validating the method as effective for organosolv lignins.

Regarding carboxymethylation, sulfomethylation, and methylation reactions, all three selected treatments proved to be effective in obtaining lignins with different properties. Diverse resulting products with differentiated characteristics were obtained depending on the lignin type employed, showing distinct behaviors and final properties for each

modification. Nevertheless, some general characteristics such as reduced OH content, higher molecular weight, and enhanced thermal stability were achieved. It was interesting to observe that carboxymethylation was effective in producing stable water dispersions for organosolv lignin but it was the least efficient for Kraft lignin. Conversely, a reversed pattern was observed with methylated samples, and similar trends were noted when sulfomethylation reactions were carried out.

These modifications are believed to bring interesting properties for turning lignin into a plausible alternative material to incorporate into diverse electrochemical energy storage devices.

5.6. REFERENCES

[1] Poveda-Giraldo JA, Solarte-Toro JC, Cardona Alzate CA. The potential use of lignin as a platform product in biorefineries: A review. Renew Sustain Energy Rev 2021;138:110688. https://doi.org/10.1016/j.rser.2020.110688.

[2] Pang T, Wang G, Sun H, Sui W, Si C. Lignin fractionation: Effective strategy to reduce molecule weight dependent heterogeneity for upgraded lignin valorization. Ind Crops Prod 2021;165:113442. https://doi.org/10.1016/j.indcrop.2021.113442.

[3] Da Costa Lopes AM. Biomass Delignification with Green Solvents Towards Lignin Valorisation: Ionic Liquids vs Deep Eutectuc Solvents. Acta Innov 2021;40:64–78.

[4] Gillet S, Aguedo M, Petitjean L, Morais ARC, Da Costa Lopes AM, Łukasik RM, et al. Lignin transformations for high value applications: Towards targeted modifications using green chemistry. Green Chem 2017;19:4200–33. https://doi.org/10.1039/c7gc01479a.

[5] Sarkanen K V., Ludwig CH. Lignins: Occurrence, formation, structure and reactions. vol. 10. 1972. https://doi.org/doi:10.1002/pol.1972.110100315.

[6] Goldstein IS. Organic Chemicals from Biomass. 1st ed. 1981. https://doi.org/https://doi.org/10.1201/9781351075251.

[7] Xiang Q, Lee YY. Production of oxychemicals from precipitated hardwood lignin. Appl Biochem Biotechnol - Part A Enzym Eng Biotechnol 2001;91–93:71–80. https://doi.org/10.1385/ABAB:91-93:1-9:71.

[8] Ma R, Guo M, Zhang X. Recent advances in oxidative valorization of lignin. Catal Today 2018;302:50–60. https://doi.org/10.1016/j.cattod.2017.05.101.

[9] García DE, Delgado N, Aranda FL, Toledo MA, Cabrera-Barjas G, Sintjago EM, et al. Synthesis of maleilated polyflavonoids and lignin as functional bio-based building-blocks. Ind Crops Prod 2018;123:154–63. https://doi.org/10.1016/j.indcrop.2018.06.065.

[10] Scarica C, Suriano R, Levi M, Turri S, Griffini G. Lignin Functionalized with Succinic Anhydride as Building Block for Biobased Thermosetting Polyester Coatings. ACS Sustain Chem Eng 2018;6:3392–401. https://doi.org/10.1021/acssuschemeng.7b03583.

[11] Bian H, Jiao L, Wang R, Wang X, Zhu W, Dai H. Lignin nanoparticles as nano-spacers for tuning the viscoelasticity of cellulose nanofibril reinforced polyvinyl alcohol-borax hydrogel. Eur Polym J 2018;107:267–74. https://doi.org/10.1016/j.eurpolymj.2018.08.028.

[12] Wang D, Lee SH, Kim J, Park CB. "Waste to Wealth": Lignin as a Renewable Building Block for Energy Harvesting/Storage and Environmental Remediation. ChemSusChem 2020;13:2807–27. https://doi.org/10.1002/cssc.202000394.

[13] Peramune D, Manatunga DC, Dassanayake RS, Premalal V, Liyanage RN, Gunathilake C, et al. Recent advances in biopolymer-based advanced oxidation processes for dye removal applications: A review. Environ Res 2022;215:114242. https://doi.org/10.1016/j.envres.2022.114242.

[14] Garedew M, Lin F, Song B, DeWinter TM, Jackson JE, Saffron CM, et al. Greener Routes to Biomass Waste Valorization: Lignin Transformation Through Electrocatalysis for Renewable Chemicals and Fuels Production. ChemSusChem 2020;13:4214–37. https://doi.org/10.1002/cssc.202000987.

[15] Xie B, Tobimatsu Y, Narita K, Yokohata S, Kamitakahara H, Takano T. Electro-Oxidation of Lignin Model Compounds and Synthetic Lignin with Transition-Metal Complexes (Manganese and Iron Complexes). ACS Sustain Chem Eng

2022;10:16701–8. https://doi.org/10.1021/acssuschemeng.2c04811.

[16] Han Z, Jiang H, Xue A, Ni G, Sun Y, Tang Y, et al. H2O2 generated through ORR on cathode in a protic ionic liquid and its utilization in lignin valorization. J Electroanal Chem 2022;923:116814. https://doi.org/10.1016/j.jelechem.2022.116814.

[17] Ma W, Liu G, Wang Q, Liu J, Yuan X, Xin J, et al. Ionic liquids enhance the electrocatalysis of lignin model compounds towards generating valuable aromatic molecules. J Mol Liq 2022;367:120407. https://doi.org/10.1016/j.molliq.2022.120407.

[18] Zeng X, Yin G, Zhou Y, Zhao J. Impact of NaOH on the Hydrothermal Oxidation of Guaiacol for the Production of Value-Added Products. Energies 2022;15:8039. https://doi.org/10.3390/en15218039.

[19] Khan S, Puss KK, Lukk T, Loog M, Kikas T, Salmar S. Enzymatic Conversion of Hydrolysis Lignin—A Potential Biorefinery Approach. Energies 2023;16:1–13. https://doi.org/10.3390/en16010370.

[20] Zhou Z, Ouyang D, Liu D, Zhao X. Oxidative pretreatment of lignocellulosic biomass for enzymatic hydrolysis: Progress and challenges. Bioresour Technol 2023;367:128208. https://doi.org/10.1016/j.biortech.2022.128208.

[21] González-Rodríguez S, Lu-Chau TA, Chen X, Eibes G, Pizzi A, Feijoo G, et al. Functionalisation of organosolv lignin by enzymatic demethylation for bioadhesive formulation. Ind Crops Prod 2022;186:115253. https://doi.org/10.1016/j.indcrop.2022.115253.

[22] Morena AG, Bassegoda A, Natan M, Jacobi G, Banin E, Tzanov T. Antibacterial Properties and Mechanisms of Action of Sonoenzymatically Synthesized Lignin-Based Nanoparticles. ACS Appl Mater Interfaces 2022;14:37270–9. https://doi.org/10.1021/acsami.2c05443.

[23] Schutyser W, Renders T, Van Den Bosch S, Koelewijn SF, Beckham GT, Sels BF. Chemicals from lignin: An interplay of lignocellulose fractionation, depolymerisation, and upgrading. Chem Soc Rev 2018;47:852–908. https://doi.org/10.1039/c7cs00566k.

[24] Ma R, Guo M, Zhang X. Selective conversion of biorefinery lignin into dicarboxylic acids. ChemSusChem 2014;7:412–5. https://doi.org/10.1002/cssc.201300964.

[25] Huskinson B, Marshak MP, Suh C, Er S, Gerhardt MR, Galvin CJ, et al. A metal-free organic-inorganic aqueous flow battery. Nature 2014;505:195–8. https://doi.org/10.1038/nature12909.

[26] Hu Y, Li S, Zhao X, Wang C, Zhang X, Liu J, et al. Catalytic oxidation of native lignin to phenolic monomers: Insight into aldehydes formation and stabilization. Catal Commun 2022;172:106532. https://doi.org/10.1016/j.catcom.2022.106532.

[27] Pradhan SR, Paszkiewicz-Gawron M, Łomot D, Lisovytskiy D, Colmenares JC. Bimetallic TiO2 Nanoparticles for Lignin-Based Model Compounds Valorization by Integrating an Optocatalytic Flow-Microreactor. Molecules 2022;27:8731. https://doi.org/10.3390/molecules27248731.

[28] Sutradhar S, Alam N, Christopher LP, Fatehi P. KOH catalyzed oxidation of kraft lignin to produce green fertilizer. Catal Today 2022;404:49–62. https://doi.org/10.1016/j.cattod.2022.08.007.

[29] Shin HY, Jo SM, Kim SS. Oxidative depolymerization of kraft lignin assisted by potassium tert-butoxide and its effect on color and UV absorption. Ind Crops Prod 2022;187:115539. https://doi.org/10.1016/j.indcrop.2022.115539.

[30] Kadla JF, Chang HM, Jameel H. Reactions of lignins with high temperature hydrogen peroxide. Holzforschung 1999;53:277–84.

https://doi.org/10.1515/hf.1999.047.

[31] Ananthi A, Kumar TN, Mathiyarasu J, Joseph J, Phani KLN, Yegnaraman V. A novel potentiometric hydrogen peroxide sensor based on pKa changes of vinylphenylboronic acid membranes. Mater Lett 2011;65:3563–5. https://doi.org/10.1016/j.matlet.2011.07.087.

[32] Majeke BM, Collard FX, Tyhoda L, Görgens JF. The synergistic application of quinone reductase and lignin peroxidase for the deconstruction of industrial (technical) lignins and analysis of the degraded lignin products. Bioresour Technol 2021;319. https://doi.org/10.1016/j.biortech.2020.124152.

[33] Suslick KS, Didenko Y, Fang MM, Hyeon T, Kolbeck KJ, McNamara III WB, et al. Acoustic cavitation and its chemical consequences. Philos Trans R Soc A 1999:335–53. https://doi.org/10.1252/kakoronbunshu.39.472.

[34] Gilca IA, Popa VI, Crestini C. Obtaining lignin nanoparticles by sonication. Ultrason Sonochem 2015;23:369–75. https://doi.org/10.1016/j.ultsonch.2014.08.021.

[35] Zhang Z, Terrasson V, Guénin E. Lignin nanoparticles and their nanocomposites. Nanomaterials 2021;11:1336. https://doi.org/10.3390/nano11051336.

[36] Mishra PK, Wimmer R. Aerosol assisted self-assembly as a route to synthesize solid and hollow spherical lignin colloids and its utilization in layer by layer deposition. Ultrason Sonochem 2017;35:45–50. https://doi.org/10.1016/j.ultsonch.2016.09.001.

[37] Yang Q, Pan X. Correlation between lignin physicochemical properties and inhibition to enzymatic hydrolysis of cellulose. Biotechnol Bioeng 2016;113:1213–24. https://doi.org/10.1002/bit.25903.

[38] Sun X, Lin J, Cheng Y, Duan L, Sun X, Li X, et al. Insight into the structure and mechanical performance of high content lignin reinforced poly (vinyl

alcohol) gel-spun fibers via the regulation of esterified hydrophilic lignin composition for better sustainability. J Appl Polym Sci 2023;140:1–12. https://doi.org/10.1002/app.53577.

[39] Zhao H, Zhu Y, Zhang H, Ren H, Zhai H. UV-blocking composite films containing hydrophilized spruce kraft lignin and nanocellulose: Fabrication and performance evaluation. Int J Biol Macromol 2023;242. https://doi.org/10.1016/j.ijbiomac.2023.124946.

[40] Alwadani N, Ghavidel N, Fatehi P. Surface and interface characteristics of hydrophobic lignin derivatives in solvents and films. Colloids Surfaces A Physicochem Eng Asp 2021;609:125656. https://doi.org/10.1016/j.colsurfa.2020.125656.

[41] Tang Q, Chen Q, Zhou M, Yang D. Preparation of nano disperse dyes using sulfomethylated lignin: Effects of sulfonic group contents. Int J Biol Macromol 2023;234:123605. https://doi.org/10.1016/j.ijbiomac.2023.123605.

[42] Chen K, Qian Y, Wu S, Qiu X, Yang D, Lei L. Neutral fabrication of UV-blocking and antioxidation lignin-stabilized high internal phase emulsion encapsulates for high efficient antibacterium of natural curcumin. Food Funct 2019;10:3543–55. https://doi.org/10.1039/c9fo00320g.

[43] Brenelli LB, Mariutti LRB, Villares Portugal R, de Farias MA, Bragagnolo N, Mercadante AZ, et al. Modified lignin from sugarcane bagasse as an emulsifier in oil-in-water nanoemulsions. Ind Crops Prod 2021;167. https://doi.org/10.1016/j.indcrop.2021.113532.

[44] Yildirim-Yalcin M, Tornuk F, Toker OS. Recent advances in the improvement of carboxymethyl cellulose-based edible films. Trends Food Sci Technol 2022;129:179–93. https://doi.org/10.1016/j.tifs.2022.09.022.

[45] Pourmadadi M, Rahmani E, Shamsabadipour A, Samadi A, Esmaeili J, Arshad

R, et al. Novel carboxymethyl cellulose based nanocomposite: A promising biomaterial for biomedical applications. Process Biochem 2023;130:211–26. https://doi.org/10.1016/j.procbio.2023.03.033.

[46] Raeisi Estabragh MA, Sajadi Bami M, Dehghannoudeh G, Noudeh YD, Moghimipour E. Cellulose derivatives and natural gums as gelling agents for preparation of emulgel-based dosage forms: A brief review. Int J Biol Macromol 2023;241:124538. https://doi.org/10.1016/j.ijbiomac.2023.124538.

[47] Rahman MS, Hasan MS, Nitai AS, Nam S, Karmakar AK, Ahsan MS, et al. Recent developments of carboxymethyl cellulose. Polymers (Basel) 2021;13. https://doi.org/10.3390/polym13081345.

[48] Jimtaisong A, Saewan N. Utilization of carboxymethyl chitosan in cosmetics. Int J Cosmet Sci 2014;36:12–21. https://doi.org/10.1111/ics.12102.

[49] Mourya VK, Inamdar NN, Tiwari A. Carboxymethyl chitosan and its applications. Adv Mater Lett 2010;1:11–33. https://doi.org/10.5185/amlett.2010.3108.

[50] Konduri MK, Kong F, Fatehi P. Production of carboxymethylated lignin and its application as a dispersant. Eur Polym J 2015;70:371–83. https://doi.org/10.1016/J.EURPOLYMJ.2015.07.028.

[51] Schieppati D, Dreux A, Gao W, Fatehi P, Boffito DC. Ultrasound-assisted carboxymethylation of LignoForce Kraft lignin to produce biodispersants. J Clean Prod 2022;366:132776. https://doi.org/10.1016/j.jclepro.2022.132776.

[52] Aldajani M, Alipoormazandarani N, Fatehi P. Two-Step Modification Pathway for Inducing Lignin-Derived Dispersants and Flocculants. Waste and Biomass Valorization 2022;13:1077–88. https://doi.org/10.1007/s12649-021-01579-8.

[53] Zhang T, Zhou J, Li H, Ma J, Wang X, Shi H, et al. Stable lignin-based afterglow materials with ultralong phosphorescence lifetimes in solid-state and aqueous solution. Green Chem 2023;25:1406–16. https://doi.org/10.1039/d2gc04370j.

[54] Yu F, You Z, Ma Y, Liu H, Wang Y, Xiao Z, et al. Modification with carboxymethylation-activated alkali lignin/glutaraldehyde hybrid modifier to improve physical and mechanical properties of fast-growing wood. Wood Sci Technol 2023;57:583–603. https://doi.org/10.1007/s00226-023-01465-7.

[55] Du B, Chai L, Zheng Q, Liu Y, Wang X, Chen X, et al. Designed synthesis of multifunctional lignin-based adsorbent for efficient heavy metal ions removal and electromagnetic wave absorption. Int J Biol Macromol 2023;234:123668. https://doi.org/10.1016/j.ijbiomac.2023.123668.

[56] Ding Z, Qiu X, Fang Z, Yang D. Effect of Molecular Weight on the Reactivity and Dispersibility of Sulfomethylated Alkali Lignin Modified by Horseradish Peroxidase. ACS Sustain Chem Eng 2018;6:14197–202. https://doi.org/10.1021/acssuschemeng.8b02826.

[57] Hopa DY, Fatehi P. Using sulfobutylated and sulfomethylated lignin as dispersant for kaolin suspension. Polymers (Basel) 2020;12:11–4. https://doi.org/10.3390/POLYM12092046.

[58] Zhang B, Yang D, Wang H, Qian Y, Huang J, Yu L, et al. Activation of Enzymatic Hydrolysis Lignin by NaOH/Urea Aqueous Solution for Enhancing Its Sulfomethylation Reactivity. ACS Sustain Chem Eng 2019;7:1120–8. https://doi.org/10.1021/acssuschemeng.8b04781.

[59] Yang R, Tang Q, Qian Y, Pang Y, Yang D, Zheng D, et al. Preparation of sulfomethylated lignin grafted by pyrrolidone for utilization as a dispersant in nano pigment paste. Ceram Int 2023;49:16578–86. https://doi.org/10.1016/j.ceramint.2023.02.015.

[60] Jiao GJ, Ma J, Li Y, Jin D, Zhou J, Sun R. Removed heavy metal ions from wastewater reuse for chemiluminescence: Successive application of lignin-based composite hydrogels. J Hazard Mater 2022;421:126722. https://doi.org/10.1016/j.jhazmat.2021.126722.

[61] Sen S, Patil S, Argyropoulos DS. Methylation of softwood kraft lignin with dimethyl carbonate. Green Chem 2015;17:1077–87. https://doi.org/10.1039/C4GC01759E.

[62] Lee JH, Kim TM, Choi IG, Choi JW. Phenolic hydroxyl groups in the lignin polymer affect the formation of lignin nanoparticles. Nanomaterials 2021;11:1–13. https://doi.org/10.3390/nano11071790.

[63] Xi Y, Yang D, Liu W, Qin Y, Qiu X. Preparation of porous lignin-derived carbon/carbon nanotube composites by hydrophobic self-assembly and carbonization to enhance lithium storage capacity. Electrochim Acta 2019;303:1–8. https://doi.org/10.1016/j.electacta.2019.01.094.

[64] Kristensen SB, van Mourik T, Pedersen TB, Sørensen JL, Muff J. Simulation of electrochemical properties of naturally occurring quinones. Sci Rep 2020;10:1–10. https://doi.org/10.1038/s41598-020-70522-z.

[65] Khetan A. High-Throughput Virtual Screening of Quinones for Aqueous Redox Flow Batteries: Status and Perspectives. Batteries 2023;9:24. https://doi.org/10.3390/batteries9010024.

[66] Sun T, Zhang W, Nian Q, Tao Z. Molecular Engineering Design for High-Performance Aqueous Zinc-Organic Battery. Nano-Micro Lett 2023;15:1–14. https://doi.org/10.1007/s40820-022-01009-x.

[67] Ding Y, Xie L, Zhang Y, Chen X, Niu Y, Xu J, et al. Carbon quantum dots modified small molecular quinone salt as cathode materials for sodium-ion batteries. J Electroanal Chem 2023;928:117054. https://doi.org/10.1016/j.jelechem.2022.117054.

[68] Adamcyk J, Beisl S, Amini S, Jung T, Zikeli F, Labidi J, et al. Production and properties of lignin nanoparticles from ethanol organosolv liquors-influence of origin and pretreatment conditions. Polymers (Basel) 2021;13:1–13. https://doi.org/10.3390/polym13030384.

[69] Beisl S, Friedl A, Miltner A. Lignin from micro- To nanosize: Applications. Int J Mol Sci 2017;18:2367. https://doi.org/10.3390/ijms18112367.

[70] Chen Y, Zheng K, Niu L, Zhang Y, Liu Y, Wang C, et al. Highly mechanical properties nanocomposite hydrogels with biorenewable lignin nanoparticles. Int J Biol Macromol 2019;128:414–20. https://doi.org/10.1016/j.ijbiomac.2019.01.099.

[71] Yang D, Wu X, Qiu X, Chang Y, Lou H. Polymerization reactivity of sulfomethylated alkali lignin modified with horseradish peroxidase. Bioresour Technol 2014;155:418–21. https://doi.org/10.1016/J.BIORTECH.2013.12.017.

[72] Witzler M, Alzagameem A, Bergs M, Khaldi-Hansen B El, Klein SE, Hielscher D, et al. Lignin-derived biomaterials for drug release and tissue engineering. Molecules 2018;23:1–22. https://doi.org/10.3390/molecules23081885.

[73] Gupta AK, Mohanty S, Nayak SK. Synthesis, Characterization and Application of Lignin Nanoparticles (LNPs). Mater Focus 2015;3:444–54. https://doi.org/10.1166/mat.2014.1217.

[74] Ma R, Guo M, Zhang X. Recent advances in oxidative valorization of lignin. Catal Today 2018;302:50–60. https://doi.org/10.1016/j.cattod.2017.05.101.

[75] Gellerstedt G, Agnemo R, Gellerstedt G. The reactions of lignin with alkaline hydrogen peroxide, Part II. Acta Chem Scand 1980:337–42.

[76] Antonino LD, Gouveia JR, de Sousa Júnior RR, Garcia GES, Gobbo LC, Tavares LB, et al. Reactivity of aliphatic and phenolic hydroxyl groups in kraft lignin

towards 4,4′ mdi. Molecules 2021;26:1–12. https://doi.org/10.3390/molecules26082131.

[77] Ramakoti B, Dhanagopal H, Deepa K, Rajesh M, Ramaswamy S, Tamilarasan K. Solvent fractionation of organosolv lignin to improve lignin homogeneity: Structural characterization. Bioresour Technol Reports 2019;7:100293. https://doi.org/10.1016/j.biteb.2019.100293.

[78] Izaguirre N, Robles E, Llano-Ponte R, Labidi J, Erdocia X. Fine-tune of lignin properties by its fractionation with a sequential organic solvent extraction. Ind Crops Prod 2022;175:114251. https://doi.org/10.1016/j.indcrop.2021.114251.

[79] Rawle A. The importance of particle sizing to the coatings industry Part 1 : Particle size measurement. Adv Colour Sci Technol 2002;5:1–12.

[80] Liu ZH, Hao N, Shinde S, Olson ML, Bhagia S, Dunlap JR, et al. Codesign of Combinatorial Organosolv Pretreatment (COP) and Lignin Nanoparticles (LNPs) in Biorefineries. ACS Sustain Chem Eng 2019;7:2634–47. https://doi.org/10.1021/acssuschemeng.8b05715.

[81] Österberg M, Sipponen MH, Mattos BD, Rojas OJ. Spherical lignin particles: A review on their sustainability and applications. Green Chem 2020;22:2712–33. https://doi.org/10.1039/d0gc00096e.

[82] Hulsmans A, Joris K, Lambert N, Rediers H, Declerck P, Delaedt Y, et al. Evaluation of process parameters of ultrasonic treatment of bacterial suspensions in a pilot scale water disinfection system. Ultrason Sonochem 2010;17:1004–9. https://doi.org/10.1016/j.ultsonch.2009.10.013.

[83] Zeng J, Zhang D, Liu W, Huang J, Yang D, Qiu X, et al. Preparation of carboxymethylated lignin-based multifunctional flocculant and its application for copper-containing wastewater. Eur Polym J 2022;164:110967. https://doi.org/10.1016/j.eurpolymj.2021.110967.

[84] Chen K, Lei L, Lou H, Niu J, Yang D, Qiu X, et al. High internal phase emulsions stabilized with carboxymethylated lignin for encapsulation and protection of environmental sensitive natural extract. Int J Biol Macromol 2020;158:430–42. https://doi.org/10.1016/j.ijbiomac.2020.04.106.

[85] Holtman KM, Chang H, Jameel H. Quantitative 13 C NMR Characterization of Milled Wood Lignins Isolated by Different Milling Techniques Quantitative 13 C NMR Characterization of Milled Wood Lignins Isolated by Different Milling Techniques 2006. https://doi.org/10.1080/02773810600582152.

[86] Chen CL, Robert D. Characterization of lignin by 1H and 13C NMR spectroscopy. Methods Enzymol 1988;161:137–74. https://doi.org/10.1016/0076-6879(88)61017-2.

6. LIGNIN-CARBON COMPOSITES

6.1. MOTIVATION

Recent efforts for the transition to more sustainable energy sources like wind or solar energy create an urge to also focus on obtaining not only green materials but also improved performances. Lithium-ion batteries (LIBs) along with supercapacitors (SCs) are considered to be key devices for the transition to more sustainable practices, and carbon materials fulfill sustainability requirements like abundance, low cost, high energy density, and long cycle life [1].

Lignin-based electrode materials are gaining interest due to their sustainability and high availability. Most of the works of lignin incorporation into batteries are based on its conversion into carbon materials and substitution of the currently used non-renewable fossil-based carbons [2]. Lignin is a promising candidate for its high carbon content and unique aromatic nature. Moreover, by modulating its structure, different carbon materials can be obtained and diverse needs for different types of batteries can be fulfilled. Porous carbons derived from lignin have been fabricated as active materials of electrodes [3]. Lignin-derived carbons have also been used as active materials for SCs [4], and different activation processes have been explored such as, carbonization and combinations with polymers like polyacrylonitrile (PAN) or different metal oxides [5]. While previous research in this domain has primarily centered around the production of carbonaceous materials derived from lignin, there is a growing interest in exploring novel approaches that utilize non-carbonized lignin as an additive or component in composites. This shift in focus is driven by the desire for less energy-intensive processes, opening new perspectives for using the potential of lignin in energy storage applications [6].

Composite or hybrid materials combining other carbonaceous materials or conducting polymers with lignin for enhanced properties have been

produced and studied in many research works. Depending on their targeted application, different properties are needed. Nevertheless, one common characteristic of enhanced properties of carbon materials is their specific surface area (SSA). The porosity is a key factor for the battery performance, as it eases the diffusion kinetics and strengthens the conductivity network of the conductive ions [7]. Activated carbon (AC) is a commonly used material for this reason, but different methodologies have been carried out to increase the SSA and pore size distribution (PSD), for a further enhanced specific capacitance. AC is used for many different applications, ranging from adsorbents to Energy Storage (ES) devices, all needing high SSA for better performance. It is also relatively inexpensive, stable, and easily processable. Several methods have been carried out to increase the SSA of AC. The most widely spread is the treatment with HNO_3. This treatment not only increases the porosity of the surface of the material but also increases the oxygen-containing functional groups, subsequently enhancing its performance [8–10]. Although the SSA plays an important role in the improvement of the capacity, it does not necessarily mean that all the pores will be electrochemically accessible in contact with the electrolyte. Indeed, the type of pore plays an important role, since mesopores (2-50 nm wide pores) can absorb more and larger ions than micropores (<2 nm wide pores) [11]. Nevertheless, micropore-sized carbon SCs have been proven to contribute to charge storage by absorbing electrolyte ions bigger than the pores of the carbon [12].

Another approach for enhanced carbon SCs is the fabrication of hybrid materials or composites. Double-layer (DL) carbon materials have been combined with pseudocapacitance materials to expand their capacitance with the addition of Faradaic processes happening on the redox groups of the materials [13]. A sustainable approach to the synthesis of hybrid materials is the incorporation of lignin into AC materials. Lignin is the

second most abundant polymer on earth and is considered a plausible substitute for many materials, such as ES device materials. It is regarded to be a pseudocapacitance material due to the hydroquinone/quinone moieties present in its molecules. Combining these lignin properties with the non-Faradaic processes happening in AC, more sustainable materials with enhanced capacitance can be obtained. Therefore another current target in the development of novel ES device materials is achieved by using inexpensive, abundant, and efficient materials for the change to more sustainable practices and energy [14].

From the different ES devices in the market and under development, SCs have gained significance in the last decades [15]. SCs, along with LIBs, are among the most promising devices for the energy transition [16]. They are usually used in cases where high currents are needed, but they have low capacitance, and therefore, can only be used for short times. SCs have a greater capacity than other devices and can also be recharged without damage, filling the gap between capacitors and conventional batteries [17].

SC electrodes are mainly based on carbonaceous materials that possess high surface area and appropriate pore-size distribution for the necessary capacitance. Many works are focusing on the development of novel materials with enhanced properties for this application, due to the estimated high demand [18]. Like in the case of batteries, lignocellulosic materials, especially lignin, are making their way to be considered as a feasible alternative. Lignin-derived carbons have been used as active materials for SCs [4,19], and studies focusing on different activation processes have been carried out, along with carbonization and combinations with polymers like PAN or different metal oxides [5].

Alternatively to SCs, LIBs are the main devices used and are expected to grow in demand as power resources in transport and consumer electronics

increase. Since the high energy density and power energy present in this type of battery have been unmatched so far, LIBs have been the focus of development for increased capacity materials [20].

Graphite (G) is widely employed as cathode and anode material in LIBs. While for cathode materials a more varied material range has been employed, graphite reaches up to 98% of the LIB anode material market. This is due to the low cost, abundance, high energy density, and long life cycles [21]. However, due to the high demand expected, numerous works to enhance the already interesting graphite properties are thoroughly encouraged. Graphite is formed by graphene layers linked by van der Waals forces. These interactions are weak and therefore, different ions can easily be intercalated in the interlayers [1]. Numerous studies have been published on the synthesis of graphene, some of them specifically emphasizing the exfoliation of oxidized graphite (GO) using ultrasound (US) forces [22–25].

The obtaining of graphene oxide composites or hybrid materials to get materials with better performance has been explored. For instance, magnetite nanoparticles were installed on graphene oxide for enhanced adsorption of heavy metal ions [26] and SnO_2 nanoparticles were loaded in GO for better capacitance as anode materials in LIBs [27]. These works are based on the same principle, which implies the utilization of US forces not only to insert new particles with diverse functionalities but also to exfoliate the GO to obtain at least partially separated sheets (graphene oxide sheets). Recently, more sustainable alternatives have been explored, based on the implementation of renewable materials like lignin [28].

Several works have been carried out to enhance the performance of graphitic materials by the incorporation of lignin molecules or lignin-derived molecules. For instance, lignosulfonates (LS) have been extensively studied as an alternative or combining material for energy storage materials.

Liu et al. 2019 [29] combined LS with graphite by ball milling and centrifugation to obtain a hybrid material that was posteriorly used as an electrode. Similarly, reduced GO was combined with lignin in a solution and mixed at 60 °C for 12 h [30]. Additionally, lignin-graphite hydrogels and aerogels were produced, both with LS [31] and alkali lignin (AL) [32] to use as electrodes in SCs. Alternatively, synthetically polymerized lignin, using lignin-derived aromatic monomers, has been combined with GO for a higher specific capacitance [33].

Like the SnO_2-graphene oxide [27] or magnetite-graphene oxide composites [26], AL has alternatively been used as an exfoliating agent for graphene obtaining. Since the graphene market is more varied and with higher value, more sustainable procedures for graphene production have been considered to substitute the traditionally used chemical vapor deposition (CVD), expensive and complex [34]. Therefore, the production of graphene from graphite through exfoliation is gaining interest as an alternative pathway. Thermal exfoliation exposes the GO precursor to high temperatures (around 550 °C), decomposing the oxygen groups and breaking the Van der Waals forces [35]. However, the high energy demands due to the high temperatures needed still require better alternatives like vacuum exfoliation, which reduces the required temperature to 200 °C, electrochemical exfoliation, or liquid-phase exfoliation (LPE). This last method is gaining interest due to its low cost, scalability, and eco-friendliness [36]. US forces are used to introduce other particles as defects, disrupting sp^2 bonds of the GO and altering the physical properties until the sheets get separated and graphene is obtained [28]. Depending on the severity of the process, totally or partially exfoliated graphene sheets or blocks can be obtained. During this process, the addition of other compounds to the solution can facilitate intercalation, leading to the formation of hybrid materials that possess not only exfoliated

characteristics but also modified properties. Applications for these materials can range from oil-water separation [37], adhesives [38], heterogeneous electrochemical biosensors [39], and different battery materials [40–42].

6.2. OBJECTIVES

The lignins employed in all the already published works for the development of ES materials are LS, or alternatively Kraft lignins. However, keeping in mind the utilization and implementation of green processes to obtain more ecological materials, the organosolv method is the most sustainable lignin isolation process. It promotes an integral biorefinery product valorization, whereas LS, although being water soluble and interesting due to its convenient properties for its incorporation in different processes, is obtained from an obsolete procedure [43]. Nevertheless, no work implementing OL can be found in the literature to the best of our knowledge. Therefore, a novel approach to implementing OL into AC and comparing the analog materials with KL has been carried out. Figure 6.1 shows the procedure followed for the obtaining of the lignin-activated carbon (L-AC) hybrid materials.

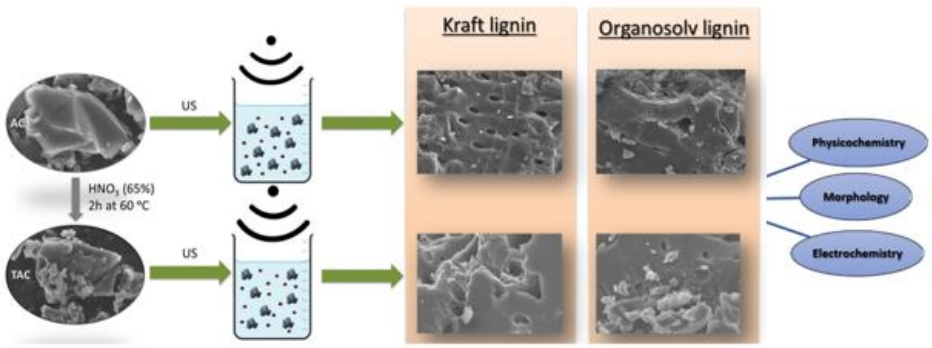

Figure 6.1. Graphical abstract of the procedure followed for the obtaining and characterization of L-AC hybrid materials.

Alternatively, partially exfoliated graphene blocks with intercalated lignin particles (L-G) were synthesized (both with KL and OL), obtained by ultrasonic-assisted liquid phase exfoliation (UALPE), shown in Figure 6.2.

The chemical and electrochemical characterization of the hybrid materials obtained with AC and G were carried out to assess the effectiveness of the treatment with the lignins and the carbon materials, verify their presence in the hybrid materials synthesized, and observe an enhanced electrochemical performance.

This study aims to fill the existing research gap by examining the specific roles and effects of these lignin variants in the context of hybrid material development and their subsequent implications on electrochemical performance.

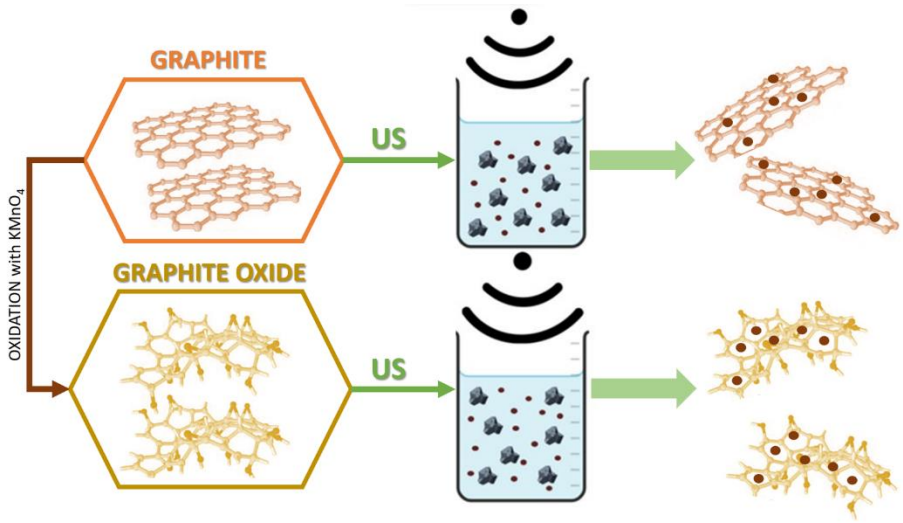

Figure 6.2. Graphical abstract of the procedure followed for the obtaining and characterization of L-G hybrid materials.

6.3. METHODOLOGY

6.3.1. TREATMENT OF ACTIVE CARBON AND GRAPHITE

The treatment of activated carbon followed was the one stated by Zhou et al. 2019 [44]. Firstly, AC was milled, and then concentrated HNO_3 (65%) was added until a 1 g/L concentration solution was obtained. The solution was heated to 80 °C and stirred at 200 rpm for 2 h. Once the reaction was finished, the product was filtered and washed under vacuum using distilled water and a 0.22 μm pore diameter nylon filter. The obtained washed product, treated active carbon (TAC), was dried overnight in an oven at 60 °C.

Graphite powder was oxidized following the procedure by Hummers et al. 1958 [45] with slight modifications [45]. Briefly, 1 g of graphite, 0.5 g of $NaNO_3$, and 23 mL of 66° H_2SO_4 were added to an ice bath under vigorous agitation. 3 g of $KMnO_4$ were added slowly, without exceeding 20 °C. The ice bath was removed, and the temperature was increased to 35 °C for 30 minutes. 46 mL of H_2O were added, and the solution was treated with 3% H_2O_2 until an intense yellow color was achieved. The suspension was filtered and washed 3 times with a total of 140 mL of water. The product, GO, was dispersed to about 5% concentration and centrifuged and dried at 60 °C overnight.

6.3.2. PREPARATION OF LIGNIN-ACTIVE CARBON AND LIGNIN-GRAPHITE COMPOSITES

The surface deposition of KL and OL onto AC, TAC, G, and GO was carried out following the procedure described by Zhou et al. (2019) [14]. Briefly, 200 mg of lignin (KL or OL) and 20 mg of AC, TAC, G, or GO were added to a 40 mL acetone/H_2O solution (7:3 v/v), combining the materials appropriately

to obtain the following combinations: AC-KL, AC-OL, TAC-KL, and TAC-OL, and G-KL, G-OL, GO-KL, and GO-OL. The solutions were treated in an ultrasound water bath for 15 min. The products were centrifuged before filtering and washed with another 40 mL of the previously mentioned acetone/water solution. The filtrate was further sonicated for another 15 minutes before centrifuging and filtering again. The solid product was dried overnight in an oven at 60 °C.

6.3.3. Physicochemical and morphological characterization

Physicochemical characterization methods like FTIR, EA and XPS were employed, along with AFM and SEM microscopies and BET method for the morphological properties determination, and DLS for particle stability measurements. The methodologies followed are explained in Annex I.

6.3.4. Electrochemical characterization

Electrochemical measurements to determine the performance were carried out using the three-electrode glass cell configuration. Cyclic Voltammetry (CV), Electrochemical Impedance Spectroscopy (EIS) and Galvanostatic Charge Discharge (GCD) measurements were performed with the parameters set at the values stated in Annex I, and polarization processes, specific capacitance values, and information about porosity were obtained.

6.4. Results

6.4.1. Physicochemical characterization

FTIR spectra were recorded for the verification of the HNO_3 treatment of activated carbon and the deposition of the lignins on the surfaces of the carbons. Figure 6.3 shows the spectra of AC and TAC, as well as the

composites obtained (AC-KL, AC-OL, TAC-KL, and TAC-OL) and the lignins (KL and OL).

From the spectra, an increment on the intensity can be observed from AC to TAC in the bands in 1700 and 1100 cm^{-1}, wavelengths attributed to C=O stretching and C-N stretching respectively, verifying the oxidation reaction and functionalization of the carbon surface with O and N. This was due to the treatment with concentrated HNO_3, which is a strong oxidizing agent that reacts with carbon yielding oxidized carbon, with different structure and properties. The main functional groups are the carboxyl (-COOH), carbonyl (-C=O) and nitro ($-NO_2$) groups, whose associated bands were observed to have increased in the FTIR analysis [46].

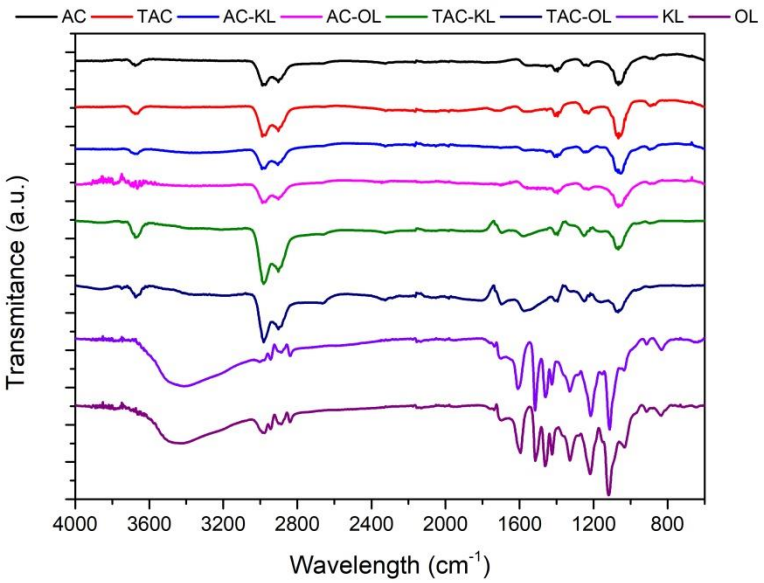

Figure 6.3. FTIR spectra of lignin-active carbon composites.

The characteristic bands of the lignins (KL and OL) and both carbons (AC and TAC), as well as their combination of bands at AC-KL, AC-OL, TAC-KL, and TAC-OL, corroborate that the treatment of the carbon enhances the

deposition of further molecules, in this case lignin, since the characteristic bands attributed to lignin are more intense in TAC-KL and TAC-OL than in AC-KL and AC-OL: O-H stretching band at 3400 cm^{-1}, C=O stretching at 1700 cm^{-1}, COO^- stretching at 1620 cm^{-1}, and C-O-C stretching at 1200 cm^{-1} [14,47,48]. It can be concluded that the spectra verify both the oxidation of activated carbon by the reaction with HNO_3 and the insertion of lignin particles onto the surface of the carbon by US treatment due the increment of the bands associated with lignin in the composite spectra.

Figure 6.4 shows the FTIR spectra obtained for G, its oxidized analog, GO, and the hybrid materials obtained when treated with KL and OL (G-KL, G-OL, GO-KL, and GO-OL). The oxidation reaction can be confirmed by observing a significant increase in the intensity of the main bands associated with oxidant functional groups from pristine graphite to graphene oxide, at 3400 cm^{-1} and 1700 cm^{-1}. Moreover, it was confirmed that the oxidation of graphite promoted the further deposition of both KL and OL particles, due to the more intense bands associated with the mentioned compounds.

Nevertheless, the mechanism by which the lignin particles attach to G or GO is presumed to be different. This difference is primarily shown by the band intensity fluctuations attributed to O-H stretching vibrations. Knowing this, the mechanism of the interaction can also be deduced. When lignin particles are introduced in the GO dispersion solution, functional groups present in KL and OL tend to interact with the OH groups of the GO, creating chemical bonds. Since G does not contain OH groups, the interactions created with the lignins are primarily based on physical interactions, promoted by the US treatment, which are considerably weaker than the chemical bonds created with the GO. Alternatively, the oxidation reaction highly increased the content of OH groups in GO particles, enabling further interactions with lignin particles, both by the previously mentioned physical, and new chemical interactions. This promotes further lignin content in GO-KL and

GO-OL samples, compared to G-KL and G-OL, with more intense bands at 2900 cm^{-1}, attributed to methyl and methylene C-H stretching vibrations, and different aromatic skeletal vibrations belonging to the lignins in the range of 1000-1600 cm^{-1}.

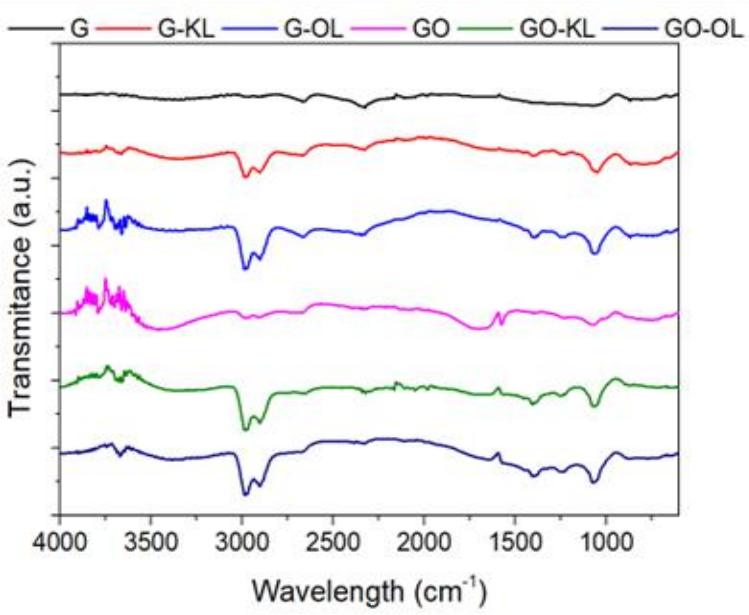

Figure 6.4. FTIR spectra of lignin-graphite composites.

Results obtained from the EA technique for the L-AC composites are shown in Figure 6.5. The main elements composing these materials were quantified (C, H, N, S, and O) and used for oxidation treatment and lignin deposition verification. It can be observed that AC is composed mainly of C, with almost 90% of the total composition, followed by O, with a little over 10% of the total composition. The other elements found (N, H and S) were minor. After the treatment of HNO_3, it can be seen that oxygen content considerably increased to over 30% of the total composition, results that match with the ones obtained in other works [49].

N content also increased, due to the insertion of N functional groups into the surface, as verified by FTIR spectra. With the deposition of KL and OL into the AC surface, some other changes in the composition can also be observed. In the case of AC-KL, sulfur content considerably increased, due to the sulfur functional groups present in KL, resulting from the lignin isolation process carried out in the industry. H content also showed a slight increase, although it was less noticeable, considering lignin's predominantly carbonaceous composition. Lignin, however, had a higher H content than AC in comparison. A similar trend can be observed with OL, but without the increase in S content, as the isolation of organosolv lignin does not imply the use of sulfur compounds. The insertion of KL and OL into the TAC particles, however, did not show a significant difference, since the C, O, and N content maintained relatively similar. Nevertheless, the overall change of the composites' composition were also verified by EA.

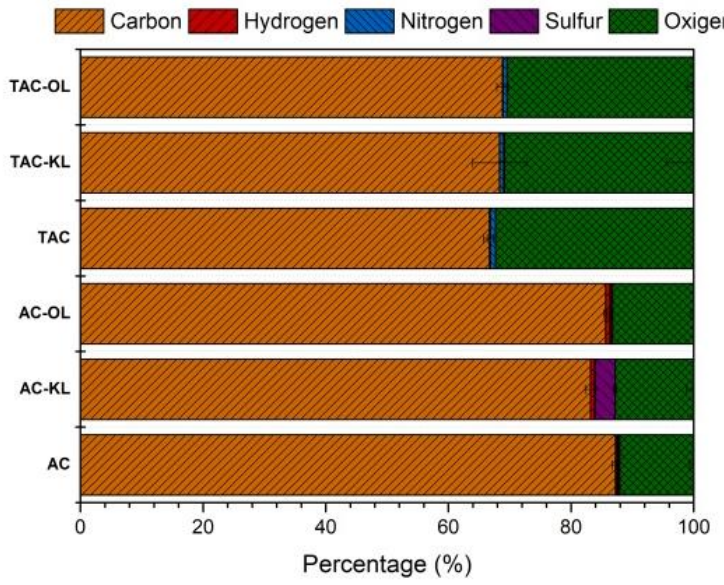

Figure 6.5. Elemental composition of the L-AC composites.

Figure 6.6. shows the EA results obtained for L-G hybrid materials, which also validate the effectiveness of the treatments. From one side, the oxidation reaction greatly increased the oxygen content of the graphite, starting from 100% C in G to almost 30% O content in GO, with an additional 3% of S obtained as a residue from the reaction with H_2SO_4. The addition of KL into G increased the O content, while for the GO-KL sample, the O content did not fluctuate, as GO and KL had similar oxygen contents. With the addition of OL, nevertheless, the O content did not significantly increase. G-OL maintained a similar composition to G, while GO-OL decreased a little on the O composition compared to GO. This might be due to the fewer amounts of oxygen groups in OL compared to KL, as it is a lignin with higher molecular weight, and therefore, less OH content.

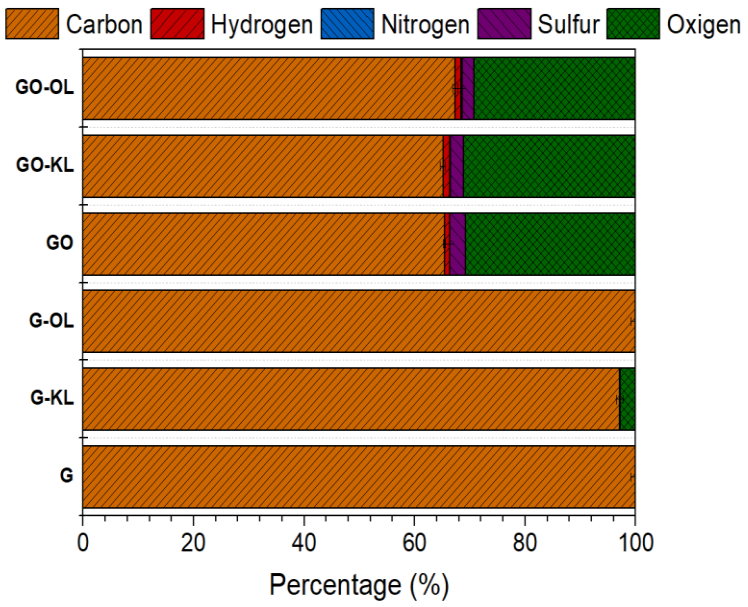

Figure 6.6. Elemental composition of the L-G hybrid materials.

Quantitative XPS analysis was carried out to verify the results obtained for the L-AC samples from FTIR and EA, as well as to observe the different linkages present in the surface of the samples. Table 6.1 shows the atomic

composition of the selected samples, while Figure 6.7 depicts the XPS surveys. It can be observed that AC was mainly composed of C atoms, a proportion that diminished after acid treatment and further decreased with lignin deposition. C content decreased from 88.2% to 78.8% and 67.6% respectively, almost proportionally increasing the O content. Although the results are in concordance with the ones obtained in EA, a higher proportion of O was obtained with XPS. This is due to the higher amount of lignin present in the surface, as analyzed by XPS, rather than the whole sample, which was analyzed by EA.

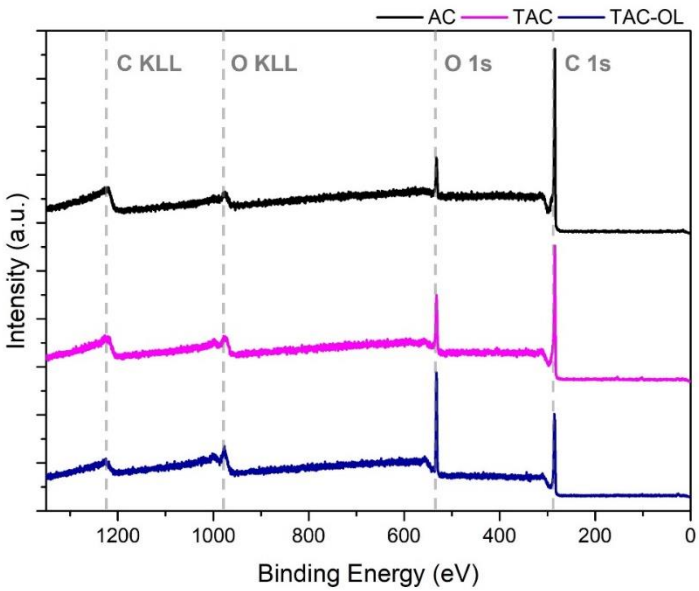

Figure 6.7. XPS of the selected samples (AC, TAC and TAC-OL).

In terms of the differences in linkages, C 1s and O 1s linkages are depicted and deconvoluted in Figures 6.8 and 6.9. As a consequence of the reduced C content, the intensity of the C 1s peak decreased throughout the process. The peak attributed to the O-C=O linkage at 288 eV remained similar in all samples. However, the presence of the C-O-C linkage (at 286 eV) increased

with the acid-treatment and the subsequent OL deposition, reaching proportions similar to those of C-C (at 284 eV) and C-O-C linkages [50].

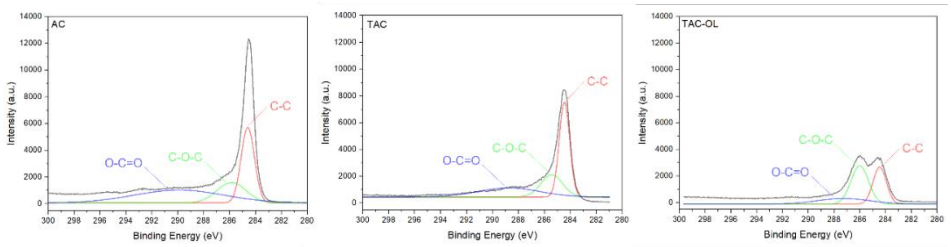

Figure 6.8. XPS high-resolution scan of C1s orbital for the samples AC, TAC and TAC-OL, with peak-deconvolution.

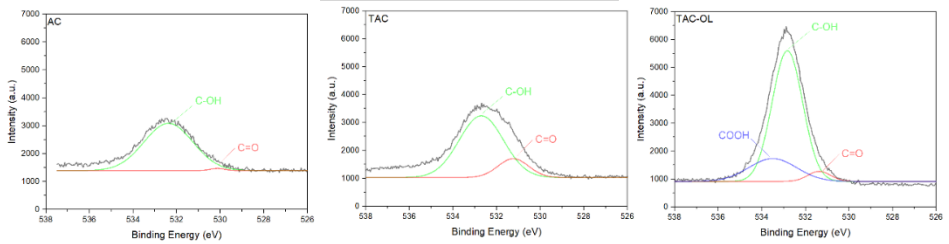

Figure 6.9. XPS high-resolution scan of O1s orbital for the samples AC, TAC and TAC-OL, with peak-deconvolution.

On the other hand, the O 1s spectra shown in Figure 6.9 showed a corresponding increase in intensity due to its higher presence. AC sample displayed an O 1s peak that belonged almost completely to the C-OH linkage at 533 eV, with a minimum presence of C=O at 530 eV. Both of these peaks increased their intensity in TAC, particularly with a more considerable presence of C=O. However, upon the incorporation of OL, this functional group slightly decreased, probably due to new linkages formed between TAC and OL, leading to a vast increase in C-OH linkage. This presence more than doubled compared to the initial AC sample. Additionally, the incorporation of the new COOH linkage at 534 eV occurred [36]. These two linkages are very common in lignin molecules, which confirms the successful deposition of lignin on TAC surface.

Table 6.1. The chemical composition (atomic %) of the surface of the selected samples (AC, TAC and TAC-OL) measured by quantitative XPS.

Sample	*C (%)*	*O (%)*	*N* (%)*	*Si* (%)*
AC	*88.2*	*11.3*		*0.5*
TAC	*78.8*	*19.5*	*0.8*	*0.8*
TAC-OL	*67.6*	*31.9*		*0.6*

*Estimated value, near-noise spectra

6.4.2. MORPHOLOGICAL CHARACTERIZATION

The adsorption isotherms obtained at the very low relative pressures were recorded and shown in Figure 6.10. The results revealed that the N_2 adsorption at the lowest P/P_o happened at the smallest pores. The higher value of adsorption indicated that the surface of the sample had more pores, suggesting that the specific surface area was higher. It can be observed that the treatments were effective on increasing the SSA, as the values increased from 839.6794 m^2/g for the AC sample, to 969.9886 m^2/g for the TAC treated with HNO_3 and further to 1103.6504 m^2/g for TAC-OL.

Z potential (mV) and particle size (nm) of the L-AC samples are shown in Figure 6.11. Dispersions of 0.5 wt% were prepared, and the pH varied from 2 to 10. Values were recorded at every pH interval. Z potential is related to the surface charge of the molecules. The higher the ZP value a molecule has (both positive and negative) the more stable it is. Moreover, pH also affects particle size. Depending on the medium of the solvent (acidic or basic), the functional groups of the particle's surface may or may not interact with the solvent or ion within, creating bigger or smaller particle suspensions. Z potential values higher than 30 mV (or lower than -30mV) are considered to show incipient stability (shown in blue in Figure 6.11). Values higher than 40 mV are considered to have good stability (shown in green in Figure 6.11). From the results obtained, higher pH values enhanced the stability of the

particles, and when the pH value reached 2, the ZP values of all samples decreased to almost 0 mV, and the particles precipitated. AC particles were the most unstable, having a low ZP in all the pH ranges. When reacted with HNO_3 (TAC) stability improved considerably, probably due to the addition of functional groups that interact with H_2O molecules. However, the particle size also increased drastically. This might be due to the interactions that happened among the functional groups of TAC and with the medium. Carbon particles stabilized even further with the deposition of lignin, especially with OL. Apart from being the most stable, AC-OL and TAC-OL were the smallest in size, followed by AC-KL and TAC-KL, which were slightly bigger. Finally, TAC particles were the biggest ones at high pHs, due to intermolecular interactions created with the solvent, but decreased to around 1000 nm when precipitated at pH 2.

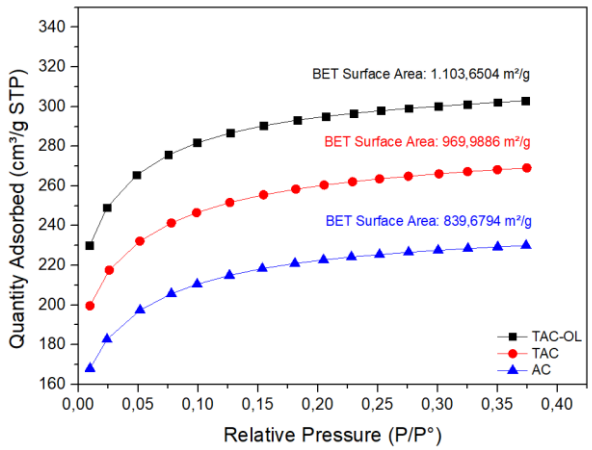

Figure 6.10. Low pressure nitrogen adsorption isotherms of the selected samples (AC, TAC and TAC-OL).

This technique was not carried out in the case of the graphite samples, because of the shape graphite particles have. Since they are not round, the values obtained with DLS would not be significant.

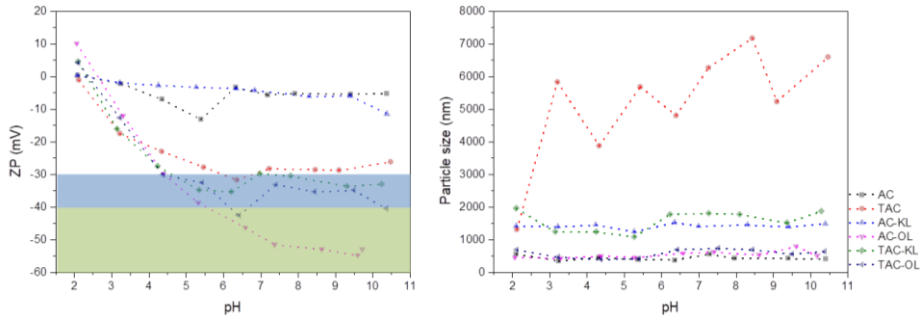

Figure 6.11. Z Potential and particle size values for different pH values.

To understand the morphological properties of the samples, AFM microscopy experiments were carried out. Images of 500x500 nm were recorded and shown in Figures 6.12 and 6.13. Differences in the surfaces of the samples could be observed along with the modifications on the surface due to the treatment and lignin deposition. AC already had a porous surface, where lignin particles deposited after the treatment with US forces. With the HNO_3 treatment, however, a variation on the surface could also be observed, where the porous structure was maintained with considerably smaller pores and an increment in the roughness.

These surface properties and the higher functionalization enabled a further deposition of the lignins, verifying the higher quantity of lignin particles in TAC molecule surfaces observed in AFM analysis. In terms of the difference between KL and OL, KL seemed to be more efficient, since a rougher surface appeared to be obtained. This probably was related to the fact that KL molecules were smaller in size and weight and were more functionalized with OH groups than OL, which had a much milder extraction procedure, and therefore, bigger molecules were obtained, hindering their ability to deposit on the pores and react with the active sites.

In the case of L-G hybrid materials, AFM imaging was also used for the particle size determination. The obtained AFM images are shown in

Figure 6.13. Moreover, the profile of different sections of the samples was measured and plotted in Figure 6.14, and the height values obtained are listed in Table 6.2. Therefore, the exfoliation degree was determined.

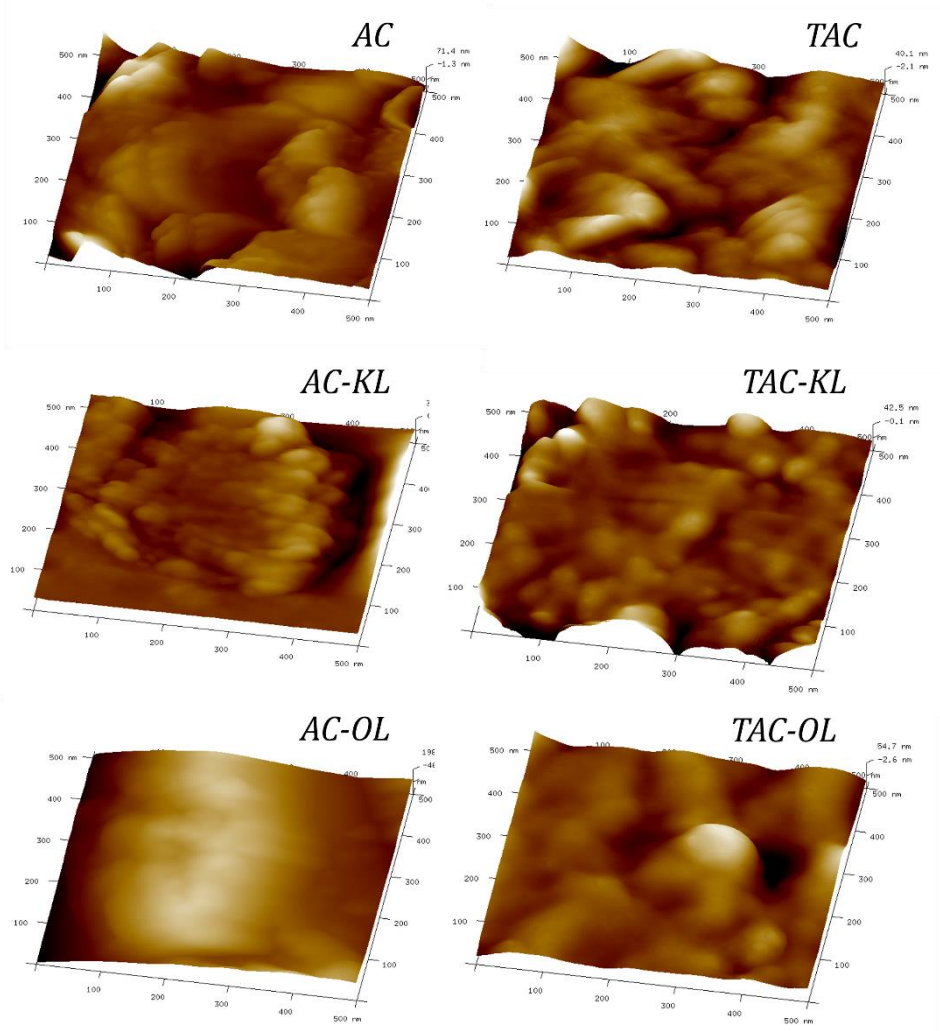

Figure 6.12. AFM images for the lignin-active carbon composites.

In the case of L-G hybrid materials, AFM imaging was also used for the particle size determination. The obtained AFM images are shown in Figure 6.13. Moreover, the profile of different sections of the samples was

measured and plotted in Figure 6.14, and the height values obtained are listed in Table 6.2. Therefore, the exfoliation degree was determined.

US forces have been reported to promote the exfoliation of graphite oxide and the subsequent obtaining of graphene. Recently more sustainable practices have considered the addition of lignin as an exfoliating agent to create more efficient and environmentally friendly graphene production [28].

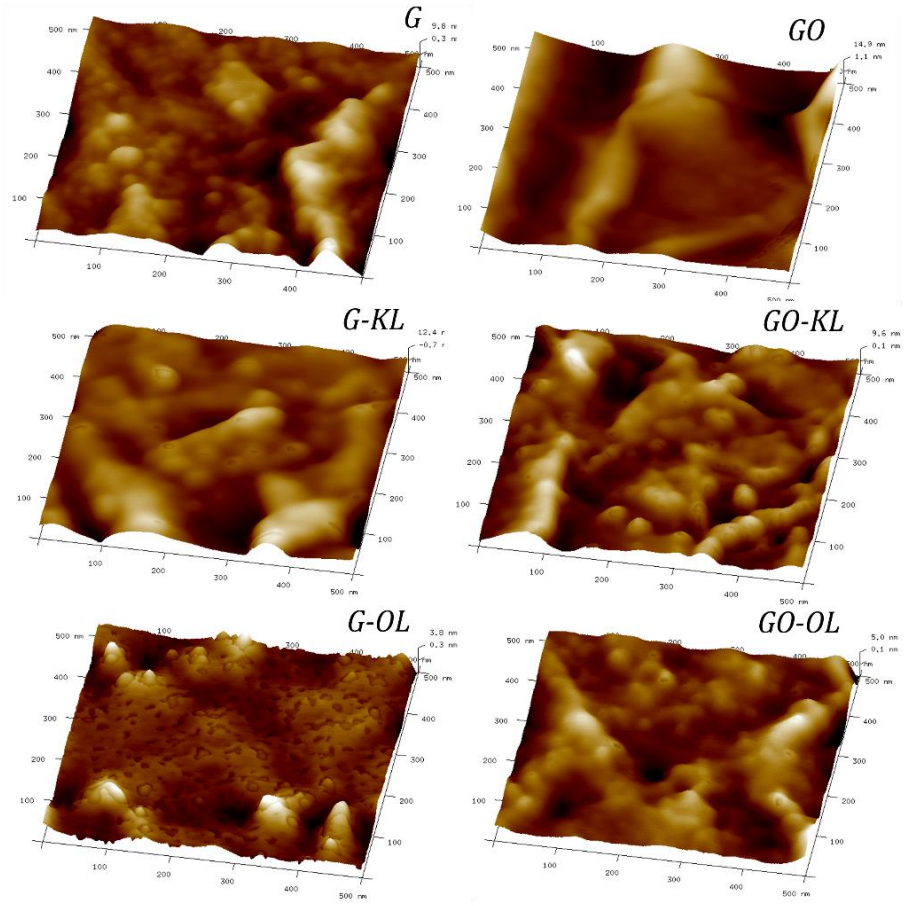

Figure 6.13. AFM images obtained for L-G samples by AFM.

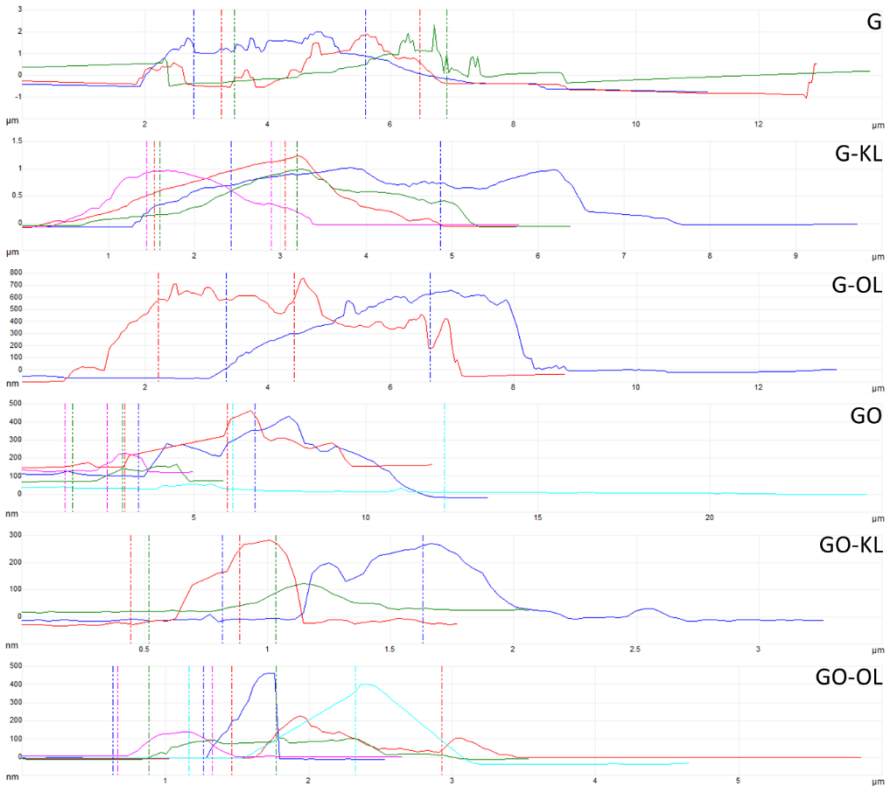

Figure 6.14. Height profiles obtained from AFM of the different L-G samples.

The results obtained from AFM showed the effectiveness of the process. The heights of the particles drastically changed as the different processes were carried out.

From one side, the oxidation of G highly promoted the exfoliation of the particles. In addition, this chemical reaction enhanced the posterior exfoliation by US forces and lignin as exfoliating agents, obtaining particles of 250 and 300 nm heights for GO-KL and GO-OL compared to the 1000 and 700 nm sized G-KL and G-OL. These results suggest that lignin particles are effective exfoliating agents, able to obtain partially exfoliated G and GO particles with US forces and short times.

Table 6.2. Mean height values of each sample obtained by AFM.

Sample	*G*	*G-KL*	*G-OL*	*GO*	*GO-KL*	*GO-OL*
Height	1500 nm	1000 nm	700 nm	400 nm	250 nm	300 nm

To obtain further morphological insight into the composites, SEM imaging was also carried out. Three images in different scales were obtained for each material type. Figures 6.15 and 6.18 show the images obtained at a 2 μm scale, Figures 6.16 and 6.19 at 5 μm, and Figures 6.17 and 6.20 at 20 μm scales. The Figures 6.15, 6.16, and 6.17 are for L-AC samples, while Figures 6.18, 6.19, and 6.20 are for L-G samples.

It can be observed that the surface of the active carbon becomes rougher. Moreover, with the deposition of KL and OL into the surface of TAC, a considerable increase in the porosity degree can be observed. Table 6.3 lists the porosity values of the composites obtained, when the porous structures could be distinguished.

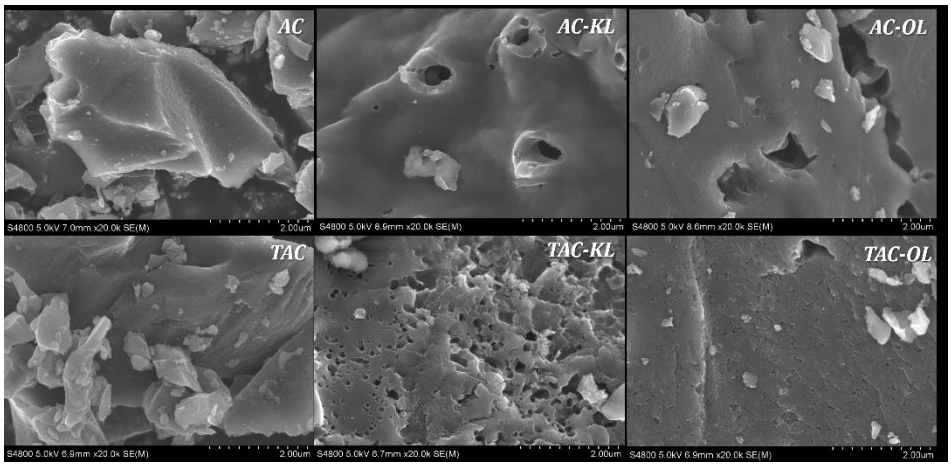

Figure 6.15. SEM images of the L-AC composite surfaces at a scale of 2 μm.

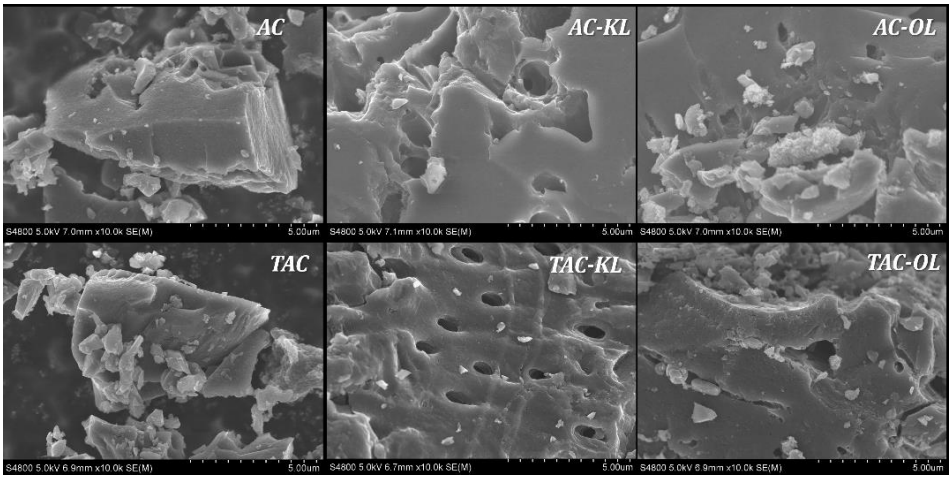

Figure 6.16. SEM images of the L-AC composite surfaces at a scale of 5 μm.

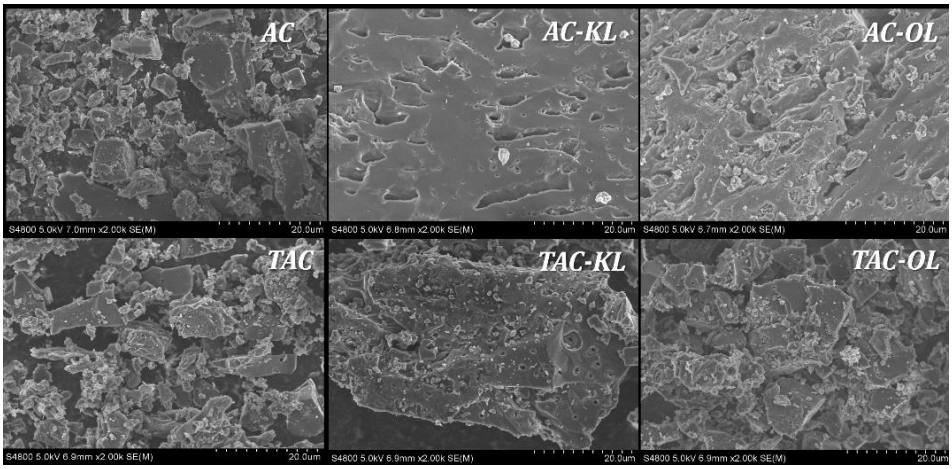

Figure 6.17. SEM images of the L-AC composite surface at a scale of 20 μm.

Table 6.3. Average porosity sizes calculated from the SEM images at 2 μm scale.

AC-KL	*AC-OL*	*TAC-KL*	*TAC-OL*
-	-	0.175 ± 0.088 μm	0.062 ± 0.033 μm

In the case of L-G samples, SEM images also show the surface morphology of the samples. It can be observed that G is formed by many layers of material. With the US treatment with KL and OL, similar morphological results could

be obtained, with slightly more separated sheets due to the insertion of the lignin particles. Nevertheless, the oxidation reaction considerably increased the exfoliation of the particles, obtaining a smoother surface. This was further enhanced by the treatment of GO with KL and OL, where even a smoother surface was obtained.

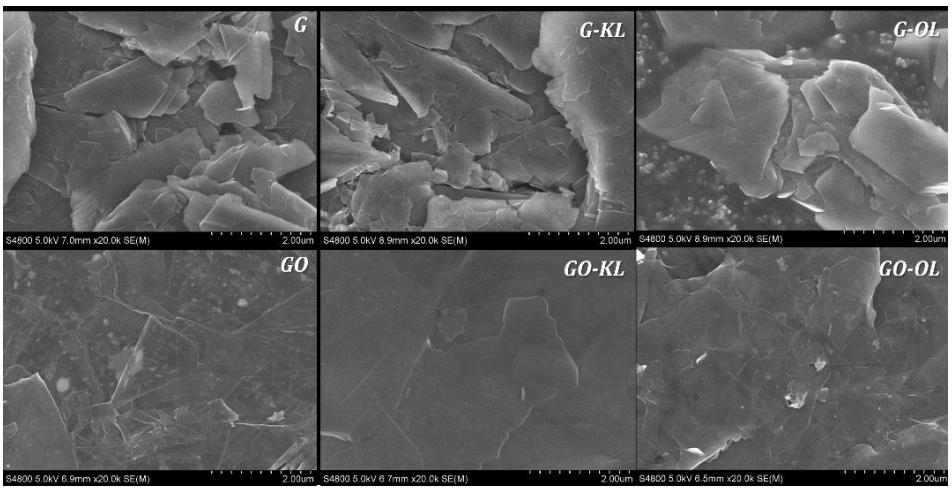

Figure 6.18. SEM images of the L-G composite surface at a scale of 2 μm.

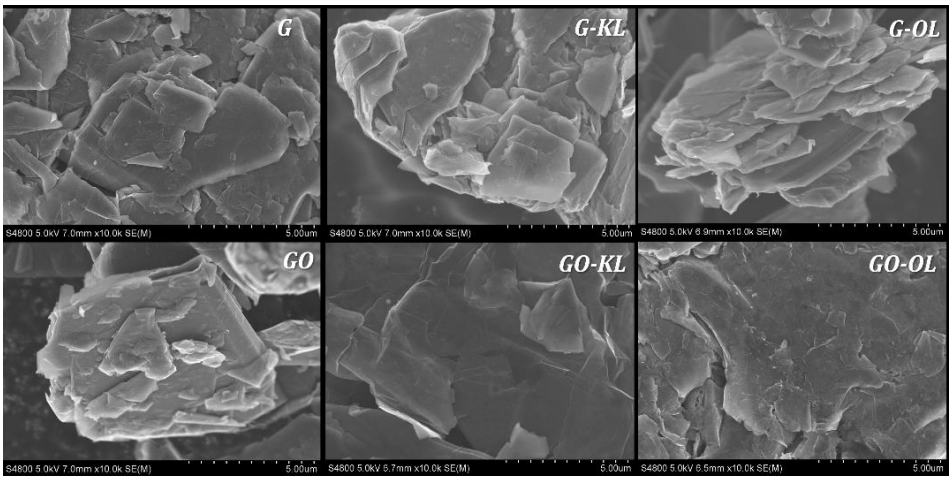

Figure 6.19. SEM images of the L-G composite surface at a scale of 5 μm.

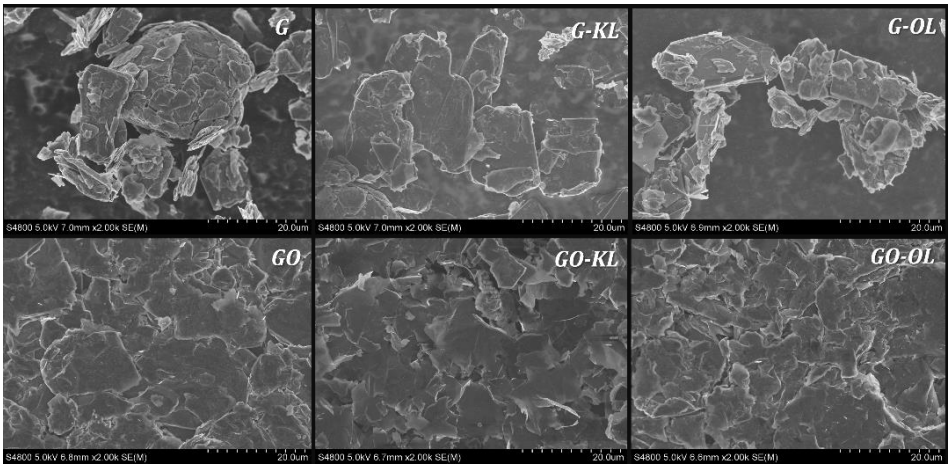

Figure 6.20. SEM images of the L-G composite surface at a scale of 20 μm.

6.4.3. ELECTROCHEMICAL CHARACTERIZATION

The composite materials obtained were used as working electrodes on a three-electrode system, where Ag/AgCl served as RE and Pt as CE, using 0.1M $HClO_4$ solution as the electrolyte. CV and EIS measurements were carried out before and after galvanostatic cycling to observe the differences caused in the materials and deduce their stability and enhancement in performance.

The Nyquist plots obtained for L-AC and L-G samples are shown in Figure 6.21 and 6.22 and the CV curves obtained from the EIS are depicted in Figure 6.22 and 6.24.

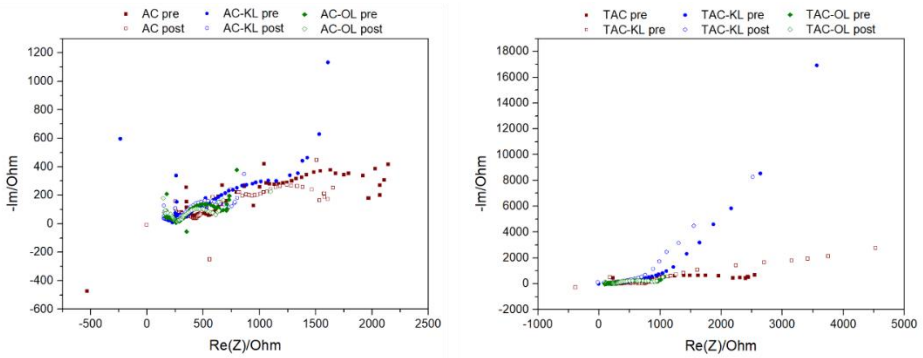

Figure 6.21. Nyquist plots of all the L-AC samples.

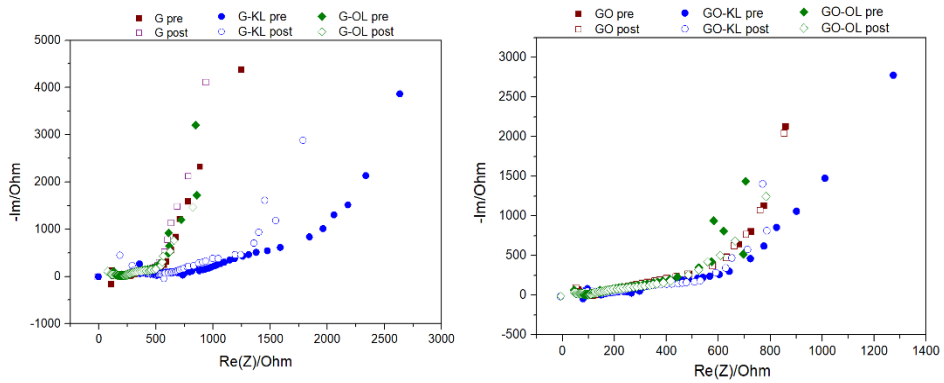

Figure 6.22. Nyquist plots of all the L-G samples.

From these EIS measurements, different polarization processes were identified. Curve fitting using ECMs was carried out, specific capacitance values were obtained, and porosity structures were deduced.

To analyze the EIS spectra obtained with the EC-Lab Software, it is essential to design an ECM that accurately represents the different polarization processes occurring in the system. This approach ensures obtaining values that align with the experimental data. This was done by the distribution of relaxation time (DRT) methodology [51–55].

EIS data were deconvoluted and the Z_{real} and Z_{imag} impedance data were converted to gamma tau ($\gamma(\tau)/\Omega$) and relaxation times (τ/s) by the use of Matlab and DRTtools toolbox [56,57].

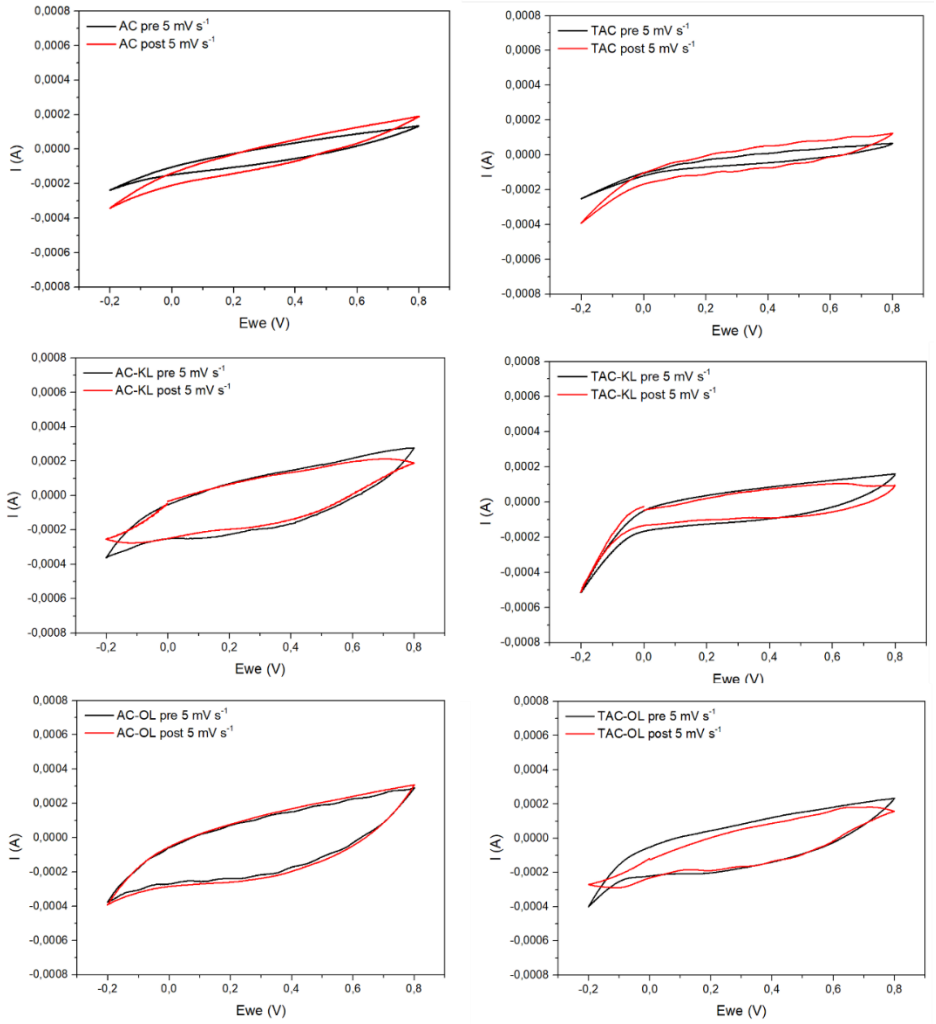

Figure 6.23. The CV cycles obtained for all the L-AC samples, pre and post GCD cycling.

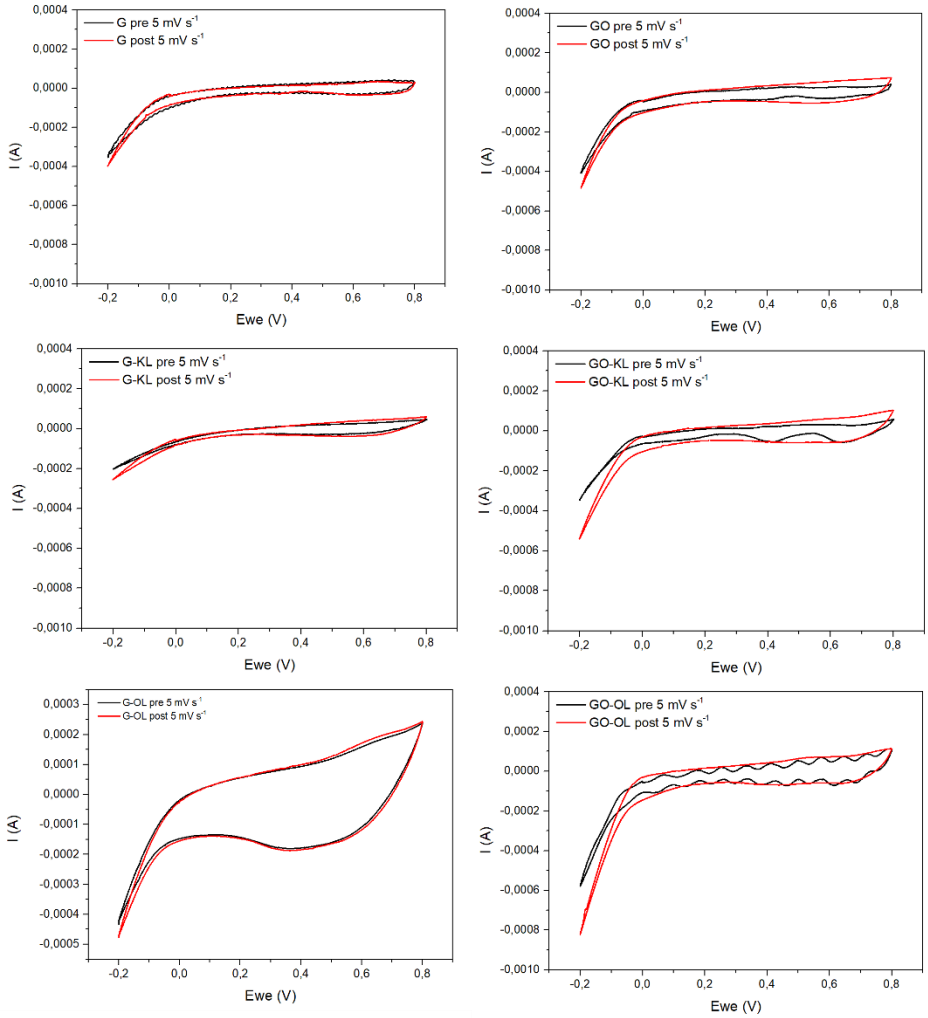

Figure 6.24. The CV cycles obtained for all the L-G samples, pre and post GCD cycling.

The DRT graphs obtained before GCD (called pre-GCD) and after GCD (called post-GCD) for all the sample are illustrated in Figures 6.25 and 6.26, for L-AC composites and L-G hybrid materials respectively. All the polarization processes taking part in the system were observed, and differences made by both composition and the charge and discharge cycles were deduced. Moreover, the frequency ranges were distinguished and the elements composing the ECM were assigned to the corresponding frequency range.

Depending on the sample, two types of polarization responses could be observed. Most of the L-AC composite materials showed polarization processes through all the frequency ranges, while in the case of TAC, TAC-KL and all the other L-G hybrid materials, the main polarization processes occurred between the low and high frequencies. Depending on that, two different ECMs were designed. Each observed polarization process was attributed to an element couple (CPE and R), except for the polarization processes happening at low frequencies, which were attributed to diffusion processes considered as the Warburg element (W_d). However, due to the huge difference in the values compared to the obtained W_d, the polarization processes happening at very high frequencies can be neglected.

As previously mentioned, the relaxation times for the DRT graphs were obtained by converting the frequency values. Therefore, it can be concluded that relaxation times ranging from 10^{-8} to 10^{-4} seconds (colored in blue) were attributed to polarization processes happening at very high frequencies (1 MHz to 100 KHz). Time intervals from 10^{-4} to 10^{-2} s (colored in red) were linked to high frequencies (100 KHz to 10 KHz); 10^{-2} to 10^{1} s to intermediate frequencies (10 KHz to 100 Hz); and finally, intervals from 10^{1} to 10^{4} s (colored in purple) were attributed to low frequencies (100 Hz to 10 mHz).

Based on the results, two different ECMs were designed and presented in Figures 6.25 and 6.26. The ECM model on top, with 3 CPE and R couples corresponds to the samples showing polarization processes at very high frequencies: AC, AC-KL, AC-OL, and TAC-OL samples. Otherwise, the ECM model below, with 2 couples, corresponds to the samples TAC and TAC-KL. These models were introduced in the EC-Lab software and fitted to the Nyquist plots experimentally obtained.

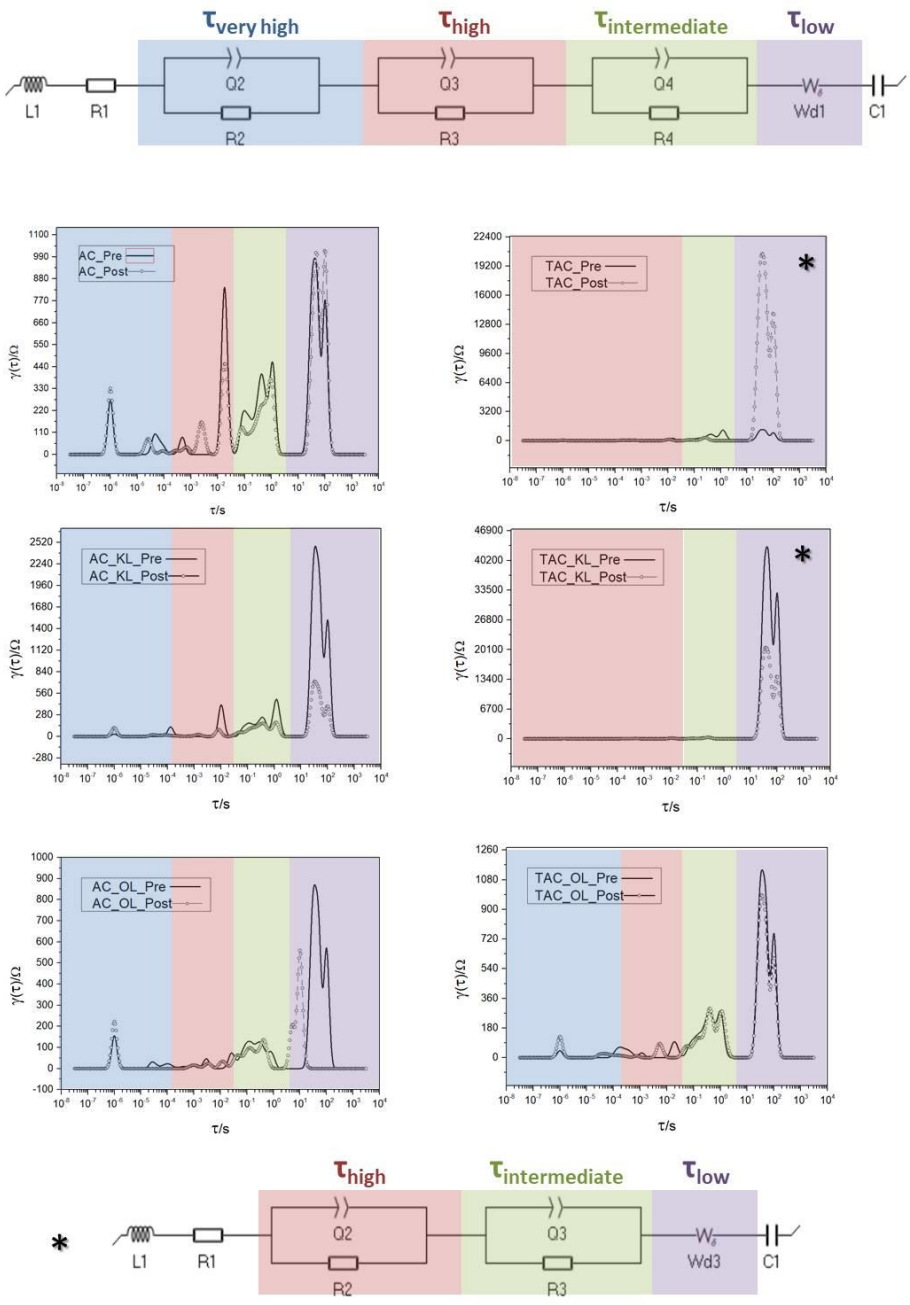

Figure 6.25. DRT and ECM of each system for L-AC composites.

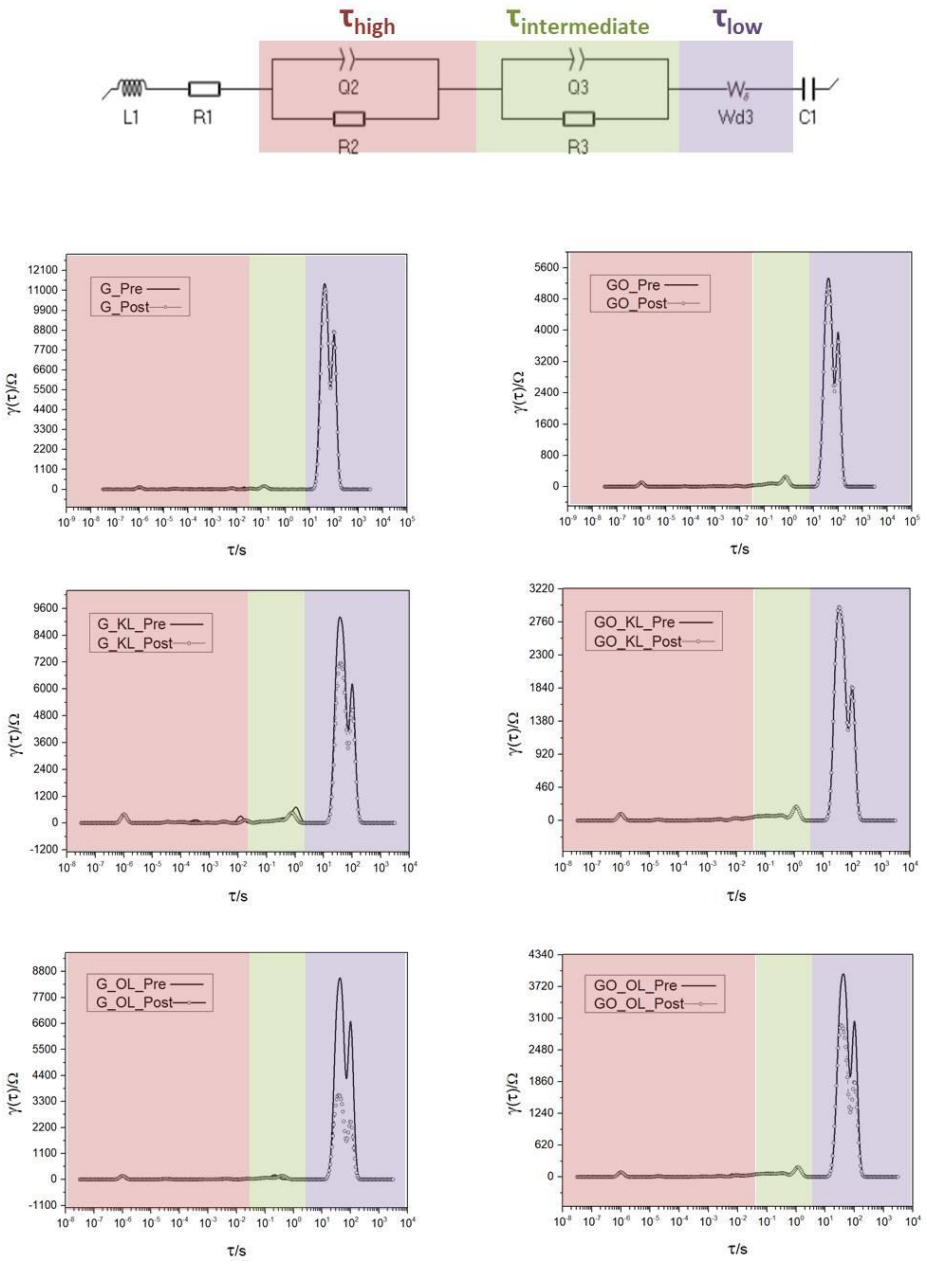

Figure 6.26. DRT and ECM of each system for L-G hybrid materials.

L1 and R1 were attached in series; L1 corresponded to external elements like cables or connections, while R1 was the resistance that the electrolyte (in this case the 0.1M $HClO_4$ solution) created in the system. Another three

groups of elements were linked in parallel (CPE2 and R2, CPE3 and R3, and CPE4 and R4). The first one (CPE2 and R2) was linked to the very high frequency range (from 1 MHz to 100 KHz), with a polarization process happening at $\tau=10^{-6}$ s, in the most external part of the samples employed as a working electrode. The CPE3 and R3 couple was associated with the high frequency area (from 100 MHz to 10 KHz), with polarization processes occurring at 10^{-2} s. The last elements in parallel (the CPE4 and R4) belonged to intermediate frequencies (from 10 KHz to 100 Hz), in a more internal area of the material, where charge transfer phenomena occurred. Finally, the low-frequency area (from 100 Hz to 10 mHz) is where diffusion processes occur, and as can be seen from the DRT graphs obtained, two elements took part in that frequency range. The first one, at around 50 s, was assigned to the Warburg element (W_d), and the second one, at around 100 s, to another C element (C1), which would be attached in series to the ECM [58,59].

The other ECM that fitted the Nyquist plots obtained for TAC and TAC-KL, as well as all the other L-G samples, was also composed of the elements L1 and R1 in series. Nevertheless, this time only two C and R couples in parallel were observed (CPE2 and R2 in the high-frequency range and CPE3 and R3 in the intermediate range). Similarly, the Warburg element corresponded to the diffusion processes happening in the low-frequency range, with a final C element. From the left graph of Figure 3, it could be observed that the polarization processes at high frequencies were so low compared to the ones obtained at low frequencies, that the elements that would correspond to $\tau_{very\ high}$ were neglected for the ECM. Moreover, to compare the C_p obtained from EIS with the ones of CV, only the elements present at low frequencies were considered since the CV measurements were carried out at constant tension and current.

In terms of changes observed due to the galvanostatic cyclings, some minor changes in the diffusion processes were observed. Some peaks showed a

shift in the relaxation time, while other elements showed a considerable value change, especially at low frequencies. The values obtained for all the elements of the ECMs identified are listed in Table 6.4 for pre-GCD values and Table 6.5 for post-GCD values of the L-AC samples, while the ones corresponding to the L-G samples are listed in Tables 6.6 and 6.7.

Table 6.4. Pre-GCD values obtained for each element of the ECM fitted to the experimental Nyquist plots.

	AC	***AC-KL***	***AC-OL***	***TAC***	***TAC-KL***	***TAC-OL***
L1	-44.33e^{-6} H	-51.89e^{-6} H	-22.07e^{-6} H	-46.06e^{-6} H	66.41e^{-9} H	-15.99e^{-6} H
R1	287.2 Ω	238.4 Ω	21.4 Ω	258.2 Ω	7.227 Ω	116.6 Ω
C2	0.7939e^{-3} F	46.91e^{-6} F	0.314e^{-3} F	72.76e^{-9} F	3.526e^{-3} F	1.446e^{-6} F
R2	961.1 Ω	746.5 Ω	323.2 Ω	546.8 Ω	3753 Ω	112 Ω
C3	12.59e^{-9} F	0.08779 F	52.9e^{-6} F	0.7464e^{-3} F	13.29e^{-9} F	0.5525e^{-3} F
R3	205.8 Ω	1059 Ω	61.68 Ω	2683 Ω	1.902 Ω	407.9 Ohm
C4	0.1376e^{-3} F	3.026e^{-3} F	0.989 3e^{-9} F			0.6093e^{-3} F
R4	540.3 Ω	74.83 Ω	282.5 Ω			329.1 Ω
R_{d1}		139 Ω	3659 Ω	41543 Ω	288.9 Ω	638.1 Ω
t_{d1}		0.527 s	14931 s	4179 s	820.5 s	354.6 s
C1		0.01486 F	0.05569 F	0.015 F	4.481e^{-3} F	0.03737 F

The AC sample showed quite pronounced polarization processes through all the frequencies. AC-KL, AC-OL, and TAC-OL samples also showed pronounced processes, especially at intermediate frequencies. In the case of TAC and TAC-KL, since the peaks at low frequencies were so high, other polarization processes were not so visible. However, they still had higher values than the other types of materials (AC had a value of 460 Ω at 1 s, while TAC had a value of 1153 Ω and TAC-KL 490 Ω at the same time). Values corresponding to the diffusion processes are the ones that should be observed more precisely. AC showed similar polarization processes pre-GCD and post-GCD at low frequencies (around 1000 Ω between 50 s and 100 s),

similar to TAC-OL. It can therefore be concluded that these were the most stable samples since no significant changes could be observed by the GCD cyclings. In the case of AC-KL and TAC-KL, GCD cycles decreased the diffusion processes. In the case of AC-KL, the values at 34 s decreased from 2500 to 720 Ω, and from 1500 to 400 Ω at 100 s, while for TAC-KL values at 40 s decreased from 43300 to 2570 Ω, and from 33000 to 14100 Ω at 100 s. The only sample that shifted diffusion times was AC-OL, where the main time fluctuated from 37 s to 9 s.

Table 6.5. Post-GCD values obtained for each element of the ECM fitted to the experimental Nyquist plots.

	AC	***AC-KL***	***AC-OL***	***TAC***	***TAC-KL***	***TAC-OL***
L1	-19.08e^{-6} H	-15.02e^{-6} H	-12.79e^{-6} H	-66.66e^{-6} H	-24.04e^{-9} H	-6.433e^{-6} H
R1	80.19 Ω	61.57 Ω	54.23 Ω	325.3 Ω	21.62 Ω	16.11 Ω
C2	0.6674e^{-3} F	8.643e^{-9} F	29.8e^{-9} F	1.253e^{-3} F	0.1011e^{-3}F	0.466e^{-3} F
R2	1066 Ω	214.8 Ω	55.04 Ω	7337 Ω	127.6 Ω	156.5 Ω
C3	17.05e^{-6} F	0.7137e^{-3} F	0.670 1e^{-3} F	0.486 6e^{-6} F	11.19e^{-9} F	0.6782e^{-3} F
R3	108.9 Ω	140.8 Ω	335.7 Ω	333.7 Ω	118.8 Ω	676.6 Ω
C4	0.942 9e^{-9} F	1.018e^{-3} F	1.299e^{-9} F			2.158e^{-9} F
R4	291.8 Ω	381.5 Ω	148.6 Ω			161.8 Ω
R_{d1}	396.9 Ω	30.14 Ω	78.1 Ω	-19377 Ω	2647 Ω	134.6 Ω
t_{d1}	0.01803 s	3.732e^{-3} s	0.03718 s	34 462 s	19.82 s	22.68 s
C1		0.04999 F	0.055 49 F	0.0149 F	2.251e^{-3} F	0.04637 F

In the case of L-G samples, shown in Figure 6.26, only three areas were differentiated due to the lack of polarization processes happening at very high frequencies. Between the other three areas (high, intermediate, and low frequencies) the last one was predominant, deducing that the main polarizations happening in the sample were induced by diffusion processes.

In terms of the difference observed due to the degradation that occurred by galvanostatic cycling, it was deduced that the least stable composite was G-OL, followed by G-KL and GO-OL. The reason might be that, since the composites of G-KL and G-OL were formed through physical interactions, which are much weaker interactions than the ones created by chemical bonds, they tend to degrade more easily, breaking the formed interactions and further degrading lignin. On the other hand, OL seemed less stable than KL, due to its higher M_w and less amount of accessible functional groups to interact with G and GO [60]. Moreover, the sulfur content present in KL also contributed to better interactions with GO and better electrochemical performances [61].

Table 6.6. Pre-GCD values obtained for each element of the ECM fitted to the experimental Nyquist plots.

	G	***G-KL***	***G-OL***	***GO***	***GO-KL***	***GO-OL***
L1	16.73e^{-6} H	9.085e^{-6} H	13.38e^{-6} H	5.868e^{-6} H	11.08e^{-6} H	5.014e-6 H
R1	119.5 Ω	162.7 Ω	98.58 Ω	9.452 Ω	86.74 Ω	5.913 Ω
C2	0,2809e^{-3} F	0.9404e^{-3} F	0.655e^{-3} F	2.832e^{-9} F	3.175e^{-6} F	3.328e^{-9} F
R2	189.3 Ω	2336 Ω	470.7 Ω	112.1 Ω	77.43 Ω	79.22 Ω
C3	0.9677e^{-6} F	2.596e^{-9} F	27.57e^{-9} F	0,0171 F	0.01087 F	0.6032e^{-3} F
R3	130.9 Ω	442.7 Ω	102.2 Ω	819.9 Ω	1851 Ω	639.3 Ω
R_{d1}	2.676 Ω	480.5 Ω	72498 Ω	252.9 Ω	220.1 Ω	213.6 Ω
t_{d1}	135.9 s	25.35 s	758492 s	0.4156 s	31.71 s	133.8 s
C1	4.276e^{-3} F	4.843e^{-3} F	5.441e^{-3} F	7.899e^{-3} F	6.667e^{-3} F	0.01113 F

Through the DRT graphs, the design of the ECM was eased, being able to identify two CPE-R couples at high and intermediate frequencies, along with the Warburg element (W_{d3}) associated with the diffusion processes, at low frequency ranges.

Table 6.7. Post-GCD values obtained for each element of the ECM fitted to the experimental Nyquist plots.

	G	***G-KL***	***G-OL***	***GO***	***GO-KL***	***GO-OL***
L1	9.841e-6 H	-56.76e-6 H	2.181e-6 H	11.9e-6 H	16.91e-6 H	7.717e-6 H
R1	23.51 Ω	31.23 Ω	17.99 Ω	48.95 Ω	132 Ω	15.07 Ω
C2	5.599e-9 F	0.01781 F	1.58e-3 F	12.85e-9 F	51.42e-6 F	0.01637 F
R2	146.3 Ω	411.6 Ω	450.3 Ω	77.27 Ω	139.9 Ω	827.1 Ω
C3	40.02e-9 F	0,2016 F	2.835e-9 F	1.347e-3 F	0.8932e-3 F	0.2992e-6 F
R3	81.73 Ω	1911 Ω	165.9 Ω	529.6 Ω	359.1 F	147.6 Ω
R_{d1}	357.9 Ω	486.6 Ω	92.9 Ω	403.8 Ω	1013 Ω	169.7 Ω
t_{d1}	0.5243 s	1.256 s	0.2773 s	19.99 s	236.9 s	0.159 s
C1	3.883e-3 F	5.848e-3 F	0,0112 F	8.918e-3 F	0.01313 F	0.01535 F

Specific capacitance values were obtained by CV, EIS and GCD data for L-AC and by CV and EIS for L-G samples, following the steps mentioned in Annex I. The mean values of the capacitance values calculated at different scan rates, and the regression line equations are illustrated in Figures 6.27 and 6.28 for L-AC and L-G samples respectively. Lower scan rates showed the highest capacitance values for most of the samples, which decreased as the scan rates increased, obtaining the smallest values at 50 mV/s, similar to other works, where a decrease in capacitance values with higher scan rates were also shown [62]. The influence of the scan rate on the capacitance obtained can be useful to determine the electrochemical charge storage mechanism of the active material and figure out if they belong to the type of electric double-layer capacitors (EDLC), pseudocapacitors (PC), or batteries, following the steps explained in Annex I.

From the lines obtained in Figure 6.27, the L-AC active materials showed an EDLC or PC behavior. Therefore, it could be deduced that the accumulated charges at the electrode-electrolyte interface created electrostatic charges without redox reactions. Nevertheless, samples TAC-KL and TAC-OL,

compared to TAC, considerably decreased the *b* value, being closer to 0.5, especially with TAC-OL. This means that the addition of lignin particles into the surface reacted having redox reactions, and slightly changing the behavior of the active material [63].

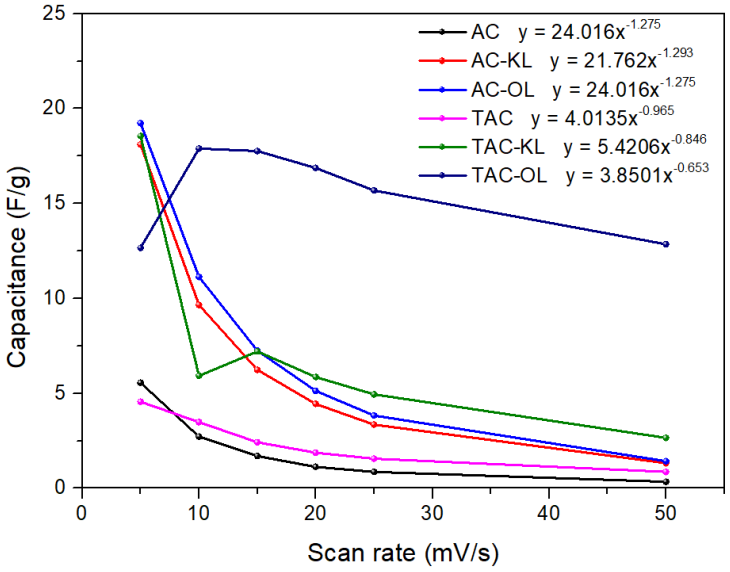

Figure 6.27. Capacitance values (F/g) of the different L-AC materials with different loadings.

Alternatively, from the trendlines obtained for the L-G hybrid materials, shown in Figure 6.28, the samples showed responses more appropriate for battery materials, reaching *b* values closer to 0.5 when the treatment with lignin was carried out.

As mentioned before, CV, EIS and GCD were used to calculate the capacitance values. These electroanalytical tests are complementary. In CV, the faradaic response generated (as a form of current) is measured by the difference of potential. In EIS, the impedance change is measured, composed of resistive, capacitive and inductive phenomena. Finally, the GCD technique charges and discharges the active material in a certain amplitude, measuring the time it

takes for each charge and discharge, dependent on the current density applied. Therefore, the bases of the measurements are different. While the CV measures the capacitive behavior at a specific frequency, EIS measurements are frequency-dependent, and GCD cyclings current density dependent. Moreover, the composition, surface area and porosity can influence the response given by different electrochemical stimuli, obtaining variations in the capacitive values obtained. Generally, CV measurements are more suitable for capturing fast surface processes, while EIS measurements can identify slow diffusion and charge transfer processes more efficiently. Having those limitations in mind, a proper electrochemical characterization of the materials can be obtained [64].

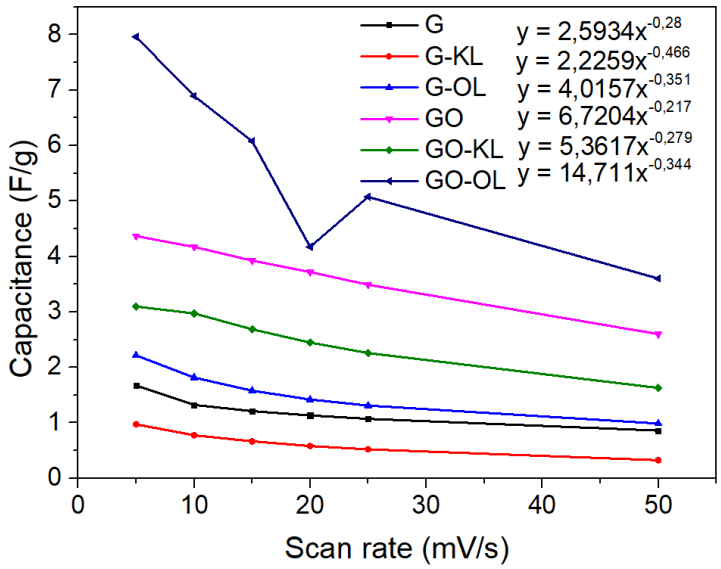

Figure 6.28. Capacitance values (F/g) of the different L-G materials with different loadings.

The data obtained by the CV measurements at different scan rates were used to calculate the C_p (CV), by applying the Equation A.2, explained in Annex I. Additionally, the C_p (EIS) values were obtained by fitting the Nyquist plots to the corresponding ECM, and finally, the C_p (GCD) at different current

densities were obtained by applying the Equation A.4, also shown in Annex I. The C_p values obtained from all three electrochemical techniques are listed in Table 6.9 and compared in Figure 6.29. The correlation of the values was carried out between the conditions in which the most similar values were obtained, low scan rate of 5 mV/s for the CV and medium-high current of 3 A for GCD measurements.

The results show that the insertion of KL and OL particles onto the surface of the AC had a positive effect on the performance of the material in terms of capacitance. C_p values obtained by CV (C_p (CV)) fluctuated from around 5 F/g for AC to almost 20 F/g for both AC-KL and AC-OL, with no detrimental effect due to the galvanostatic cycling. A similar effect could be observed with the TAC composites, where the insertion of KL and OL also favored both pre- and post-C_p (CV) values. In terms of the values obtained by EIS (C_p (EIS)), an overall similar tendency could be observed but with some differences. Composites usually show a better performance, but in this case, the ones that were conformed with OL, both AC-OL, and TAC-OL exhibited the best results. Their C_p experienced a significant increase both pre- and post-GCD cycles, with enhanced performance after the cycles. Nevertheless, the results obtained from the GCD differ slightly. The insertion of KL and OL into AC resulted in a negative effect compared to the value of AC, while TAC-KL showed similar results to TAC, and TAC-OL higher values than the TAC analogue. As explained above, the differences observed between the techniques can be attributed to the basis of the measurements. The overall C_p (CV) values are considerably lower than the C_p (EIS), probably due to the conductivity mechanism that the synthesized materials have, which is likely to be based primarily in diffusion processes.

In terms of the L-G sample results, shown in Figure 6.32, the same trend could be observed, with some variances, since the exfoliation and lignin intercalation treatment onto the graphite interlayers enhanced the overall

capacitance of the materials. The oxidation treatment of the G into GO more than doubled the C_p value obtained, which was further increased by the treatment with OL. A higher improvement with OL rather than KL can also be observed with G (G-KL vs G-OL) which denotes more suitability as not only exfoliating agent (seen from the results obtained in AFM) but also as an aggregate in active materials for battery applications.

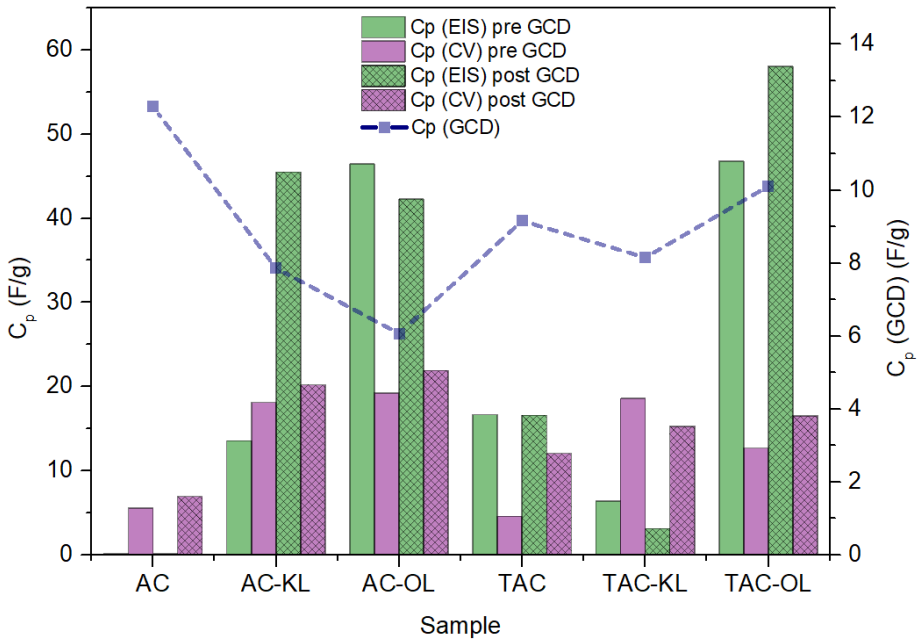

Figure 6.29. Comparison of C_p values (F/g) calculated by the different electrochemical measurements (CV, EIS and GCD) of the L-AC samples.

Table 6.8. C_p values obtained with CV, EIS and GCD at F/g.

	AC	AC-KL	AC-OL	TAC	TAC-KL	TAC-OL
C_p (CV) pre GCD						
5 mV/s	5.56	18.10	19.23	4.56	18.55	18.55
10 mV/s	2.72	9.65	11.13	2.28	5.93	17.90
15 mV/s	1.70	6.24	7.25	2.42	7.20	7.20
20 mV/s	1.13	4.44	5.13	1.88	5.86	5.86
25 mV/s	0.86	3.35	3.83	1.56	4.94	4.94
50 mV/s	0.34	1.33	1.43	0.86	2.65	2.65
C_p (CV) post GCD						
5 mV/s	6.93	20.20	21.85	12.04	15.27	16.52
10 mV/s	3.29	10.95	12.58	7.23	10.69	19.39
15 mV/s	1.89	7.11	8.10	5.23	8.35	18.69
20 mV/s	1.24	5.05	5.71	4.01	6.81	18.10
25 mV/s	0.92	3.85	4.27	3.24	5.73	16.85
50 mV/s	0.35	1.54	1.59	1.69	5.84	13.33
C_p (EIS) pre GCD						
	0.12	13.54	46.41	16.66	6.4	46.75
C_p (EIS) post GCD						
	0.08	45.45	42.24	16.55	3.11	58
C_p (GCD)						
0.2 A	132.18	166.55	16.82	52.92	50.93	105.87
3 A	12.28	7.86	6.06	9.15	8.15	10.10
5 A	8.84	7.16	10.44	6.11	7.82	6.64

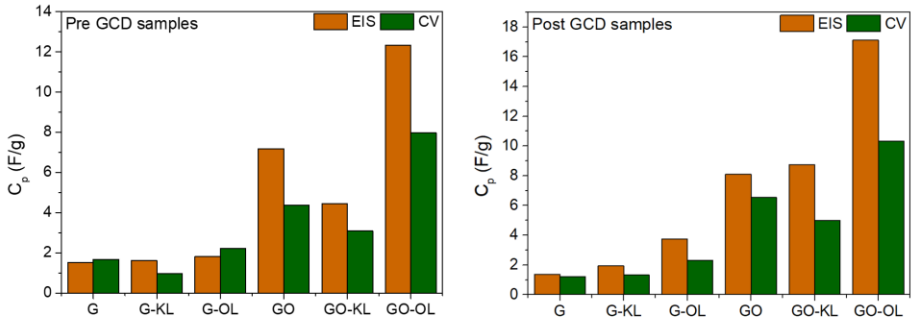

Figure 6.30. C_p (F/g) values for all the L-G samples measured by EIS and CV, pre-GCD values (left), and post-GCD values (right).

A characteristic closely related to the capacity of the material is its porosity. The pore size (mesoporous or microporous) dictates the electrolyte penetration and its overall performance [48,59]. Mesopores enable a fast power delivery due to the low ion resistance while micropore structures are more appropriate for high energy density. Therefore, a way to reach both fast power and high energy density is by obtaining an electrode material with micro-, meso-, and macro-pores [59]. These morphological characteristics were analyzed by SEM, which confirmed that the AC treatment and the addition of lignin to the material were beneficial for a hierarchical pore structure.

Moreover, this property was further analyzed and confirmed by EIS analysis, which is also capable of expressing phenomenological information derived from the structure of the surface material. This representation type is called Bode plot and it is further explained in Annex I. Bode plots obtained for L-AC samples are shown in Figure 6.31, while the ones for the L-G samples are shown in Figure 6.32. Micro- and meso-pores show different resistance, therefore, the resistance associated with each pore type appear in different parts of the Bode plot depending on the morphology. Micropores, due to their smaller size and higher resistance, appear at lower frequencies, while mesopores, having lower resistance, are visible at higher frequencies. From

the results obtained, it can be concluded that the treatment of active carbon with lignin was helpful for the formation of both micro- and meso-pores. AC sample did not show any significant peak in the range of different frequencies, while in TAC a clear peak could be seen in the micropore area and another small but clear peak in the mesopore area. When hybrid or composite materials were obtained with the lignin insertion, slight differences could be observed. The deposition of KL helped especially for an enhanced mesopore formation in untreated AC (AC-KL). This was corroborated with the results obtained from SEM, where big pores were observed. In the case of OL deposited in AC (AC-OL), the micropore response obtained was the most significant of all the samples analyzed. For composites obtained from treated AC, similar impedance responses were observed for all TAC, TAC-KL, and TAC-OL, where slight micropore responses were seen, along with a more significant mesopore response.

Nevertheless, a common difference between TAC-OL from TAC and TAC-KL is that the micropore response happened at lower frequencies, which might lead to the formation of smaller micropores and a higher energy density material. Again, this can be corroborated with the SEM images, where TAC-OL shows significantly smaller pores than TAC-KL.

The Bode plots for all the L-G samples are shown in Figure 6.32. Several differences can be observed because of the treatments. G had some slight porous structures since a small peak between the low and intermediate frequency range and another at high frequency were observed. With the oxidation treatment, where GO was obtained, the microporous structure of the material was enhanced, obtaining another polarizable element at higher frequencies. Nevertheless, the highest difference was observed when the treatments with lignin were carried out. In the case of KL, both G-KL, and GO-KL showed an intense peak in the mesoporous-microporous region, evidencing the formation of hierarchically porous surfaces. This effect was

more prominent in the case of GO-KL, probably due to the higher efficacy of the lignin treatment as the GO contained oxygen groups that chemically interact with KL particles. In the case of OL, the porosity difference was not that visible, having fewer interactions in the mesoporous-microporous region.

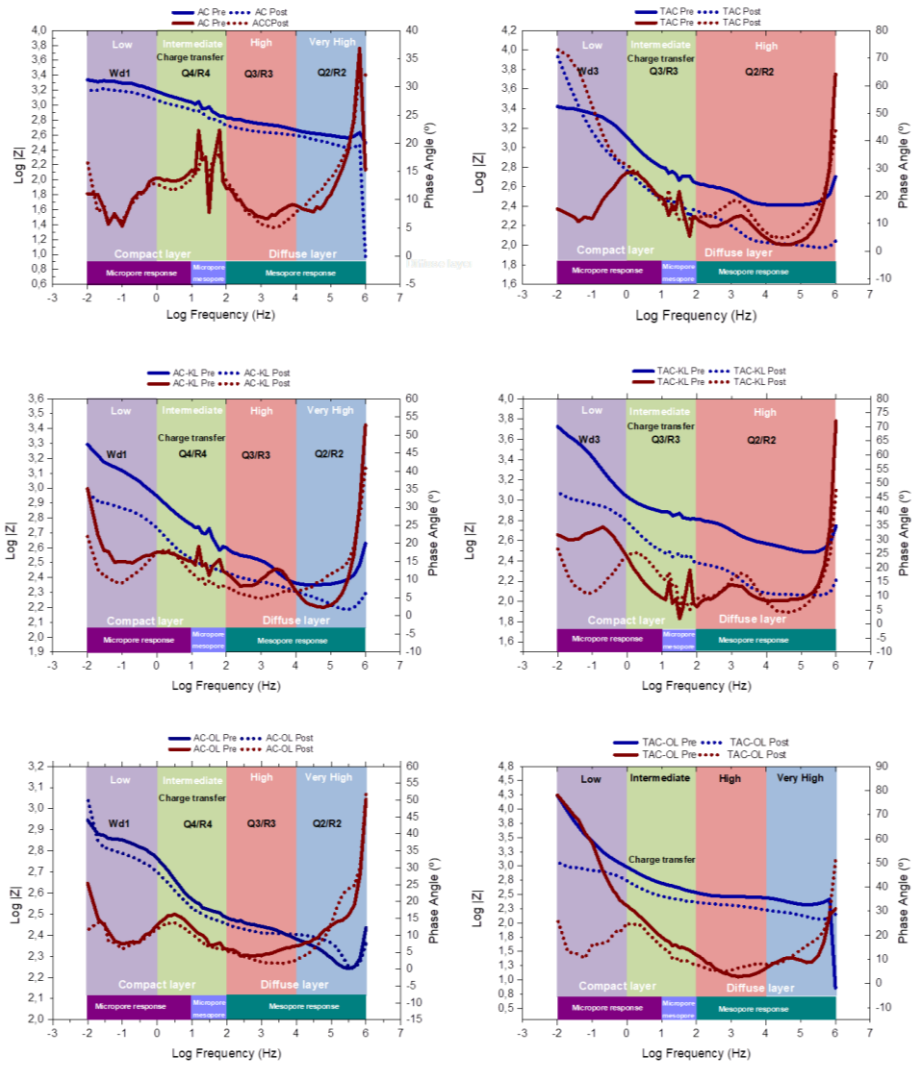

Figure 6.31. Bode plots for L-AC samples.

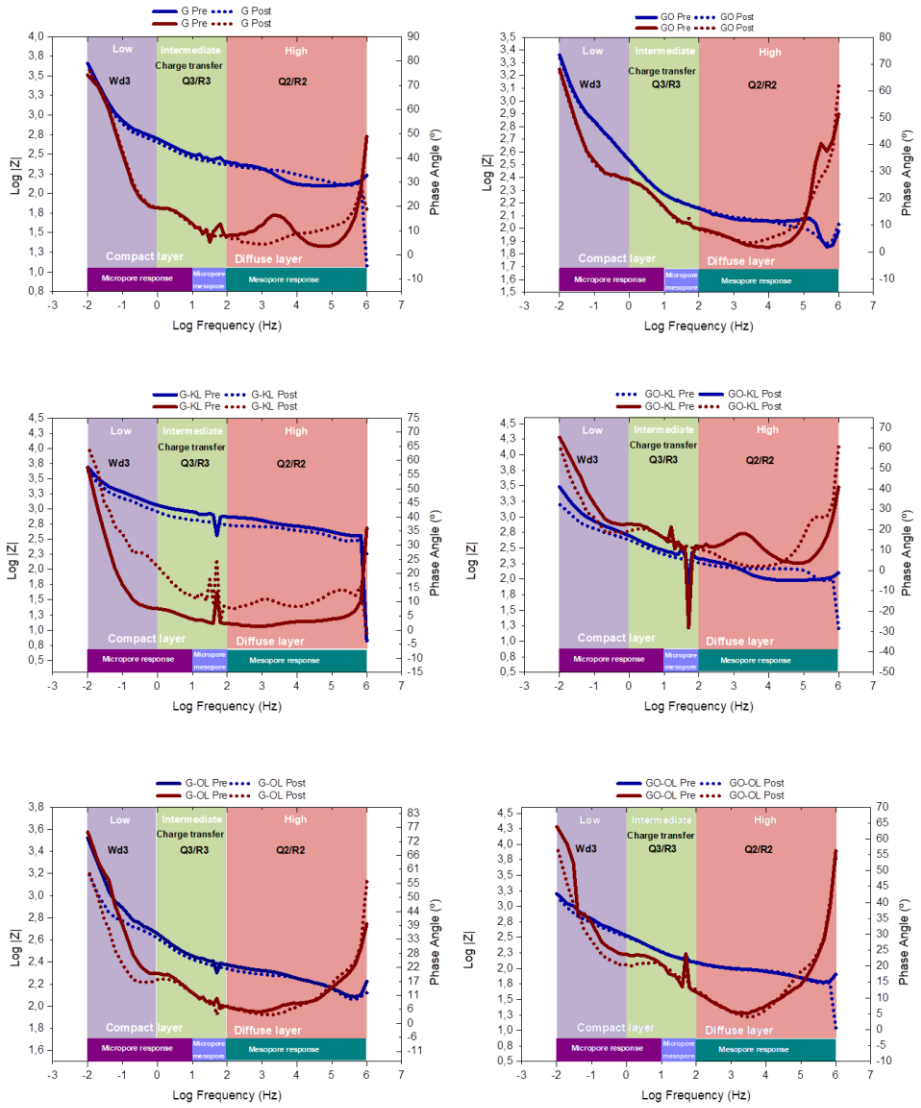

Figure 6.32. Bode plots for L-G samples.

6.5. CONCLUSIONS

This chapter aimed to develop active materials for both SCs and LIBs with properties enhanced by treatments where lignin was used. In the first case, the development of SC active materials based on acid-treated active carbon and lignin was carried out. It was concluded that the acid treatment was effective on the further lignin deposition on the carbon surface. Moreover, it was found that the type of lignin used had diverse effects; while in the treatment with KL more hierarchically porous structures were obtained, more mesoporous structures were produced with OL, influencing the electrochemical characteristics in a more positive way than KL due to the higher C_p values obtained.

On the other side, the hybrid materials obtained through the exfoliation of graphite and graphite oxide through ultrasound forces and lignin as an exfoliating agent also showed positive outcomes. It was observed that lignin particles intercalated between the graphite layers, enhancing the effect when the graphite oxide was used. The oxidized functional groups in graphite oxide promoted the formation of chemical bonds with the lignin particles, creating strong bonds that were later validated with enhanced electrochemical performance and lower degradation due to cyclings.

Finally, the C_p values obtained for the composite and hybrid materials by CV and EIS electroanalytical tests revealed notable differences between them. Overall, this study demonstrates the potential of the developed process to obtain electrode materials with enhanced electrochemical performance by sustainably implementing lignin.

6.6. REFERENCES

[1] Zhang H, Yang Y, Ren D, Wang L, He X. Graphite as anode materials: Fundamental mechanism, recent progress and advances. Energy Storage Mater 2021;36:147–70. https://doi.org/10.1016/j.ensm.2020.12.027.

[2] Espinoza-Acosta JL, Torres-Chávez PI, Olmedo-Martínez JL, Vega-rios A, Flores-gallardo S, Zaragoza-Contreras EA. Lignin in storage and renewable energy applications: A review. J Energy Chem 2018;27:1422–38. https://doi.org/10.1016/j.jechem.2018.02.015.

[3] Chen W-J, Zhao C-X, Li B-Q, Yuan T-Q, Zhang Q. Lignin-derived materials and their applications in rechargeable batteries. Green Chem 2022:565–84. https://doi.org/10.1039/d1gc02872c.

[4] Zhang K, Liu M, Zhang T, Min X, Wang Z, Chai L, et al. High-performance supercapacitor energy storage using a carbon material derived from lignin by bacterial activation before carbonization. J Mater Chem A 2019;7:26838–48. https://doi.org/10.1039/c9ta04369a.

[5] Tong Y, Yang J, Li J, Cong Z, Wei L, Liu M, et al. Lignin-derived electrode materials for supercapacitor applications: progress and perspectives. J Mater Chem A 2022;11:1061–82. https://doi.org/10.1039/d2ta07203c.

[6] Wu X, Jiang J, Wang C, Liu J, Pu Y, Ragauskas A, et al. Lignin-derived electrochemical energy materials and systems. Biofuels, Bioprod Biorefining 2020;14:650–72. https://doi.org/10.1002/BBB.2083.

[7] Wang L, Morishita T, Toyoda M, Inagaki M. Asymmetric electric double layer capacitors using carbon electrodes with different pore size distributions. Electrochim Acta 2007;53:882–6. https://doi.org/10.1016/j.electacta.2007.07.069.

[8] Choma J, Burakiewicz-Mortka W, Jaroniec M, Li Z, Klinik J. Monitoring changes in surface and structural properties of porous carbons modified by

different oxidizing agents. J Colloid Interface Sci 1999;214:438–46. https://doi.org/10.1006/jcis.1999.6246.

[9] Shim JW, Park SJ, Ryu SK. Effect of modification with HNO3 and NaOH on metal adsorption by pitch-based activated carbon fibers. Carbon N Y 2001;39:1635–42. https://doi.org/10.1016/S0008-6223(00)00290-6.

[10] Boehm HP. Surface oxides on carbon and their analysis: A critical assessment. Carbon N Y 2002;40:145–9. https://doi.org/10.1016/S0008-6223(01)00165-8.

[11] Zhang Y, Feng H, Wu X, Wang L, Zhang A, Xia T, et al. Progress of electrochemical capacitor electrode materials: A review. Int J Hydrogen Energy 2009;34:4889–99. https://doi.org/10.1016/j.ijhydene.2009.04.005.

[12] Chmiola J, Yushin G, Gogotsi Y, Portet C, Simon P, Taberna PL. Anomalous increase in carbon at pore sizes less than 1 nanometer. Science (80-) 2006;313:1760–3. https://doi.org/10.1126/science.1132195.

[13] Aida T, Yamada K, Morita M. An advanced hybrid electrochemical capacitor that uses a wide potential range at the positive electrode. Electrochem Solid-State Lett 2006;9:534–6. https://doi.org/10.1149/1.2349495.

[14] Zhou B, Liu W, Gong Y, Dong L, Deng Y. High-performance pseudocapacitors from kraft lignin modified active carbon. Electrochim Acta 2019;320:134640. https://doi.org/10.1016/j.electacta.2019.134640.

[15] Sopčić S, Antonić D, Mandić Z. Effects of the composition of active carbon electrodes on the impedance performance of the AC/AC supercapacitors. J Solid State Electrochem 2022;26:591–605. https://doi.org/10.1007/s10008-021-05112-8.

[16] Gu H, Zhu YE, Yang J, Wei J, Zhou Z. Nanomaterials and Technologies for Lithium-Ion Hybrid Supercapacitors. ChemNanoMat 2016;2:578–87. https://doi.org/10.1002/cnma.201600068.

[17] Koohi-Fayegh S, Rosen MA. A review of energy storage types, applications and recent developments. J Energy Storage 2020;27. https://doi.org/10.1016/J.EST.2019.101047.

[18] Karnan M, Raj AGK, Subramani K, Santhoshkumar S, Sathish M. The fascinating supercapacitive performance of activated carbon electrodes with enhanced energy density in multifarious electrolytes. Sustain Energy Fuels 2020;4:3029–41. https://doi.org/10.1039/c9se01298b.

[19] Madhu R, Periasamy AP, Schlee P, Hérou S, Titirici MM. Lignin: A sustainable precursor for nanostructured carbon materials for supercapacitors. Carbon N Y 2023;207:172–97. https://doi.org/10.1016/J.CARBON.2023.03.001.

[20] Grey CP, Hall DS. Prospects for lithium-ion batteries and beyond—a 2030 vision. Nat Commun 2020;11:2–5. https://doi.org/10.1038/s41467-020-19991-4.

[21] Yang Z, Zhang J, Kintner-Meyer MCW, Lu X, Choi D, Lemmon JP, et al. Electrochemical energy storage for green grid. Chem Rev 2011;111:3577–613. https://doi.org/10.1021/cr100290v.

[22] Gu X, Zhao Y, Sun K, Vieira CLZ, Jia Z, Cui C, et al. Method of ultrasound-assisted liquid-phase exfoliation to prepare graphene. Ultrason Sonochem 2019;58:104630. https://doi.org/10.1016/j.ultsonch.2019.104630.

[23] Krishnamoorthy K, Kim GS, Kim SJ. Graphene nanosheets: Ultrasound assisted synthesis and characterization. Ultrason Sonochem 2013;20:644–9. https://doi.org/10.1016/j.ultsonch.2012.09.007.

[24] Li C, Lin J, Shen L, Bao N. Quantitative analysis and kinetic modeling of ultrasound-assisted exfoliation and breakage process of graphite oxide. Chem Eng Sci 2020;213:115414. https://doi.org/10.1016/j.ces.2019.115414.

[25] Zhang W, He W, Jing X. Preparation of a stable graphene dispersion with high

concentration by ultrasound. J Phys Chem B 2010;114:10368–73. https://doi.org/10.1021/jp1037443.

[26] Yoo J, Kim HS, Park SY, Kwon S, Lee J, Koo J, et al. Instantaneous integration of magnetite nanoparticles on graphene oxide assisted by ultrasound for efficient heavy metal ion retrieval. Ultrason Sonochem 2020;64:104962. https://doi.org/10.1016/j.ultsonch.2020.104962.

[27] Deosarkar MP, Pawar SM, Sonawane SH, Bhanvase BA. Process intensification of uniform loading of SnO2 nanoparticles on graphene oxide nanosheets using a novel ultrasound assisted in situ chemical precipitation method. Chem Eng Process Process Intensif 2013;70:48–54. https://doi.org/10.1016/j.cep.2013.05.008.

[28] Marchi C, Loh HA, Lissandrello F, Lucotti A, Sierros KA, Magagnin L. Biocompatible rapid few-layers-graphene synthesis in aqueous lignin solutions. Carbon Trends 2022;7:100169. https://doi.org/10.1016/j.cartre.2022.100169.

[29] Liu L, Solin N, Inganäs O. Scalable lignin/graphite electrodes formed by mechanochemistry †. RSC Adv 2019;9:39758–67. https://doi.org/10.1039/c9ra07507k.

[30] Kim SK, Kim YK, Lee H, Lee SB, Park HS. Superior pseudocapacitive behavior of confined lignin nanocrystals for renewable energy-storage materials. ChemSusChem 2014;7:1094–101. https://doi.org/10.1002/cssc.201301061.

[31] Li F, Wang X, Sun R. A metal-free and flexible supercapacitor based on redox-active lignosulfonate functionalized graphene hydrogels. J Mater Chem A 2017;5:20643–50. https://doi.org/10.1039/c7ta03789a.

[32] Ye W, Li X, Luo J, Wang X, Sun R. Lignin as a green reductant and morphology directing agent in the fabrication of 3D graphene-based composites for high-

performance supercapacitors. Ind Crops Prod 2017;109:410–9. https://doi.org/10.1016/J.INDCROP.2017.08.047.

[33] Yang W, Wang X, Jiao L, Bian H, Qiao Y, Dai H. Synthetic polymers based on lignin-derived aromatic monomers for high-performance energy-storage materials. J Mater Chem A 2020;8:24065–74. https://doi.org/10.1039/d0ta08635e.

[34] Zhang YI, Zhang L, Zhou C. Graphene and Related Applications. Acc Chem Res 2013;46:2329–39.

[35] McAllister MJ, Li J, Adamson DH, Schniepp HC, Abdala A a, Liu J, et al. Single Sheet Functionalized Graphene by Oxidation and Thermal Expansion of Graphite. Chem Mater 2007;19:4396–404. https://doi.org/10.1021/cm0630800.

[36] Tyurnina A V., Morton JA, Kaur A, Mi J, Grobert N, Porfyrakis K, et al. Effects of green solvents and surfactants on the characteristics of few-layer graphene produced by dual-frequency ultrasonic liquid phase exfoliation technique. Carbon N Y 2023;206:7–15. https://doi.org/10.1016/j.carbon.2023.01.062.

[37] Hou S, Zhu T, Shen W, Kang F, Inagaki M, Huang ZH. Exfoliated graphite blocks with resilience prepared by room temperature exfoliation and their application for oil-water separation. J Hazard Mater 2022;424:127724. https://doi.org/10.1016/j.jhazmat.2021.127724.

[38] Jin S, Xing J, Liu T, Li K, Zhang F, Cao J, et al. Organic-inorganic building block of phytic acid intercalated graphene oxide for performance enhancement of plant-derived adhesives. Ind Crops Prod 2023;201:116919. https://doi.org/10.1016/j.indcrop.2023.116919.

[39] Ma Z, Wang J, Lu X, Zhou G, Wu Y, Zhang D, et al. A dual-blocker aided and dual-label-free electrochemical biosensor based on mbHCR / rGO

nanocomplexes for ultrasensitive DNA detection. Talanta 2023;260. https://doi.org/10.1016/j.talanta.2023.124646.

[40] Jia Z, Bai C, Zhang X, Qian M, Tsai H-S, Xiong Y. Effect of intercalated molybdenum atoms on structure and electrochemical properties of Mo1+xS2 synthesized by hydrothermal method. Nanotechnology 2023:1–8. https://doi.org/10.1088/1361-6528/acc2c7.

[41] Kigozi M, Kasozi GN, Tebandeke E, Aswini S, Anusha TV, Jain PK, et al. Electrochemical exfoliation and deposition of sodium-graphene oxide composite for high specific capacity cathode/anode for dual-carbon sodium ion battery application. Chem Phys Lett 2023;822:140499. https://doi.org/10.1016/j.cplett.2023.140499.

[42] Luo J, Shao L, Yu L, Shi X, Xu J, Sun J, et al. Self-intercalated quasi-2D structured V5Se8 wrapped with multi-walled carbon nanotubes toward advanced sodium ion batteries. Mater Today Phys 2023;35. https://doi.org/10.1016/j.mtphys.2023.101099.

[43] Zevallos Torres LA, Lorenci Woiciechowski A, de Andrade Tanobe VO, Karp SG, Guimarães Lorenci LC, Faulds C, et al. Lignin as a potential source of high-added value compounds: A review. J Clean Prod 2020;263. https://doi.org/10.1016/j.jclepro.2020.121499.

[44] Zhou B, Liu W, Gong Y, Dong L, Deng Y. High-performance pseudocapacitors from kraft lignin modified active carbon. Electrochim Acta 2019;320. https://doi.org/10.1016/J.ELECTACTA.2019.134640.

[45] Hummers WS, Offman RE. Preparation of Graphitic Oxide. J Am Chem Soc 1958;80:1339.

[46] Xiao-mei S, Shu-quan Z, Wen-hui Z. Effect of surface modification of activated carbon on its adsorption capacity for NH3. J China Univ Min Technol 2007;18:261–74. https://doi.org/10.1080/19443994.2012.749052.

[47] Suktha P, Chiochan P, Iamprasertkun P, Wutthiprom J, Phattharasupakun N, Suksomboon M, et al. High-Performance Supercapacitor of Functionalized Carbon Fiber Paper with High Surface Ionic and Bulk Electronic Conductivity: Effect of Organic Functional Groups. Electrochim Acta 2015;176:504–13. https://doi.org/10.1016/j.electacta.2015.07.044.

[48] Ren TZ, Liu L, Zhang Y, Yuan ZY. Nitric acid oxidation of ordered mesoporous carbons for use in electrochemical supercapacitors. J Solid State Electrochem 2013;17:2223–33. https://doi.org/10.1007/s10008-013-2088-1.

[49] Lisovskii A, Shter GE, Semiat R, Aharoni C. Adsorption of sulfur dioxide by active carbon treated by nitric acid: II. Effect of preheating on the adsorption properties. Carbon N Y 1997;35:1645–8. https://doi.org/10.1016/S0008-6223(97)00122-X.

[50] Bober P, Gavrilov N, Kovalcik A, Mičušík M, Unterweger C, Pašti IA, et al. Electrochemical properties of lignin/polypyrrole composites and their carbonized analogues. Mater Chem Phys 2018;213:352–61. https://doi.org/10.1016/J.MATCHEMPHYS.2018.04.043.

[51] Ciucci F. Modeling electrochemical impedance spectroscopy. Curr Opin Electrochem 2019;13:132–9. https://doi.org/10.1016/j.coelec.2018.12.003.

[52] Saccoccio M, Wan TH, Chen C, Ciucci F. Optimal regularization in distribution of relaxation times applied to electrochemical impedance spectroscopy: Ridge and Lasso regression methods - A theoretical and experimental Study. Electrochim Acta 2014;147:470–82. https://doi.org/10.1016/j.electacta.2014.09.058.

[53] Ivers-Tiffée E, Weber A. Evaluation of electrochemical impedance spectra by the distribution of relaxation times. J Ceram Soc Japan 2017;125:193–201. https://doi.org/10.2109/jcersj2.16267.

[54] Klotz D, Schmidt JP, Weber A, Ivers-Tiffée E. The Distribution of Relaxation Times as Beneficial Tool for Equivalent Circuit Modelling of Batteries and Fuel Cells. ECS Meet Abstr 2011;MA2011-02:2611–2611. https://doi.org/10.1149/ma2011-02/46/2611.

[55] Weiß A, Schindler S, Galbiati S, Danzer MA, Zeis R. Distribution of Relaxation Times Analysis of High-Temperature PEM Fuel Cell Impedance Spectra. Electrochim Acta 2017;230:391–8. https://doi.org/10.1016/j.electacta.2017.02.011.

[56] Dierickx S, Weber A, Ivers-Tiffée E. How the distribution of relaxation times enhances complex equivalent circuit models for fuel cells. Electrochim Acta 2020;355:136764. https://doi.org/10.1016/j.electacta.2020.136764.

[57] Danzer MA. Generalized distribution of relaxation times analysis for the characterization of impedance spectra. Batteries 2019;5:1–16. https://doi.org/10.3390/batteries5030053.

[58] Ragoisha G, Aniskevich Y. Comment to the article “How to measure and report the capacity of electrochemical double layers, supercapacitors, and their electrode materials” [1]. J Solid State Electrochem 2021;25:753. https://doi.org/10.1007/s10008-020-04880-z.

[59] Mishra GK, Kant R. Modular theory for DC-biased electrochemical impedance response of supercapacitor. J Power Sources 2020;473. https://doi.org/10.1016/j.jpowsour.2020.228467.

[60] Izaguirre N, Robles E, Llano-Ponte R, Labidi J, Erdocia X. Fine-tune of lignin properties by its fractionation with a sequential organic solvent extraction. Ind Crops Prod 2022;175:114251. https://doi.org/10.1016/j.indcrop.2021.114251.

[61] Hirai N, Kubo S, Magara K. Combined cyclic voltammetry and in situ electrochemical atomic force microscopy on lead electrode in sulfuric acid

solution with or without lignosulfonate. J Power Sources 2009;191:97–102. https://doi.org/10.1016/j.jpowsour.2008.10.090.

[62] Ge Y, Xie X, Roscher J, Holze R, Qu Q. How to measure and report the capacity of electrochemical double layers, supercapacitors, and their electrode materials. J Solid State Electrochem 2020;24:3215–30. https://doi.org/10.1007/s10008-020-04880-z.

[63] Yu F, Huang T, Zhang P, Tao Y, Cui FZ, Xie Q, et al. Design and synthesis of electrode materials with both battery-type and capacitive charge storage. Energy Storage Mater 2019;22:235–55. https://doi.org/10.1016/j.ensm.2019.07.023.

[64] Bard AJ, Faulkner LR, White HS. Electrochemical Methods: Fundamentals and Applications. Wiley; 2022.

7. Implementation of lignin as binder material for LIB anodes

7.1. MOTIVATION

The incorporation of batteries into various sectors is crucial for the transition to long-term sustainable practices. They play a crucial role in the mentioned transition due to some of the following reasons: they can store the intermittent energies produced by renewable sources like solar and wind, and release it when needed, creating a more reliable supply and therefore, diminishing the reliance on fossil fuels, and reducing greenhouse gas emissions [1]. Moreover, it can contribute to more efficient energy use, by managing the energy demand and scheduling the energy storage when the most energy-intensive activities are finished, and the energy cost is the lowest [2]. Additionally, they reduce the dependence on centralized power plants and distribution networks and bring energy to areas with limited or no access to electricity grids [3].

Nevertheless, there are some drawbacks to the system since these devices imply the use of advanced and scarce materials and technologies. Therefore, current research works are focused on overcoming and minimizing these issues to reduce their productions' environmental impact [4]. One approach involves designing devices that can be easily disassembled. This concept is also closely related to the easier recycling and reuse of the materials composing the devices. Embracing this principle of circularity enables the minimization of waste while promoting a more sustainable use of resources [5,6].

Another approach is to ensure appropriate sourcing of raw materials, thereby reducing both social and environmental impact associated with mining processes for obtaining metal raw materials such as lithium, cobalt, and nickel [7,8]. Efforts to substitute the currently used scarce materials for alternative materials are also playing an important role in sustainability [9].

Batteries are complex devices composed of a diverse range of materials, the composition of which varies depending on the type of battery. Nevertheless, all the battery devices are composed of anode, cathode, electrolyte, separator, current collectors, binders, and additives. Additionally, they feature a case and enclosure, along with supplementary systems such as cooling mechanism or sensors , designed to maintain the safety and monitor the state of the battery [10,11].

The most common cathode materials used for LIBs are Lithium Cobalt Oxide ($LiCoO_2$), Lithium-Ion Phosphate ($LiFePO_4$), and Lithium Nickel Cobalt Manganese Oxide (NCM), each with their performance characteristics. $LiCoO_2$ is commonly used in consumer electronics [12], while $LiFePO_4$ is used in electric vehicles and stationary storage [13], like the NCM [14]. In terms of anode materials, graphite, and other carbon materials are widely employed, which can store and release the lithium ions during the charging and discharging processes [15]. These electrodes, both the cathode and anode, can also incorporate additive materials that enhance the overall performance, stability, and safety of the battery. Similarly, binder materials can be added to maintain the integrity of the electrode material together, ensuring a homogeneous composition [16].

Substituting these materials with more abundant and sustainable alternatives can help in reducing the environmental impact on battery production [17,18]. An alternative gaining more attention is the implementation of biobased products, due to their high availability and carbon-neutral production. Lignin has widely been explored as an electrode and substitute for traditional carbon sources such as synthetic graphite. These materials range from biochar to lignin- or cellulose-derived carbon, with good conductivity and high surface area [19,20]. Alternatively, biobased polymers have been proposed as an alternative to synthetic binders and separators [21,22].

In this term, lignin is a plausible alternative. It is a byproduct of industrial processes like paper and pulp and biofuel production, and it is an interesting biopolymer due to its complex aromatic structure [23]. Depending on the extraction process carried out, and other factors like the lignocellulosic materials source and climatic conditions, its physicochemical properties and general characteristics can differ, making it a challenge for its large-scale processing [24]. Nevertheless, great efforts have been focused on the study of an alternative additive or binder material in battery electrodes [25].

The most widely used binder material is a synthetic polymer known as polyvinylidene fluoride (PVDF). While it offers some advantages such as excellent adhesion, chemical stability, and mechanical strength, it has limited ionic conductivity. This limitation can increase the resistance to the transportation of Li-ions through the electrodes, consequently reducing the capacity and performance of the battery. This is why conductive additives like carbon black are necessary [26]. Moreover, despite being widely available and cost-effective, specialized equipment and techniques are required due to its high melting point as well as the environmental concerns related to petroleum-derived materials [27,28].

Carboxymethyl cellulose (CMC) is a biobased polymer with great potential to substitute the currently used synthetic binders like PVDF due to its biobased nature and renewability [29]. However, CMC can swell in the presence of some electrolytes, along with some undesired interactions that can jeopardize the stability and performance of the electrode-electrolyte interface, reducing the cycling stability and performance of the battery [30].

A similar approach has been taken concerning the use of lignin as a commercial binder substitute. Lignin is biobased and renewable, similar to CMC. It has shown good compatibility with the active material and conductive additives such as carbon black. Lignin has the potential to

enhance the electrode performance, providing additional porosity to the electrode and improving the ion transportation [31–34].

Nevertheless, due to its novelty and the complex and heterogeneous structure of lignin, the process needs to be optimized. This optimization entails finding the ideal formulation for the electrode composition and fine-tuning the lignin by examining various types of lignin. These lignin variants come with diverse physicochemical and morphological properties, as well as a variety of functional groups. This comprehensive exploration is essential to assess the influence of lignin's structure on its performance as binder material for LIBs electrodes.

7.2. OBJECTIVES

The main objective of this work was to implement lignin as a battery material in anodic electrodes for LIBs and study the differences in the performance and stability of the batteries affected by the different physicochemical properties of the lignins.

To conduct this research, several lignin samples obtained throughout the different chapters of this work were implemented, and their differences were observed and justified. The study aimed to determine if the type of lignin (Kraft and organosolv) had a significant effect on the performance of the battery as a binder material for anodes. This exploration was crucial since these two types of lignin have not been employed in this manner before, and further research is necessary to broaden both the potential applications of lignin and diversify the options for binder materials in battery electrodes.

Moreover, other lignin characteristics such as molecular weight and polydispersity index were examined. Large and small molecular weight

lignin fractions, obtained in Chapter 4, were tested as binder materials. Chemically modified lignins, synthesized in Chapter 5, were also explored as potential binder materials. Different approaches were employed to obtain a variety of modified lignins with diverse functionalization and therefore, properties. The study tested whether an oxidized nanolignin, with higher carbonyl and hydroxyl content, enhanced the capacity and performance of the battery. Conversely, it investigated whether the reduction of these functional groups through the methylation reaction, brought more stability.

Furthermore, other modifications such as carboxymethylation and sulfomethylation were carried out. These strategies aimed to obtain materials similar to CMC but derived from lignin instead of cellulose. There were also attempts to produce materials similar to the lignosulfonates, which are interesting due to their water solubility and easy processability. These diverse modifications broadened the spectrum of potential binder materials derived from lignin for battery applications.

To assess the anode properties, a commercially available active material and an additive material were selected. The results obtained using the different lignins were compared with each other and with other commonly used commercial binder materials, namely, PVDF and CMC.

Half-batteries were assembled and cyclic voltammetry (CV), electrochemical impedance spectroscopy (EIS), and galvanostatic charge discharge cyclings (GCD) were conducted. These tests aimed to determine the capacity of the anode materials formulated for LIBs. Through these analyses, the performance of the different binder materials was thoroughly assessed and compared, providing valuable insights into their effectiveness in enhancing the properties of LIB anodes.

7.3. EXPERIMENTAL PROCEDURE

7.3.1. ANODIC ELECTRODE PREPARATION AND HALF-BATTERY COIN CELL ASSEMBLY

Different lignins obtained throughout the thesis were employed as binder material for the preparation of anodic electrodes for LIBs and compared with widely employed commercial biomaterial CMC binder, since it is more similar to our samples than the PVDF, and the chosen preparation method matches to the CMC process. The selected lignin samples to use as binder were the following: KL, BKL, SKL, OxKL, OL, BOL, SOL, OxOL, CMKL, SMKL and MKL.

The formulation used for the preparation of all the electrodes was the following: 92% of active material (Biohard Carbon (HC) Type 2 (5 m)), 3% conducting additive (Carbon Black C45, since the solvent used for the slurry preparation was deionized water), and 5% of binder. The slurry was homogenized using an automatic mixer. The conditions were set at 20000 rpm for 3 minutes, and the process was repeated twice, until a homogeneous 5 wt% concentration slurry mixture was obtained.

Once the slurry was obtained, the electrodes were assembled. For that, Cu foil was used as the current collector, and the slurry was spread by a doctor blade with a 150 μm thick gap to produce thin electrode layers. The slurry was dried at room temperature overnight, cut at 10 mm diameter disks, and dried at 120 °C overnight under vacuum before storing them in the glove box under argon atmosphere.

2032 coin-type cells were assembled for the electrochemical characterization of the anode. For that, $LiFePO_4$ was used as the counter electrode (12 nm diameter), a Whatman filter paper was used as the

separator, and 200 μL of 1M $LiPF_6$ in a 50:50 volume mixture of ethylene carbonate (EC) and dimethyl carbonate (DMC) as electrolyte.

The cells were extracted from the glove box and CV, EIS, and GC measurements were carried out as explained in Annex I, section A.5.2.

7.4. Results and Discussion

After a thorough study of the physicochemical and morphological properties of the different lignin samples obtained in the previous chapters, their electrochemical performance was tested. Half batteries were assembled and tested to explore the Li^+ storage performance and how that affected to the overall performance of the electrode.

First, voltammetry cyclings were carried out, followed by impedance spectroscopy, to observe general electrochemical characteristics of the samples. Following these observations, galvanostatic cyclings were performed on the rechargeable lithium half-cell batteries. During these cycling experiments, various parameters such as cycling performances, voltage profiles, and line profiles were obtained.

Voltammetry is used to observe the behavior of the electroactive species of the electrode caused by the linearly changing potential applied, measured as the resulting current. Figure 7.1 shows the CV curves and Nyquist plots obtained from the EIS measurements for the reference material used (CMC). Figure 7.2 and Figure 7.3 depict the voltammetry curves and Nyquist plots of the lignins derived from KL and OL, respectively. Both KL and OL have been treated through the different chapters of the thesis, obtaining lignins with different characteristics and properties that might influence the performance of the application in mind. Therefore, the big and small lignin fractions obtained in Chapter 4 (BKL, BOL, SKL and SOL) and the oxidized

nanolignins obtained in Chapter 5 (OxKL and OxOL) were implemented as binder material in the anodic electrode formulation. The redox reactions happening during the voltammetry cycles and their reversibility was assessed.

As mentioned before, Figure 7.1 displays the voltammetry results obtained for CMC used as binder. The 1st cycle exhibited an irreversible peak at 0.6 V, which is also evident in the 2nd cycle, though less intense and broader. This could be attributed to the formation of the SEI (solid electrolyte interphase). It resulted from several irreversible reactions where lithium salts, solvent decomposition products, and other reaction byproducts synthesized, forming a thin layer on the electrode. The formation of the SEI is crucial for many reasons: it prevents undesired reactions and degradation by acting as a protective shield, creating a barrier between the electrode and the electrolyte. This prevents direct contact thus ensuring stability and preventing battery failure. Additionally, it facilitates selective ion movement by restricting some ion transport while providing a pathway to lithium ions.

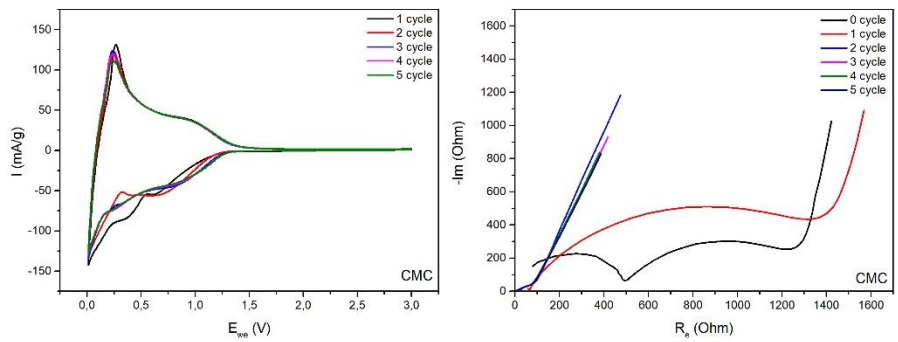

Figure 7.1. CV cycles and Nyquist plot of the reference used (CMC).

While SEI formation can enhance battery stability, performance, and lifespan, it can also have detrimental effects when the SEI layer becomes too thick or unstable. This hinders ion transport, increases resistance, and

subsequently, reduces the capacity of the battery [35,36]. Figure 7.1 shows that the SEI formed in CMC electrodes did not adversely impact the performance, as the values remained relatively stable before and after the formation.

In the case of Kraft and organosolv lignin and their modifications, slightly different behaviors were observed. Figure 7.2 shown the CV and EIS results obtained for KL and its fraction or modified analogues. KL, the most heterogenous lignin sample used, showed an intense irreversible redox peak at 0.6 V, which disappeared in the 2nd cycle. Its performance remained relatively similar throughout subsequent cycles. Nevertheless, this peak at 0.6 V did not appear in the first cycles of the BKL, SKL and OxOL. Since these lignins were much more homogenous than the KL, it can be deduced that the intense peak at 0.6 V was a result of undesired side reactions.

Regarding the differences between BKL and SKL, similar currents were obtained. However, BKL exhibited a decline in the performance as the cycle number increased, indicating that smaller lignin provided greater stability to the electrode. OxKL displayed a similar behavior to SKL but with enhanced current due to the higher presence of oxidizing functional groups like carboxyl or hydroxyl groups. Additionally, its higher surface area, due to the smaller particle size studied in Chapter 5, also contributed to enhance the current.

In Figure 7.3, the results obtained with OL and its fraction or modified analogues as binder are depicted, showing very different outcomes. The results were not stable enough to draw any conclusions, whereas OL and OxOL exhibited curves more in line with the expected. OL showed two irreversible peaks, at 0.5 V and at 0.7 V, which did not reappear in subsequent cycles. These peaks might be attributed to degradation reactions, rendering them unsuitable for electrode formulations due to the

lack of required stability. OxOL, showed higher current intensities, possibly owing to the increased functionalization achieved through the methodology designed in Chapter 5. Nevertheless, a decrease in intensity was evident, as along with irreversible peaks, also attributed to degradation processes.

Although EIS measurements provide very complex information, the Nyquist plots depicted in Figures 7.1, 7.2 and 7.3 offer information on the resistance of the system. Nyquist plots typically consist of one or two semicircles and a 45° angle line. The line represents capacity-like behavior resistances, while the semicircles are associated with the resistance created by contributions of functional groups, defects, or interfacial impedance occurring at the interphase of current collector and active material. The capacity-like behavior resistance appears at low frequencies, whereas the semicircle associated to charge transfer (R_{ct}) and mass transfer (R_{mt}) resistances, emerge at slightly higher frequencies. Electrolyte resistance (R_{∞}) occurs at even higher frequencies, followed by electrode resistance (R_p).

The evolution of the resistance is also depicted as different phenomena occurred within the electrode. In the 0 cycle (measured before any CV was conducted) two semicircles were observed in the case of CMC, attributed to R_{ct}, R_{mt}, and R_{∞}. After the first cycle and the subsequent SEI formation, a single semicircle appeared, followed by the further reduction in resistance in the following cycles. This reduction occurred as the semicircle and capacity-like behavior line resistances appeared at much higher frequencies.

A similar trend was observed for the different KL samples in Figure 7.2, where the 0 and 1 cycle exhibited considerably higher resistances than the later cycles. However, this was not observed in some of the OL samples mentioned earlier as unstable, where no differences in resistance were noted. The OL and OxOL samples did show a similar behavior to the rest of the samples, including the CMC used as reference and KL, where resistance

values decreased significantly after some cycles and considerably more stable electrodes were obtained, compared to their BOL and SOL analogues.

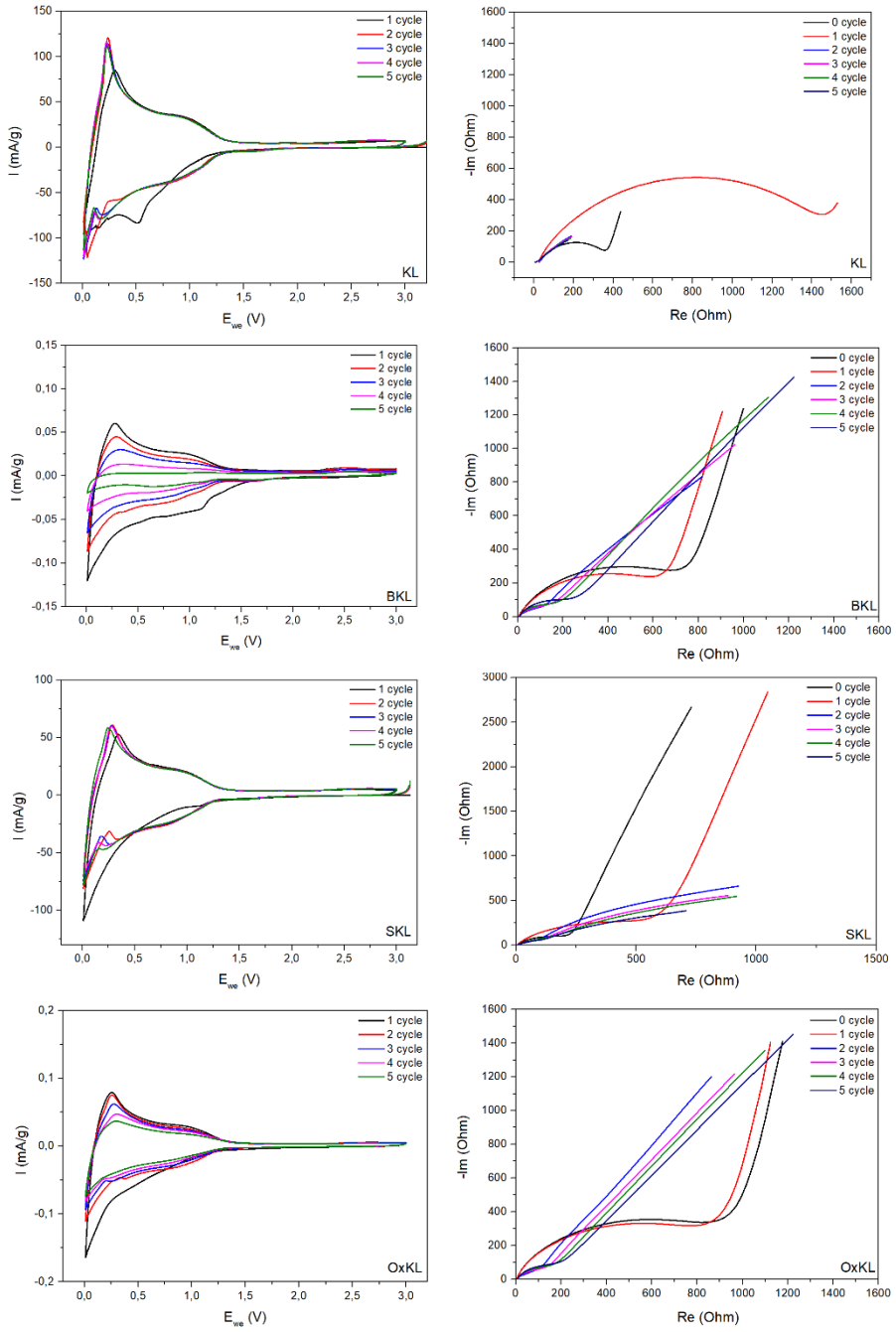

Figure 7.2. CV cycles and EIS curves for the samples KL, BKL, SKL, and OxKL.

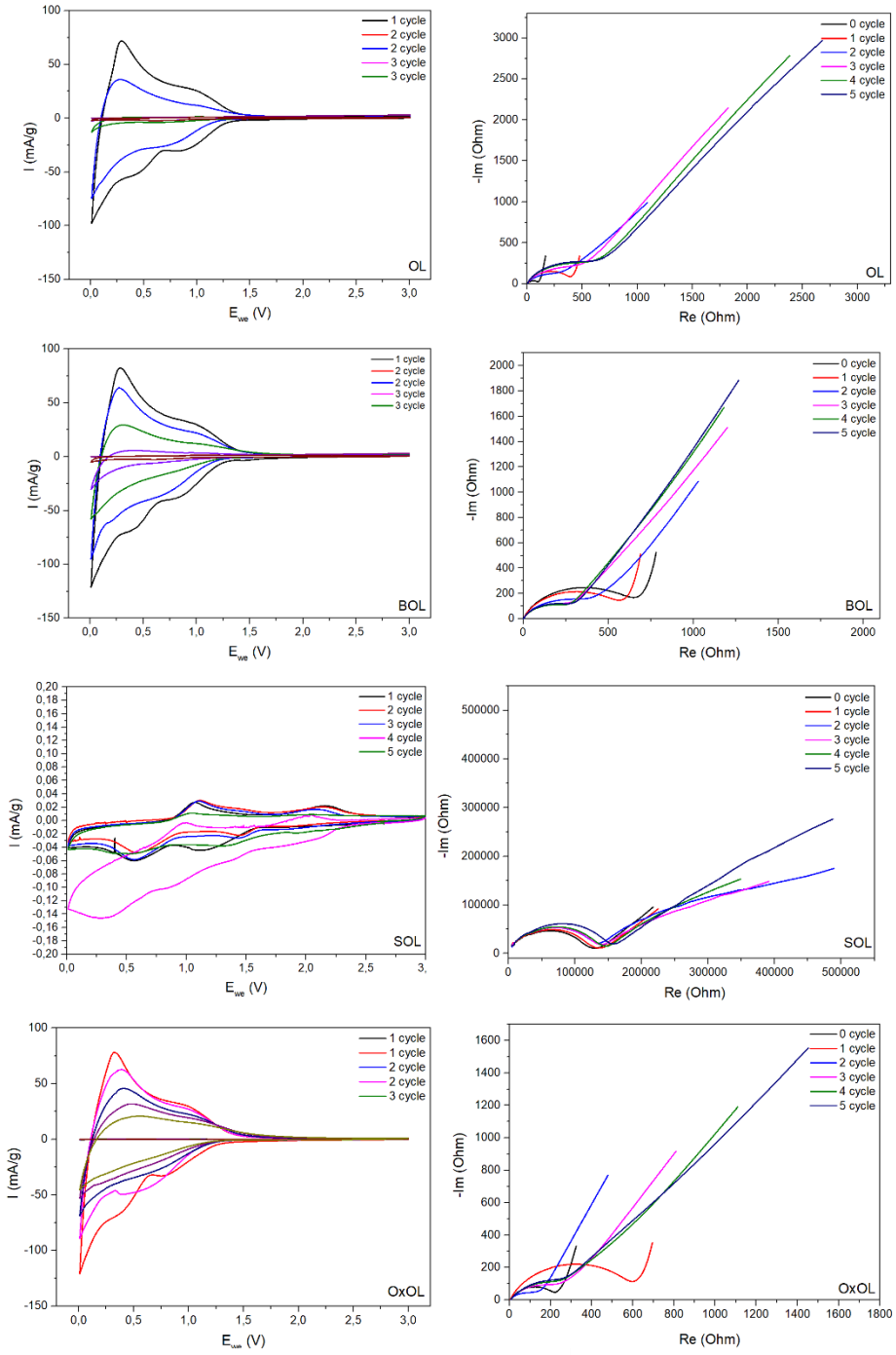

Figure 7.3. CV cycles and Nyquist plots of OL, BOL, SOL and OxOL.

The specific charge and discharge capacities and Coulombic efficiencies (CE) obtained from the galvanostatic cycling measurements are presented in Figure 7.4 for CMC and Figure 7.5 for the different KL samples. It was observed in Figure 7.4 that, although the CE remained relatively stable, the capacity decreased drastically for all samples. This was attributed to the poor conditions of the electrolyte used, which was later found to be degraded. However, despite the inconclusive nature of the results, some interesting observations could be made.

CMC, as commercially used binder material, demonstrated the required properties for the correct performance of LIBs. An initial capacity of 150 mA h g^{-1} was measured at a current density of 20 mA h g^{-1} which drastically increased as the current density (I_m) increased. The capacity values reached extremely low levels at the highest I_m (1000 mA h g^{-1}). A similar phenomenon was observed for the different lignins derived from Kraft process. Most of the samples, except for SKL which exhibited even lower values, showed a decrease in capacity at the lowest current density (20 mA), obtaining values of 50 mA h g^{-1} that further decreased as the charge and discharge cycles were carried out and the current density increased.

Therefore, preliminary studies suggest that KL is more suitable than OL to use as binder, as it brings more stability to the electrode and gives better performance. Similarly, the oxidized lignin nanoparticles, showed good stability in both OxKL and OxOL samples. Nevertheless, preliminary studies on the obtained results suggest that KL and SKL exhibited worse performance than BKL and OxKL, indicating that larger molecules demonstrated higher stability, while oxidized lignin nanoparticles showed enhanced capacity.

Since the obtained results were not satisfactory, the chemical modifications already explained in Chapter 5, involving carboxymethylation,

sulfomethylation and methylation were applied. These modified lignins were used the same way as binder materials, aiming to further explore the effect of the lignin functionalization on the battery stability and performance. Due to the diverse natures of the modifications and the resulting products, noticeable differences were observed.

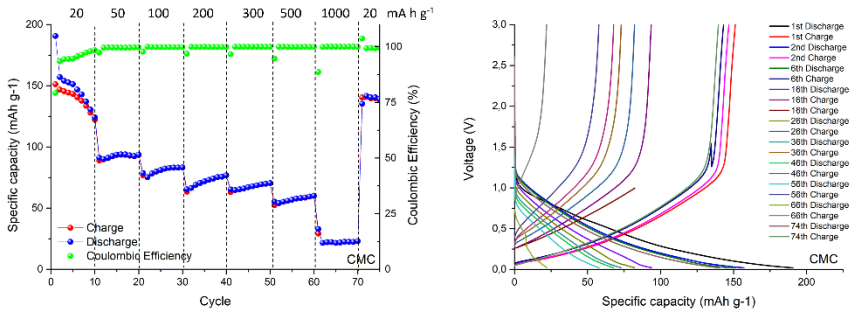

Figure 7.4. GCD cycling and line profiles of the anodes with CMC as binder.

For instance, methylated lignin showed a considerable decrease in polarity due to the reduction of the naturally polar OH groups that reacted to yield methoxy groups. This reduction in polarity proved to be detrimental during the electrode preparation process. Although a homogeneous slurry was achieved, some issues arose during the casting process onto copper foil. As the binder was apolar, the adhesion obtained from the dried slurry was insufficient for manipulation and use in the coin cell assembly. Consequently, no electrochemical measurements were obtained on the electrodes formulated with methylated lignin.

Nevertheless, carboxymethylated (CMKL) and sulfomethylated (SMKL) lignin samples exhibited interesting results. Following the preparation of the CMKL and SMKL, new CMC electrodes were prepared, 2032 coin cells were assembled and electrochemical measurements were conducted. The CV and EIS measurements depicted in Figure 7.6 displayed different behavior from what was observed in Figure 7.1, with significantly higher currents obtained in the CVs and lower resistance values in the Nyquist plots.

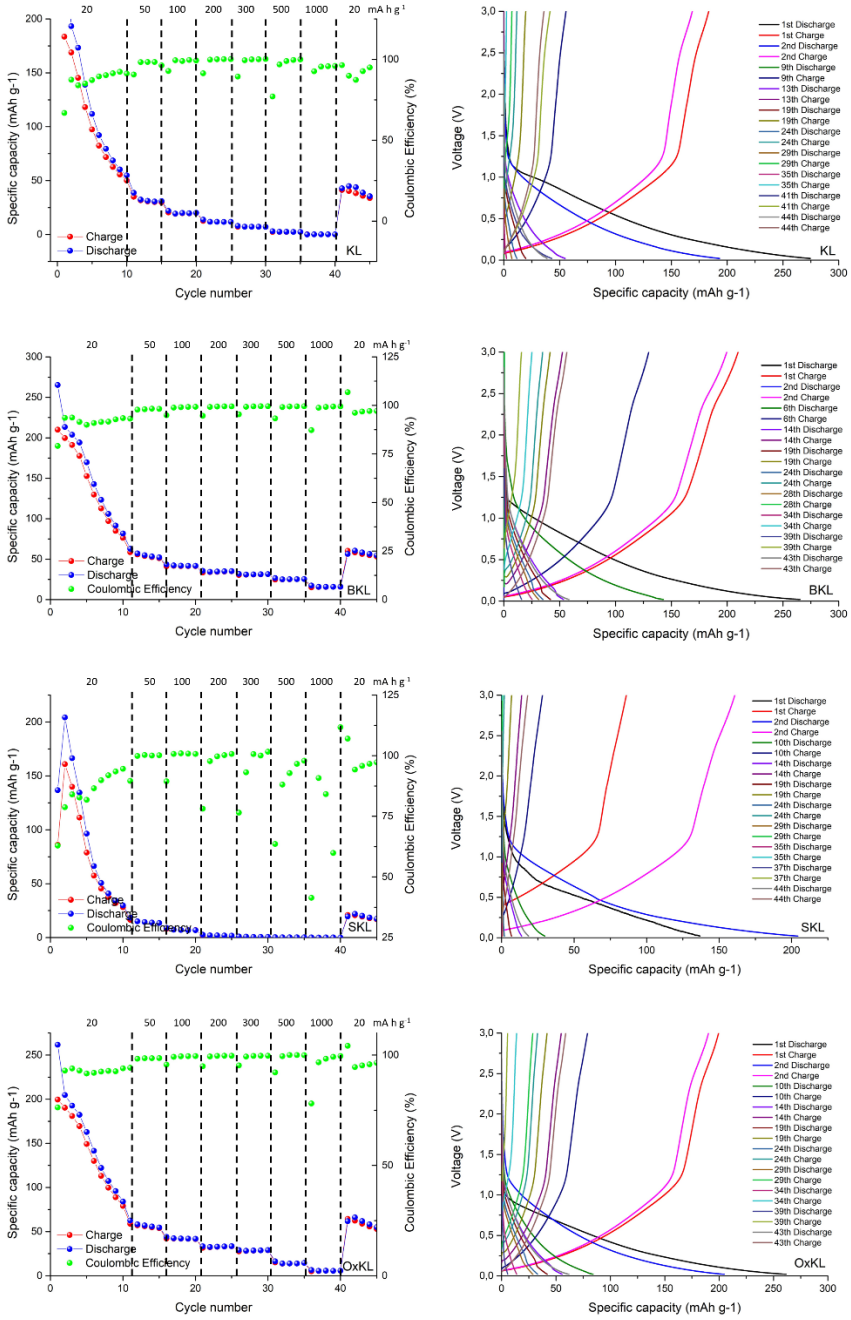

Figure 7.5. GCD cycling and line profile of the anodes formulated with KL, BKL, SKL and OxOL as binder.

Regarding the unmodified KL, which was also tested under the same conditions but with a new electrolyte, some irreversible redox reaction peaks were observed in the 1st cycle. These peaks were previously attributed to certain degradation reactions due to heterogeneity. However, in the case of CMKL and SMKL, both samples exhibited a single peak at 0.6 V for the 1st cycle, and another one at 0.85 V for the 2nd cycle. Remarkably, the current remained relatively stable throughout the cycling, without any noticeable performance losses. Additionally, the Nyquist plots for CMKL and SMKL showed semicircle and lines at much lower frequencies of the electrodes' resistance values, indicating significantly lower resistance in the system.

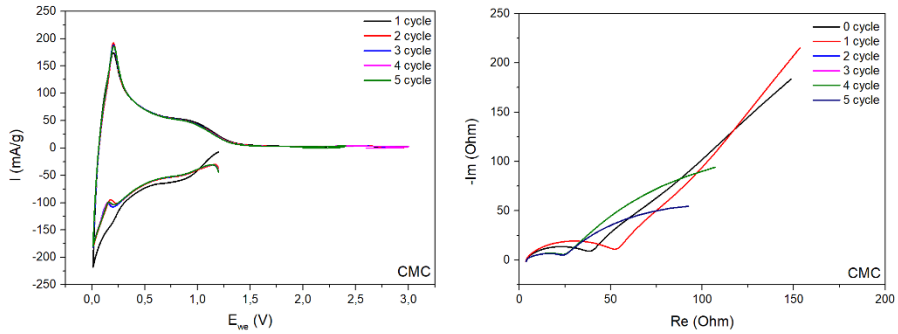

Figure 7.6. CV cycles and Nyquist plot for CMC.

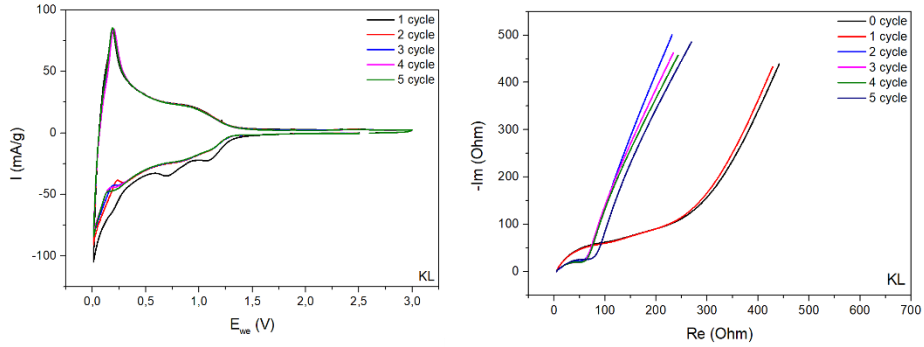

Figure 7.7. CV cycles and Nyquist plot for KL.

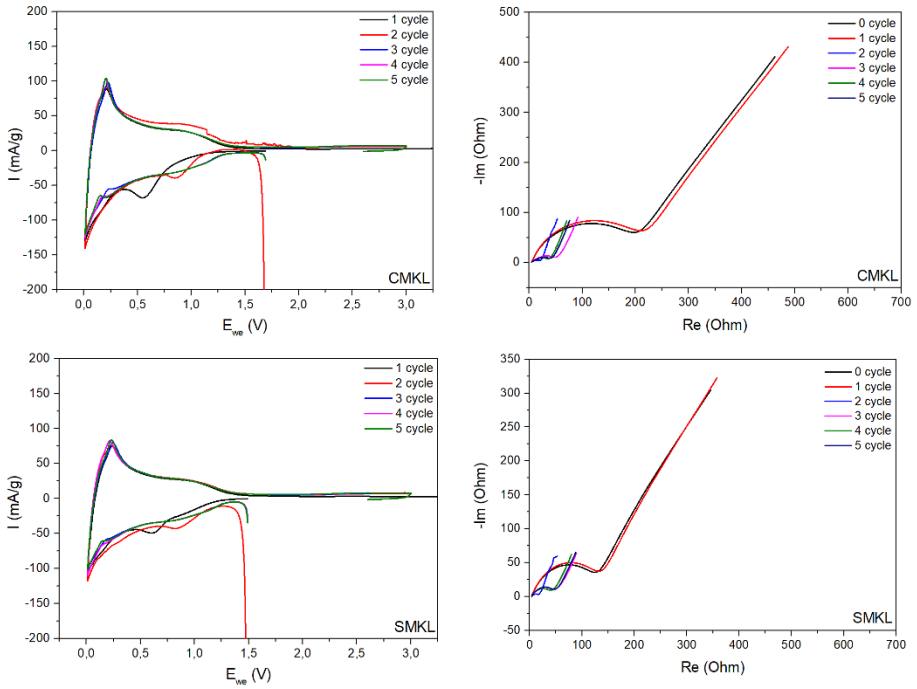

Figure 7.8. CV cycles and Nyquist plot for CMKL and SMKL.

GCD cyclings were also performed at different current densities, and SC and CE were calculated, with line profiles displayed. Figure 7.9 presents the results obtained from the new measurements conducted for CMC, serving as reference for comparison with the new KL samples and the modified CMKL and SMKL.

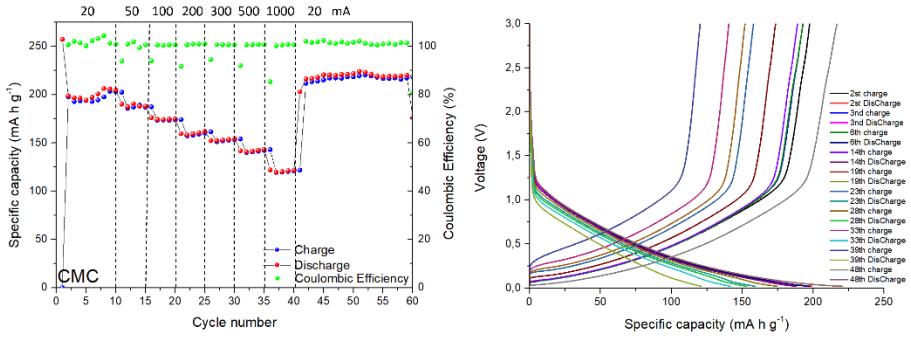

Figure 7.9. GCD cycling and line profile of the anodes formulated with CMC.

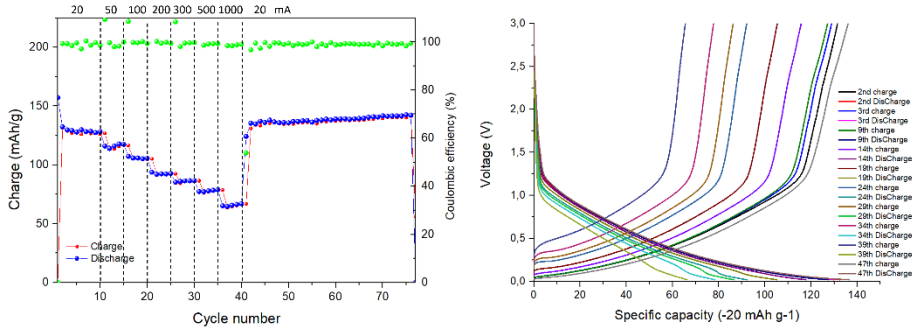

Figure 7.10. GCD cycling and line profile of the anodes formulated with KL as binder.

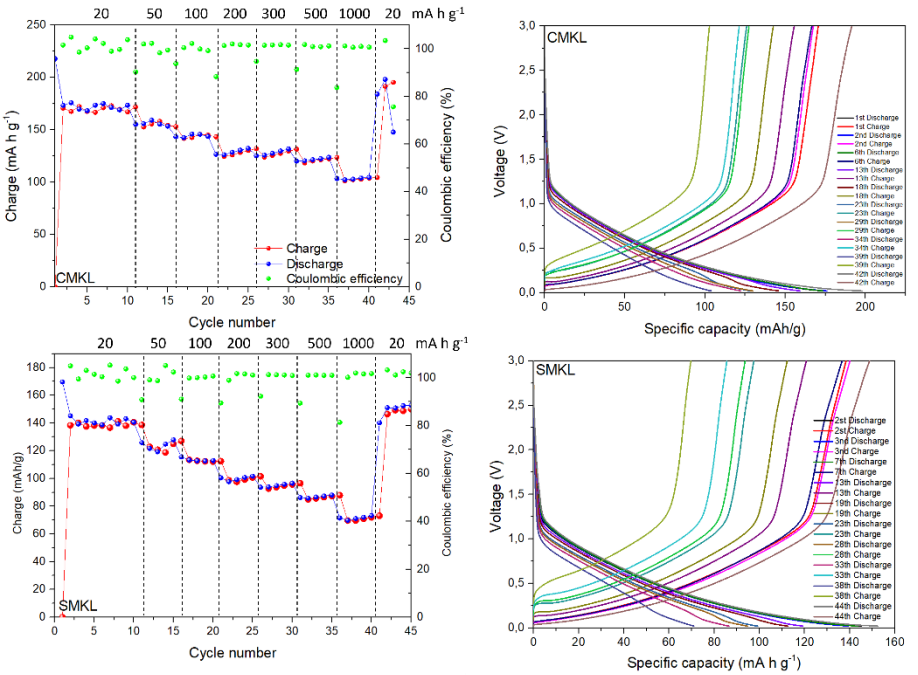

Figure 7.11. GCD cycling and line profile of the anodes formulated with CMKL and SMKL as binder.

CMC exhibited good capacity, with values of 200 mA h g^{-1} at the lowest current density, which slightly decreased as the I_m decreased. In contrast, the electrode composed of KL showed lower capacity values, around 125 mA h g^{-1}, decreasing to 65 mA h g^{-1} at the highest current density.

However, the carboxymethylation and sulfomethylation modifications showed improved properties compared to their KL counterpart. The capacity increased to 175 mA h g^{-1} for CMKL and 140 mA h g^{-1} for SMKL, maintaining good capacity even at higher I_m-s. This is due to the higher charge density obtained for carboxymethylated and sulfomethylated lignin particles, which not only helped in obtaining a well dispersed slurry for the electrode formulation and a good adhesion to the Cu used as current collector of the anode, but also and, more importantly, added charge density for the enhanced performance of the anode as a component of the LIBs.

7.5. CONCLUSIONS

The results obtained in this study, combined with the findings from Chapter 5 where various physicochemical properties were analyzed, lead to the conclusion that the synthesized lignin products are suitable materials to incorporate as binder materials on the formulation of anodic electrodes for LIBs. This discovery opened up promising opportunities to valorize this complex biomaterial derived from wood, which is traditionally considered as waste. It can serve as a viable substitute for the currently employed synthetic and highly toxic analogues such as PVDF. The potential to utilize lignin in this manner not only addresses environmental concerns associated with waste management but also contributes to the development of more sustainable and eco-friendly energy storage technologies. It was found out that the most effective lignin modification for enhanced performance was the carboxymethylation, which provided lignin particles with an added charge density that was beneficial both for the electrode preparation and its perfprmance. Moreover, the procedure for the CMKL was quite straightforward.

7.6. REFERENCES

[1] Hannan MA, Wali SB, Ker PJ, Rahman MSA, Mansor M, Ramachandaramurthy VK, et al. Battery energy-storage system: A review of technologies, optimization objectives, constraints, approaches, and outstanding issues. J Energy Storage 2021;42:103023. https://doi.org/10.1016/J.EST.2021.103023.

[2] Afgan NH, Al Gobaisi D, Carvalho MG, Cumo M. Sustainable energy development. Renew Sustain Energy Rev 1998;2:235–86. https://doi.org/10.1016/S1364-0321(98)00002-1.

[3] Torreglosa JP, García-Triviño P, Fernández-Ramirez LM, Jurado F. Decentralized energy management strategy based on predictive controllers for a medium voltage direct current photovoltaic electric vehicle charging station. Energy Convers Manag 2016;108:1–13. https://doi.org/10.1016/j.enconman.2015.10.074.

[4] Díaz-Ramírez MC, Ferreira VJ, García-Armingol T, López-Sabirón AM, Ferreira G. Environmental Assessment of Electrochemical Energy Storage Device Manufacturing to Identify Drivers for Attaining Goals of Sustainable Materials 4.0. Sustainability 2020;12.

[5] Zhang J, Li B, Garg A, Liu Y. A generic framework for recycling of battery module for electric vehicle by combining the mechanical and chemical procedures. Int J Energy Res 2018;42:3390–9. https://doi.org/10.1002/er.4077.

[6] Zhang B, Li J, Yue X. Driving mechanism of power battery recycling systems in companies. Int J Environ Res Public Health 2020;17:1–21. https://doi.org/10.3390/ijerph17218204.

[7] Liu G, Zhao Z, Ghahreman A. Hydrometallurgy Novel approaches for lithium extraction from salt-lake brines : A review. Hydrometallurgy 2019;187:81–

100. https://doi.org/10.1016/j.hydromet.2019.05.005.

[8] Ilyas S, Ranjan R, Kim H, Ilyas N, Sattar R. Separation and Puri fi cation Technology Extraction of nickel and cobalt from a laterite ore using the carbothermic reduction roasting-ammoniacal leaching process. Sep Purif Technol 2020;232:115971. https://doi.org/10.1016/j.seppur.2019.115971.

[9] Dhanalekshmi KI, Magesan P, Ma X, Zhang X, Jayamoorthy K. Sustainable development of anode materials for non-aqueous potassium ion batteries. J Energy Storage 2023;68:107691. https://doi.org/10.1016/j.est.2023.107691.

[10] Peng J, Zhang W, Wang J, Li L, Lai W, Yang Q, et al. Processing Rusty Metals into Versatile Prussian Blue for Sustainable Energy Storage 2021;2102356:1–6. https://doi.org/10.1002/aenm.202102356.

[11] Jin C, Nai J, Sheng O, Yuan H, Zhang W, Tao X, et al. Biomass-based materials for green lithium secondary batteries. Energy Environ Sci 2021;14:1326–79. https://doi.org/10.1039/d0ee02848g.

[12] Chu B, Guo Y, Shi J, Yin Y, Huang T, Su H. Cobalt in high-energy-density layered cathode materials for lithium ion batteries. J Power Sources 2022;544.

[13] Zhao Q, Zhang S, Hu M, Wang C, Jiang G. Recent Advances in LiFePO 4 Cathode Materials for Lithium-Ion. Int J Electrochem Sci 2021;16:211226. https://doi.org/10.20964/2021.12.11.

[14] Malik M, Ho K, Azimi G. Review on the synthesis of LiNixMnyCo1-x-yO2 (NMC) cathodes for lithium-ion batteries. Mater Today Energy 2022;28:101066. https://doi.org/10.1016/j.mtener.2022.101066.

[15] Nzereogu PU, Omah AD, Ezema FI, Iwuoha EI, Nwanya AC. Applied Surface Science Advances Anode materials for lithium-ion batteries : A review. Appl

Surf Sci Adv 2022;9:100233. https://doi.org/10.1016/j.apsadv.2022.100233.

[16] Rana S, Kumar R, Bharj RS. Current trends , challenges , and prospects in material advances for improving the overall safety of lithium-ion battery pack. Chem Eng J 2023;463:142336. https://doi.org/10.1016/j.cej.2023.142336.

[17] Vandepaer L, Cloutier J, Amor B. Environmental impacts of Lithium Metal Polymer and Lithium-ion stationary batteries. Renew Sustain Energy Rev 2017;78:46–60. https://doi.org/10.1016/j.rser.2017.04.057.

[18] Gu X, Ieromonachou P, Zhou L, Tseng M. Developing pricing strategy to optimise total pro fi ts in an electric vehicle battery closed loop supply chain. J Clean Prod 2018;203:376–85. https://doi.org/10.1016/j.jclepro.2018.08.209.

[19] Puziy AM, Poddubnaya OI, Sevastyanova O. Carbon Materials from Technical Lignins: Recent Advances. vol. 376. Springer International Publishing; 2018. https://doi.org/10.1007/s41061-018-0210-7.

[20] García-Negrón V, Phillip ND, Li J, Daniel C, Wood D, Keffer DJ, et al. Processing–Structure–Property Relationships for Lignin-Based Carbonaceous Materials Used in Energy-Storage Applications. Energy Technol 2017;5:1311–21. https://doi.org/10.1002/ente.201600646.

[21] Andrew JJ, Dhakal HN. Sustainable biobased composites for advanced applications: recent trends and future opportunities – A critical review. Compos Part C Open Access 2022;7. https://doi.org/10.1016/j.jcomc.2021.100220.

[22] Schlemmer W, Selinger J, Hobisch MA, Spirk S. Polysaccharides for sustainable energy storage – A review. Carbohydr Polym 2021;265. https://doi.org/10.1016/j.carbpol.2021.118063.

[23] Putro JN, Soetaredjo FE, Lin SY, Ju YH, Ismadji S. Pretreatment and conversion of lignocellulose biomass into valuable chemicals. RSC Adv 2016;6:46834–52. https://doi.org/10.1039/C6RA09851G.

[24] Balakshin MY, Capanema EA, Sulaeva I, Schlee P, Huang Z, Feng M, et al. New Opportunities in the Valorization of Technical Lignins. ChemSusChem 2021;14:1016–36. https://doi.org/10.1002/cssc.202002553.

[25] Espinoza-Acosta JL, Torres-Chávez PI, Olmedo-Martínez JL, Vega-Rios A, Flores-Gallardo S, Zaragoza-Contreras EA. Lignin in storage and renewable energy applications: A review. J Energy Chem 2018;27:1422–38. https://doi.org/10.1016/J.JECHEM.2018.02.015.

[26] Gómez Cámer JL, Morales J, Sánchez L, Ruch P, Ng SH, Kötz R, et al. Nanosized Si/cellulose fiber/carbon composites as high capacity anodes for lithium-ion batteries: A galvanostatic and dilatometric study. Electrochim Acta 2009;54:6713–7. https://doi.org/10.1016/j.electacta.2009.06.085.

[27] Figoli A, Marino T, Simone S, Nicolò E Di, Li X, He T, et al. Towards non-toxic solvents for membrane preparation : a review 2014:4034–59. https://doi.org/10.1039/c4gc00613e.

[28] Zou D, Nunes SP, Vankelecom IFJ, Figoli A, Lee YM. Recent advances in polymer membranes employing non-toxic solvents and materials. Green Chemisntry 2024;23:9815–43. https://doi.org/10.1039/d1gc03318b.

[29] Bresser D, Buchholz D, Moretti A, Passerini S, Varzi A, Buchholz D. Alternative binders for sustainable electrochemical energy storage – the transition bio-derived polymers. Energy Environ Sci 2018;11:3096. https://doi.org/10.1039/c8ee00640g.

[30] Akhlaq M, Mushtaq U, Naz S. Carboxymethyl cellulose-based materials as an alternative source for sustainable electrochemical devices: a review. RSC Adv 2023;13:5723–43. https://doi.org/10.1039/d2ra08244f.

[31] Tran VC, Mastantuoni GG, Belaineh D, Aminzadeh S, Berglund LA, Berggren M, et al. Utilizing native lignin as redox-active material in conductive wood for electronic and energy storage applications. J Mater Chem A 2022;10:15677–88. https://doi.org/10.1039/d1ta10366k.

[32] Liu H, Xu T, Liu K, Zhang M, Liu W, Li H, et al. Lignin-based electrodes for energy storage application. Ind Crops Prod 2021;165. https://doi.org/10.1016/j.indcrop.2021.113425.

[33] Jia G, Yu Y, Wang X, Jia C, Hu Z, Yu S, et al. Highly conductive and porous lignin-derived carbon fibers. Mater Horizons 2023. https://doi.org/10.1039/d3mh01027a.

[34] Wang J, Deng Y, Ma Z, Wang Y, Zhang S, Yan L. Lignin promoted the fast formation of a robust and highly conductive deep eutectic solvent ionic gel at room temperature for a flexible quasi-solid-state supercapacitor and strain sensors. Green Chem 2021;23:5120–8. https://doi.org/10.1039/d1gc01512e.

[35] Song W, Scholtis S, Sherrell PC, Tsang DKH, Ngiam J, Lischner J, et al. Electronic structure influences on the formation of the solid electrolyte interphase. Energy Environ Sci 2020;13:4977–89. https://doi.org/10.1039/d0ee01825b.

[36] Young BT, Nguyen CC, Lobach A, Heskett DR, Woicik JC, Lucht BL. Role of binders in solid electrolyte interphase formation in lithium ion batteries studied with hard X-ray photoelectron spectroscopy. Jouranl Mater Res 2019;34:97–106. https://doi.org/10.1557/jmr.2018.363.

[37] Zhou B, Liu W, Gong Y, Dong L, Deng Y. High-performance pseudocapacitors from kraft lignin modified active carbon. Electrochim Acta 2019;320. https://doi.org/10.1016/J.ELECTACTA.2019.134640.

8. Conclusions and future works

8.1. FINAL CONCLUSIONS

The present work was focused on obtaining fine-tuned and modified lignins from different extraction processes, namely Kraft and organosolv for their application in the formulation of materials for energy storage devices. Comprehensive characterization techniques and methodologies were employed to assess the differences in terms of chemical composition, physicochemical attributes, thermal behavior, morphological structure, and electrochemical properties. The incorporation of lignin into materials intended for energy storage devices showed interesting results, making them plausible alternatives to the currently used synthetic polymers or additives. These findings suggest that lignin can serve as a promising substitute, enhancing the performance of active materials in energy storage applications.

Moreover, some more specific conclusions referring to each chapter can be obtained. First of all, the fractionation process, based on the sequential organic solvent extraction, was developed to obtain different M_w fractions with enhanced homogeneity and consequently, different properties. This method was successfully designed and tested on different types of lignin, showing its effectiveness and versatility across different lignin sources while delivering similar results. Moreover, the use of the greenest possible organic solvents rendered the process relatively environmentally friendly. Notably those solvents used are recyclable, highlighting the sustainability of the approach as they can be recovered and reused, further contributing to its green credentials.

Secondly, various lignin modifications were carried out to observe the differences for their intended applications. Additionally, lignin was oxidized under mild conditions and was enhanced with ultrasound forces, which not only resulted in lignin with richer oxidizing functional groups, but also

nanosized lignin particles. These particles contained highly interesting properties suitable for a wide range of applications, enhancing the lignin valorization for high-value purposes. Another strategy for modifying lignin involved reactions with the most common functional group of lignin, the hydroxyl group, to obtain functional groups with different characteristics. Methylation resulted in more apolar lignin, characterized by the conversion of hydroxyl groups into methoxy groups. In contrast, carboxymethylation and sulfomethylation reactions increased the polyionic properties of lignin, proving to be particularly advantageous for energy storage material applications.

In addition to lignin fractionation and modification, conducting materials were synthesized incorporating lignin as a component. One approach, involved creating hybrid materials composed of AC and lignin (KL and OL). Lignin particles were deposited on the AC surface, enhancing morphological properties that significantly influenced the performance of the active material. This process enhanced conductive properties and increased the material's capacity. Lignin was also employed as an exfoliating agent of graphite oxide, which was also intercalate between the GO sheets. It was found that besides being an effective exfoliating agent, lignin also improved the capacitance values of the material.

Finally, the previously mentioned fractionated and modified lignins were incorporated into the formulation of anodic electrode materials and tested in half-cell LIBs. Although more in-depth analysis is required to draw comprehensive conclusions, differences in battery performance were observed based on the lignin type, molecular weight and functionality. Kraft lignins exhibited better results compared to organosolv lignins, and lignins with larger molecular sizes demonstrated higher stability than smaller ones. In terms of the modifications carried out, oxidized lignin nanoparticles also displayed promising performance. However, the most interesting results

were obtained for carboxymethylated lignin, followed by sulfomethylated lignin. These findings suggest plausible opportunities to consider lignin as binder material for electrode preparation, introducing new possibilities for biobased and sustainable battery component materials.

8.2. FUTURE WORKS

Some studies following a similar route to the work presented can be taken into consideration for possible future works.

The anodic electrodes discussed in Chapter 7 could be subjected to further exploration, by assembling full-cell batteries and analyzing their performance. Moreover, it would be valuable to investigate properties associated to the binder performance such as mechanical properties, chemical stability, dispersive capabilities, and the analysis of electrode microstructure. These analyses would contribute to a complete characterization of the material, providing a deeper understanding of its behavior and potential applications.

Alternatively, innovative materials based on lignin could be designed for various components of energy storage devices, such as cathode, separators, and electrolytes among others. Exploring combinations of lignin with other biobased materials and biopolymers could yield highly sustainable alternatives to substitute the currently used materials.

This focus could also be expanded to different devices such as supercapacitors, fuel cells, or solar cells, among others. Additionally, exploring alternative battery materials could be considered, including solid-state batteries, or batteries utilizing alternative metals to lithium such as sodium-ion, nickel-ion or silicium-ion batteries. Metal-air batteries also present intriguing possibilities for research and development.

Finally, additional research into lignin valorization could be pursued. Given its proven versatility in many different applications, another approach following the work in this thesis would involve identifying other suitable applications for the lignins obtained through the fractionation and modifications. Exploring optimal employments for both high or small molecular weight lignin particles, as well as implementing the synthesized oxidized lignin nanoparticles, carboxymethylated and sulfomethylated lignins, open new avenues for maximizing the potential of lignin in diverse industrial applications.

8.3. SCIENTIFIC PRODUCTION

The following section lists the produced publications related to the doctoral thesis:

1. *Authors:* **Izaguirre, N.**, Robles, E., Llano-Ponte, R., Labidi, J., Erdocia, X.
   Title: Fine-tune of lignin properties by its fractionation with a sequential organic solvent extraction
   Journal: Industrial Crops and Products
   Year: 2022
   DOI: 10.1016/j.indcrop.2021.114251
   Impact factor: 5.9 (2022)
   JCR: Agricultural Engineering (3/14) Q1

2. *Authors:* **Izaguirre, N.**, Fernández-Rodríguez, J., Robles, E., Labidi, J.
   Title: Sonochemical oxidation of technical lignin to obtain nanoparticles with enhanced functionality
   Journal: Green Chemistry
   Year: 2023
   DOI: 10.1039/d3gc01037

Impact factor: 9.8 (2022)

JCR: Green & Sustainable Science & Technology (9/46) Q1

3. *Authors:* **Izaguirre, N.**, Alberro, M., Erdocia, X., Labidi, J.
   Title: Kraft and Organosolv Lignin-Active Carbon Composites for Supercapacitor Electrode Materials
   Journal: Journal of Energy Storage (under revision)
   Year: 2023
   DOI:
   Impact factor: 9.4 (2022)
   JCR: Energy & Fuels (19/119) Q1

4. *Authors:* **Izaguirre, N.**, Alberro, M., Erdocia, X., Labidi, J.
   Title: Partially Exfoliated Graphene and Lignin Composites for Battery Electrode Materials
   Journal: Journal of Cleaner Production (submitted)
   Year:
   DOI:
   Impact factor: 11.1 (2022)
   JCR: Green & Sustainable Science & Technology (8/46) Q1

5. *Authors*: **Izaguirre, N.**, Erdocia, X., Labidi, J.
   Title: Exploring Chemical Reactions to Enhance Thermal and Dispersion Stability in Kraft and Organosolv Lignin
   Journal: International Journal of Biological Macromolecules (submitted)
   Year:
   DOI:
   Impact factor: 8.2 (2022)
   JCR: Polymer Science (5/86) Q1

6. *Authors:* **Izaguirre, N.**, Lingua, G., Mecerreyes, D., Labidi, J., Gerbaldi, C. (under development)
   Title: Chemically modified kraft lignin as water processable binder materials for LIB anodes
   Journal:
   Year:
   DOI:
   Impact factor:
   JCR:

Moreover, other publication and collaborations non-related to the topic of the thesis have also been published and written:

1. *Authors:* Wolf, M.H., **Izaguirre, N.**, Pascual José, B., Teruel Juanes, R., Labidi, J., Ribes-Greus, A.
   Title: Dielectric Characterisation of Chitosan-based Composite Membranes containing fractionated Kraft and Organosolv Lignin
   Journal: Reactive and Functional Polymers (submitted)
   Year:
   DOI:
   Impact factor: 5.1 (2022)
   JCR: Applied Chemistry (16/73) Q1

2. *Authors:* Robles, E., **Izaguirre, N.**, Baraka, F., Barandiaran, I., Csóka, L., Labidi, J.
   Title: Study of the deterioration of cellulose nanofibers through recycling of cellulose nanopapers
   Journal: Cellulose (submitted)
   Year:
   DOI:
   Impact factor: 5.7 (2022)

JCR: Materials Science, Paper & Wood (1/21) Q1

3. *Authors:* Tahari, N., de Hoyos-Martinez, P. L**., Izaguirre, N.**, Houwaida, N., Abderrabba, M., Ayadi, S., Labidi, J.
   Title: Preparation of chitosan/tannin and montmorillonite films as adsorbents for Methyl Orange dye removal
   Journal: International Journal of Biological Macromolecules
   Year: 2022
   DOI: 10.1016/j.ijbiomac.2022.04.231
   Impact factor: 8.2 (2022)
   JCR: Polymer Science (5/86) Q1

4. *Authors:* Robles, E., **Izaguirre, N.**, Martin, A., Moschou, D., Labidi, J.
   Title: Assessment of bleached and unbleached nanofibers from pistachio shells for nanopaper making
   Journal: Molecules
   Year: 2021
   DOI: 10.3390/molecules26051371
   Impact factor: 4.6 (2022)
   JCR: Chemistry, Multidisciplinary (63/178) Q2

5. *Authors:* **Izaguirre, N.**, Gordobil, O., Robles, E., Labidi, J.
   Title: Enhancement of UV absorbance and mechanical properties of chitosan films by the incorporation of solvolytically fractionated lignins
   Journal: International Journal of Biological Macromolecules
   Year: 2020
   DOI: 10.1016/j.ijbiomac.2020.03.162
   Impact factor: 8.2 (2022)
   JCR: Polymer Science (5/86) Q1

7. *Authors:* Robles, E., **Izaguirre, N.**, Dogaru, B. I., Popescu, C. M., Barandiaran, I., Labidi, J.
   Title: Sonochemical production of nanoscaled crystalline cellulose using organic acids
   Journal: Green Chemistry
   Year: 2020
   DOI: 2020-08-04
   Impact factor: 9.8 (2022)
   JCR: Green & Sustainable Science & Technology (9/46) Q1

8. *Authors:* Sillero, L., Barriga, S., **Izaguirre, N.**, Labidi, J., Robles, E.
   Title: Fractionation of non-timber wood from Atlantic mixed forest into high-value lignocellulosic materials
   Journal: Journal of Wood Chemistry and Technology
   Year: 2020
   DOI: 10.1080/02773813.2020.1737132
   Impact factor: 2 (2022)
   JCR: Materials Science, Paper & Wood (7/21) Q2

The following contribution in the redaction of the mentioned Book Chapter was also published during the thesis:

> Erdocia, X., Hernández-Ramos, F., Morales, A., **Izaguirre, N.**, de Hoyos-Martínez, P. L., Labidi, J., 2021. Lignin extraction and isolation methods in: Lignin-based Materials for Biomedical Applications: Preparation, Characterization, and Implementation. Elsevier Inc., pp. 61-104. 10.1016/B978-0-12-820303-3.00004-7.

Contributions to the following works presented in the following scientific conferences have also been carried out throughout the thesis:

1. *Authors:* **Izaguirre, N.**, Gordobil, O., Guerreiro, L., Labidi J.
   Title: Lignin fractionation by means of organic solvents
   Conference: ECCE12-ECAB5
   Presentation: Poster
   Place: Florence (Italy)
   Date: 09/15/2019-09/19/2019

2. *Authors:* **Izaguirre N.**, Gordobil O., Robles E., Labidi J.
   Title: Sequential organic solvent extraction and characterization of kraft and organosolv lignins
   Conference: 1st GREENERING International Conference
   Presentation: Poster
   Place: Lisbon (Portugal) - online
   Date: 02/15/2021-02/16/2021

3. *Authors:* Robles, E., **Izaguirre N.**, Martin A., Moschou D., Labidi J.
   Title: Comparison of Bleached and Unbleached Nanopaper from Pistachio Shells
   Conference: 1st GREENERING International Conference
   Presentation: Oral
   Place: Lisbon (Portugal) - online
   Date: 02/15/2021-02/16/2021

4. *Authors:* **Izaguirre, N.**, Robles, E., Llano-Ponte, R., Labidi, J., Erdocia, X.
   Title: Lignin Fractionation for Fine-Tuned Properties
   Conference: WasteEng2022
   Presentation: Oral
   Place: Copenhagen (Denmark)
   Date: 06/27/2022-06/28/2022

5. *Authors:* Robles, E., **Izaguirre, N.**, Martín, A., Labidi, J.
   Title: Use of pistachio shells for lignocellulosic biomass
   Conference: WasteEng2022
   Presentation: Oral
   Place: Copenhagen (Denmark)
   Date: 06/27/2022-06/28/2022

6. *Authors:* **Izaguirre, N.**, Erdocia, X., Llano-Ponte, R., Labidi, J.
   Title: Deposition of lignin particles on the surface of treated and non-treated active carbon
   Conference: NINE23
   Presentation: Oral
   Place: Venice (Italy)
   Date: 06/25/2023-06/27/2023

7. *Authors:* **Izaguirre, N.**, Fernández-Rodríguez, J., Robles, E., Labidi, J.
   Title: Sonochemical oxidation for nanolignin production
   Conference: ECCE14-ECAB7
   Presentation: Oral
   Place: Berlin (Germany)
   Date: 09/17/2023-09/21/2023

8. *Authors:* Wolf, M., Pacual-Jose, B., **Izaguirre, N.**, Labidi, J., Ribes-Greus, A.
   Title: Study of Sulfonation of Chitosan-based Composite Membranes containing fractionated Kraft and Organosolv Lignin for Fuel Cell Applications
   Conference: ESAM2023
   Presentation: Oral
   Place: Gandía (Spain)
   Date: 10/15/2023-10/18/202

ANNEX I

A.1. RAW MATERIAL CHARACTERIZATION

Moisture (T 412 om-16), ash (TAPPI T 211 om-16, 2016), solvent extractives (TAPPI T 204 cm-07, 2007) (using toluene instead of benzene), acid-insoluble and soluble lignin (TAPPI T 222 om-11, 2011), and hemicellulose [1] and cellulose [2] content were determined for the characterization of the raw materials.

A.1.1. MOISTURE

2.00 ± 0.01 g of sample were weighed before and after drying at 105 °C for 24 h and the moisture content was calculated gravimetrically [3].

A.1.2. ASH CONTENT

1.00 ± 0.01 g of sample were heated at 525 ºC for 3 h, cooled until RT and weighted to calculate the ash content gravimetrically [4].

A.1.3. EXTRACTIVES CONTENT

4.00 ± 0.1 g of sample were introduced in a cellulose cartridge, assembled in a Soxhlet extractor, and the extractives were solubilized in 150 mL toluene/ethanol mixture (2:1 v/v ratio), in multiple cycles for a maximum of 6 h period. The extractives were dried at 105 °C for 24 h and weighed [5].

A.1.4. ACID SOLUBLE LIGNIN (ASL) AND ACID INSOLUBLE LIGNIN (AIL) CONTENT

Quantitative Acid Hydrolysis (QAH) was used for the determination of the ASL and AIL. 0.25 ± 0.001 g of sample were heated in a water bath at 30 °C for 1 h with 2.5 mL of 72% H_2SO_4 solution. The solution was transferred to autoclave bottles and diluted to around 4% H_2SO_4. The bottles were autoclaved at 121 ºC for 1 h, and the solid was filtered and washed until

neutral pH. This solid phase, which is the AIL, was recovered and dried at 105 °C until constant weight. The liquid obtained was used for the ASL determination. The liquid was diluted using 1 M H_2SO_4, until the absorbance values obtained at 205 nm by UV–vis spectrophotometry were around 0.1-0.9, and they were recorded in triplicate [6]. The absorbance values were inserted in the following equation:

$$\%ASL = \frac{A \cdot B \cdot C}{D \cdot E} \times 100 \qquad Eq.A.1.$$

where A is the absorbance value at 205 nm, B is the dilution factor, C is the filtrate volume, D is the extinction factor (100 g/L cm), and E is the sample weight. 1M H_2SO_4 was used as the blank solution for the UV-vis measurements.

A.1.5. HOLOCELLULOSE CONTENT

2.5 ± 0.1 g of extractive free sample were dissolved in 80 mL hot water and introduced in a bath at 70 ºC. Hourly additions of 0.5 mL acetic acid glacial and 2.6 mL of 25% (w/w) $NaClO_2$ were completed during 6–8 h, and the solution was maintained on the bath overnight before filtering it. The solid was dried and weighed for the holocellulose determination.

A.1.6. CELLULOSE CONTENT

2.0 ± 0.1 g of the holocellulose obtained was used for the cellulose determination. 10 mL of 17.5% (w/w) NaOH were added, and 3 more additions of 5 mL of the same solutions were made every 5 min. Finally, 33 mL of deionized water were added, and the solution was left to settle for 1 h before filtering. The solid was washed by adding 100 mL of 8.3% (w/w) NaOH and 2 more additions of 100 mL of hot deionized water. The fibers were then covered using 15 mL of 10% (v/v) acetic acid for 3 min and

washed with water until neutral pH. The solid was dried overnight at 100 °C and weighed.

A.1.7. HEMICELLULOSE CONTENT

The hemicellulose content was determined by the subtraction of cellulose from the holocellulose.

A.2. PHYSICOCHEMICAL CHARACTERIZATION METHODS

A.2.1. ELEMENTAL ANALYSIS (EA)

The elemental analyzer equipment used was Leco TruSpec Micro. An amount of 2 mg of sample was heated at 1050 °C, and pure helium (3X Nippon Gas) and extra pure oxygen (4X Nippon Gas) was used as carrier gas and test gas, respectively. The samples were analyzed in triplicate, and sulfamethazine Leco (C=51.78%; H=5.07%; S=11.52%; O=11.5%; N=20.13%) was used for the calibration [7] of the lignin samples. For the carbon-lignin composite samples acetanilide (C=71.09%, H=6.71%, N=10.36%, O=11.84%) was used as calibration.

A.2.2. FOURIER TRANSFORMED INFRARED (FTIR) SPECTROSCOPY

FTIR spectra were recorded employing a PerkinElmer Spectrum Two FTIR Spectrometer equipped with a Universal Attenuated Total Reflectance accessory with internal reflection diamond crystal lens to observe the chemical structure of the lignins and identify their characteristic functional groups. The wavenumber range was defined from 4000 to 600 cm^{-1}, with a resolution of 4 cm^{-1} and 64 scans. The assignment of the main bands obtained are listed in Table A.1.

Table A.1. Assignment of the main bands obtained in FTIR spectrophotometry.

Absorption frequency range (cm^{-1})	***Assignment***
3400	ν(O-H) stretching of phenolic hydroxyl and aliphatic hydroxyl groups
2940 and 2840	ν(C-H) methyl (-CH3) and methylene (-CH2-) groups
1708	ν(C=O) stretching of unconjugated ketones, conjugated aldehydes and carboxylic acids
1610 and 1515	Aromatic skeletal vibrations (guaiacyl-syringyl)
1460	δ(C-H) methyl (-CH3) and methylene (-CH2-) groups
1425	Aromatic skeletal vibrations combined with δ(C-H) (in-plane)
1329	ν(C-O) syringyl
1217	ν(C-O) guaiacyl
1150	ν(C-O) aliphatic ethers
1033	ν(C-O-C) ether linkage and phenolic hydroxyl groups
910	δ(C-H) (out-of-plane) aromatic
835	ν(C-O) aliphatic ethers

A.2.3. Gel Permeation Chromatography (GPC)

GPC determined molecular weight (Mw) and polydispersity index (PI) of lignins. A Jasco LC-Net II/ADC device equipped with a RI-2031 Plus Intelligent refractive index detector, two PolarGel-M columns (300 mm × 7.5 mm) placed in series and PolarGel-M guard (50 mm 7.5 mm) was used. 20 µL of 50 ppm lignin solution was injected for each measurement. The solvent of the solution was N,N-dimethylformamide (DMF) with 0.1% of lithium bromide (LiBr), also used as the mobile phase of the column. The column eluded the mobile phase at 40 ºC and a flow rate of 0.7 mL/min. Polystyrene with molecular weights ranging from 266 to 70,000 g/mol was used as the standard for the calibration curve.

A.2.4. PHOSPHOROUS-31 NUCLEAR MAGNETIC RESONANCE SPECTROSCOPY (^{31}P NMR)

^{31}P NMR was used for the quantitative determination of hydroxyl groups and the S/G ratio. Pyridine (Py) and deuterated chloroform ($CDCl_3$) were used as a solvent in a ratio of 1.6:1 (v/v), respectively. 50 mg of each lignin sample were solubilized in 0.5 mL of the solvent, and 0.1 mL of Internal Standard (IS) was added to each sample. The IS solution was prepared, adding 5 mg of chromium (III) acetylacetonate ($Cr(acac)_3$) and 18 mg of N-Hydroxy-5-norbornene-2,3-dicarboxylic acid imide (NHND) per 1 mL. Once the samples were dissolved, 0.1 mL of 2-Chloro-4,4,5,5-tetramethyl-1,3,2-dioxaphospholane (TMDP) was added to carry on the phosphitylation. ^{31}P NMR spectra were recorded in a Bruker AVANCE 500 MHz, using the parameters recommended by Meng et al. 2019 [8], and MestReNova 11.0 was used for the data processing. The typical ^{31}P NMR spectra obtained for lignin samples is shown in Figure A.1, where the area used for the quantification is colored in blue (152-132 ppm), while Figure A.2 shows each region of the spectra. Specific spectral regions can be associated with different hydroxyl types: 144–137 ppm corresponds to the total phenolic OH content (from 144 to 141.5 ppm are C5-substituted OH groups, that are considered equivalent to S unit OH groups, from 140.5 to 139 ppm are G unit OH groups, and from 139 to 137 ppm are H unit OH groups), 150–145 ppm range corresponds to aliphatic OH groups and 136–134 ppm to carboxylic acid OH groups. The integrated areas of these regions were compared with the standard internal signal, and the concentrations of the OH groups were quantified.

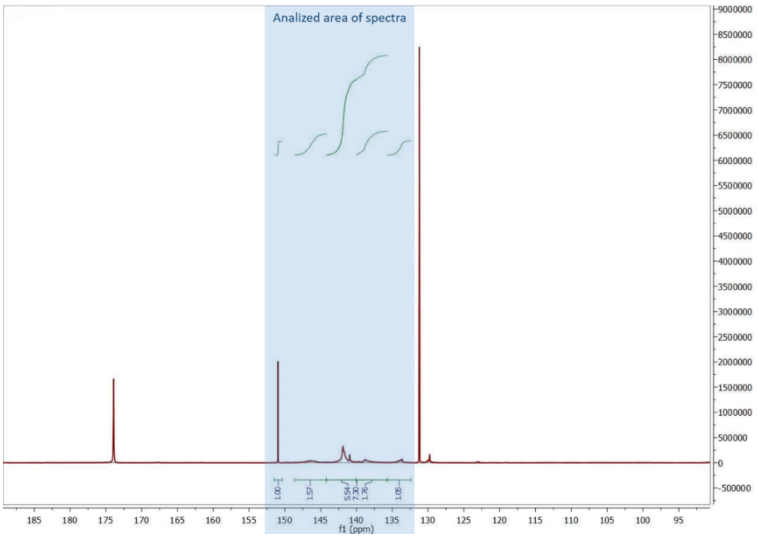

Figure A.1. The ^{31}P NMR spectra for lignin samples, and the area selected for the OH content determination.

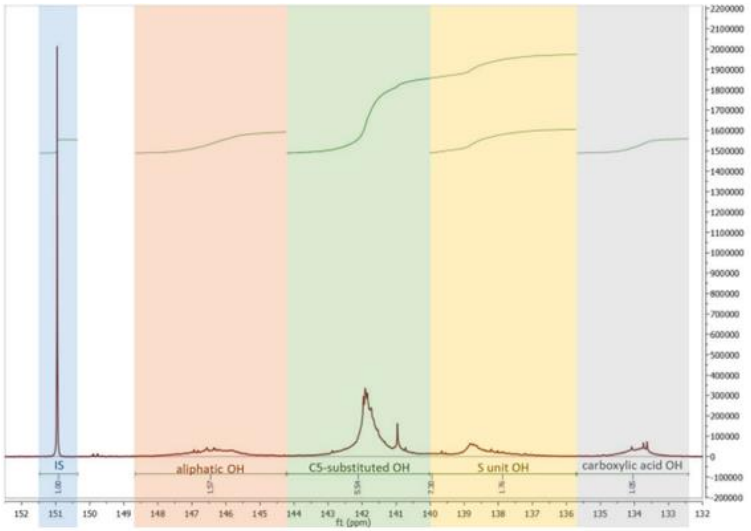

Figure A.2. Specific spectral regions associated with different hydroxyl types.

A.2.5. Carbon-13 nuclear magnetic resonance (^{13}C NMR)

^{13}C NMR spectroscopy was used to further elucidate the chemical structures of the samples. DMSO-d_6 was used as the solvent, and sample solutions of 100 mg/mL were prepared. The spectra were recorded in a Bruker AVANCE 500 MHz. These spectra provide information on the nature of all the carbon atoms of the molecules.

A.2.6. Ultraviolet–visible spectrophotometry (UV-vis)

UV–vis spectrophotometry (Jasco V-630 spectrophotometer) was used to determine the conjugated and non-conjugated OH groups following the method proposed by Yuan et al. 2009 [9]. Briefly, 5 mg of lignin was dissolved in 10 mL of dioxane/H_2O 95% (v/v). Next, 1 mL of that solution was diluted in 10 mL of dioxane/H_2O 50% (v/v). The final solvent was analyzed by measuring the absorbance values in the range of 400–260 nm.

The spectrophotometric method of Folin-Ciocalteau was used to determine the total phenolic content of the oxidized lignins. The following procedure was followed: lignin samples were dissolved in dymethylsulfoxyde (DMSO) (2 g/L), and Na_2CO_3 was dissolved in water (200 g/L). 0.5 mL of lignin sample, 2.5 mL of Folin-Ciocalteau reagent, and 5 mL of Na_2CO_3 solution were added to a flask. H_2O was added until the volume reached 50 mL. Flasks were protected from the light and heated in a bath at 40 °C for 30 minutes. For the calibration curve, six different concentrations of gallic acid ranging from 1000 to 100 mg/L were prepared and analyzed following the procedure described by García et. al. 2012 [10].

A.2.7. Pyrolysis - gas chromatography / mass spectrometry (Py-GC/MS)

The gases from the pyrolysis of the original lignin samples and their fractions were analyzed. For this, a gas chromatograph coupled to a mass spectrometer (Agilent Techs. Inc. 6890 GC/5973 MSD), a 5150 Pyroprobe filament pyrolyser (CDS Analytical Inc., Oxford, PA), and an Equity-1701 (30 m × 0.20 mm×0.25 μm) fused-silica capillary column were used. The method followed was described by Herrera et al. 2014 [11]. The samples were introduced in a quartz crucible and heated with a 20 °C/min (ramp-off) heating rate until 600 °C of temperature was reached and maintained for 15 s while keeping the interface at 260 °C. Helium gas was used to provide inert conditions for the purge of the pyrolysates from the pyrolysis interface to the gas chromatograph injector. The oven program started at 50 °C, was held for 2 min, and raised to 120 °C at 10 °C/min. Next, it was held for 5 min. After that, it was raised to 280 °C at 10 °C/min, held for 8 min before finally raising it to 300 °C at 10 °C/min and held for 10 min. For identifying the compounds, the obtained mass spectra were compared to those reported by the National Institute of Standards Library (NIST Number 69) and other compounds reported in the literature [12–15], and the most commonly identified lignin derivative compounds are listed in Table A.2.

Table A.2. Py-GC/MS derivative compounds identified.

Unit	*Compound*	*m/z*
H	Catechol	110/64/63
	4-Methylphenol	107/108/77
	Phenol	94/66/65
	K-Cresol	121/136/77
G	Eugenol	164/103/77
	3-Methoxycatechol	140/125/97
	Guaiacyl acetone	137/180/122
	Guaiacol	109/124/81
	4-Methylguaiacol	138/123/95
	4-Methylcatechol	124/123/95
	4-Ethylguaiacol	137/152/122
	4-Vinylguaiacol	135/150/107
	Acetoguaiacone	151/166/123
	3-Methylguaiacol	123/138/77
	4-Carboxy-2-methoxyphenol	153/168/125
	Vanillin	151/152/81
	Propioguaiacone	151/180
	3-Methoxy-5-methylphenol	138/109/107
	4-Propylguaiacol	137/166/122
S	Syringol	154/139/111
	4-Ethylsyringol	167/182/168
	4-Propenylsyringone	194/91/119
	Acetosyringone	181/196/153
	Syringaldehyde	182/181/111
	4-Propylsyringone	181/182/210
	Propiosyringone	181/182/210
	4-Vinylsyringol	180/165/137
	4-Methylsyringol	168/153/125

A.2.8. X Ray Photoelectron Spectroscopy (XPS)

X Ray Photoelectron Spectroscopy (XPS) measurements were carried out in a Versaprobe III Physical Electronics (ULVAC) with Al Kα (148.7 eV) monochromatic radiation source. An initial analysis was carried out to determine the elements present (wide scan: step energy 0.2 eV, pass energy

24 eV), followed by the detailed analysis of the detected elements (detail scan: step energy 0.05 eV, pass energy 27 eV, time per step 20 ms) with an electron exit angle of 45^0. The spectrometer was previously calibrated with Ag (Ag 3d5/2, 368.26 eV). The spectra were adjusted using the software CasaXPS 2.3.26, which models the contributions after a base subtraction (Shirley). The Gaussian deconvolution of the peaks was carried out by OriginPro 2009.

A.3. THERMAL PROPERTIES CHARACTERIZATION

A.3.1. THERMOGRAVIMETRIC ANALYSIS (TGA)

A TGA/SDTA RSI analyzer (Mettler Toledo) was used for the thermogravimetric analyses, heating 5-10 mg of sample from 25 ºC to 800 ºC, at a rate of 10 ºC/min in an inert atmosphere, from which the main thermal degradation parameters were identified.

A.3.2. DIFFERENTIAL SCANNING CALORIMETRY (DSC)

DSC was performed using a DSC822e (Mettler Toledo). The process consisted of heating from -25 ºC to 225 ºC at 10 ºC/min, followed by cooling to -25 ºC at the same rate. Finally, a second heating to 225 ºC was done with the same parameters as the first one. This scan was used for the determination of the glass transition temperature (T_g) of each sample.

A.4. MORPHOLOGICAL CHARACTERIZATION

A.4.1. DYNAMIC LIGHT SCATTERING (DLS)

The particle size and Z Potential of the lignin macromolecules were determined by DLS. A ZetaSizer Ultra (Malvern Panalytical) equipped with a He–Ne laser source (=633 nm) and a scattering angle of 173° was used. Particles were dispersed in deionized water at a concentration of 0.1 wt%

and immersed for 15 min in an ultrasonic bath. The dispersions were measured at room temperature, and an average of 20 collections were recorded for each result [16].

The composites created out of lignin and active carbon and graphite were also characterized by DLS. The sample preparation procedure followed was similar, with some modifications. 0.5 wt. % of dispersed sample solutions was prepared. The solutions were stirred overnight, and US forces were applied for better homogeneity. Additionally, three different solutions were prepared and used as titrants: a 0.5M HCl solution, a 0.1M HCl solution, and a 0.5M NaOH solution. These solutions were slowly added for obtaining pH values from 2 to 10 and observe how the media affected the particle size and Z Potential of the composites.

A.4.2. Atomic Force Microscopy (AFM)

AFM images of the sample surfaces were recorded in tapping mode, using a Nanoscope IIIa scanning probe microscope (Multimode TM Digital instruments) and a cantilever/silicon probe, generating an integrated force. The cantilever's length was 125 μm, and the tip radius was 5–10 nm. 0.035 wt.% aqueous dispersions were prepared, and indirect ultrasonication was applied. A drop of the sample solution was deposited in the holder and analyzed when dried. Particle sizes and/or thicknesses were calculated using the software NanoScope Analysis.

A.4.3. Transmission Electron Microscopy (TEM)

Electron microscopy analysis were carried out using a TECNAI G2 20 TWIN operated at 200 kV and equipped with LaB6 filament. Samples were prepared by first preparing a 0.1 wt.% aqueous suspension, a drop of which was then suspended onto a TEM copper grid (300 Mesh) covered by a pure carbon film for 1 min. The grid was afterward blotted with filter paper and

placed onto a drop of 2% uranyl acetate for 20 seconds. It was finally washed twice using distilled water for 20 seconds each time. Particle sizes were calculated using the software Image J, and ten particles of each sample were calculated to get the average particle size values.

A.4.4. Scanning Electron Microscopy (SEM)

SEM images were recorded with a Hitachi S-4800 FEG-SEM operating at an accelerating voltage of 5kV. Samples were previously coated with a 15 nm gold layer in an Emitech K550x ion sputter.

A.4.5. Brunauer–Emmett–Teller (BET) method

The surface area and pore characteristics were analyzed by the Brunauer–Emmett–Teller (BET) method. The selected samples were dried at 200 °C for 16 h and measured at 77 K by a nitrogen adsorption-desorption analyzer (Micrometrics ASAP 2420 V2.09). The isotherms were carried out in the range in which the BET equation can be applied for the SSA determination (P/P_o from 0.01 to 0.4). The used adsorption gas was nitrogen, and the set temperature was 77.3 K.

A.5. Electrochemical characterization

A.5.1. Three-electrode glass-cell

For the electrochemical analysis of the active material composite synthesized, a three-electrode glass-cell was used. For that, a working electrode (WE) was assembled using the active material synthesized. 30 mg of composite material were dissolved in 250 µL of NMP (10% dry mass of PVDF). The solution was stirred until its complete dissolution and 10 µL of the solution were poured in a glassy carbon membrane (7 x 7 x 0.5 mm), used as a current collector, and dried at 60 °C overnight. The reference

electrode (RE) used was composed of Ag/AgCl (KCl 3.5M) and a Pt wire was used as the counter electrode (CE). A BioLogic VSP potentiostat/galvanostat was used for the measurements. The scheme of the setup is shown in Figure A.3.

CV measurements were carried out from -0.2 to 0.8 V at different scan rates (5, 10, 15, 20, 25 and 50 mV/s). The CV cycles obtained were used for the capacity determination, using the absolute value of their integration as the area value in the following equation (Equation A.2.):

$$C_p = \frac{A}{2\ m\ k\ \Delta V} \qquad Eq.A.2$$

where C_p is the capacity (F/g), A is the area of the CV curve (A·V), m is the mass of the active material (g), k is the scan rate (V/s) and ΔV is the voltage range (V).

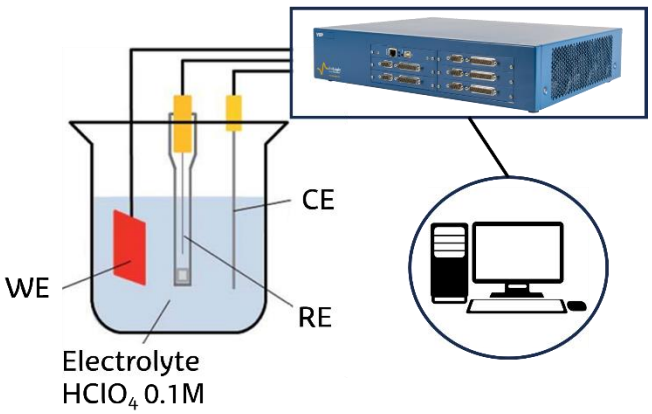

Figure A.3. The three-electrode glass-cell employed.

The influence of the scan rate on the capacitance obtained can be useful to determine the electrochemical charge storage mechanism of the active material. There are three types: electric double-layer capacitors (EDLC),

pseudocapacitors (PS), and batteries. Faradaic processes happen in the first two types, and the reactions are surface-controlled. Meanwhile, the third type is generated by non-Faradaic processes, and they are controlled by diffusion processes. Consequently, the kinetics of the processes happening are also different. To identify the type of process, Equation A.3 can be applied:

$$i = a \cdot v^b \qquad Eq.A.3$$

where i is the current, a and b are constants, and ν is the scan rate.

The b value reflects the kinetics of the reaction. When b equals 1.0 means that the process is surface-limited, and if b is 0.5 it means that the main phenomenon happening is a diffusion-controlled redox reaction [17].

EIS measurements were performed from 1MHz to 10 mHz. Each experiment was split into four sequences: very high (from 1 MHz to 100 KHz), high (from 100 KHz to 10 KHz), intermediate (from 10 KHz to 100 Hz), and low (from 100 Hz to 10 mHz), with 6, 10, 20, and 31 points per decade respectively. Once the spectra were obtained, the data was processed through Matlab R2022a and the DRTtools extension to obtain the Distribution of the Relaxation Time (DRT) graphs, which was useful for the identification of the elements and design of the Equivalent Circuit Models (ECM). The ECM designed was introduced in the EC-Lab software and fitted to the experimental Nyquist plot. Once a proper fit was obtained, the values of each of the elements conforming the ECM were recorded. Moreover, EIS C_p values were calculated using the PseudoC tool of the EC-Lab, equivalent value to the Constant Phase Element (CPE) value obtained from the ECM.

Moreover, porosity characteristics of the sample were also observed by representing the Bode plot and observing the phase angle variations. The

polarization processes, and consequently, their relaxation times, are linked to the CPE-R couple that operates in that frequency range, and consequently, in the layer in which the material (inner or outer) is working in that frequency. From that CPE-R couple, the equivalent specific capacitance will be obtained, which will therefore be linked to the porosity of the material and the ease with which it accepts charge and discharge [18]. Mesopores (2–50 nm) provide low resistive ion transport pathways essential for fast power delivery, while the micropores (<2 nm) provide higher specific surface area essential for high energy density. Moreover, the length of these pores and the surface heterogeneity will also depend on the specific capacitance obtained size [19–21]. To observe the porosity effect on the EIS results, impedance modulus (Log|Z|($\Omega \cdot cm^2$) and impedance phase angles ($\varphi(^o)$) were plotted against the frequency.

Galvanostatic charge/discharge (GCD) cycles were also performed to observe the durability of the materials and measure the Cp of each cycle at different current densities (I_m). Three different current densities ranging from 0.2 to 5 A/g were used, and 100 cycles of charge and discharge were carried out in the potential range of -0.2 and 0.8 V. The specific capacitance of selected cycles was calculated by the following Equation A.3:

$$C_p = \frac{I_m \cdot \Delta t}{\Delta V} \qquad Eq.A.3$$

where C_p is the capacity (F/g), I_m is the current density (A/g), Δt is the time range of discharge (s) and ΔV is the potential range of the discharge (V) [22,23].

CV and EIS results are obtained both pre-GCD and post-GCD.

A.5.2. TWO-ELECTRODE HALF-CELL

Two-electrode half-cell batteries were used for the analysis of the stability of the anodic electrodes prepared. Different lignins were used as binder in the formulation of anodes, and their performance was compared to the electrodes formulated with water based carboxymethylcellulose (CMC) and NMP based Polyvinylidene fluoride (PVDF) as binder.

The formulation of the anode used was 92% of active material, 3% of additive material, and 5% of binder. The active material used was Biohard Carbon Type 2 (5 μm) and the additives were Carbon Black C45 in the case of water-based slurries and C65 for NMP based slurries. The solvent used was distilled water, and the solid content of the slurry obtained was around 30-35 wt%. The slurry solution was deposited in a copper (Cu) foil, with a set thickness of 150 μm. The electrode was dried under the fumehood at low flux.

Once the Cu deposition was dry, 12 mm or 10 mm diameter electrodes were punched and dried under vacuum at 120 °C overnight, depending on the cell type assembled. Swagelok cells and 2032 coin cell batteries were used for the assembly of the half-cells. For that, a 12 mm diameter $LiFePO_4$ was introduced, along with a glass fiber separator, 200 μL of electrolyte (1M $LiPF_6$ dissolved in 1/1 DMC/EC (LP30)), and the anodic electrode. Schemes of the cells for two-electrode half-battery analyses are shown in Figures A.4 and A.5.

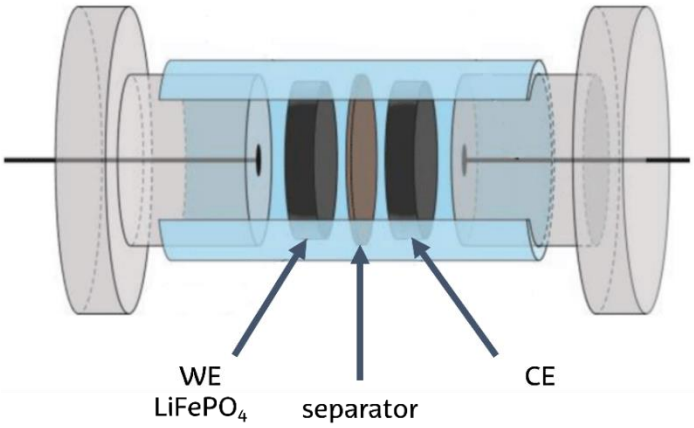

Figure A.4. The scheme of a Swagelok cell battery.

5 cycles of CV and EIS measurements were carried out. CVs were performed at 0.1 mV/s scan rate, and in the range from 0.01 to 3.00 V. The EIS measurements were carried out before and after each CV cycle, from 300 kHz to 1 Hz.

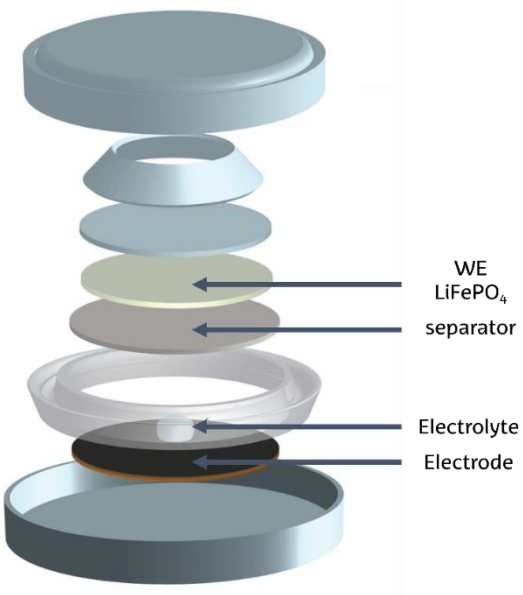

Figure A.5. 2032 coin cell battery.

Once the CV and EIS measurements were finished, Galvanostatic Charge Discharge (GCD) analysis were carried out. Different cycles at different currents, between 5 and 10 cycles for each cycle, were performed for the Coulombic efficiency and charge and discharge capacity measurements of each cycle, in the following order:

- 10 cycles at 20 mA h g^{-1}
- 5 cycles at 50 mA h g^{-1}
- 5 cycles at 100 mA h g^{-1}
- 5 cycles at200 mA h g^{-1}
- 5 cycles at 300 mA h g^{-1}
- 5 cycles at 500 mA h g^{-1}
- 5 cycles at 1000 mA h g^{-1}
- 5 cycles at 20 mA h g^{-1}

A.6. REFERENCES

[1] Wise LE, Maxime M, D'Addieco A. Chlorite holocellulose, its fractionation and bearing on summative wood analysis and on studies on the hemicelluloses. Tech Assoc Pulp Pap Ind 1946;29:210–8.

[2] Rowell RM. The chemistry of solid wood. Based on a short course and symposium sponsored by the Division of Paper and Textile Chemistry at the 185th meeting of the American Chemical Society, Seattle, Washington, March 20-25, 1983., 1984.

[3] T 412 om-16. Moisture in pulp, paper and paperboard. Peachtree Corners, GA: 2016.

[4] TAPPI T 211 om-16. Ash in wood, pulp, paper and paperboard: combustion at 525 degrees. Peachtree Corners, GA: 2016.

[5] TAPPI T 204 cm-07. Solvent extractives of wood and pulp. Peachtree Corners, GA: 2007.

[6] A. Sluiter, B. Hames, R. Ruiz CS, Slui J, ter, D. Templeton and DC. Determination of Structural Carbohydrates and Lignin in Biomass: Laboratory Analytical Procedure (LAP). Tech Rep NREL/ TP -510 -42618 2008:1–15.

[7] De Menezes FF, De Rocha GJM, Filho RM. Obtainment and characterization of lignin from enzymatic hydrolysis of sugarcane bagasse of 2G ethanol process in pilot scale. Chem Eng Trans 2016;50:397–402. https://doi.org/10.3303/CET1650067.

[8] Meng X, Crestini C, Ben H, Hao N, Pu Y, Ragauskas AJ, et al. Determination of hydroxyl groups in biorefinery resources via quantitative 31P NMR spectroscopy. Nat Protoc 2019;14:2627–47. https://doi.org/10.1038/s41596-019-0191-1.

[9] Yuan TQ, He J, Xu F, Sun R-C. Fractionation and physico-chemical analysis of degraded lignins from the black liquor of Eucalyptus pellita KP-AQ pulping. Polym Degrad Stab 2009;94:1142–50. https://doi.org/10.1016/j.polymdegradstab.2009.03.019.

[10] García A, González Alriols M, Spigno G, Labidi J. Lignin as natural radical scavenger. Effect of the obtaining and purification processes on the antioxidant behaviour of lignin. Biochem Eng J 2012;67:173–85. https://doi.org/10.1016/j.bej.2012.06.013.

[11] Herrera R, Erdocia X, Llano-Ponte R, Labidi J. Characterization of hydrothermally treated wood in relation to changes on its chemical composition and physical properties. J Anal Appl Pyrolysis 2014;107:256–66. https://doi.org/10.1016/j.jaap.2014.03.010.

[12] Del Río JC, Gutiérrez A, Hernando M, Landín P, Romero J, Martínez ÁT. Determining the influence of eucalypt lignin composition in paper pulp yield using Py-GC/MS. J Anal Appl Pyrolysis 2005;74:110–5. https://doi.org/10.1016/j.jaap.2004.10.010.

[13] Fernández-Rodríguez J, Gordobil O, Robles E, González-Alriols M, Labidi J. Lignin valorization from side-streams produced during agricultural waste pulping and total chlorine free bleaching. J Clean Prod 2017;142:2609–17. https://doi.org/10.1016/j.jclepro.2016.10.198.

[14] Li H, McDonald AG. Fractionation and characterization of industrial lignins. Ind Crops Prod 2014;62:67–76. https://doi.org/10.1016/j.indcrop.2014.08.013.

[15] Vane CH. The molecular composition of lignin in spruce decayed by white-rot fungi (Phanerochaete chrysosporium and Trametes versicolor) using pyrolysis-GC-MS and thermochemolysis with tetramethylammonium hydroxide. Int Biodeterior Biodegrad 2003;51:67–75. https://doi.org/10.1016/S0964-8305(02)00089-6.

[16] Gupta AK, Mohanty S, Nayak SK. Synthesis, Characterization and Application of Lignin Nanoparticles (LNPs). Mater Focus 2015;3:444–54. https://doi.org/10.1166/mat.2014.1217.

[17] Yu F, Huang T, Zhang P, Tao Y, Cui FZ, Xie Q, et al. Design and synthesis of electrode materials with both battery-type and capacitive charge storage. Energy Storage Mater 2019;22:235–55. https://doi.org/10.1016/j.ensm.2019.07.023.

[18] Mishra GK, Kant R. Modular theory for DC-biased electrochemical impedance response of supercapacitor. J Power Sources 2020;473. https://doi.org/10.1016/j.jpowsour.2020.228467.

[19] Largeot C, Portet C, Chmiola J, Taberna PL, Gogotsi Y, Simon P. Relation between the ion size and pore size for an electric double-layer capacitor. J Am Chem Soc 2008;130:2730–1. https://doi.org/10.1021/ja7106178.

[20] Wang H, Wen J. Biomass porous carbon-based composite for high performance supercapacitor. Mater Res Express 2020;7. https://doi.org/10.1088/2053-1591/abc442.

[21] Chmiola J, Yushin G, Gogotsi Y, Portet C, Simon P, Taberna PL. Anomalous increase in carbon at pore sizes less than 1 nanometer. Science (80-) 2006;313:1760–3. https://doi.org/10.1126/science.1132195.

[22] Bilal M, Landskron K. Activated Carbon Electrodes with Enhanced Supercapacitive Swing Adsorption of Carbon Dioxide. ECS Meet Abstr 2023;MA2023-01:2683–2683. https://doi.org/10.1149/ma2023-01552683mtgabs.

[23] Mathis TS, Kurra N, Wang X, Pinto D, Simon P, Gogotsi Y. Energy Storage Data Reporting in Perspective—Guidelines for Interpreting the Performance of Electrochemical Energy Storage Systems. Adv Energy Mater 2019;9:1–13. https://doi.org/10.1002/aenm.201902007.

List of Figures

CHAPTER 1

CHAPTER 4

CHAPTER 5

CHAPTER 6

CHAPTER 7

ANNEX I

LIST OF TABLES

CHAPTER 1

CHAPTER 4

CHAPTER 5

CHAPTER 6

ANNEX I